University of Strathclyde
Department of Electronic and Electrical Engineering

Black-Start Provision from Grid-Forming Converters: A New Network Restoration Paradigm

Abdulrahman Alassi

A thesis submitted in fulfilment of the requirements for the degree of
Doctor of Philosophy

2023

This thesis is the result of the author's original research. It has been composed by the author and has not been previously submitted for examination which has led to the award of a degree.

Signed: Abdulrahman Samir Alassi

Date: 14/02/2023

Acknowledgments

I would like to start by thanking my supervisors at the University of Strathclyde Dr. Khaled Ahmed and Dr. Agusti Egea-Alvarez for their continuous guidance and support throughout my PhD journey. They were always there whenever needed even on the non-technical fronts. I would also like to extend my gratitude to my industrial supervisor Dr. Colin Foote for his support and contribution to align the work to the industrial interests of ScottishPower.

A special thanks goes to Iberdrola for providing me with this unique opportunity to combine academic and industrial experiences by sponsoring my PhD and supporting my growth. My extended appreciation to Mr. Santiago Bañales Lopez and my amazing team at Iberdrola Innovation Middle East.

I am extremely grateful to my parents, family, friends and my wife Sara for their continuous encouragement and patience over the past few years. This endeavor would not have been possible without their support.

Lastly, I would also like to thank the composers of Game of Thrones, The Lord of the Rings, and Attack on Titan music. I spent countless hours listening to their soundtracks while working on my thesis, which certainly helped!

Abstract

Black-start service has been long associated with conventional power plants such as large synchronous generators. Given the rising penetration of converter-based resources such as solar, wind and battery storage, this thesis addresses black-start provision from the power electronic-based grid-forming converters (GFCs). Key challenges for converters black-start utilization can be attributed to their input resources intermittency, limited overcurrent capabilities against high network energization inrush currents, in addition to identifying suitable controllers for reliable GFC operation and black-start compatibility.

To tackle these points, the investigations in this thesis begin by proposing an innovative energy management system (EMS) that aims to maintain the converter input DC side reliable operation for prolonged periods, especially when a GFC is interfaced to a DC network consisting of multiple resources. The EMS is validated through simulations and a scaled lab setup. Then, the high transformer energization inrush currents are addressed through analyzing techniques that require direct GFC control manipulation such as soft energization (SE), against classical methods such as controlled switching (CS). Detailed theoretical transformer models are derived to quantify inrush current influencing factors. A new SE voltage ramp-rate estimation framework is then introduced, given the arbitrary ramp-rates definition in the literature. These techniques are tested in a detailed case study, where a GFC is used to energize a large network consisting of multiple transformers, and under various sensitivity scenarios.

Four GFC controllers are benchmarked to assess their SE and black-start compatibility, namely: droop, power synchronizing control (PSC), virtual synchronous machine (VSM), and matching control. VSM grid-forming control is selected based on the comparison, and modifications to its classical form are proposed to improve its black-start compatibility such as voltage support and grid-synchronization. The modified controller is validated in complete black-start scenarios, through simulation and novel power hardware in the loop (PHiL) experiments that enable testing hardware converters to energize and synchronize to simulated networks in digital real-time simulation (DRTS) platforms. Overall, the presented in-depth analysis and investigations aim to provide thorough insights to researchers and industrial engineers on black-start feasibility from GFCs.

List of Acronyms

AC	Alternating Current
ADC	Analog to Digital Converter
BESS	Battery Energy Storage System
CB	Circuit Breaker
CHiL	Control Hardware in the Loop
DRTS	Digital Real-Time Simulator
DAC	Digital to Analog Converter
DC	Direct Current
dVOC	dispatchable Virtual Oscillator Control
DER	Distributed Energy Resource
DSO	Distribution System Operator
EMS	Energy Management System
GFC	Grid-forming Converter
HIL	Hardware in the Loop
HuT	Hardware Under Test
HVDC	High-Voltage DC
ITM	Ideal Transformer Method
LPF	Low Pass Filter
MPPT	Maximum Power Point Tracking
MVDC	Medium-Voltage DC
MPC	Model Predictive Control
OLTC	On-Load Tap Changer
PCD	Partial Circuit Duplication
PMSG	Permanent Magnet Synchronous Machine
P&O	Perturb and observe
PV	Photovoltaic
PCC	Point of Common Coupling
PoW	Point-on-Wave
PA	Power Amplifier

PEC	Power Electronic Converter
PHiL	Power Hardware in the Loop
PSC	Power Synchronizing Control
PSL	Power Synchronizing Loop
PIR	Pre-Insertion Resistor
PI	Proportional Integral
PR	Proportional Resonant
PWM	Pulse Width Modulation
RoCoF	Rate of Change of Frequency
RES	Renewable Energy Source
RMS	Root-Mean-Square
SCR	Short-Circuit Ratio
STC	Standard Test Conditions
SoC	State-of-Charge
SG	Synchronous Generator
VSM	Virtual Synchronous Machine
VR	Voltage Regulation
VSC	Voltage Source Converter

Table of Contents

List of Figures

List of Tables

Chapter 1 Introduction

The rising penetration of power-converters based resources into the power grid is gradually offsetting classical generation units. The utilization of new resources to provide ancillary services that have been dominated by synchronous generators is thus becoming an operational necessity. To that end, this thesis provides an in-depth investigation on the use of grid-forming converter (GFC) technology for black-start and network energization applications. The investigation starts by studying the anchor converter input DC side readiness for black-start. Expanding into the AC network restoration, the limited converters overcurrent capabilities necessitate analyzing and proposing suitable inrush current mitigation techniques that are coupled with AC network energization. Transformer energization techniques that are compatible with GFC control are thus analyzed and benchmarked against classical techniques that rely on network assets operation such as circuit breakers and relays. The GFC controller used for black-start should also be compatible with network energization and synchronization requirements. Thus, a comprehensive investigation is carried out to identify suitable grid-forming control techniques and propose relevant modifications to facilitate the black-start process. Large-scale practical testing of black-start provision through GFCs is a challenging task due to the vast ratings and the variable nature of network configurations. Power Hardware in the Loop (PHiL) is thus explored in this thesis as a potential flexible method that enables hardware GFCs testing under the highlighted network variations and dynamic conditions.

1.1. New Power System Paradigm

Large-scale electricity generation has historically been reliant on synchronous generators (SGs). In addition to their primary generation function, SGs possess inherent network stability support characteristics such as inertial response and high fault current levels. Generation-load balance has been known as a stochastic process that is difficult to predict, which makes it inevitable to face power imbalances within electricity networks. An inherent SG inertial support capability allows it to react very quickly to these events by releasing/absorbing kinetic energy stored in the machine rotor to slow/accelerate its

rotation when a load disturbance is detected. Following the inertial response, other high-level controllers (e.g., secondary control) are implemented to restore the system frequency value to its nominal and restore generation-load balance [1].

On the other hand, the increased renewable energy sources (RES) and Distributed Energy Resources (DER) penetration has been contributing to a significant change in this classical network-operating paradigm. Many of the RES and energy storage systems require Power Electronic Converters (PECs) for their grid-integration. A PEC lacks many of the synchronous generator inherent stability characteristics. Key grid-integration examples through PECs are wind and solar photovoltaic (PV) generation resources and battery energy storage systems (BESS). The total global installed capacity of these three asset types was 18% of the global total in 2019, which is expected to reach 64% by 2050 according to Bloomberg [2]. This trend signals a clear necessity to update conventional PECs control and energy management techniques to accommodate the requirements imposed by this new paradigm and to provide ancillary services that have been classically attributed to synchronous generators. One of the key ancillary services is black-start, which is used to restore networks that are exposed to blackout conditions. Investigating and validating black-start provision from converter-based resources is the main focus of this PhD thesis.

1.2. Black-Start between Classical and Modern Approaches

Although extremely rare, the occurrence of a system-level cascaded blackout results into the network operators and stakeholders bearing numerous costs [3]. For instance, the recent Texas blackout in 2021 is reported to have caused direct and indirect economic losses in the order of magnitude of tens of billions of dollars [4]. Classical approach considers SGs as main black-start resources, and several works address optimal allocation and the sequence of black-start under the assumptions that the process is undertaken by classical generation assets, while renewables are disconnected due to their intermittency, with the exception of hydro power plants [3, 5, 6]. The classical approach is quite effective since synchronous generators are strong sources that are inherently capable of establishing an electrical island and supporting its loads. That said, the highlighted increase in RES

penetration is offsetting conventional generation. It thus becomes necessary to consider renewable and battery storage resources as serious participants in the black-start market as anchor units to shorten blackouts duration and improve electrical networks reliability.

The grid-integration of many DERs is performed through Voltage Source Converters (VSC). These converters have classically been controlled in the 'grid-following' mode, operating the VSC as a current source to exchange active and reactive power with the grid, following its voltage measurement [7]. In a blackout scenario, this voltage measurement does not exist, and thus a VSC that is equipped only with grid-following control mode cannot be used as an anchor unit for black-start. On the other hand, the use of power converters in grid-forming mode enables them to establish an independent AC voltage at their terminals without relying on external measurements [8]. Grid-forming converter (GFC) technology is thus a key asset for improved utilization of black-start from renewable and distributed energy resources.

Based on the aforementioned points, two key approaches may be followed to preserve system strength and the network black-start readiness as a result of the emerging power systems paradigm and the increase in renewables grid integration: a) introducing a group of partially loaded synchronous generators/condensers as standby units for black-start, which adds more operational cost. b) operating/controlling the grid-following converters in grid-forming mode as independent voltage sources that are able to mimic a set of synchronous generators characteristics including black-start provision [9]. The latter alternative can also be combined with auxiliary synchronous condensers in the network bottlenecks in case the network Short-Circuit Ratio (SCR) value becomes critically low for increased reliability.

Successful utilization of GFCs as reliable black-start resources also serves an economic objective since the RES/DER network proportion is already increasing, thus minimizing the additional investments to provide such ancillary services on the long term. Therefore, utilities around the world are particularly interested in verifying such capabilities of VSC connected resources. For instance, National Grid in the United Kingdom (UK) released a three-reports study in June 2019 about the potential of DERs utilization for black-start applications [10]. One of the main study recommendations is to re-visit the existing black-

start standards that are currently carried out in the UK, mainly through using large-scale generators connected to the 400/275 kV network, due to the enormous magnitude of required/expected supply from such individual resources during a black-start event (e.g., requirement of a 100 MVAr for energizing the immediate connected network). Evidently, existing standards require thorough revision to accommodate the use of DERs for black-start at different voltage levels, and considering the aggregated performance and capabilities of interconnected smaller units. For instance, the energization of transformers and lines during network restoration can be performed, in principle, using soft-energization from grid-forming converters to avoid the excessive inrush current requirements [11, 12]. Though, several factors should be investigated such as the control robustness, and the compatibility of this technique with existing converter control and the effects/trade-offs of the voltage ramp duration.

1.3. Grid-forming Converters Compatibility

Operating an existing converter in grid-forming control mode might require simple software upgrades but might also require more expensive hardware installations to achieve reliable operation. Generally, a DC-AC converter is advised to have a controlled input DC voltage to reliably operate in grid-forming mode through dedicating its closed-loop voltage control objective to the AC side, thus expanding the grid-forming mode operating range. In this subsection, a brief overview is provided on main renewable sources (solar PV and wind turbines) and battery storage through common grid-connection topologies, with high-level assessment of their reliable grid-forming control operation compatibility. The relevance of this comparison stems from the fact that a VSC interfaced unit should be grid-forming compatible to be assigned as a black-start resource by the utility grid.

1.3.1. Type IV Wind Turbines

Wind turbines generate variable-frequency AC output that is dependent on factors such as wind speed. This output cannot be fed directly into 50 or 60 Hz networks and thus requires multiple-stage energy conversion. A common configuration based on Permanent Magnet Synchronous Machine (PMSG) uses AC-DC-AC converters to decouple the wind turbine variable frequency, and consequently the blades inertia, from its grid-connected output as

shown in Figure 1.1(a). The machine-side converter can be configured to maintain the DC link voltage while allowing the grid-side converter to operate in grid-forming mode. Several variations exist in the literature for operating Type IV wind turbines as grid-forming units, while also highlighting the positive impact of coupling the wind power output with BESS to maintain the required energy buffer for extended system operating range in the grid-forming mode.

1.3.2. Solar PV and BESS Variations

Standalone solar PV output is typically grid-connected through single-stage (DC-AC) or two-stage (DC-DC-AC) converters. Considering the grid-following two-stage configuration as an example, then the DC-DC converter scales the output PV voltage and tracks its Maximum-Power-Point (MPP), whereas the second stage controls the DC voltage and follows the AC grid reference. Figure 1.1(b) demonstrates the generic standalone solar PV implementation. While several implementations of GFC control are reported for both the single-stage [13] and two-stage [14] topologies, the operating grid-forming range can be limited since the solar PV may operate outside the MPP region to provide a power 'head-room' that enables the PV to operate as a dispatchable source [14]. The ongoing research on similar configurations is expected to improve their feasibility as reliable standalone grid-forming resources [15].

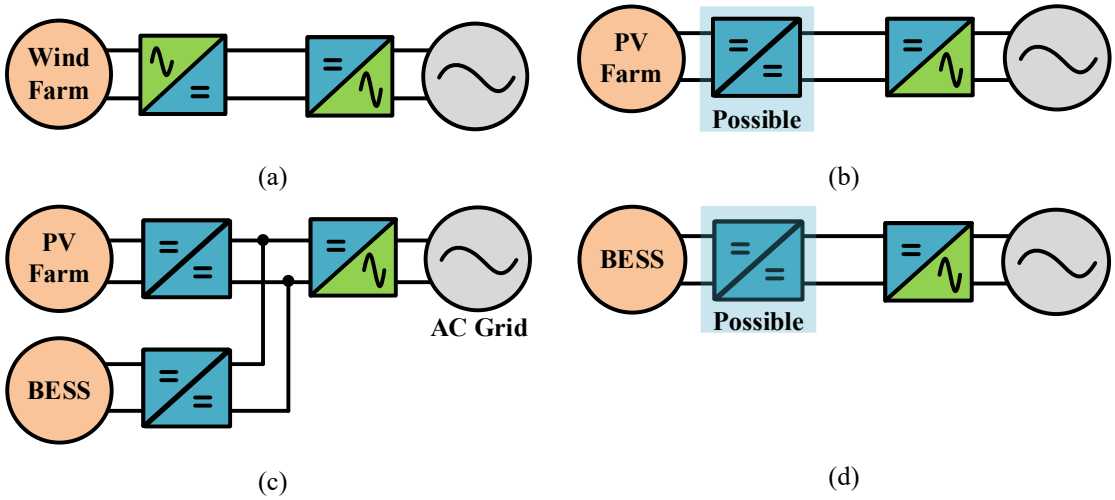

Figure 1.1: Common grid-connection PEC configurations for wind/PV and BESS: (a) Type IV wind farm, (b) PV farm, (c) PV and BESS, (d): standalone BESS.

Storage system (e.g., Battery Energy Storage System – BESS) topology is dependent on the standalone vs. co-located configuration with another source. For instance, if a BESS is DC-coupled with a PV system then a common structure is for the PV converter to track its Maximum Power Point through MPPT techniques, while the battery converter controls the DC-link voltage at the grid inverter input as in Figure 1.1(c). This enables the inverter to operate in the grid-forming mode with extended range. Finally, a standalone BESS system can be either directly grid-interfaced through an inverter, or through an intermediate DC-DC conversion stage that scales its output DC voltage as in Figure 1.1(d). Both options are in principle compatible with the main GFC operation requirements.

1.4. Research Motivation

Utilizing VSC integrated resources for black-start is still in its early stages with some reported trials [16, 17]. Several challenges are being addressed in the literature to fully exploit the grid-forming converters grid-support capabilities, including black-start. Key challenges for GFCs black-start deployment are presented in the 2019 UK National Grid study highlighted earlier [10]. The main black-start challenges identified from the three reports generated by this study are summarized in Table 1.1. The relevant topics are classified into three pillars: power converters, power systems and statistical analysis related. For each pillar, research lines are identified, with the key challenges and potential solutions. For instance, the power converter aspect revolves around identifying suitable control techniques that can be implemented to enable DERs to act as anchor units and achieve successful black-start sequences, such as innovative grid-forming controllers. The limited overcurrent capability of VSCs is another pressing issue. This is because of the high inrush currents that may arise from transformers and cables energization. Converters overcurrent capabilities are limited and typically restricted to 1.5 pu for very short durations [18], whereas transformer inrush currents for instance are known to approach several times the transformer rating. Integrating suitable inrush current mitigation techniques within the black-start framework thus becomes an important design factor for reliable operation. From power systems perspective, optimal sizing and allocation of black-start resources and the definition of a suitable energization sequence for the target

network are questions that are attracting research and industrial focus. This similarly applies to energization from single or combined resources. In the latter case, the emerging trend of DC networks (e.g., medium-voltage RES output collection grids) can be utilized where a DC network is combined into a unified entity that restores neighboring AC networks in the event of a blackout. Maintaining the DC side supply reliability and constant DC voltage is important in such cases to enable smooth GFC operation and to dedicate the grid-forming voltage control objective to the AC side. Proposing suitable energy management strategies to achieve the DC side black-start readiness thus similarly form an interesting research question. Power systems simulation is considered as an effective validation tool for black-start testing. Understandably, hardware testing on a real distribution network scale is a challenging task.

Table 1.1: Main research lines relevant to VSCs utilization in black-start.

	Power Converters	**Power Systems**	**Statistical Analysis**
Research Line	**Innovative Converters Control Algorithms**	**Power System Studies for Black-Start Capability**	**Storage SoC Estimation/ DER Output Forecast**
Key Challenges	Most converters operate in grid-following mode Limited converters overcurrent capabilities Low inertia and SCR of converters-based systems	The optimal size and location of black-start assets Limited validation prototypes for DER black-start capabilities Effectiveness of black-start energization sequences	DER availability for blackout responding Planning for SoC availability in black-start RES intermittency
Potential Solutions	Incorporating grid-forming capabilities in converters Identifying suitable inrush current mitigation methods Virtual inertia-based control techniques utilization	Developing methodologies for black-start sources size/locations Flexible testing and validation techniques such as PHiL Using high-fidelity models to test black-start sequencing algorithms	Real-time estimation of the available DERs for black-start Limiting the storage SoC_{min} to maintain readiness Developing flexible tools for DER output prediction

Utilizing flexible technologies such as Control Hardware in the Loop (CHiL) and Power Hardware in the Loop (PHiL) is thus an interesting path to provide flexibility between the tested anchor black-start source (partially or fully in hardware) and the energized network (in simulation). Statistical analysis due to the stochasticity associated with the renewable energy and storage resources availability is also an important factor when these resources are to be used for critical tasks such as black-start.

Collectively, the research lines reported in Table 1.1 form the basis for the thesis research motivation, which attempts to address different black-start related angles in the new power networks paradigm. In particular, the first pillar related to the power converter is investigated through addressing grid-forming control operation, identifying suitable controllers, and proposing relevant control modifications to improve the GFC black-start compatibility. An intersection between the first and second pillars is addressed through detailed investigation to identify suitable transformer inrush current mitigation techniques that fit the distributed networks restoration and grid-forming control requirements. The power system pillar is also addressed through carrying out comprehensive case studies for network energization as well as proposing flexible system validation through PHiL. Finally, the third pillar in Table 1.1 is also approached through the DC energy management system (EMS) that addresses resources availability for black-start.

1.5. Aim and Objectives

Based on the identified research gaps, the investigations carried out in this thesis aim to provide insightful analysis and methods for black-start execution from grid-forming resources, through addressing research questions that are related to the following points:

- Energy management in DC networks considering their black-start readiness.
- Inrush current mitigation for power transformers energization during black-start.
- GFC control techniques that are suitable for black-start requirements.
- Synchronization between different AC networks after black-start.
- Flexible real-time validation tools for the use of GFCs in black-start testing.

The abovementioned points cover the three components in a GFC driven black-start scenario that are demonstrated in Figure 1.2. Starting by the DC source or network that are used to power the GFC, and moving to the AC side of the network by developing suitable models for transformers to study inrush current transients and identify/propose suitable mitigation techniques. The GFC itself is addressed through analyzing different controllers and identifying the ones suitable for black-start and proposing relevant modifications for black-start compatibility. PHiL is then proposed as a flexible validation tool for black-start using hardware GFC integrated to a simulated network in a digital real-time simulation (DRTS) platform. This technique is typically employed to test converters in grid-following mode. The reported investigations thus consider a new angle for GFCs validation through PHiL.

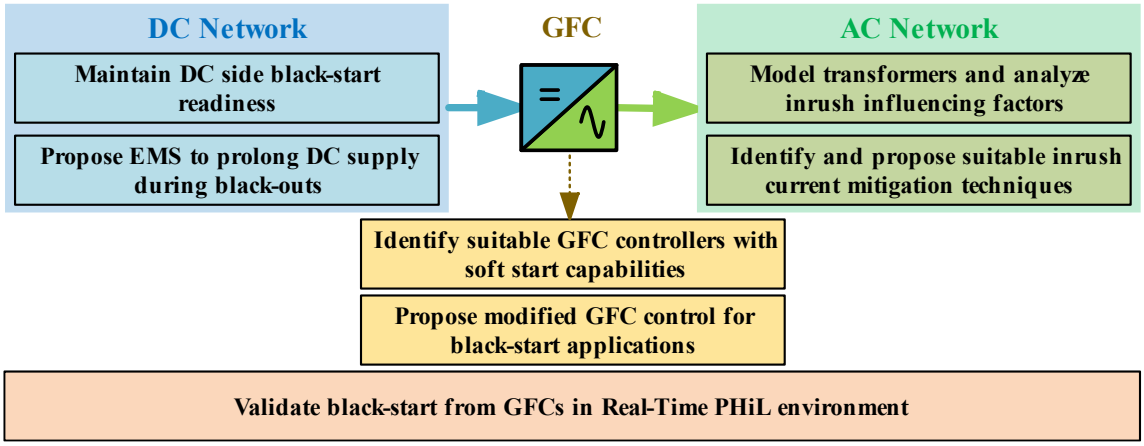

Figure 1.2: Key research points addressed in this thesis.

1.6. Publications

The presented work resulted into several conference and journal publications, in addition to industrial reports as part of the industrial Distributed ReStart project. The reported publications are listed as below, whereas the specific related contributions to the scientific body of knowledge are summarized in Chapter 8.

1.6.1. Journal Papers

[1] **A. Alassi** *et al.*, "Grid-forming VSM Control for Black-Start Applications with Experimental PHiL Validation", *International Journal of Electrical Power & Energy Systems*, 2023. *(Under Review)*

[2] **A. Alassi**, K. Ahmed, A. Egea-Alvarez, C. Foote, "Transformer Inrush Current Mitigation Techniques for Grid-Forming Inverters Dominated Grids", *IEEE Transactions on Power Delivery*, 2022.

[3] **A. Alassi**, K. Ahmed, A. Egea-Alvarez, O. Ellabban, "Innovative Energy Management System for MVDC Networks with Black-Start Capabilities", *Energies*, 14, 2021.

1.6.2. Conference Papers

[1] Z. Feng, **A. Alassi**, M. Syed, R. Alzola, K. Ahmed, G. Burt, "Current-type power hardware-in-the-loop interface for black-start testing of grid-forming converter", *in the 48th IECON Conference*, Brussels, Belgium, 2022.

[2] **A. Alassi**, K. Ahmed, A. Egea-Alvarez, and C. Foote, "Soft Transformer Energization: Ramping Time Estimation Method for Inrush Current Mitigation", *in the 56th UPEC Conference*, Middlesbrough, UK, 2021.

[3] **A. Alassi**, K. Ahmed, A. Egea-Alvarez and C. Foote, "Modified Grid-forming Converter Control for Black-Start and Grid-Synchronization Applications", *in the 56th UPEC Conference*, Middlesbrough, UK, 2021.

[4] **A. Alassi**, K. Ahmed, A. Egea-Alvarez, and O. Ellabban, "Performance Evaluation of Four Grid-Forming Control Techniques with Soft Black-Start Capabilities", *in the 9th ICRERA Conference*, Glasgow, UK, 2020.

1.6.3. Industrial Reports

[1] **A. Alassi**, Z. Feng, M. Syed, A. Egea-Alvarez, K. Ahmed, "Distributed ReStart: RTDS Based Network Energization from Grid Forming Converters". *A Study published by National Grid ESO in two parts between* 2021 *and* 2022.

[2] **A. Alassi**, "Distributed ReStart: Tx Energization and GFC for Black-Start Applications", *National Grid ESO,* 2021.

1.7. Thesis Structure

The remaining of this thesis documents the investigation, analysis, simulations, and experiments performed for the three GFCs black-start stages, as detailed below.

- **Chapter 2:** An innovative energy management system is proposed for maintaining the supply reliability in distribution DC networks and their black-start readiness through robust DC side voltage control for prolonged durations. This is achieved by shifting the operating mode of renewable energy resources between maximum power point tracking (MPPT) and voltage regulation (VR) modes when necessary. In addition to managing the charging and discharging action of the battery energy storage systems. The EMS also incorporates load clustering into different priority levels to manage shedding and restoration events, while maximizing the critical DC loads supply period.
- **Chapter 3:** Moving to the AC network aspect of black-start and the problem of high transformers energizing inrush current that is coupled with limited GFCs overcurrent capabilities, this chapter presents comprehensive power transformer modeling for inrush current mitigation transient studies. The derived models cover energization from constant-amplitude and ramping voltage sources to quantify key inrush current influencing factors. The models are based on switched inductors piecewise transformer magnetizing branch representation, and are validated against industrial simulation tools such as PSCAD/EMTDC. Inrush current behavior during hard, controlled, and soft transformer energization is also demonstrated and linked to the derived theoretical models.
- **Chapter 4:** Analysis of controlled transformer switching from three-pole circuit breakers and soft energization techniques are presented in the context of GFCs black-start. A new soft energization framework for ramp-rate estimation is also introduced in this chapter to address the industrial question of defining suitable ramp durations. Then, a detailed case study is carried out to energize a large network consisting of multiple transformers from a GFC, with the aim of assessing the suitability of controlled and soft transformer energization techniques for black-start under different residual flux combinations and sensitivity cases.

- **Chapter 5:** Following the validation of soft transformer energization as a viable inrush current suppression technique that is compatible with GFCs, identifying suitable GFC controllers that are also compatible with black-start requirements is carried out. Four controllers are benchmarked, namely: droop, power synchronizing, matching and virtual synchronous machine (VSM) controls. VSM is selected from the investigated alternatives for further investigation of its black-start capabilities. A preliminary investigation is also presented to analyze the perceived impact of incorporating inner control loops with current reference saturation limit into the GFC control, in terms of transformer inrush current mitigation.
- **Chapter 6:** A modified virtual synchronous machine (VSM) grid-forming control is proposed in this chapter with black-start supporting capabilities. In addition to the soft start compatibility, the VSM $(Q - V)$ loop is modified to incorporate voltage support functionality at the PCC. Whereas the control $(P - f)$ loop is adjusted to incorporate a synchronizing control that is activated when grid-synchronization is required. A simulation case study is presented to showcase the modified controller operation and validate its performance.
- **Chapter 7:** The use of PHiL is studied for flexible GFCs black-start testing. Ideal transformer method (ITM) power interface techniques are investigated, between current (I-ITM) and voltage (V-ITM) modes. A time delay compensation method is also presented to offset the impact of communication channels, filters, and measurement delays. Successful experimental demonstration is carried out for the modified VSM capabilities (implemented into a hardware GFC). The GFC is used to energize a simulated network in a DRTS platform through a complete PHiL black-start scenario, including soft energization, load pickup and grid-synchronization.
- **Chapter 8:** The thesis conclusion is presented in this chapter with its key scientific contributions and possible future research routes, relevant to the covered topics such as DC energy management, inrush current mitigation techniques that further exploit the GFC control flexibility, as well as the flexible PHiL testing.

Chapter 2 Innovative DC Energy Management System with Black-Start Compatibility

The DC supply of a grid-forming converter used for AC network restoration may be through single source (e.g., battery storage or a renewable source) but it may also be through a combination of these resources or a DC network. DC networks are recently attracting an increased research and industrial interest due to the array of benefits they provide from operational and energy transmission perspectives. For instance, key industrial manufacturers are proposing the use of MVDC solutions in distribution networks such as the MVDC Plus technology from Siemens [19]. Recently, ABB has also mentioned some implemented MVDC projects in various fields such as distribution networks and RES collection grids [20]. Definitions for the medium DC voltage vary in the literature. The range is commonly defined between 5 and 50 kV, with some papers suggesting an upper limit of 100 kV [21]. MVDC networks are typically connected to the AC grid through bidirectional DC-AC converters. The DC network connected to the converter DC side can in principle be used in network restoration. This requires the DC network to be operational with sufficient energy resources availability, and to maintain the DC voltage at the grid-converter interface point to acceptable levels for reliable DC-AC conversion. This chapter thus considers an innovative energy managements system design to sustain MVDC networks supply reliability and black-start readiness when facing prolonged network contingencies.

2.1. MVDC Networks during Grid-Side Contingencies

When a DC distribution system is disconnected from the AC network because of a grid-side blackout, the MVDC distribution system must swiftly respond to maintain its stable operation. First, to maintain critical loads supply reliability, and second, to be black-start and grid-synchronization ready when receiving the restoration signal command from the network operator. The timescale of such network contingencies can range from short-term that are tackled within moments, to long-term that are resolved in hours, or in worst cases up to days as happened in Japan earthquake in 2011 [22]. The existence of autonomous

small-scale systems in Japan such as Roppongi Hills microgrid helped preserving critical loads supply during three days of blackout [23].

This uncertainty associated with such events makes it necessary to implement a robust energy management system (EMS) that maintains the system operation while achieving the required power balance between available generation/storage assets and load requirements. The following case illustrates the issue further during AC system blackout: if the combined RES output in an MVDC network exceeds the load requirements while the storage connected to the same DC bus is fully charged, then the DC link voltage will increase proportionally to the excess power available at the DC bus based on the following conventional power equation (2.1).

$$\Delta P_{DC} = \frac{(V_{DC_{new}}^2 - V_{DC_{nominal}}^2)}{Z_{Load}} \tag{2.1}$$

where, $V_{DC_{nominal}}$ and $V_{DC_{new}}$ represent the DC bus voltage before and after the excess power violation, respectively. ΔP_{DC} is the excess power at the DC bus (equal to zero under normal power balance conditions), and Z_{Load} represents the combined loads at the DC bus. Under excess power conditions, the DC voltage can be restored to its rated value by either:

- Connecting dump loads at the DC bus to absorb the excess power [24]: This approach requires installing expensive variable controllable loads that track the power output from the RES to attain voltage stability, making it a complex and expensive option.
- Controlling the RES output to match the DC link voltage requirements [25-27]. This approach requires shifting the RES operating mode between maximum power point tracking (MPPT) and voltage regulation (VR) based on the network conditions, in addition to achieving adequate power sharing in case of multiple operating RES units.

On the other hand, undervoltage can also occur at the DC bus if no sufficient power is available from RES or storage in cases of prolonged contingencies, high loading or limited supply. These cases are represented by negative ΔP_{DC} in equation (2.1). Maintaining the

DC link voltage balance in this case requires prioritized load shedding. This partial shedding should be proportional to the shortage to maintain a constant DC voltage.

When isolated from the grid under network contingency, distribution systems with local generation can be considered as independent electrical entities that require their own energy management system (EMS) to maintain stable DC bus voltage for load supply reliability and ancillary services provision. Several MVDC system topologies can be practically implemented, depending on the number of resources, grid interface points, etc. Figure 2.1 shows a generic high-level block diagram of an MVDC distribution system, composed of multiple RES sources (e.g., solar or wind), storage and loads, and interfaced to AC grid through a centralized voltage source converter (VSC) and a three-phase transformer, in addition to the utility grid synchronization switch (S_{sync}) which is closed under normal operating conditions and open under grid-side network contingency.

To identify the required improvements on DC networks EMS to achieve the supply reliability and black-start readiness objectives, a survey is first conducted on the existing systems with their merits and limitations and is presented in the following subsection.

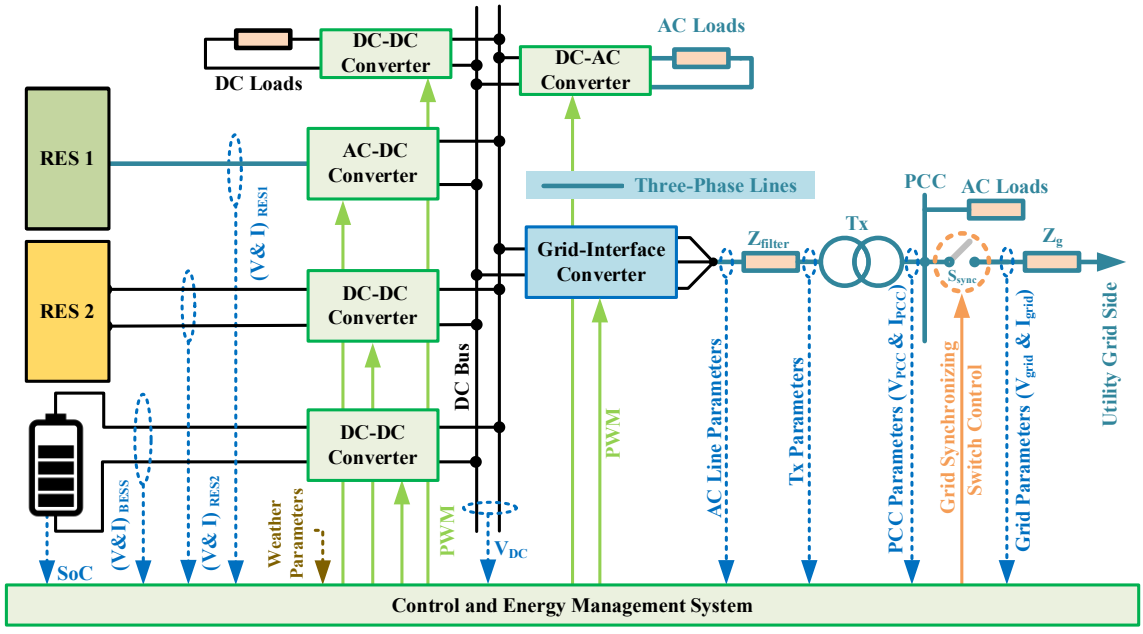

Figure 2.1: High-level block diagram for a generic MVDC distribution network and its grid interface.

2.2. Overview of DC Networks Energy Management Systems

The defined objectives and case studies by each energy management system design in the literature have been observed to dictate the DC side EMS functionalities and complexity. Research works in this area tend to approach EMS designs in one of the following ways.

- Designing the EMS with technical/economic objectives, assuming the existence of continuous grid-connection to supply/absorb any shortage/surplus power [28, 29].
- Designing the isolated EMS for batteries state of charge (SoC) optimization and lifecycle extension, without considering the described special operating cases [30].
- Designing the system with RES mode shift between MPPT and VR taken into consideration, without accounting for shedding under light supply conditions [26].
- Considering the load shedding requirement in the design for the whole load as a bulk, without taking load prioritizing into account to prolong critical loads supply [31].

The work presented in [32] has considered a DC network with a similar configuration to that in Figure 2.1. The paper proposed a leader-follower droop control for DC voltage stabilization in grid-connected DC networks to balance the load supply contribution between the grid-connected VSC and battery storage system. Being grid-connected, the DC EMS does not consider RES mode shift to preserve the DC bus voltage. On the other hand, the authors of [33] have expanded the droop application in isolated DC networks into a pseudo droop control mode, which resembles the RES mode-shifting between MPPT and VR through controlling the solar PV converter based on DC link voltage feedback in oversupply periods. Load shedding has been briefly addressed as a DC voltage stabilizing requirement under low supply conditions, but with limited implementation details or recommendations. Similarly, the authors in [26] have developed an optimal VR scheme with a proposal of an adaptive droop EMS for isolated DC distribution systems, but without considering undersupply constraints. In [34], a model predictive control (MPC) based EMS for a DC distribution system consisting of multiple resources has been presented. The paper considered the system design under normal operating conditions with load and weather forecast to achieve system power balance and stabilize DC voltage. The RES mode shift (termed as power curtailment mode) and load shedding were

acknowledged in the paper but excluded from its scope. In [28], the EMS was designed to achieve autonomous DC distribution system operation under most conditions but grid-connection was used to cover any shortage or surplus from the DC network. Similarly, the work presented in [35] considered the autonomous operation mode for a DC distribution system, but without the abovementioned power imbalance considerations. On the other hand, the EMS in [36] has implemented both RES mode shift and load shedding, but with the latter considered in a single step without prioritization. The authors of [37] have presented a new unified controller for a simplified PV/BESS network that smooths control mode transitions between MPPT and VR, yet with no considered load prioritization. Conversely, the work presented in [31] did not take RES mode shifting into account, and resorted to proposing the use of dump loads instead. Another consideration in [27, 36] is the limitation of battery charge/discharge power through using dual loop PI with inner current control. Taking this limit into account is important to comply with storage protection requirements.

Network design planning can also contribute to mitigating EMS operational uncertainties. For instance, the intermittent nature of solar and wind power favors the consideration of robust weather forecasts and stochastic system optimization design techniques. Techno-economic considerations for initial network assets and storage system sizing were covered in [38, 39]. Multi-objective optimization techniques have also been proposed in literature to minimize both short-term uncertainties (e.g., RES intermittency and load variations) and long-term uncertainties (e.g., falling storage costs) in planning for hybrid systems design and operation [40].

Building on the identified EMS state-of-the-art, the proposed EMS for MVDC networks management in this thesis preserves the distribution network functionality of the impacted MVDC system through maintaining a constant DC bus voltage, maximizing critical load supply duration, and maintaining the MVDC system black-start readiness.

2.3. Proposed Energy Management System

The proposed EMS aims to guarantee an extended supply reliability to the isolated MVDC network segments in post AC grid contingency scenarios, while maintaining the black-start readiness of these DC segments. The EMS continuously verifies whether the DC network is grid-connected. If so, normal operation persists through the grid-inverter in Figure 2.1. RES units simultaneously operate in MPPT mode for maximum power extraction, and the storage operates according to its design objectives, such as energy trading or ancillary services provision [41, 42].

If a grid-isolation is detected, then the central converter is disconnected and the MVDC system swiftly shifts to operate in islanded mode under the proposed DC energy management system. From Figure 2.1, the battery DC-DC converter assumes control of the DC voltage and the RES units operate in MPPT or VR modes based on the existing power-balance conditions. Equation (2.2) presents the main power-balance equation that should be always satisfied to properly operate the standalone MVDC distribution network using the designed EMS.

$$P_{RES} = P_{Load} + P_{Bat} \quad \forall\, V_{DCmin} \leq V_{DC} \leq V_{DCmax} \tag{2.2}$$

where, P_{RES} is the collective renewable energy sources power output, P_{Load} is the total connected load power and P_{Bat} is the charge/discharge storage power, V_{DCmin} and V_{DCmax} are the DC bus voltage permissible limits. P_{Bat} is positive when the battery storage is charging, and negative when it is being discharged.

The EMS is designed to accommodate both single large-scale and multiple RES units. The former case shifts the operation of the individual unit between MPPT and VR, while the latter scenario also achieves power-sharing between the different RESs under VR mode. Smart load clustering, shedding and restoration are embedded into the EMS design to prolong critical load supply (e.g., hospitals) during low RES generation periods.

The EMS design also considers maintaining a minimum battery storage state of charge (SoC_{min}) that is sufficient to energize the AC network assets, supply its auxiliary loads and maintain the AC island supply during the black-start process as required by the network configuration in the targeted area. After that, the EMS grid-synchronization path

ensures that the created AC island voltage matches that of the extended active grid prior to closing the synchronizing circuit breaker.

The storage SoC is an important control parameter that is used as a primary decision variable for the different EMS operating modes, and thus acquiring accurate estimates of this parameter is important for proper EMS operation. Several EMS estimation techniques exist in literature such as voltage, impedance or adaptive techniques as discussed in [43]. Mathematically, the SoC of a battery is defined as the ratio of its current capacity $Q(t)$ to its nominal rated capacity Q_n as illustrated by equation (2.3).

$$SoC(t) = \frac{Q(t)}{Q_n} \tag{2.3}$$

During the MVDC system isolated operation following a grid contingency, the network operates between MPPT and VR modes with additional load shedding and restoration paths within EMS design. When the grid restoration signal is received, the black-start and grid synchronization modes of the EMS are activated. The following subsections explain the different MVDC network operating modes under the proposed EMS design, where Figure 2.2 shows a high-level flowchart for the proposed energy management system operation.

2.3.1. Maximum Power Point Tracking Modes

Under the proposed EMS design, the available RES units operate in MPPT mode when their maximum instantaneous output is not sufficient to cause an over-voltage to the DC bus in the islanded system. For instance, if $P_{RES} > P_{Load}$, and the storage unit can still be charged (i.e., $SoC < SoC_{max}$), then the surplus RES power is used to charge the battery. Likewise, RES units should still operate in MPPT mode if $P_{RES} < P_{Load}$, with the battery operating in its discharge mode to satisfy equation (2.2).

A. Load Shedding Path

If the combined RES output power is consistently below a power cutoff point (P_{cutoff}) that can be defined based on network-specific environmental resources availability and critical load requirements, then the RES units still operate in MPPT mode to extract the

maximum power output. The shift from normal operation path to load shedding path in Figure 2.2 should be designed to activate after a certain drop in battery charge level (e.g., 30%) to avoid scattered mode switching that could result from RES output intermittency.

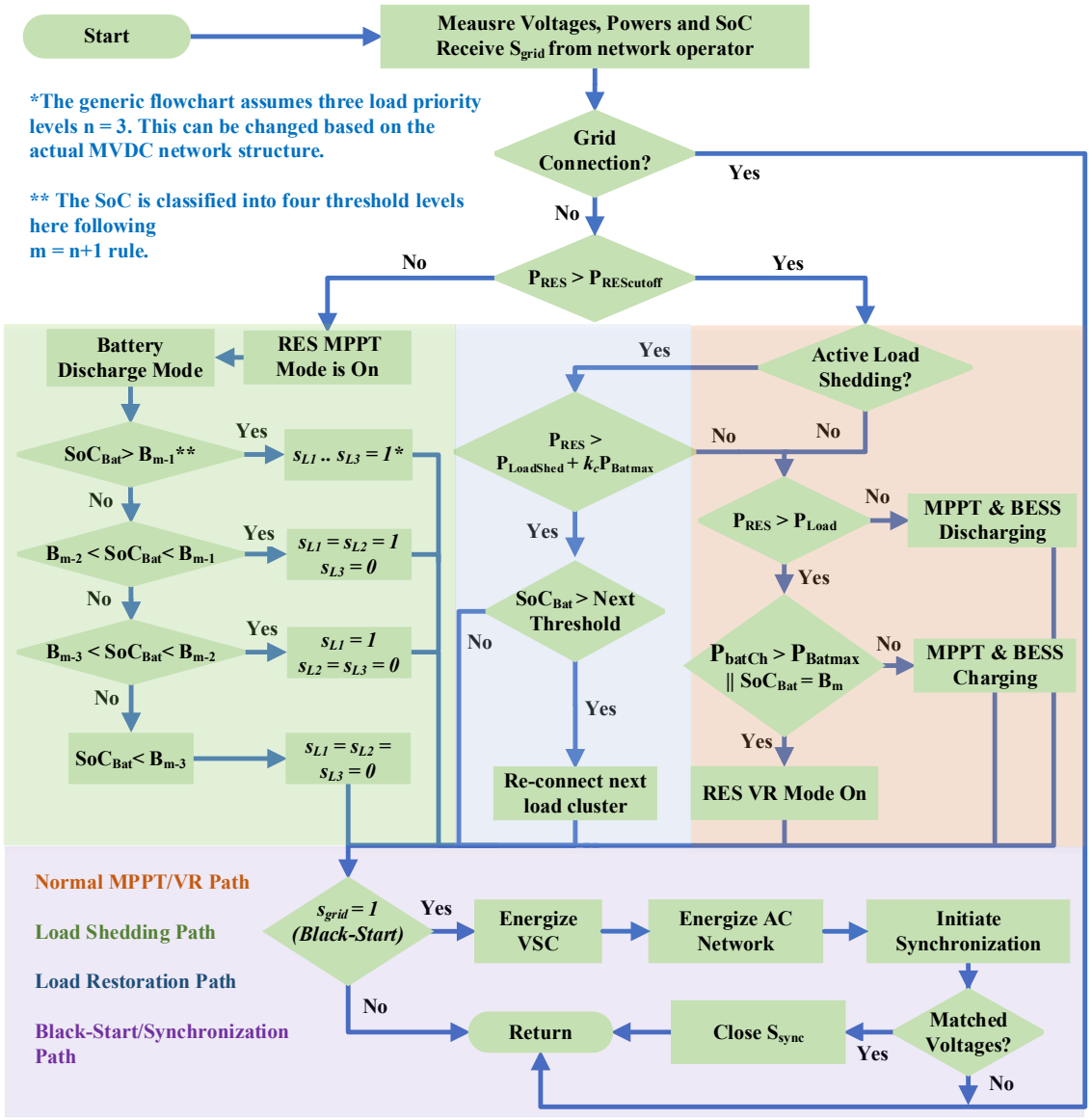

Figure 2.2: Detailed EMS design flowchart with multiple operating modes.

Once load shedding path is activated, the remaining load power is supplied by the battery in discharge mode. In this case, clustering the load into different prioritized categories becomes important to maximize the most critical load supply duration while also partially

supplying the other loads. A simplified example is considered for illustration, where a single offshore wind farm is connected as the power generation source. If the local wind speed is expected to be below the operating cutoff point for the next *x* hours, then the local storage should be able to maintain the critical load supply based on its current SoC. The local loads in this case are segmented into *n* clusters based on their criticality level, while SoC is segmented into m levels between SoC_{min} and SoC_{max}, where $m = n + 1$. The least critical cluster is disconnected in load shedding path when the SoC falls below the first segment lower threshold at $m - 1$, thus elongating the supply period for the remaining load. If the same condition persists until the SoC reaches $m - 2$, then the second least-critical load cluster is disconnected. If the weather forecast used to predict the wind farm output has underestimated the plant disconnection period and the SoC eventually falls below the $m - n$ level (i.e., SoC_{min}), then the last resort in this case is for the most critical load to also be temporarily disconnected until the RES plant generation is restored. Figure 2.2 demonstrates the load shedding logic for a three load clusters case ($n = 3$) within the load shedding EMS path. Whereas equation (2.4) illustrates the generic load clustering into *n* clusters, and equation (2.5) mathematically summarizes the load shedding path requirement for each cluster.

$$P_{Load} = s_{L1}P_{L1} + s_{L2}P_{L2} + \cdots + s_{Ln}P_{Ln} \tag{2.4}$$

$$s_{Li(shed)} = \begin{cases} 1 : SoC \geq B_i \\ 0 : SoC < B_i \end{cases} \ \forall \ P_{RES} < P_{cutoff} \tag{2.5}$$

where, s_{Li} is the i^{th} load cluster switch, with i in this case ranging from 1 to *n*, and B_i is the lower SoC threshold for the corresponding sector. SoC minimum threshold occurs at $B_{min} = B_1 = B_{m-n}$ and the maximum at $B_{max} = B_m = B_{n+1}$ when the battery is charged to its maximum practical capacity.

B. Load Restoration Path

The proposed EMS design only considers load restoration possibility once consistent and sufficient RES power output is accumulated to avoid continuous shedding/restoration modes switching. Based on their availability, weather forecasts (i.e., wind speed, solar

irradiance and temperature) can be used to support the decision-making logic as an adaptive co-factor to the load restoration sequence and thresholds definition for increased EMS reliability. If load shedding exists in the network, then battery charging is prioritized, and restoration of the next load cluster is allowed once the battery is charged to its restoration threshold level. Progressive load re-connection is then carried out as the storage SoC evolves through the *m* threshold levels. Equation (2.6) summarizes the load restoration path requirements, whereas Figure 2.2 highlights the path execution within the EMS context.

$$S_{Li_{(restoration)}} = \begin{cases} 1 : SoC \geq B_i \\ 0 : SoC < B_i \end{cases} \forall\ P_{RES} > P_{Loadshed} + k_c P_{Batmax} \tag{2.6}$$

where, $P_{Loadshed}$ is the partial connected load at the considered instant/segment, k_c is a safety factor that can be set between 0 and 1 (higher values provide more safety margin with respect to the available surplus battery charging power to activate load restoration), and finally, *i* is defined similarly to equation (2.5). When this path is activated, the RES units operate in MPPT mode if the required conditions are met, and in VR mode otherwise as explained in the following subsection.

2.3.2. Voltage Regulation Operating Mode

This mode is activated in one of two cases, either if $P_{RES} > P_{Load}$ and the battery is fully charged, or if the battery is charging at its maximum power P_{batmax} and the charging current is limited by its protective control, that is when $P_{RES} > P_{Load} + P_{batmax}$. In either of these cases, the surplus P_{RES} can cause an overvoltage at the DC bus, and thus shifting the RES units operating mode to VR becomes essential to maintain constant DC bus voltage. Consequently, the battery DC-DC converter control design should consider the overcurrent protection, which can be implemented in different ways, such as dual-loop PI control as illustrated on a high-level in Figure 2.3, where LPF refers to a low-pass filter.

Operation within VR mode is also possible in the load restoration path if the following condition is met: $P_{RES} > P_{LoadShed} + P_{batmax}$. This can be considered as a design choice and is prioritized here compared to direct connection of the shed load before the SoC climbs back to the next segment threshold to avoid scattered mode switching.

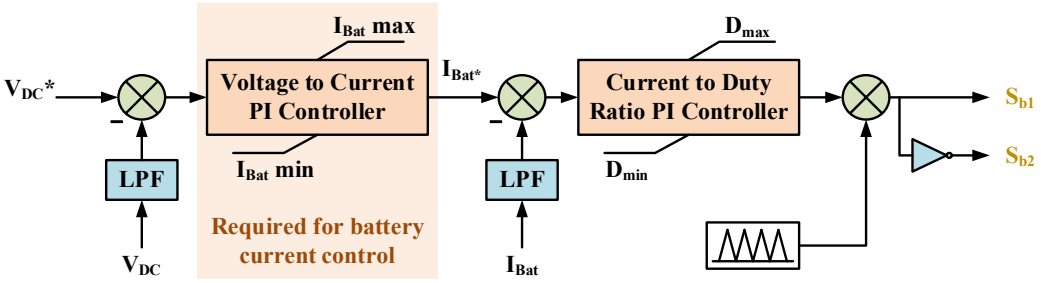

Figure 2.3: Battery DC-DC converter control with overcurrent protection (bidirectional boost converter).

Shifting the RES operation mode from MPPT to VR and vice versa for a single RES unit requires shifting the MPPT converter operation point to a new level that stabilizes the DC bus voltage. For instance, if a single PV unit operates in the network, then the DC-DC converter duty ratio is shifted to a new equilibrium. This can be done using several techniques such as modified P&O [27] or modified voltage reference signal through a switched PI controller [36]. An illustration of the operating-mode shift concept is presented in Figure 2.4 for a solar PV array. The test system configuration is simplified to include solar PV and battery storage with DC-DC converters. The connected load is 1.5 kW, and the maximum battery charging power is 3 kW. The highest power point is tracked for the solar PV by the MPPT algorithm at $V_{mpp} = 110\ V$, nearly generating 4.9 kW under standard test conditions (STC).

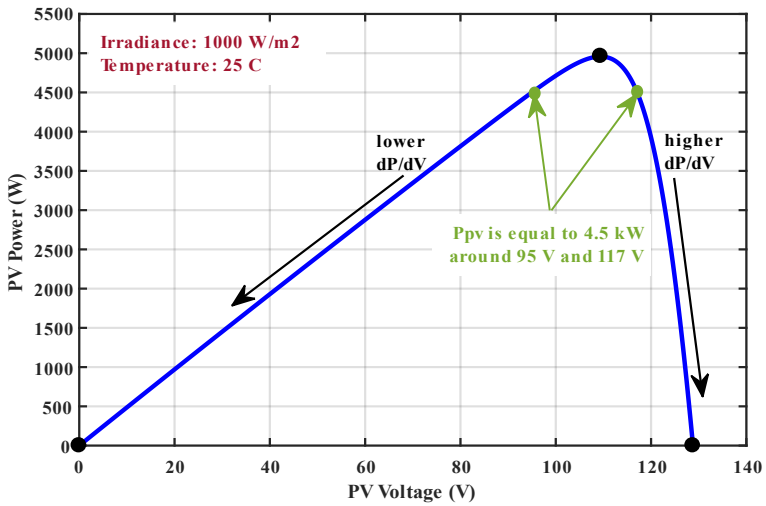

Figure 2.4: Demonstration of the MPPT to VR mode shift options in the tested PV system in terms of the dP/dV response steepness.

In this example, $P_{Load} + P_{batmax} = 4.5\,kW$. Thus, the VR mode shifts the operating point on the PV curve to 4.5 kW to maintain the DC link voltage. Two voltage values on the PV curve satisfy this criteria: 95 V and 117 V as shown in Figure 2.4. The MPPT algorithm can be modified to move the operating point in either directions. However, the lower voltage is recommended since the PV curve is less steep at voltages lower than V_{mpp} compared to higher voltages on the right-hand side of the curve peak point. Higher fluctuations are observed to result if the latter direction is followed against the same P&O step-size.

A. Multiple RES Units: Power Sharing in VR Mode

In cases where multiple RES units are operational in the MVDC system, power sharing should also be considered. Here, a technique inspired from droop control is proposed. When parallel generation units operate in the islanded DC network presented in Figure 2.1 and a switch to VR mode is required, then different possibilities exist to achieve this objective. For instance, shifting the operating point of the largest units only to achieve VR might be feasible. Though, normalized distribution between the different units is adopted in this case to minimize the impact of possible large RES units output intermittency.

An analogous principle similar to AC networks droop is presented. The power reference set-point P_{refVR_j} of the j^{th} RES unit operating in VR mode is set proportionally to its standard test conditions (STC) rating P_{STC}. This is mathematically illustrated in equation (2.7) for u RES units, thus achieving collaborative, proportional power sharing instead of violent set-point variation of a single unit, where P_{Load} refers to the connected load at that instant.

$$P_{refVR_j} = \begin{cases} \frac{P_{STC_j}}{\sum_{j=1}^{u} P_{STC_j}} (P_{Load} + P_{Batmax}) & : SoC < SoC_{max} \\ \frac{P_{STC_i}}{\sum_{j=1}^{u} P_{STC_j}} P_{Load} & : SoC = SoC_{max} \end{cases} \tag{2.7}$$

To account for possible power mismatches, a supervisory DC bus voltage control can be embedded to avoid oversupply and the consequent voltage rise. Namely, if a unit is not able to achieve its new power set-point from equation (2.7) due to output shortage, then

the EMS should instruct the other RES units with higher output availability to increase their power participation for DC bus voltage stabilization. Simultaneously, the power reference is decreased for the units with low output to maintain power balance until environmental conditions allow for proportional sharing again. This can be done through imposing converter set-point changes that correspond to DC voltage variations at each generation node through the dynamic EMS power sharing module. Figure 2.5 illustrates the proposed EMS power sharing principle for a simplified case with two RES units, where k_v is a proportional scaling factor for the supervisory DC voltage control. The overall control objective is to push the VR error to zero for all units through combining the DC voltage regulation and the dynamic reference power set-point from equation (2.7). Finally, the internal RES controller design depends on the RES type (e.g., solar or wind).

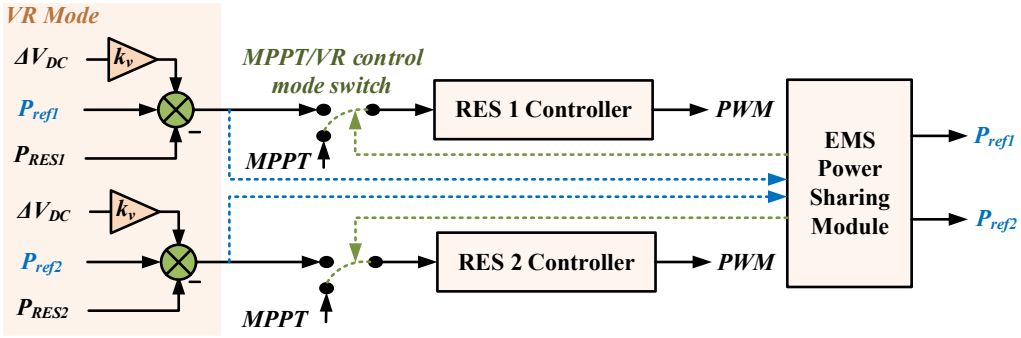

Figure 2.5: Multiple RES units power sharing control in the EMS VR mode.

2.3.3. Black-Start and Grid-Synchronization Path

Different network segments may be operated in isolation following large-scale elongated network contingency. Once the issue is alleviated, these segments can be gradually grouped and used to black-start neighboring areas [44]. In case the investigated DC distribution network is required to participate in such black-start scenario upon receiving a request from the utility operator, then it should be ready to energize its AC grid-interfacing assets by operating the interface converter in grid-forming mode, energizing the AC network assets with minimal inrush current, supply critical loads for energization within the AC network, and to be able to synchronize to neighboring AC islands or the main grid by matching the synchronizing voltages amplitude, frequency and phase angle.

From the DC network side control perspective, this implies maintaining adequate energy supply for the EMS to be black-start ready. Given the renewables intermittency, the proposed option is to maintain a minimum battery SoC during isolated MVDC operation, where SOC_{min} specific definition should be set based on network planning and contracted capacity with the utility.

2.4. Proposed EMS Validation

This section presents two case studies with results illustrating the proposed EMS robustness under different DC network operating conditions and scenarios using simulated models and a scaled experimental laboratory setup. The first case study is simulation-based using MATLAB/Simulink and is designed to test different EMS operating stages with two solar PV resources and DC switched loads to test the power-sharing VR module functionality.

The second case study is experimental and uses a scaled down laboratory setup. It aims to verify the proposed EMS operation in its main modes using a relevant hardware configuration. Table 2.1 summarizes the tests and their objectives, where all the used converters in the simulation study are assumed to have ideal components and are built in MATLAB/Simulink using average model assumptions. In practice, conventional DC-DC converters, such as boost type have limited gain due to their switching losses and parasitic elements at higher duty ratios. Different topologies are presented in literature to maximize the gain such as cascading different stages or using isolated converters, and the topology selection depends on the required gain, efficiency, and application requirements. Detailed consideration of such topologies can be found in [45-47].

Table 2.1: EMS design verification tests.

Test	Objective
RES mode shift	Verifying MPPT-VR mode shift for DC bus voltage regulation under variable environmental and loading conditions.
RES Power Sharing (*multiple units*)	Verifying power sharing functionality between multiple units in EMS VR mode.
Load shedding/restoration sequence	Verifying load clustering, shedding and restoration sequence under variable RES output conditions.

In both simulation and experimental tests, perturb and observe (P&O) MPPT technique is used for PV DC-DC converters, with a modified duty ratio perturbation logic to achieve VR under shifted operating mode. The solar PV systems are simulated using the single-diode model. Dual loop PI is used for the battery storage control for charge/discharge current protection (Figure 2.3). Finally, it should be noted that the EMS can operate with different device-level controllers (e.g., proportional-integral, sliding mode control … etc) as the EMS mainly operates as a secondary level control structure, adding more user design flexibility.

2.4.1. Case Study 1: EMS Test with Multiple RES Units (Power Sharing)

The test network in this case study is composed of two parallel-operated PV farms, interfaced to the DC bus through boost DC-DC converters, in addition to a large battery that is interfaced to the DC bus through a bidirectional boost converter. The connected loads are divided into three priority clusters ($n = 3$) and controlled through separate switches S_{L1} to S_{L3}. The SoC thresholds ($m = 4$) are selected to be at 100%, 70%, 50% and 20%, where the latter is assumed to be the minimum network requirement to guarantee a successful black-start in case of low RES output at that instant to support auxiliary AC loads. The AC system interfacing is performed using a two-level three phase voltage source converter via a three-phase power transformer. Figure 2.6 shows the configuration used for the EMS simulated tests. From the three parallel connected DC-DC converters in isolated mode, the battery bi-directional converter is responsible for maintaining DC bus voltage, and its charge/discharge operation depends on the power balance defined in equation (2.2) to maintain reliable connected load supply. Similarly, the two uni-directional PV converters operate either in MPPT or VR mode based on the set of constraints defined in Figure 2.2. In VR mode, the control of both converters is modified to achieve proportional, droop like, power sharing as described in Figure 2.5. Finally, simulation of the AC side connection when a black-start command is received by the EMS from the system operator is presented, showing the potential danger of high inrush currents if appropriate measures are not considered. Key simulated system parameters are summarized in Table 2.2.

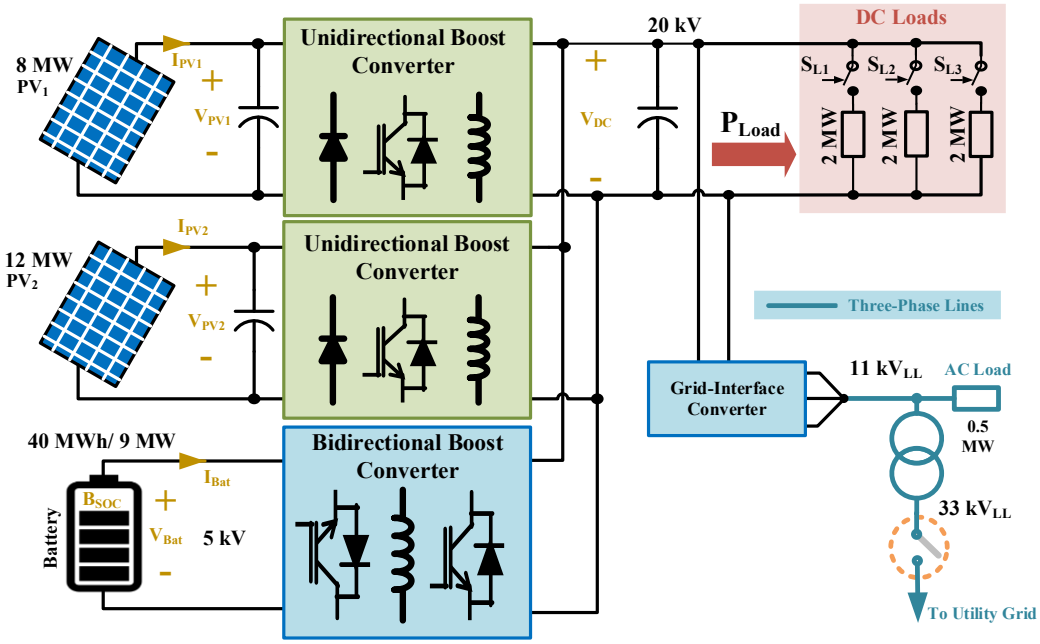

Figure 2.6: Test network used for EMS case study 1 with key parameters.

The designed ratings and parameters are selected to reflect a medium-power network with a generation capacity exceeding local loads for power export under grid-connected conditions. This is to verify MPPT-VR transitions during the MVDC distribution network isolated operation when excess power cannot be exported to the grid.

Table 2.2: Case 1 simulated System Parameters.

Parameter (unit)	Value	Parameter (unit)	Value
PV_1 - PV_2 Rating (MW)	$8-12$	P_{Load} Per Cluster (MW)	2 (n = 3, total 6 MW)
PV_1 and PV_2 V_{oc} (kV)	1.5	*SoC* Thresholds	20%, 50%, 70%, 100%
V_{DC} (kV)	20	P_{batmax} (MW)	9
V_{bat} (kV)	5	*Battery Capacity* (MWh)	40
Line VSC Voltage (kV)	11	*PCC Line Voltage* (kV)	33
Transformer Rating (MVA)	25	*AC Aux. Load* (MW)	0.5

A. RES Mode Shift and Power Sharing Test

In this simulated scenario, the system initially operates within the main EMS path from Figure 2.2, since load shedding conditions are not met. Figure 2.7 shows the simulation scenario results through averaged simulations. Initially, the irradiance is set to 600 W/m^2.

Both PV systems operate in MPPT and collectively output 12 MW, while the total connected load is 6 MW, and thus the battery is charged with the excess 6 MW, below its maximum charging power of 9 MW. The irradiance is then increased to 700 $\mathrm{W/m^2}$ with $P_{RES} = 14$ MW and the MPPT operation mode persists since the power condition $P_{RES} < P_{Load} + P_{batmax}$ (15 MW) is still satisfied.

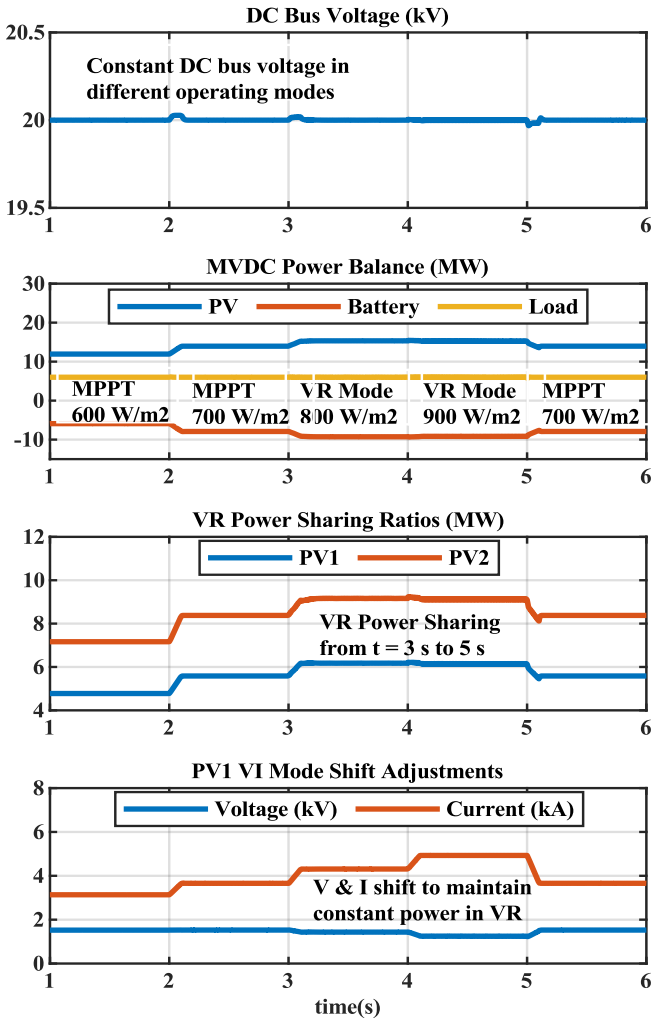

Figure 2.7: MPPT-VR-MPPT mode shift to maintain constant DC link voltage.

However, when the irradiance is increased to 800 W/m^2, then the PV output becomes at the MPPT-VR modes barrier as it approaches 15 MW. More evidently, an irradiance of 900 W/m^2 would have resulted in P_{RES} around 18 MW if MPPT persisted. Though, the

VR mode forces the power sharing functionality in this case to adjust both PV operating points according to equation (2.7), forcing PV_1 and PV_2 to collectively operate around 15 MW. This requires modifying the operating point on the PV curve. Figure 2.7 also illustrates this shift between $t = 3\ s$ and $t = 5\ s$ in the voltage and current for PV_1. That is, irradiance increments in solar PV mainly increases the power through current increments with minimal voltage impact, whereas the voltage is noticeably decreased to counter the current increments, thus drifting away from the maximum power to achieve VR and maintain constant DC voltage, in an analogous fashion to that shown in Figure 2.4. Finally, the irradiance is decreased to 700 W/m^2, restoring the operation of both PV systems to MPPT, and showcasing successful mode shift from VR back to MPPT.

B. Load Shedding/Restoration Test

For this test, the battery SoC is initially set just above 50%, with the irradiance set to zero to simulate a case when the least critical load cluster is already disconnected because SoC < 70% with insufficient RES output (see the test parameters in Table 2.2). The total connected load at the beginning of the simulation is thus 4 MW, fully supplied by the battery, and the proposed EMS operates following the load shedding path. The test results are summarized in Figure 2.8.

At $t = 1\ s$, SoC falls below 50%, and the second load cluster is disconnected to prolong the supply period of the most critical load cluster. On the other hand, the PV systems are switched on at $t = 2\ s$ with an irradiance pump from 0 to 700 $\mathrm{W/m^2}$. The collective output power from PV_1 and PV_2 is initially used to charge the battery until it exceeds its maximum power, then the rest is supplied to the total connected load. The shedding load cluster can be reconnected through the load restoration path once the battery SoC exceeds 50% again. This sequence is recommended to accelerate the battery SoC buildup, but can be adjusted by changing k_c in equation (2.6). The least critical load cluster can eventually be reconnected once SoC exceeds 70% based on the EMS design, unless an override command is issued. It can be observed from Figure 2.8 that the DC bus voltage is maintained nearly constant during this process. Clearly, the used timescales are exaggerated to cover different modes in a combined visualization window.

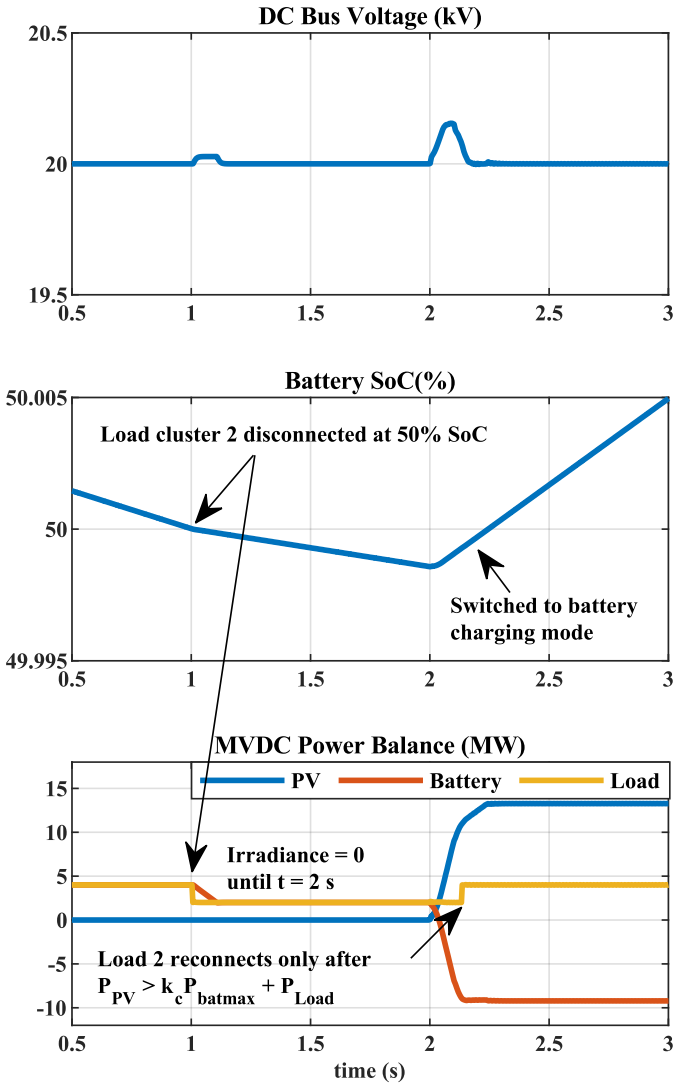

Figure 2.8: load shedding and restoration sequence results.

C. AC Black-Start Test

The black-start route in the proposed EMS is subject to receiving a restoration signal from the network operator, and the existence of a minimal SoC in the battery storage. The presented test aims to demonstrate the impact of uncontrolled energization of the AC network from the DC side, by means of activating the VSC upon receiving the restoration command, which may lead to high inrush currents in the connected transformer and any connected cables. Here, the PV systems are operated at low irradiance that is selected to be just above the cutoff power for this design ($100\ \mathrm{W/m^2}$ at $\sim 2\ MW\ output$) to avoid falling into the shedding/restoration path. This relatively low power is also selected to

better visualize the battery and DC bus voltage interactions with AC side during the uncontrolled black-start. Simultaneously, the load is fully connected, and the battery supplies 4 MW of the total 6 MW demand. As illustrated in Figure 2.9, the black-start activation signal is received at $t = 2\ s$, and the converter is energized with a 1 pu voltage instantly, which is simultaneously applied at the transformer and the AC auxiliary load terminals (see Figure 2.6). Very high current pulses in kilo-amperes are generated at the saturated transformer cores, resulting in violent DC link voltage and battery power variations to generate/absorb this inrush power.

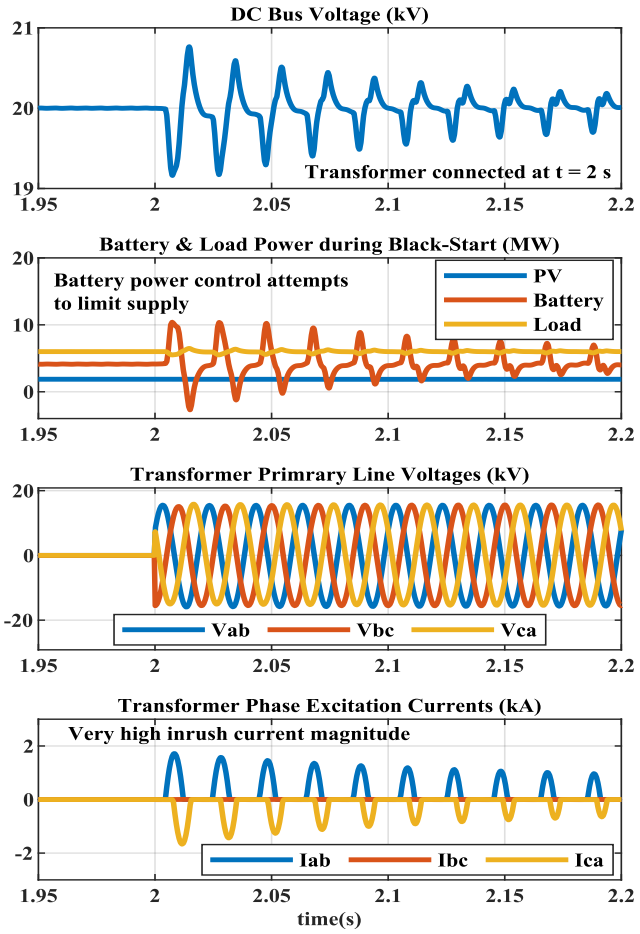

Figure 2.9: Simulation results of EMS black-start using uncontrolled transformer energization.

The results of this test demonstrate the importance of developing a thorough understanding of AC network energization requirements, and to propose suitable energization techniques that can achieve smooth network energization. Inrush current mitigation, grid-forming

control, and grid synchronization aspects are comprehensive topics that are investigated individually in the next chapters. The analysis presented in these chapters will not be limited to the presented EMS, but also extend to AC networks energization and black-start applications in general.

2.4.2. EMS Experimental Verification

Key EMS functionalities are experimentally verified using a scaled microgrid setup in Iberdrola Innovation Middle East laboratory. The used part of this setup for the EMS validation consists of a flexible and controllable load and battery emulators from CINERGIA, and a TerraSAS PV emulator. The network unidirectional and bidirectional DC-DC boost converters are controlled through a dedicated dSPACE SCALEXIO interface. Figure 2.10 illustrates the experimental setup block diagram and physical layout.

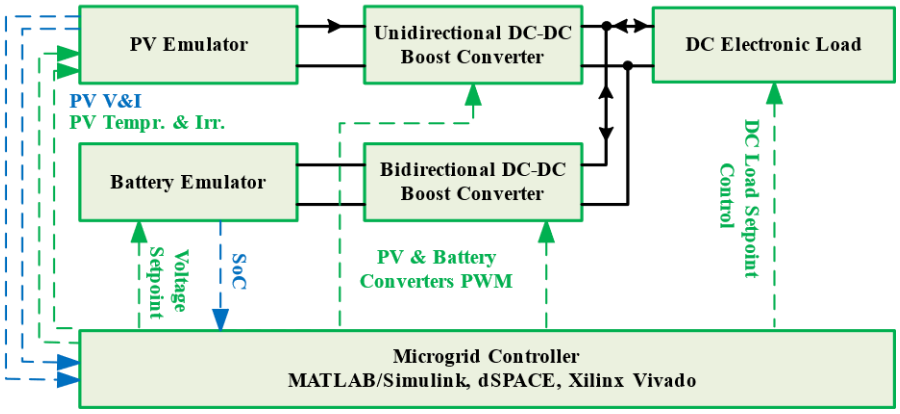

(a)

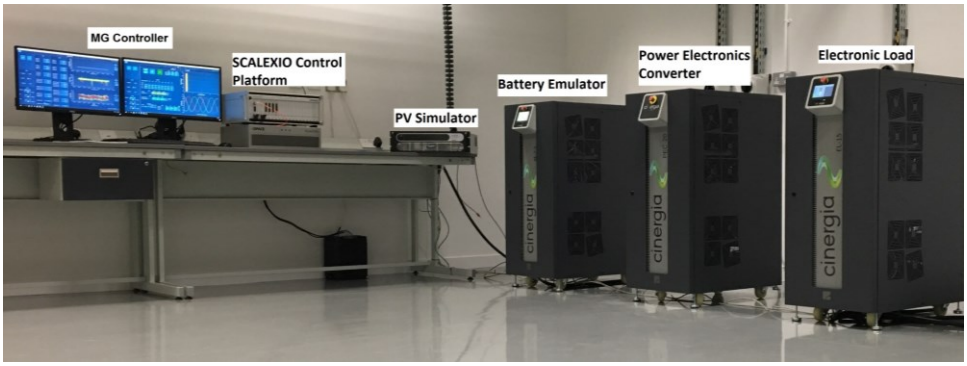

(b)

Figure 2.10: Experimental EMS validation setup: (a) block diagram, (b) physical setup.

On the other hand, the experimental test parameters are summarized in Table 2.3. The setup is similar to that used for the simulated case study, with the difference being the existence of a single PV source emulator. The conducted tests as part of this experimental validation aim to verify the RES mode shift in response to load changes vs. an operation case without active EMS in the isolated network operation mode.

Table 2.3: Case 2 experimental system parameters.

Parameter (unit)	Value	Parameter (unit)	Value
***Maximum PV Power* (kW)**	3.6	***DC Bus Voltage* (V)**	650
***Nominal Load Power* (kW)**	2.0	P_{batmax} **(kW)**	2.2
V_{bat} **(V)**	450	***Disturbance Load Power* (kW)**	1.0
V_{bat} **(kV)**	5	***Battery Capacity* (MWh)**	40

A. Experimental EMS MPPT-VR Test Results

The simulated analogous test verified the proposed EMS operation against irradiance variations and the power sharing functionality in VR mode. The experimental tests expand on different scenarios, and include low loading conditions to cover more operating possibilities within the thesis span. First, the issue of operating the network with no active EMS under this mode is experimentally illustrated. Namely, the PV is initially operating in MPPT mode with a 3.6 kW output, against a 2 kW connected DC load with the surplus power used to charge the battery. P_{Batmax} is defined around 2 kW, with V_{Bat} = 450 V. Figure 2.11 illustrates the results of this test. At $t = 2\ s$, the connected DC load is reduced to 1 kW and back to 2 kW around $t = 7.25\ s$. Between these two points, the PV remains operational at MPPT, and the excess power is fed to the battery until P_{Batmax} is reached. The surplus power can only then be forced into the load in this case as in equation (2.8), increasing the DC voltage, load consumption and risking its damage.

$$P_{surplus} = \left(\frac{V_{DC_{new}}^2 - V_{DC_{nominal}}^2}{Z_{Load}}\right) = (P_{MPPT} - P_{Batmax} - P_{Load} - P_{Losses}) \qquad (2.8)$$

In equation (2.8), P_{Load} refers to the connected load power and P_{Losses} symbolizes the system power losses.

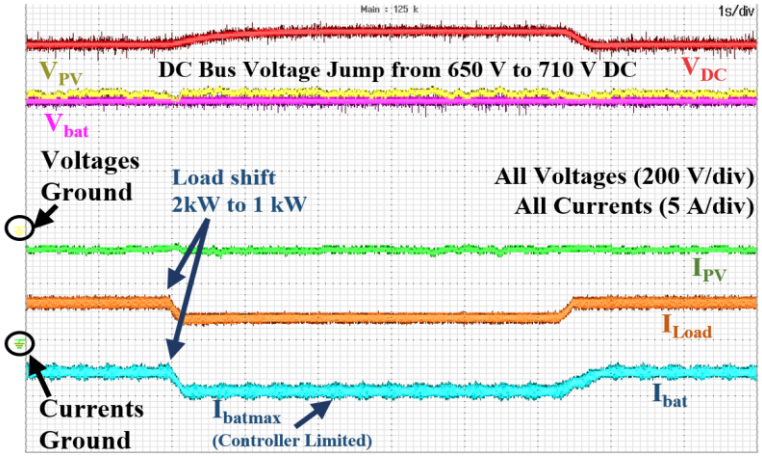

(a)

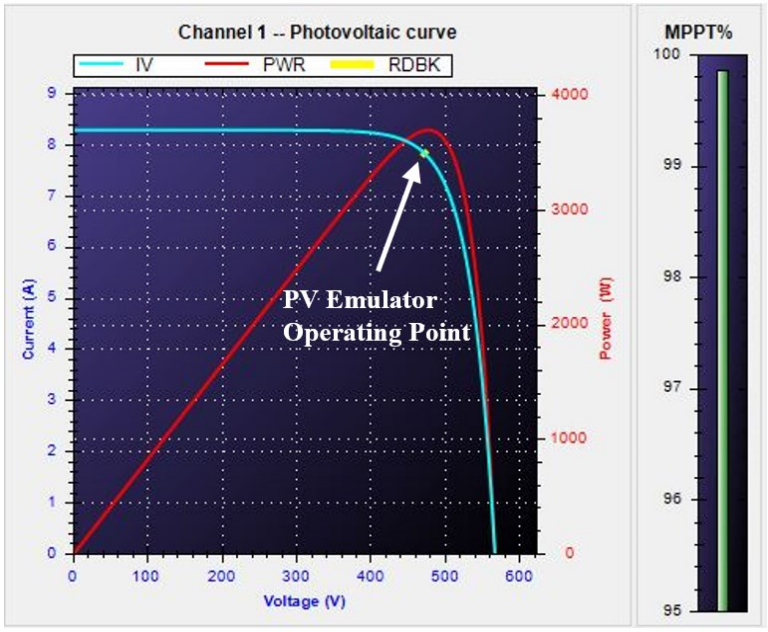

(b)

Figure 2.11: Experimental test results before activating the EMS: (a) Excess PV generation leads to overvoltage violation, (b) MPPT operation of the hardware PV emulator.

On the other hand, when the proposed EMS is activated, the load shift from 2 kW to 1 kW is met with a shift in RES operating mode to preserve DC bus voltage as illustrated in Figure 2.12. This is achieved through adjusting the PV output to a lower voltage and higher current point, effectively reducing its output nearly to 3 kW to satisfy the power balance requirement for DC voltage control. Finally, the PV operating point is shifted again to MPPT when the connected load power is stepped back to 2 kW as in Figure 2.12(b).

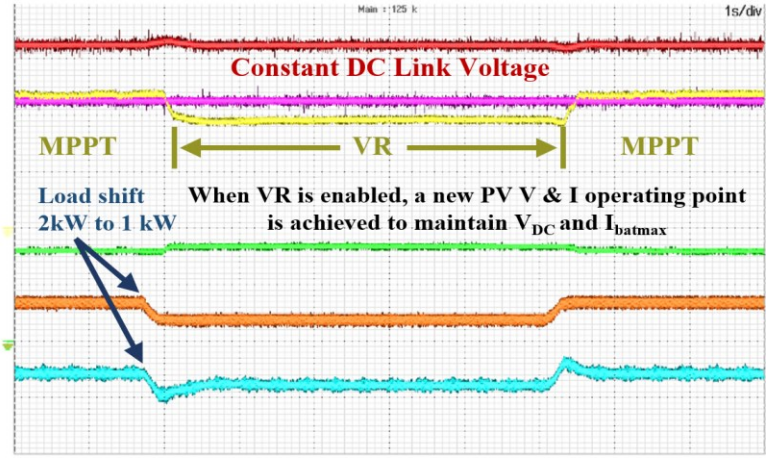

(a)

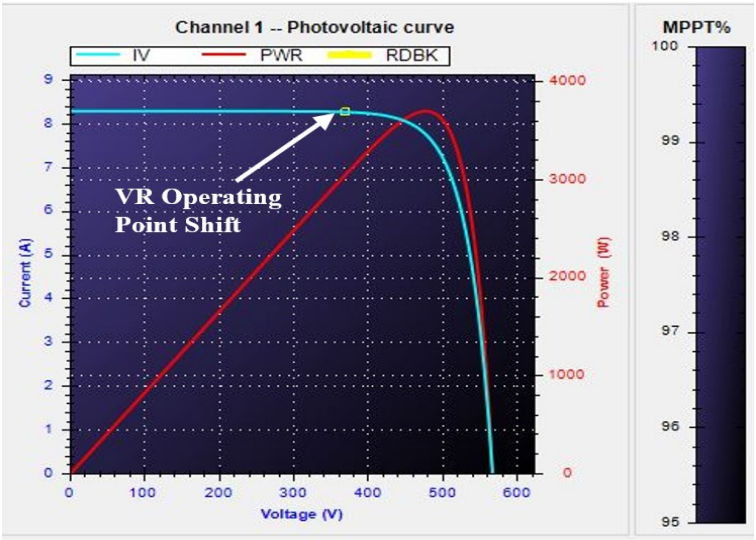

(b)

Figure 2.12: Experimental test results after activating the EMS: (a) MPPT-VR-MPPT mode shift is achieved to maintain voltage, (b) Operating point shift of the PV emulator.

2.5. Summary

In this chapter, a new energy management system has been proposed for MVDC networks with black-start capabilities to preserve the operation of isolated MVDC networks in a post elongated contingency scenario, and to maintain their black-start readiness. The proposed EMS is comprehensively designed to cover various operation paths to achieve these targets. The issue of power oversupply and overvoltage violations in islanded DC systems has been addressed through proposing mode shifts in RES set-points to participate

in voltage regulation (VR) when required instead of continuously operating in MPPT. A power sharing strategy has been proposed to proportionally distribute the power between different RES units in VR mode. The proposed EMS design is agnostic to the generation source type and can operate different assets such as wind turbines and solar PV. Moreover, an innovative partial load shedding and restoration strategy with load prioritizing and clustering has been presented to overcome undersupply conditions and prolong the supply duration of critical load assets. Minimum battery SoC requirement has also been presented to support black-start readiness. The EMS design operates on a secondary control level, allowing for more flexibility on the primary level control of different devices based on the application requirements (e.g., PI, sliding mode, model predictive control … etc).

The preliminary AC black-start simulations in this chapter showcased network energization inrush current as a significant bottleneck that can draw currents exceeding the equipment rating and cause protection tripping, or in more severe cases, equipment damage. Investigating techniques to mitigate inrush current, achieve successful network energization and a smooth transition to grid-connected mode are all important issues to be addressed, and extend beyond the scope of the presented EMS into generic AC networks energization. Thus, these topics are addressed comprehensively in the following chapters to propose effective network energization strategies, starting with understanding the transformer inrush current driving factors and mitigation techniques in the next chapter.

Chapter 3 Power Transformers Modeling for Transient Studies

It has been established that the limited overcurrent capabilities of GFCs necessitate investigating suitable inrush current mitigation techniques when power converters are used for black-start. This is because of the high-amplitude transient inrush currents that could arise from large power transformers energization. The black-start investigation is thus expanded in this chapter to the AC network side. In particular, tackling transformer inrush current, to identify suitable inrush current mitigation techniques for GFC-based black-start. Classical transformer energization studies are typically based on methods that rely on network assets, such as circuit breakers and relays through increasing the circuit damping or switching the transformer at an optimal-instant. In GFC dominated grids, these techniques may still be of relevance due to their perceived effectiveness. In this context, the merits and limitations of classical inrush current mitigation techniques should be quantified and studied against newer methods that rely on converter control modifications such as soft energization. The analysis in this chapter begin by first deriving theoretical models to identify key factors influencing inrush current buildup in transformer cores, and possible ways to mitigate them. The derived models include the classical constant-amplitude source energization and extend to a new model for transformer energization through a ramping voltage source to mimic soft energization conditions. The theoretical derivations are benchmarked against common transformer models in industrial simulation software tools such as PSCAD/EMTDC and MATLAB/Simulink. Hard transformer energization, pre-insertion resistors (PIR), classical controlled switching and soft energization are analyzed as potential inrush mitigation techniques in single and three phase transformers, and correlated to the derived models.

3.1. Power Transformers Saturation

Power transformers inrush currents arise from the transformer magnetic core non-linearity and saturation behavior. Transformers are typically designed to operate in the linear region of the flux (ϕ) and magnetizing current (i_m) curve near the curve knee-point. Operation

in saturation region is experienced when core flux exceeds saturation point. The magnetizing curve inflection point is typically referred to as the knee-voltage, at which 10% voltage increase leads to 50% increase in magnetizing current [48]. A typical knee-voltage design ranges between 1.1 and 1.3 pu [49, 50]. Although it is referred to as the knee-voltage, saturation can take place even when the applied voltage does not exceed 1 pu. A more appropriate definition for saturation is thus linked to the core flux, which is linked to the applied voltage through Faraday's law as illustrated in equation (3.1).

$$V_m \sin(\omega t + \alpha) = N \frac{d\phi}{dt} \tag{3.1}$$

where, N is the number of transformer turns, V_m is the voltage amplitude across the core, ω is the angular frequency, and α is the energizing voltage angle. Both quantities (voltage and flux) are correlated through a time derivative, creating $90°$ phase shift. Thus, if a transformer is energized at zero voltage crossing point ($\alpha = 0$), then the flux peak takes place at $180°$ and can theoretically reach $2\phi_m + \phi_r$. ϕ_m is the peak flux and ϕ_r is the residual or remanent flux that remains in the core after the previous de-energization, or the flux remaining in the magnetic material after the applied magnetizing force becomes zero [51]. The applied voltage in this case does not exceed 1 pu, but the flux could surge beyond 2 pu, leading to high inrush current that can be as high as 10 times the transformer rating [52]. This is visually illustrated in Figure 3.1, comparing two cases: a) normal operating condition where a transformer flux oscillates between -1 and 1 pu, and the reflection of that on i_m, and b) saturated condition that shifts the flux curve in either directions, creating a dc-offset. Depending on the shift magnitude and the core magnetizing curve, the transformer can go into deep saturation, causing very high amplitude inrush currents against small flux increments in the saturation region.

Practically, transformers are non-ideal and exhibit different losses such as copper (I^2R), leakage, and eddy-current losses [53]. Many single and three phase power transformer models are presented in the literature considering the highlighted losses, ranging from ideal to non-ideal electric or magnetic models for low and high frequency operating conditions [54-56].

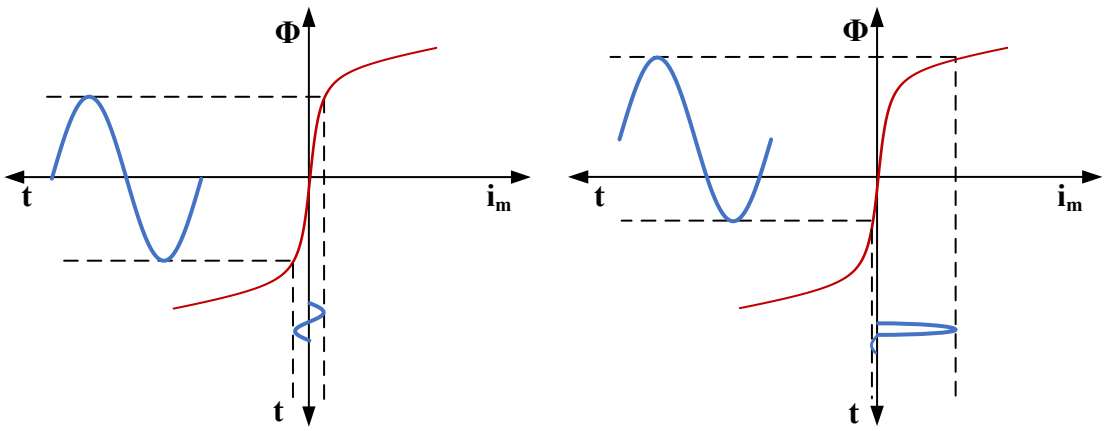

Figure 3.1: Generic transformer saturation curve: (a) under normal operating conditions, (b) with saturated core in the positive direction.

3.2. Transformer Equivalent Circuit Representation

Electrically, a common representation of a single-phase transformer equivalent circuit that is typically used for low-frequency steady-state and transient studies is presented in Figure 3.2. Here, R_1, L_1, R_2, L_2 are the primary and secondary winding resistances and leakage inductances, respectively. The series resistances represent windings copper loss, whereas inductances represent core leakage. The magnetizing transformer core is modeled as a shunt branch consisting of a large resistance R_m, and L_m as the magnetizing inductance. The magnetizing branch resistance is typically of a very large value and is omitted in many representations for simplicity [57-59]. In Figure 3.2, R_m is greyed-out to represent this and simplify the upcoming analysis.

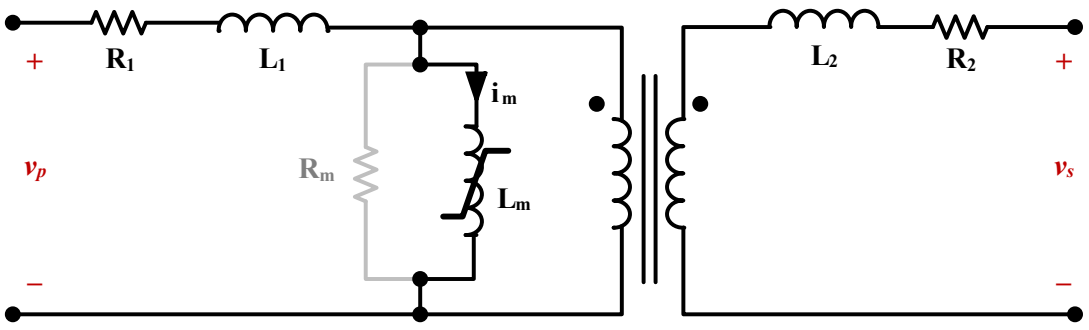

Figure 3.2: Electrical model for a single-phase transformer.

During normal operation in the transformer linear region, $L_m \approx L_{nom}$, which is typically represented as a high inductance value to limit the steady-state magnetizing current to negligible values. However, if the core runs into saturation, then the effective L_m seen by the energizing source drops drastically and approaches what is known as air-core inductance L_{sat}. The equivalent value of this inductance is very low and causes the transformer to draw very high inrush currents, depending on how low L_{sat} is and how deep the core has gone into saturation. In many energization studies, transformers are unloaded and thus the secondary side impedance is ignored. This simplification is common and is considered as a basis for the analysis presented in this chapter. That said, additional impedances, whether from the secondary side or external, can also be combined with the ones in Figure 3.2. Overall, transformer modeling should be considered as an approximation tool to help in identifying trends and linking theoretical predictions to experimental behavior, this is because of the assumptions and simplifications made as part of model development.

Three-phase transformers modeling is often an extension to single-phase transformers, with some variations depending on the used topology. For instance, $Y_g - Y_g$ transformers with three single-phase units can be modeled as three independent single-phase units. The existence of a Δ winding or three-windings core creates inter-dependency between the different phases (i.e., such that the flux summation in all phases adds to zero) [60, 61]. That said, the per-phase representation remains similar to the one presented in Figure 3.2.

3.2.1. Transformer Saturation Curve Models

Two methods are conventionally used to illustrate and model the saturation curve for simulations (i. e. , L_m). First, through hysteresis loops (more realistic), and the second through approximated piecewise linear segments to represent the $\phi\ vs.\ i_m$ curve (widely used approximation, preserving key saturation trends at reduced complexity). Figure 3.3 illustrates different versions of the two approximations, where $\phi(t_0) = \phi_r$ is the residual flux and ϕ_{sat} is the saturation flux.

The hysteresis approximation in Figure 3.3(a) is used in PSCAD/EMTDC and MATLAB/Simulink software tools, and the magnetizing inductance L_m is estimated as

the slope of the saturation curve $L_m = d\phi/di_m$. Using the piecewise approximation, one can notice that the slope in Figure 3.3(b) approaches infinity at the zero current point to approximate zero magnetizing current within the residual flux range, and miniature before saturation. MATLAB/Simulink software model is also compatible with adjustable piecewise approximation, allowing for ϕ_r range along the flux axis (y-axis) with zero i_m, in addition to user-defined combinations. A simpler version of piecewise linear modeling that is used in [58, 59] include only two slopes, one for linear region and another for saturation region, whereas other approximations include a mirrored version of the two-slopes curve to cross zero in $\pm\phi_r$ points to mimic hysteresis behavior. Figure 3.3(c) and Figure 3.3(d) show both approximations.

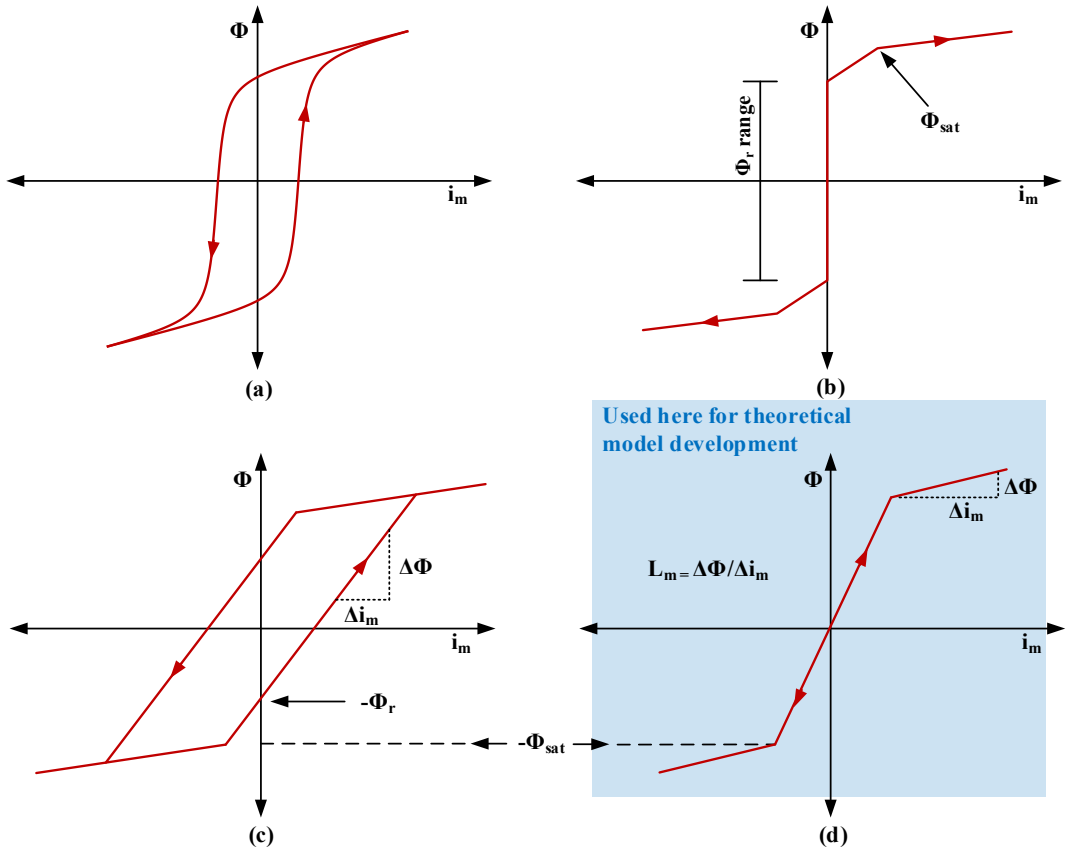

Figure 3.3: Transformer core magnetizing curve: (a) hysteresis loops, (b) piecewise linear segments, (c) piecewise approximation of hysteresis behavior, (d) two-segments piecewise saturation curve.

To understand and study the key factors influencing transformers saturation and the inrush current driving force in a simplified format for non-ideal transformers, the simple two-slopes curve is utilized from Figure 3.3(d) for deriving the theoretical models in this chapter. In the first region, $L_m = L_{nom}$, whereas the saturation region inductance is $L_m = L_{sat}$. When effective L_m is reduced to L_{sat} after saturation, the current is theoretically limited only by the low impedance of the transformer winding and the saturation inductance, which may cause very high current transients.

3.2.2. Magnetizing Branch Circuit Representation

From electric circuits perspective, the piecewise approximation is typically represented by variable or switched parallel inductors, or through a controlled current source. In current-source representation, the voltage across the magnetizing branch is integrated to produce the flux. The measured flux is fed into a look-up table (LUT) that links the flux to magnetizing current, and interpolates the current according to the flux operating point. This technique is illustrated in Figure 3.4(a), and is also used in transformer models in simulation software packages such as MATLAB/Simulink and PSCAD/EMTDC [62, 63]. Switched inductors can also be successively connected in the alternate representation by a similar concept, where the flux operating region is used to switch on/off inductors to produce the desired equivalent value as demonstrated in Figure 3.4(b). Here, L'_{sat} is equal to the value that would drive the parallel equivalent of both inductors to L_{sat}, with a value that is typically very close to L_{sat}, and is demonstrated in (3.2).

$$L'_{sat} = \frac{L_{nom} L_{sat}}{L_{nom} - L_{sat}} \tag{3.2}$$

The current-source technique produces good results and is the standard used in many simulation tools. Though, the switched inductors method is adopted to facilitate mathematical derivations using common circuit parameters, while identifying the key transformer model performance trends.

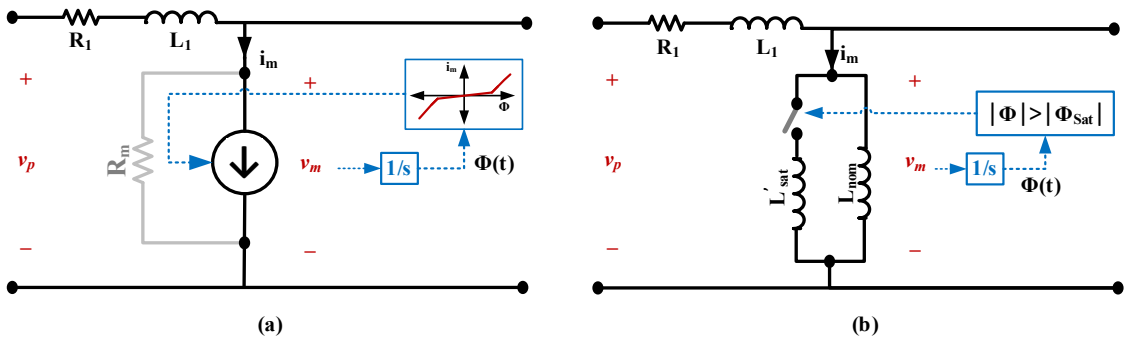

Figure 3.4: Electrical model saturation representations: (a) through controlled current source, (b) through switched inductors.

3.3. Electrical Transformer Model: Constant-Amplitude Source

Using the RL circuit representation in steady state, with the assumption that the transformer is energized from a constant-amplitude voltage source, a mathematical representation that is commonly used in research papers is derived for the flux [52, 64], as shown in equation (3.3).

$$\phi \approx \frac{-L_m V_p \cos(\omega t+\alpha)}{\sqrt{(\omega L_T)^2+(R_1)^2}} + \left(\phi_r + \frac{L_m V_p \cos(\alpha)}{\sqrt{(\omega L_T)^2+(R_1)^2}}\right) e^{-\frac{R_1 t}{L_T}} \tag{3.3}$$

$$L_T = L_1 + L_m \tag{3.4}$$

This equation shows nicely the main parameters influencing the core flux as: the peak applied voltage V_p, energization angle with respect to voltage waveform α, network and transformer impedance (R_1 and $L_T = L_1 + L_m$) and the residual flux ϕ_r. Equation (3.3) is composed of a steady-state time-dependent term, and a constant-decaying term that depends on the energization instant and the residual flux. Although equation (3.3) shows elegantly the flux influencing factors, it falls short of providing accurate result if it is used for time-domain simulations, especially those resulting into saturation conditions. This is due to the continuous change in L_m whenever the flux passes its saturation limit in either directions between L_{nom} and L_{sat}. This leads to the simulated flux using (3.3) repeatedly fluctuating between both extreme values due to the sudden jumps occurring to L_m within consecutive time-steps. This is demonstrated in Figure 3.5, for a simulation that uses the transformer parameters illustrated in Table 3.1, with $\phi_r = 0$ & $\alpha = 0$.

Table 3.1: Base transformer parameters for single-phase transformer simulations.

Parameter	Value	Parameter	Value
$Tx\ Rating\ (MVA)$	17.67	$R_1\ (pu)$	0.002
$V_p\ (kV)$	$11\sqrt{2/3}$	$L_1\ (pu)$	0.08
$f_n\ (Hz)$	50	$L_{nom}\ (pu)$	500
$\phi_{base}\ (wb.turn)$	28.58	$L_{sat}\ (pu)$	0.32
$Z_{base}\ (\Omega)$	2.283	$\phi_{sat}\ (pu)$	1.20

The reported parameters are based on a combination of default MATLAB/Simulink transformer model (pu impedances core saturation curve). The transformer rating is 17.67 MVA for single phase and triple this value (53 MVA) for three phase transformers to mimic a medium-voltage 11/33 kV transformer rating in Chapelcross network in Scotland. The absolute base voltage and impedance values vary in three-phase tests according to the considered transformer topology (i.e., $\Delta - Y_g\ vs. Y_g - Y_g\ \ldots etc$), and thus per-unit representation is maintained for consistency.

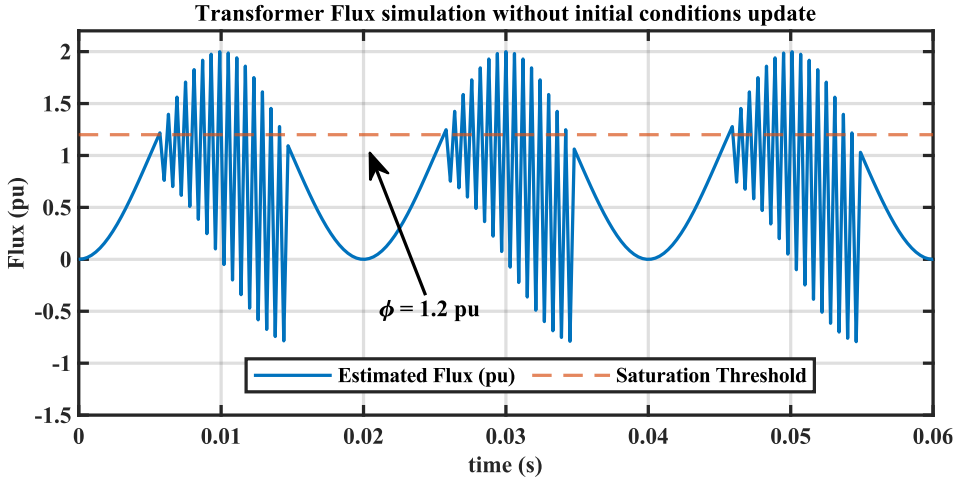

Figure 3.5: Flux time-simulation using equation (3.3) with variable L_m due to saturation transition.

Figure 3.5 shows that when L_m is varied between the two extreme values at the saturation region boundary ($\phi = \pm 1.2\ pu$), then equation (3.3) can no longer be used to approximate the time-varying flux at transformer core with high accuracy, nor is the decay rate dependent only on $R_1/(L_1 + L_{nom})$ or $R_1/(L_1 + L_{sat})$ ratio. Alternatively, the differential

equation for the circuit shown in Figure 3.4(b) is re-derived in a piecewise fashion to avoid the observed discontinuity.

$$L_T \frac{di}{dt} = V_p \sin(\omega t + \alpha) - R_1 i(t) \tag{3.5}$$

$$L_m \frac{di}{dt} = \frac{d\phi}{dt} \tag{3.6}$$

Equation (3.5) is first solved with respect to the input current (i), where the solution is found to be of the form illustrated in equation (3.7).

$$i(t) \approx (i(t_0) + i_{dc})\, e^{-\frac{R_1}{L_T}(t-t_0)} + i_{ac} \tag{3.7}$$

The DC (transient) and AC (steady state) terms are expressed in equation (3.8)-(3.9), where $\beta = \tan^{-1}(\omega L_T / R_1)$ is introduced to simplify the expression.

$$i_{dc} = \frac{-V_p(R_1 \sin(\omega t_0+\alpha) - \omega L_T \cos(\omega t_0+\alpha))}{R_1^2+(\omega L_T)^2} = \frac{-V_p \sin(\omega t_j+\alpha-\beta)}{\sqrt{R_1^2+(\omega L_T)^2}} \tag{3.8}$$

$$i_{ac} = \frac{V_p \sin(\omega t+\alpha-\beta)}{\sqrt{R_1^2+(\omega L_T)^2}} \tag{3.9}$$

The dc term captures a snapshot of the current value at $t = t_0$ (initial condition at $t = 0$, or any consequent saturation region boundary crossing instant $t = t_j$) to guarantee the piecewise function continuity and avoid the jumps observed in Figure 3.5. In other words, this term is updated every time the saturation flux threshold is crossed in either direction (entering or leaving saturation region). The boundary-crossing time t_j is similarly updated to match that instant. This is shown in the piecewise representation in equation (3.10), which is written generically for one cycle to be suitable for time-domain simulations (i.e., t_0 in (3.8) is replaced with the initial time in each segment).

$$i(t) \approx \begin{cases} \left(i(t_o{}') + i_{dc(t_0{}')}\right) e^{-\frac{R_1}{L_1+L_{nom}}(t-t_0')} + i_{ac} : t_0' \le t < t_1 \\ \left(i(t_1) + i_{dc(t_1)}\right) e^{-\frac{R_1}{L_1+L_{sat}}(t-t_1)} + i_{ac} : t_1 \le t < t_2 \\ \left(i(t_2) + i_{dc(t_2)}\right) e^{-\frac{R_1}{L_1+L_{nom}}(t-t_2)} + i_{ac} : t_2 \le t < T \end{cases} \tag{3.10}$$

where, t_1 is the point when the transformer enters saturation during each period, and t_2 is the time when the flux is below saturation threshold. t_0' is equal to $t_0 = 0$ in the first cycle, and then equal to t_2 from the previous saturation cycle. This is because after the first saturation cycle, the $t_0' \leq t < t_1$ current segment becomes a continuation to the third segment from the previous cycle. T represents the cycle time-period (0.02 s for a 50 Hz signal). It should be noted that β in equation (3.10) also switches between both L_T values, depending on the operating segment. If saturation is not experienced throughout the simulation, then continuous operation within the first segment is observed.

Typically, the value of β in i_{dc} and i_{ac} terms is very close to 90° due to the inductive nature of transformers, so equations (3.8)-(3.9) can be approximated by using the cosine function with negligible β impact, in a similar fashion to the representation commonly found from literature as in equation (3.3). However, this approximation loses its validity when the equation is used to estimate the flux and current in the presence of large resistance between the energizing source and the transformer. To maintain generality, this approximation is not used since pre-insertion resistors (PIR) energization technique is investigated. In terms of flux equation, then equation (3.5) can be solved similarly for ϕ using the flux-current correlation. The solution form is analogous to that presented in equation (3.7) for current, as below.

$$\phi(t) \approx (\phi(t_0) + L_m\, i_{dc})\, e^{-\frac{R_1}{L_T}(t-t_0)} + L_m i_{ac} \tag{3.11}$$

Consequently, the piecewise version of equation (3.11) is presented as below.

$$\phi(t) \approx \begin{cases} (\phi(t_0') + L_m\, i_{dc(t_0')})\, e^{-\frac{R_1}{L_1+L_{nom}}(t-t_0')} + L_m i_{ac} : t_0' \leq t < t_1 \\ \phi(t_1) + L_m\, i_{dc(t_1)}\, e^{-\frac{R_1}{L_1+L_{sat}}(t-t_1)} + L_m i_{ac} \quad : t_1 \leq t < t_2 \\ (\phi(t_2) + L_m\, i_{dc(t_2)})\, e^{-\frac{R_1}{L_1+L_{nom}}(t-t_2)} + L_m i_{ac} \quad : t_2 \leq t < nT \end{cases} \tag{3.12}$$

It is observed empirically that equation (3.12) resembles the behavior of the current source model (used in MATLAB/Simulink and PSCAD/EMTDC) more accurately when the exponential decay term is not multiplied by initial flux in the time segment $t_1 \leq t < t_2$.

Thus, this approximation is maintained hereafter for flux equations as it presents more accurate results and inrush decay trends during the inrush transient. Finally, the methodology for implementing the piecewise model is illustrated in Figure 3.6, where t_f refers to the simulation end time. This flowchart can be coded using software tools such as Python or MATLAB. In this investigation, MATLAB software is used, and the model is implemented using a step-time in the microseconds order of magnitude for increased results resolution ($T_s = 1\ \mu s$).

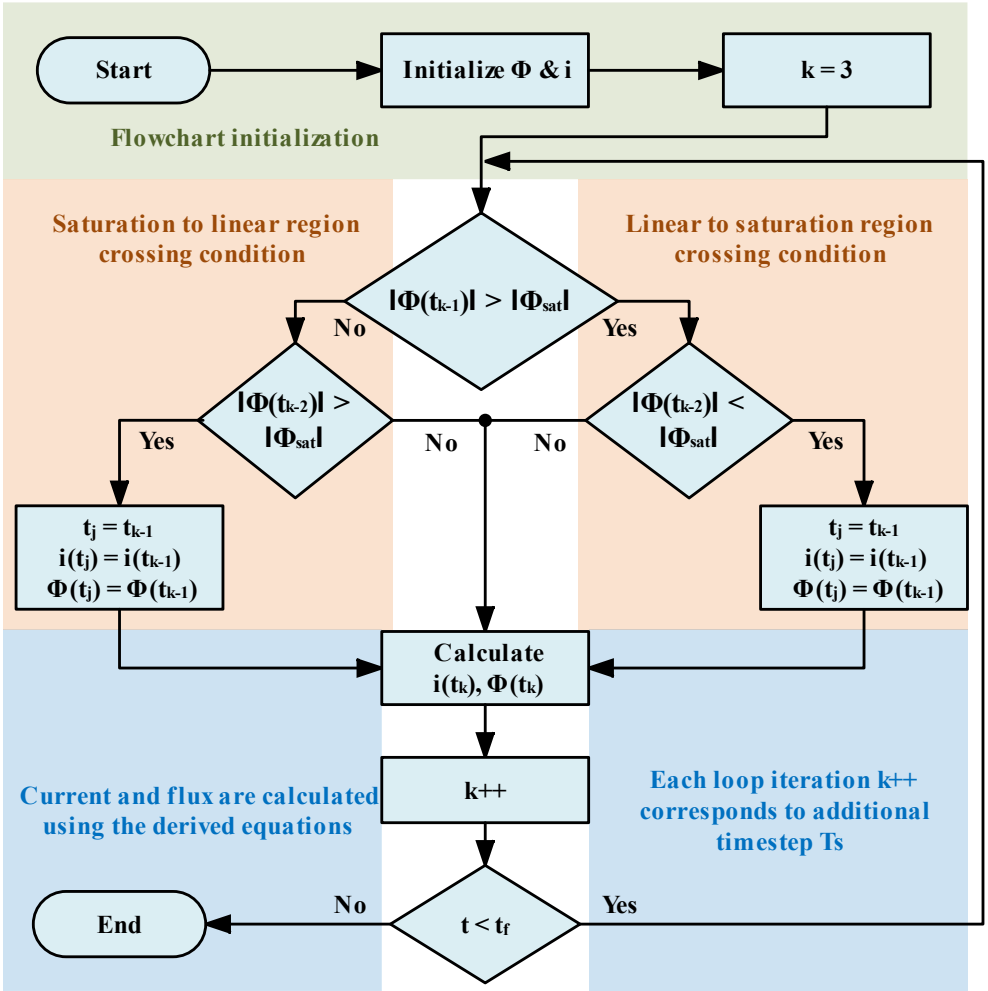

Figure 3.6: Flowchart for implementing the derived piecewise model for single-phase transformer inrush transient studies.

3.3.1. Model Validation

The derived model is compared against single-phase transformer simulation in PSCAD/EMTDC software. This tool is considered as a benchmark since it is widely used by industry, utilities, and consulting firms [65-68]. The simulated PSCAD transformer model is programmed with a knee-point of 1.2 pu and similar parameters to those reported in Table 3.1. Three cases are considered to benchmark the derived model performance against PSCAD. The first case is parametrized with $\phi_r = 0$ and $\alpha = 0$ to test the model response for demagnetized transformers. Then, the residual flux is set to an arbitrary value (e.g., $\phi_r = 0.5\,pu$) to validate the model performance with varying initial conditions in the second case, followed by the last scenario with $\alpha = 45°$ and $\phi_r = 0$.

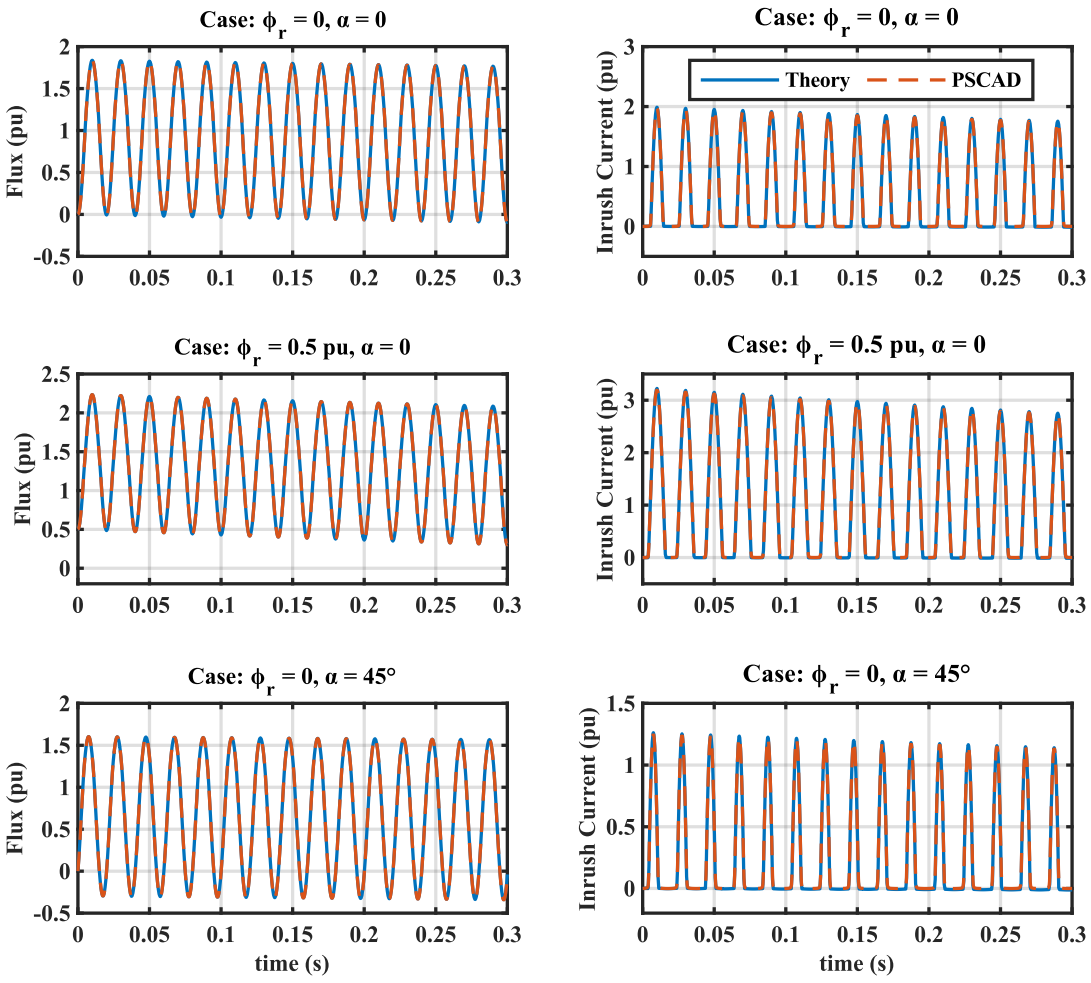

Figure 3.7: Theoretical model performance against PSCAD under three cases. Each row represents flux and inrush current for a separate case: (a) $\phi_r = \alpha = 0$, (b) $\phi_r = 0.5\,pu\,, \alpha = 0$, (c) $\phi_r = 0, \alpha = 45°$.

The simulation is carried for 15 cycles in each case to capture the initial transient and consequent decay. Results are summarized in Figure 3.7, showing very close agreement between both models for both flux and current waveforms. The first case in Figure 3.7 considers a demagnetized core that is energized at $\alpha = 0$. It should be noted that the peak flux should theoretically occur at 2 pu in undamped (ideal) transformers. Whereas the existing damping in this case through the series impedance leads to slightly less peak flux. The test transformer flux-current characteristics lead to a peak inrush current of nearly 2 pu, coinciding with the peak flux. The increased ϕ_r in the second case with the same α leads to a higher peak flux, deeper into the saturation region. Consequently, resulting into higher inrush current amplitude that follows the defined saturation curve characteristics with $L_{sat} = 0.32$ pu beyond $\phi_{sat} = 1.2\,pu$. Finally, the last case energization at a different angle $\alpha = 45°$ leads to a reduced peak flux compared to the first case, and a reduced inrush current peak.

After confirming the theoretical derived model performance, it is used to identify key trends and theoretical basis for key inrush current mitigation techniques. To start with, the exponential decay rate term in both magnetizing current and flux equations varies between $-R_1 t/L_{nom}$ and $-R_1 t/L_{sat}$. If only one operating mode is considered, then simulations have shown that the flux decay rate is equivalent to typical RL circuit rate. However, with the switching action between both inductance values, simulations from the derived model and PSCAD show that the decay rate is neither of these two extremes, and instead falls in between them, closer to L_{sat} rate since the linear region has very large time constant that the term can essentially be approximated to zero in the transient period where the core transits between both regions. These trends are illustrated in Figure 3.8 for the flux, using the parameters from Table 3.1 with $\phi_r = 0.8\,pu$ and $\alpha = 0$.

Another information that can be directly deduced from the derived model is whether or not the energization parameters lead to transformer saturation, and to identify the time of first saturation instant, if any. This is done by manipulating the first segment in equation (3.12) to obtain t_1. Given the very large time constant typically associated with the linear region due to L_{nom} large value, the exponential decay within that region can be assumed to have no impact in the first cycle's initial segment.

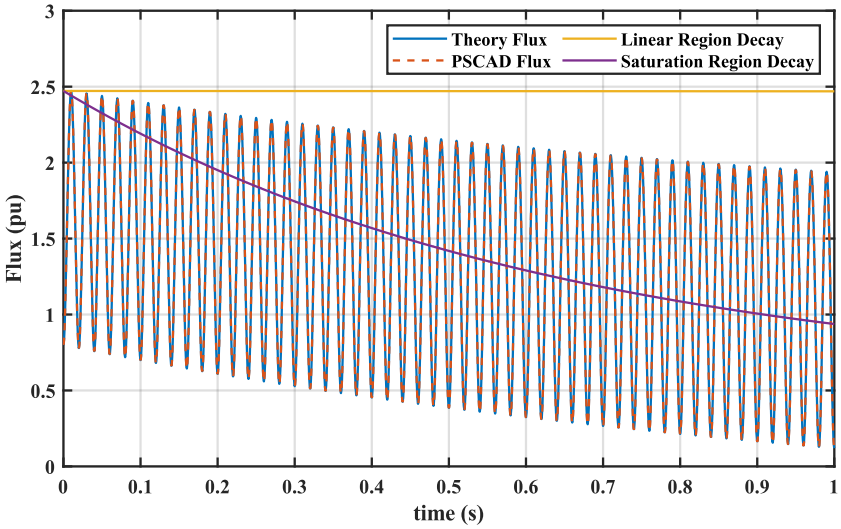

Figure 3.8: Flux decay rate demonstration against saturation and linear region time constants.

For simplicity, the constant term $L_m V_p / \sqrt{R_1^2 + (\omega L_T)^2}$ can be denoted as ϕ_{pk}. Then, the first segment in equation (3.12) can be re-written as follows.

$$\phi(t) \approx \phi_{pk} \sin(\omega t_1 + \alpha - \beta) + \phi_r - \phi_{pk} \sin(\alpha - \beta) \tag{3.13}$$

It is desired to identify the first saturation instant, which corresponds to $\phi(t) = \phi_{sat}$ or $\phi(t) = -\phi_{sat}$ at $t = t_1$. Solving equation (3.13) for t_1 after ϕ_{sat} substitution yields the following.

$$t_1 = nT + \left\{ \begin{array}{ll} \frac{\sin^{-1}(\phi_{sat(pu)} - \phi_{r(pu)} + \sin(\alpha-\beta)) - (\alpha-\beta)}{\omega} & : \phi(t_1) = +\phi_{sat} \\ \frac{-(\sin^{-1}(-\phi_{sat(pu)} - \phi_{r(pu)} + \sin(\alpha-\beta)) + (\alpha-\beta) + \pi)}{\omega} & : \phi(t_1) = -\phi_{sat} \end{array} \right\} \tag{3.14}$$

where, nT is a constant equal to the n^{th} time-period, and both residual and saturation fluxes are defined in pu. Both segments of equation (3.14) should be used for the saturation estimate to cover positive and negative saturation possibilities. When a saturation condition exists, one of them should produce a real number as a feasible solution, whereas the other generates a complex, infeasible, solution. If the saturation flux is not reached within the first period, then both segments should return infeasible complex solutions. This takes place when the $\sin^{-1}(x)$ function has an argument exceeding $|1|\, pu$, or when both $\pm\phi_{sat(pu)} - \phi_{r(pu)} + \sin(\alpha - \beta)$ variations exceed $|1|\, pu$. From this

analysis, it can be observed that the key parameter which can be manipulated during the transformer energization is α. Selecting an appropriate energizing angle α is thus a determining factor on whether the transformer goes into saturation in first place. This simple idea is the basis behind the controlled switching energization technique, which is discussed along with other techniques in the following subsection.

3.3.2. Model-Compatible Inrush Current Mitigation Techniques

Transformer energization techniques for inrush current mitigation range from physical modification to the equivalent circuit in Figure 3.2, to changes in the energizing source or circuit breaker (CB) closing times with a unified objective of eliminating or mitigating inrush current by avoiding or damping the operation in the transformer core saturation region. The rising penetration of renewable energy and storage resources with their power electronic converters grid-interface is once again putting more emphasis on inrush mitigation, given the established converters limited overcurrent ability. Before moving to soft energization model, two transformer energization techniques are introduced and discussed in the context of the derived constant-amplitude transformer model. Results for single-phase transformers are first presented, followed by scaling up to three-phase transformers to validate the observations.

A. Pre-Insertion Resistors (PIR)

A well-established technique in literature and industry is based on inserting physical resistors (PIRs) between the energizing source and the transformer phases to mitigate inrush current. This can effectively be represented in equations (3.7)-(3.12) through adding the PIR value to that of R_1 in series. PIR mainly contributes to: a) reducing the inrush peak, and b) faster transient decay [69-71]. This technique is used commonly in high-voltage applications, typically through dedicated breakers that 'insert' the resistors temporarily for energization [72], and then disconnects them to avoid the increased losses resulting from the high used resistance. The use of resistive superconducting fault current limiters (R-SFCL) is recently proposed in [68] to perform the PIR task with significant inrush current amplitude mitigation.

To illustrate PIR principle of operation, an example is presented and linked to the

theoretically derived equations. The example uses a transformer model with similar parameters to those reported in Table 3.1. In addition, residual flux and energizing angle are defined arbitrarily as: $\phi_r = 0.5\,pu$, and $\alpha = 0$. Four different values for R_1 are used, namely: [0.002, 0.02, 0.2, 2] pu to demonstrate the increasing resistance impact between the energizing source and the transformer. When applying PIR, the β approximation to 90° in equation (3.3) is no longer valid, as the value deviates further from this default when increasing the effective R_1 (decreasing the impedance X/R raio). This is evident from the results presented in Figure 3.9.

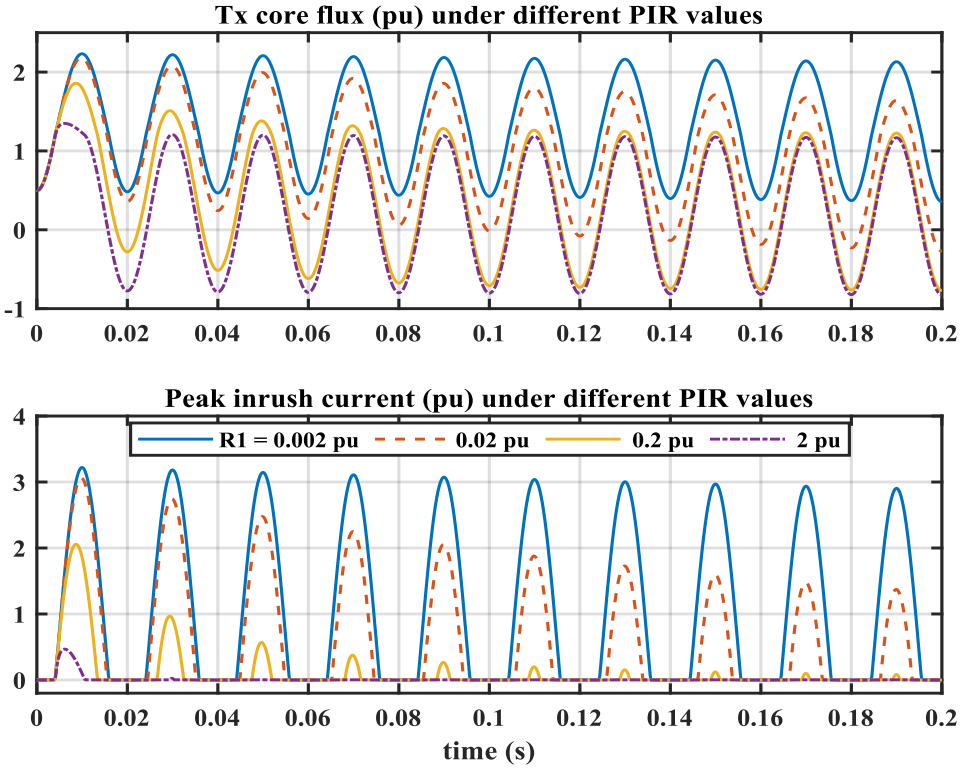

Figure 3.9: Flux and inrush current response against different effective R_1 values.

That is, in addition to the reduced peak and accelerated decay observed for high PIR values, the first flux and magnetizing current peaks for $R_1 = 0.2$ pu and $R_1 = 2$ pu occur at visibly different phase angles to those reported for low R_1 values where the $\beta \approx 90°$ is still valid. This is because when the core is saturated and $L_m \approx L_{sat}$, the circuit impedance is highly influenced by the high R_1 value, which causes a higher voltage-drop across the

PIR, leading to an altered phase angle between the source and the transformer core. Consequently, the core voltage integral produces lower ϕ peak at a different angle.

Next, the same technique is applied to a three-phase $\Delta - Y_g$ transformer to showcase the trends similarity between both models, while keeping in mind the inter-phases dependency of voltage and flux due to the delta (Δ) winding existence. The same per-unit transformer parameters are maintained as before in the MATLAB/Simulink model, while tripling the rating from 17.67 MVA to 53 MVA. When the three-phases are simultaneously energized, the inherent $120°$ phase shift between them can be considered as a shift in α for phase B and C. Namely, if $\alpha_v = -30°$, then phase A of the transformer energizes at $\alpha_A = 0°$ to account for Δ phase shift, whereas the transformer B and C windings energize at an equivalent $\alpha_{eq} = \alpha_A \mp 120°$, respectively. This causes different flux and inrush current behavior across all phases, even if ϕ_r in each phase is zero. To illustrate this behavior, along with the PIR impact of using $R_1 = 0.2$ pu, an example is presented with $\phi_r = [0.5, 0, -0.5]$ pu. Since the transformer is energized from delta side, α is chosen to be $-30°$ such that $\alpha_A = 0$. Simulation results are shown in Figure 3.10. It is noted that the flux and inrush current behavior in phase A are highly similar to Figure 3.9 as the same per unit parameters are used to energize them. The peak inrush in transformer phase A is equal to the single-phase case with PIR = 0.2 pu, whereas the other two transformer phases (B and C) follow patterns that correspond to their ϕ_r and α combinations (i.e., $\alpha_B = 120°, \alpha_C = -120°$). The presented three-phase transformer results are based on simulation with three single-phase transformer units. Similar trends are also observed with the single-core model, with slight current variations due to the additional flux path. Though, current and flux peaks are observed to be of similar orders of magnitude.

Overall, the PIR technique requires installing additional equipment (PIR circuit breaker), and increases the overall system cost and losses. A recent variation aims to utilize virtual damping through grid-forming converter control to mimic the PIR behavior for an offshore windfarm HVDC link [67], paving the way to extend the method application to virtual impedance based on GFC control modifications. Another recent work has proposed modifying the reference inverter voltage or current references for inrush mitigation.

Experimental results using a 1 MVA battery to energize a network show significant inrush mitigation [16]. Though, the presented analysis does not take ϕ_r impact into account.

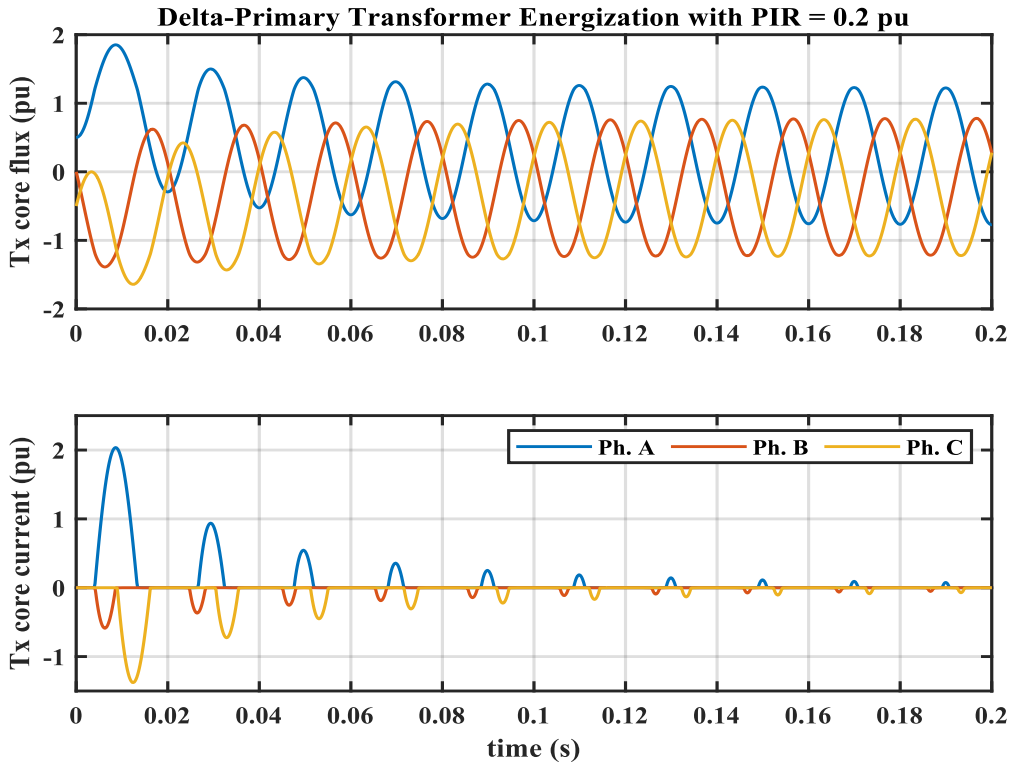

Figure 3.10: Hard energization with PIR = 0.2 pu for a three-phase ($\Delta - Y_g$) transformer.

B. Controlled Switching

This technique, also known classically as Point-on-Wave (PoW) switching, relies on energizing the transformer in the instant when the core residual flux is equal to the 'prospective flux' to eliminate the dc component impact in equation (3.13). The prospective flux (ϕ_{prosp}) for a transformer core is estimated by integrating the voltage at the open transformer terminals as in (3.15), and the CB closing scheme requirement under PoW switching is represented in (3.16).

$$\phi_{prosp} = \int V_n \sin(\omega t)\ dt \tag{3.15}$$

$$CB = 1 \Leftrightarrow (\phi_r = \phi_{prosp}) \tag{3.16}$$

Since ϕ_r is a constant, the variable that can be manipulated is the switching angle α. In controlled switching, selecting the optimal transformer energization instant causes the flux to peak at $\pm 1\ pu$ and to continue oscillating between these two points, thus preventing the core from going into saturation in first place, and neutralizing inrush current impact.

Theoretically, the circuit breaker closing angle corresponding to the requirement in (3.16) can be calculated for a single-phase transformer by equating the time invariant terms in (3.13) to zero and solving for α. The optimal closing angle α_{cs}, and corresponding time t_{cs} equations, are consequently illustrated as below.

$$\alpha_{cs} = \sin^{-1}\left(\phi_{r(pu)}\right) + \beta \tag{3.17}$$

$$t_{cs} = (n-1)T + \frac{\alpha_{cs}}{\omega} \tag{3.18}$$

where, n denotes the cycle number. For transformers with $\beta \approx 90°$, and equivalent expression to that in (3.17) can be derived using the inverse cosine function. Two examples are presented to showcase the effectiveness of this technique. In the first example, ϕ_r is set to 0.5 pu. Using the transformer parameters in Table 3.1, the $\beta \approx 90°$ is valid since X >> R. Applying equation (3.17) corresponds to an optimal switching angle at $\alpha_{cs} = 120°$, at $t_{cs} = (n-1)T + 6.67\ ms$. Matching simulation results are obtained as illustrated in Figure 3.11(a), where $n = 4$. Another example is presented in Figure 3.11(b) with $\phi_r = -0.7\ pu$. The switching angle and time are adjusted accordingly by the circuit breaker control algorithm to $\alpha_{cs} = 45°$ at $t_{cs} = (n-1)T + 2.5\ ms$. In both cases, inrush current is eliminated, and the transformer continues operating in the linear region after energization. The two reported ϕ_r values are selected as examples with opposite signs to showcase the technique effectiveness, and the same controlled switching principle applies equally to any other residual flux value.

In practice, a circuit breaker closing delay typically exists between the time of issuing the command and the actual circuit breaker closing instant, which causes deviation in the closing instant. If the error is significant and not well-compensated, then inrush currents could still flow to the transformer, with magnitude that depends on the breaker closing error as will be illustrated in Chapter 4. Compensation algorithms should thus be

considered when applying this technique. In principle, implementing controlled switching also requires measuring ϕ_r, which might not be always available, depending on the measurement devices installed at the transformer substation. Recent works proposed core pre-fluxing before energization to avoid this requirement [52].

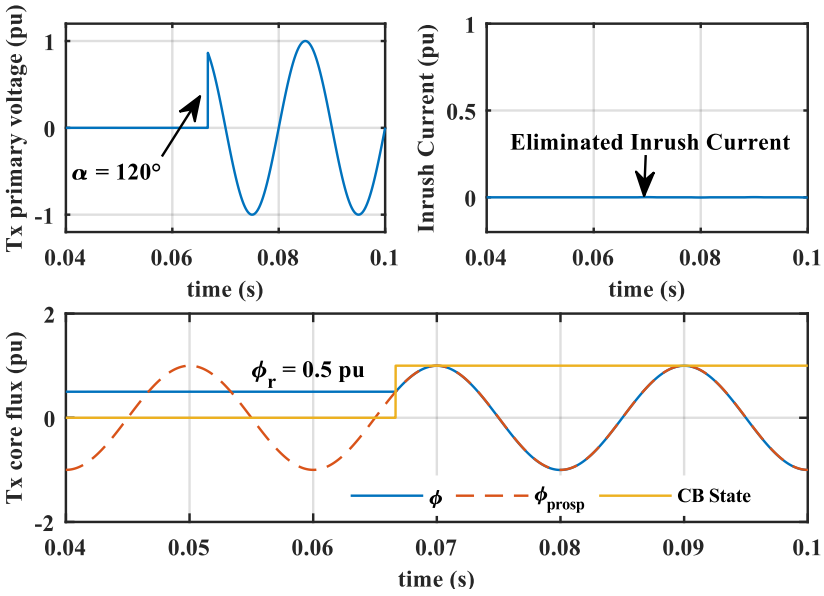

(a)

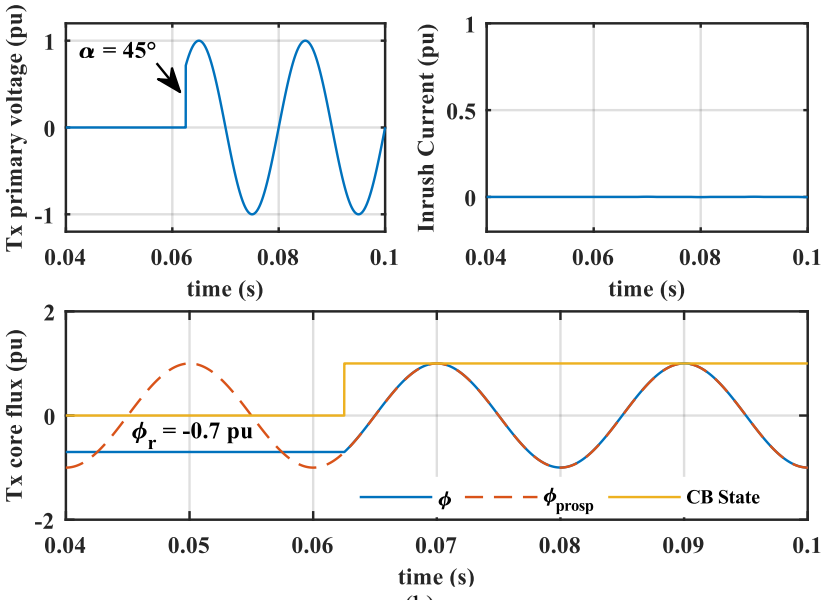

(b)

Figure 3.11: Controlled Switching technique validation with: (a) $\phi_r = 0.5\ pu$, (b) $\phi_r = -0.7\ pu$.

C. Controlled Switching Extension to Three-Phase Transformers

When extended to three-phase transformers, the classical controlled switching technique requires independent control of the breaker phases to close at their corresponding optimal closing instants, with varying logic depending on the transformer topology. As an example, when a three-core $Y_g - Y_g$ transformer is energized, then the phases are considered independent in the sense that if one phase breaker is energized then a voltage would form between the corresponding phase winding and the ground independently from the other phases as in Figure 3.12(a), whereas in Δ winding energization, two phases are required to operate simultaneously to create the line-to-line voltage required to energize one winding. The other two windings are partially energized to equalize the delta voltage loop (i.e., generating voltages that add up to equalize the voltage formed on the first energized winding) as in Figure 3.12(b). This also leads to oscillatory fluxes in the remaining two cores that similarly act to equalize the energized core flux.

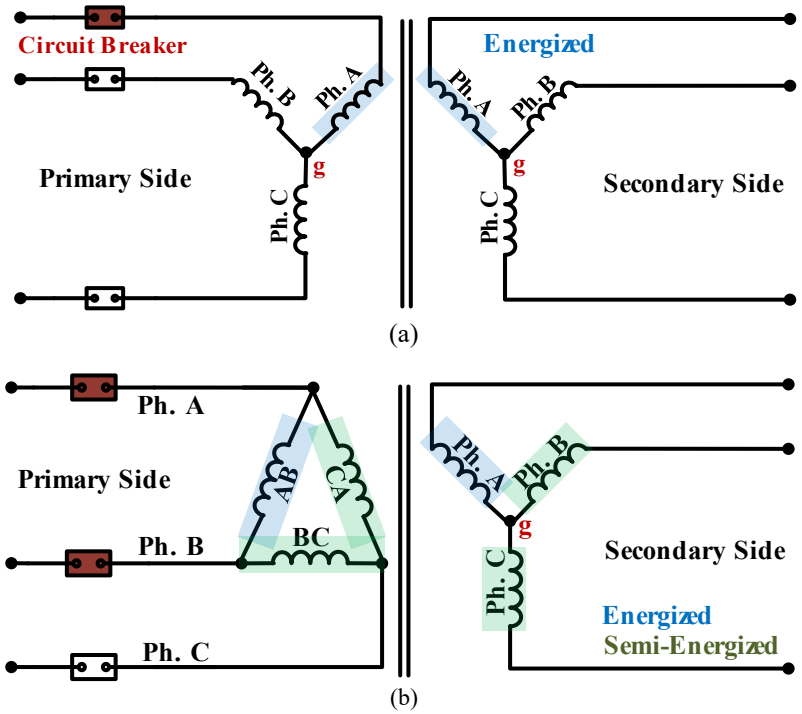

Figure 3.12: Configuration-based variation in controlled transformer energization sequence: (a) three core wye-wye transformer, (b) three core delta-wye transformer, red indicates closed breaker.

Simulation tests are carried for both discussed configurations ($\Delta - Y_g$ and $Y_g - Y_g$) to validate the theoretical predictions, using $\phi_r = [-0.7, -0.1, 0.8]$ pu. This residual flux combination is selected arbitrarily for demonstration, with relatively high ϕ_r values to showcase the technique inrush suppression effectiveness. For the $\Delta - Y_g$ transformer, the AB winding is energized first following the criteria in equations (3.17)-(3.18). As expected, the flux in the other two windings follows an oscillatory pattern. It is observed that applying a similar criteria to CA winding (transformer phase C) such that the oscillatory flux is equal to the prospective flux, and closing the circuit breaker at that instant, similarly eliminates the inrush at the other two windings and causes their flux to follow the prospective flux path with eliminated inrush current. This is because BC and CA windings are observed to have simultaneous intersecting points between their oscillatory and prospective fluxes as illustrated in Figure 3.13(a).

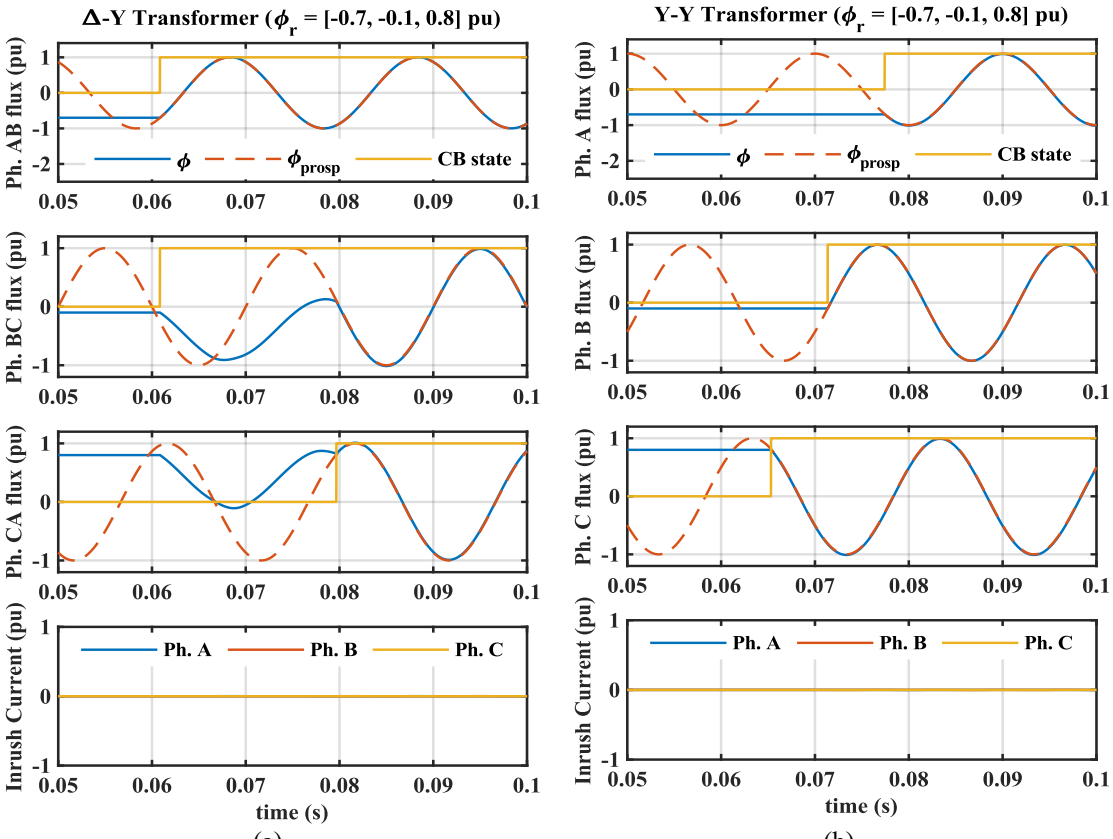

Figure 3.13: Three-phase controlled switching results: (a) $\Delta - Y_g$ transformer, (b) $Y_g - Y_g$ transformer.

This trend has been tested on different ϕ_r combinations, which were found to produce results aligned to this observation. On the other hand, Figure 3.13(b) shows the results of energizing a $Y_g - Y_g$ transformer comprised of three single-phase units. The windings are energized independently at their corresponding optimal points, and inrush current is eliminated. Slight delays are introduced between the closing actions for improved visualization.

Finally, the $Y_g - Y_g$ energization trends are observed to be slightly altered when a single-core configuration is used due to the additional flux path between the phases. Namely, when the first phase is energized, the remaining two exhibit oscillatory flux patterns in the opposite direction but can still be energized independently. Overall, the controlled switching technique for transformers energization is very effective in suppressing inrush current. However, the unavailability of required control relays, poor delay compensation or missing/high residual flux measuring errors can lead to mis-operation and still cause inrush current. These aspects should be considered for a proper technique implementation.

3.4. Electrical Transformer Model for Soft Energization

The voltage control flexibility of grid forming converters can be exploited in network energizations through manipulating the control voltage reference. This helps in inrush current mitigation from transformers and cables. A typical approach to achieve this task is through soft energization, where the voltage is slowly ramped up between zero and 1 pu during a time period equal to T_{ramp} as shown in equation (3.19).

$$V = \begin{cases} \dfrac{t}{T_{ramp_{j_j}}} V_p \sin(\omega t + \alpha) : t \leq T_{ramp} \\ V_p \sin(\omega t + \alpha) \qquad : t > T_{ramp} \end{cases} \tag{3.19}$$

The voltage reference envelope that is applied to the grid-forming converter voltage control with this technique is illustrated in Figure 3.14, where the voltage reference refers to the peak value. To demonstrate how soft energization works, an example using PSCAD single-phase transformer model is presented, with the results summarized in Figure 3.15. The transformer model is also parameterized as in Table 3.1 with variable ϕ_r and T_{ramp}.

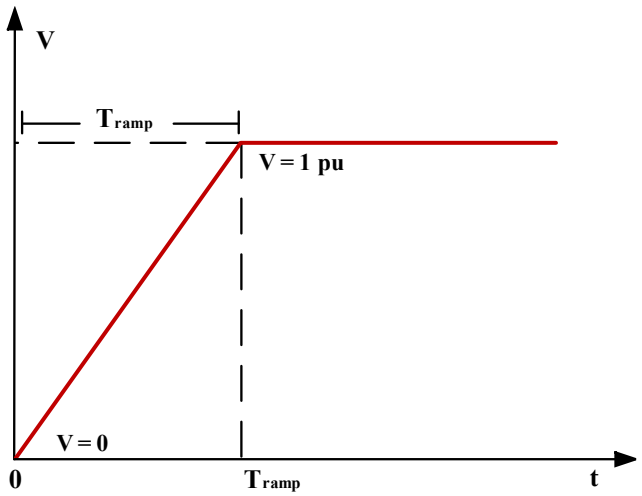

Figure 3.14: Soft energization ramping control voltage reference.

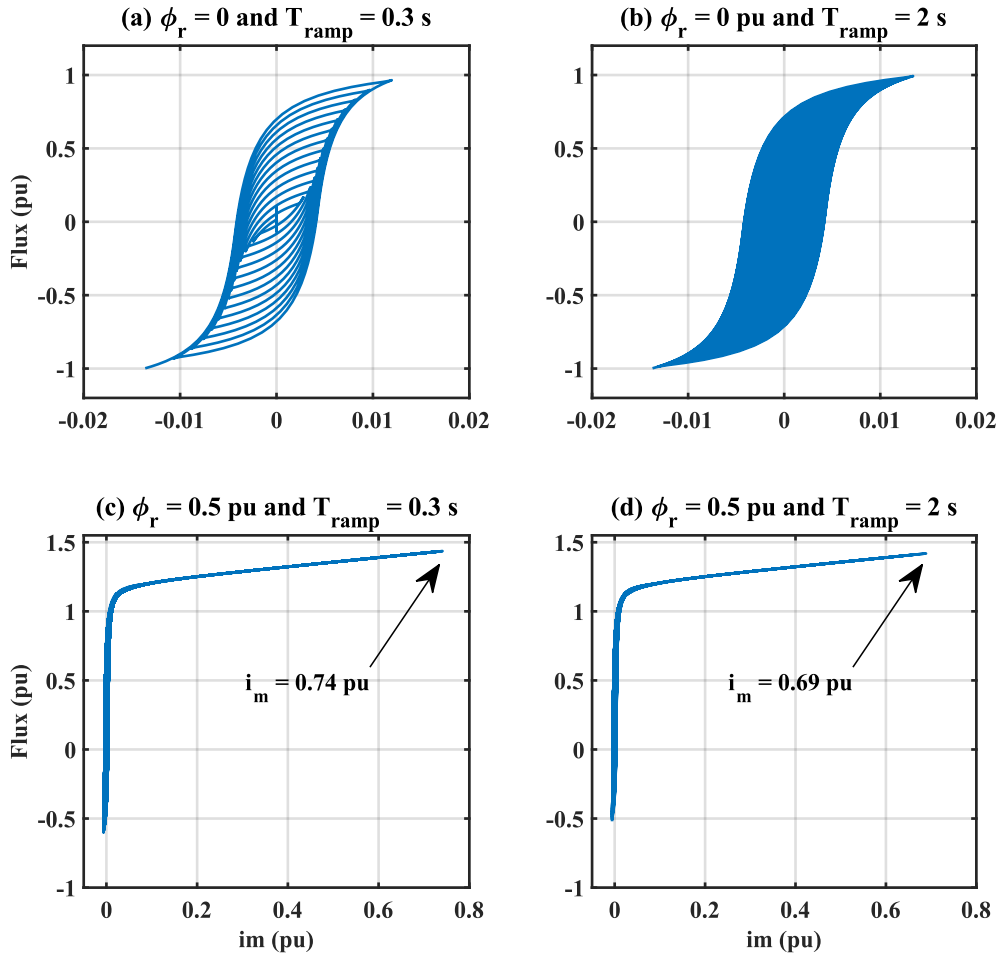

Figure 3.15: Ramping voltage impact on transformer saturation curve: (a) $\phi_r = 0$ and $T_{ramp} = 0.3\ s$, (b) $\phi_r = 0$ and $T_{ramp} = 2\ s$, (c) $\phi_r = 0.5\ pu$ and $T_{ramp} = 0.3\ s$, (d) $\phi_r = 0.5\ pu\ and\ T_{ramp} = 2\ s$.

This example is composed of four different scenarios for demonstration. In the first case, ϕ_r is zero and T_{ramp} is set to 0.3 s. As shown in Figure 3.15(a), the flux ramps up from the zero point in small, minor, hysteresis loops and builds up until reaching the major loop between -1 and 1 pu, while operating in the linear region since $\phi_{pk} < \phi_{sat}$, which is equal to 1.2 pu. The number of minor loops corresponds to the number of cycles, which for a 50 Hz source is 15 for $T_{ramp} = 0.3\ s$. Then, the core continues operating normally in the rated conditions. Another example with demagnetized core and $T_{ramp} = 2\ s$ is shown in Figure 3.15(b), the longer ramp duration results into 100 minor loops, leading to a denser $\phi - i_m$ curve. In the third case, ϕ_r is set to 0.5 pu, with $T_{ramp} = 0.3\ s$. The ramping action starts from $\phi = 0.5$ pu, and continues until $t = 0.3\ s$. However, the core runs into saturation with high magnitude inrush current due to insufficient ramp-up time as shown in Figure 3.15(c). If a case with the same starting point ($\phi_r = 0.5\ pu$) is simulated with $T_{ramp} = 2\ s$, then a lower peak current is generated at $t = T_{ramp}$ as shown in Figure 3.15(d). The presented results cover the ramping duration, after that, the exponential decay dominates because of damping, and the flux starts going slowly back to ± 1 pu interval.

3.4.1. Soft Energization Ramp-Rate Selection in Literature

Lately, soft transformer energization has been increasingly used in literature as a technique to mitigate inrush currents in high voltage or distribution level applications, given the highlighted increased VSCs penetration in electrical networks. Defining the voltage ramp duration has not usually been a justified parameter and is instead provided as a value or a range of values as part of wider analysis. For instance, the authors of [73] used a 50 MVA generator with 10 seconds ramp to energize a series of transformers. In [17], the authors defined a soft energization range between 15 and 30 seconds for a wind turbines case study. The impact of a voltage source converter ramp requiring tens of seconds or minutes from a protection perspective was discussed in [74], and a simulation case with 2 seconds ramp was presented. The authors of [12] tested soft energization from a wind turbine with up to 100 seconds duration. On the other hand, the authors of [75] presented a soft energization case using a grid-forming converter with a one second voltage ramp duration,

and a 3 seconds ramp was presented in [76] for energizing a wind farm. Clearly, there is a missing consensus on setting the energization ramping time, and the key factors influencing this selection.

3.4.2. Mathematical Model Derivation

To better understand soft energization drivers and the impact of different parameters and voltage ramp-rates, a new model is derived using the switched inductor saturation curve approximation. This is because while the transformer model introduced in section 3.3 can be used for energization studies from fixed-amplitude voltage sources and is suitable to study and evaluate the impact of classical energization techniques such as controlled switching and pre-insertion resistors, it fails to accurately predict the behavior during soft energization, since the source voltage behavior no longer follows the steady-state 1 pu sinusoid. Thus, the derived model cannot be directly applied with high accuracy in the interval when $t \leq T_{ramp}$. Instead, it requires re-solving the system differential equation to reflect this change. The updated differential equation for the circuit shown in Figure 3.2 is thus presented in (3.20), for a ramping voltage source between 0 and 1 pu at $t = T_{ramp}$.

$$L_T \frac{di}{dt} = \frac{t}{T_{ramp}} V_p \sin(\omega t + \alpha) - R_1 i(t) : t \leq T_{ramp} \tag{3.20}$$

This differential equation is solved for current and flux. Solutions are found to be of a similar final form to the model derived before, but with different dc and ac terms to reflect the ramping action impact. The updated soft energization terms are summarized as follows in equations (3.21)-(3.25).

$$i_{soft}(t) \approx \left(i(t_o) + i_{dcsoft}\right) e^{-\frac{R_1}{L_T}(t-t_0)} + i_{acsoft} \tag{3.21}$$

$$i_{dcsoft} = \frac{-V_p\left((R_1 Z_{RL} t_j + Z'_{RL} L_T)\sin(\omega t_j + \alpha) - \omega L_T (2RL_T - Z_{RL} t_j)\cos(\omega t_j + \alpha)\right)}{T_{ramp} Z_{RL}^2} \tag{3.22}$$

$$i_{acsoft} = \frac{V_p\left((R_1 Z_{RL} t + Z'_{RL} L_T)\sin(\omega t + \alpha) + \omega L_T (2R_1 L_T - Z_{RL} t)\cos(\omega t + \alpha)\right)}{T_{ramp} Z_{RL}^2} \tag{3.23}$$

$$Z_{RL} = (\omega L_T)^2 + R_1^2 \tag{3.24}$$

$$Z'_{RL} = (\omega L_T)^2 - R_1^2 \tag{3.25}$$

where Z_{RL} and Z'_{RL} are introduced to simplify the expressions, and the RL components are the same as those demonstrated in Figure 3.2. The time-domain solution contains terms with t to represent the ramping behavior of current and flux during this period. The current and flux peaks are inversely proportional to T_{ramp}, and are also influenced by the network impedance. The flux equation in soft energization follows a similar pattern as before with respect to current, as illustrated in equation (3.26).

$$\phi_{soft}(t) \approx (\phi(t_0) + L_m\, i_{dcsoft})\, e^{-\frac{R_1}{L_T}(t-t_0)} + L_m i_{acsoft} \tag{3.26}$$

The piecewise version of current and flux equations are also of a similar form to that presented earlier, with the difference being that after the soft ramp is done ($t > T_{ramp}$), a transition to equations (3.10) and (3.12) should be made for current and flux estimations as shown below. The subscript (agg) refers to the aggregate combination between the equations derived for energizing from a ramping source in the interval ($t \leq T_{ramp}$) and a constant amplitude source within the interval ($t > T_{ramp}$).

$$i_{agg}(t) \approx \begin{cases} i_{soft}(t) : t \leq T_{ramp} \\ i(t) \quad\quad : t > T_{ramp} \end{cases} \tag{3.27}$$

$$\phi_{agg}(t) \approx \begin{cases} \phi_{soft}(t) : t \leq T_{ramp} \\ \phi(t) \quad\quad : t > T_{ramp} \end{cases} \tag{3.28}$$

At the transition instant between the ramping and steady-state energizing source operation, the flux and current should be assigned the values of the previous time step to avoid sudden jumps. Then, the use of constant-amplitude voltage source model equations is resumed normally for the rest of the simulation.

3.4.3. Model Validation

The derived soft energization model is also validated against PSCAD/EMTDC software. Three cases are selected where T_{ramp} is set to 2 seconds, against three different residual flux values, namely: $[0.1, 0.5, 0.8]$ pu. This residual flux variability serves to illustrate different operating conditions of the model with high accuracy. The result of these three cases are presented in Figure 3.16 to Figure 3.19, showcasing the flux and inrush current behavior during both the ramping and steady-state source voltage segments, and compared to simulated tests run using PSCAD/EMTDC standard transformer model with similar parameters.

The first case results with $\phi_r = 0.1$ pu are illustrated in Figure 3.16, where it is noted that theoretical and PSCAD model results are nearly identical. The figure also demonstrates a zoom-in version around $t = T_{ramp}$, showing the matching models behavior. Given the low residual flux value, the peak flux at $t = T_{ramp}$ is observed to remain under saturation, leading to minimal inrush current that is limited by the high linear region inductance.

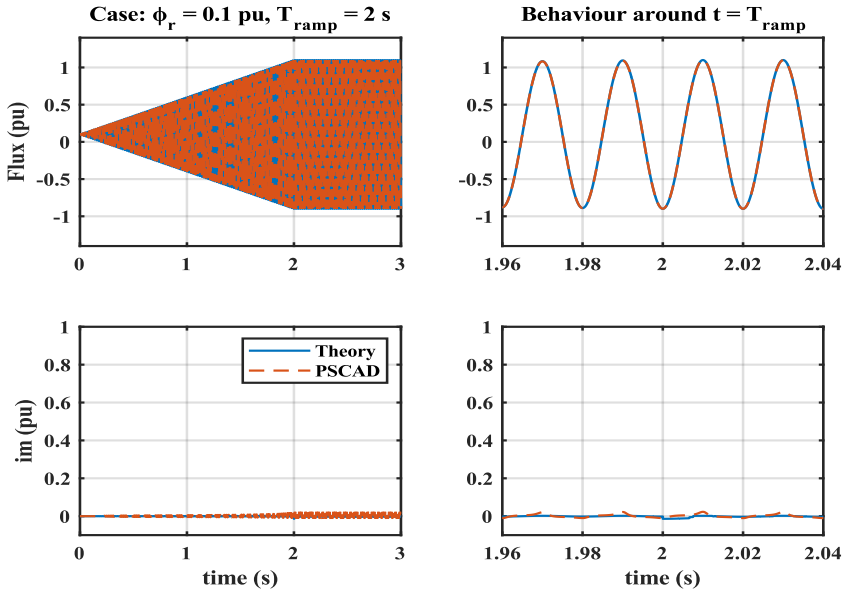

Figure 3.16: Theoretical soft energization transformer model performance against PSCAD for $\phi_r = 0.1$ pu and $T_{ramp} = 2$ s.

Compared to the hard energization results presented in Figure 3.7 with $\alpha = 0$ and a demagnetized core, the use of soft energization is shown here to be an effective tool to suppress the impact of α using $T_{ramp} = 2\ s$ (the same transformer parameters are used to validate both models). This is because in soft energization, the voltage amplitude is minimal in the first few cycles, thus the impact of voltage angle is eliminated when T_{ramp} is selected to be higher than the first few cycles duration. This is illustrated in Figure 3.17(a) for a demagnetized core and T_{ramp} set to 0.205 s (i.e., 10 cycles and 90 degrees to stimulate worst-case angle). Theoretically, if a very low ramp time is selected (e.g., 0.01 s within the first cycle), then the impact of α will not be fully neutralized. An interesting contrast is observed for some T_{ramp} values within the first cycle. For instance, setting $\alpha = 0$ generates worst-inrush current in hard energization of a demagnetized core with $\phi_r = 0$, while $\alpha = 90°$ is the optimal switching instant from (3.17). Whereas, setting T_{ramp} to 0.01 s effectively reverses these roles in soft energization as illustrated in Figure 3.17(b). This is because at $t = 0.01\ s$, the voltage has already built-up to 1 pu, and so this

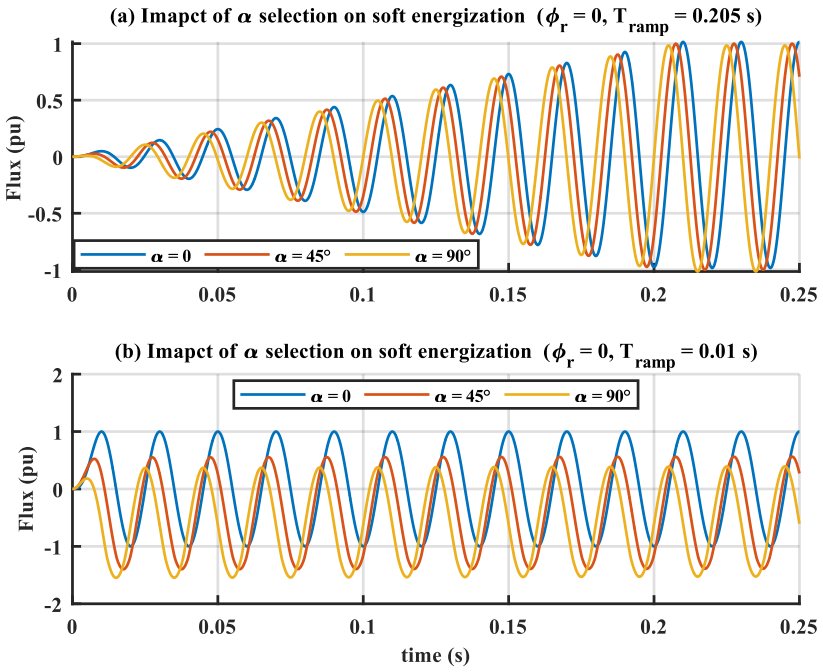

Figure 3.17: Impact of energizing angle α on soft energization of demagnetized cores (a): neutralized impact at $T_{ramp} = 0.205$ s, (b): visible impact at much faster ramps.

instant can be approximated as the starting point of a quasi-hard energization event. That is, for $\alpha = 0\ and\ \phi_r = 0$, the voltage angle at $t = 0.01\ s$ is at 180°, and the flux is at 1 pu (peak). This combination, when considered as a hard energization initial point ($\alpha = 180°, \phi_o = 1\ pu$) results into inrush elimination according to (3.17). On the other hand, $\alpha = 90°$ is projected into $\alpha = 270°$ at $t = 0.01\ s$, where the flux at this angle is estimated at -0.667 pu. Applying (3.17) for this value as a quasi-ϕ_r results into an angle that is substantially different than 270°, leading to the observed core flux saturation in Figure 3.17(b). Although such low ramp times are impractical, this illustration shows the interesting theoretical impact of setting such low ramp values.

Results for the two remaining model validation cases are presented in Figure 3.18 and Figure 3.19. Due to the higher residual flux used in these two cases, one can observe two opposing trends acting against each other: a) the exponential decay of the transient mainly caused by residual flux since α impact is largely neutralized, and b) the flux build-up from the ramp. The nearly matching behavior of the theoretical model and PSCAD results is evident, thus validating the model as a capable tool to deduce transient inrush trends and analyze them, similar to the constant-amplitude energizing source model.

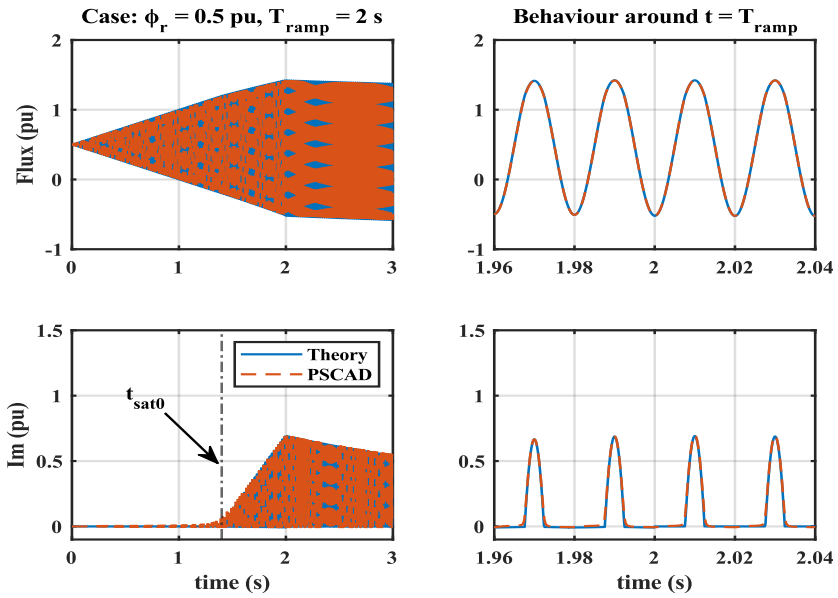

Figure 3.18: Theoretical soft energization transformer model performance against PSCAD for $\phi_r = 0.5$ pu and $T_{ramp} = 2$ s.

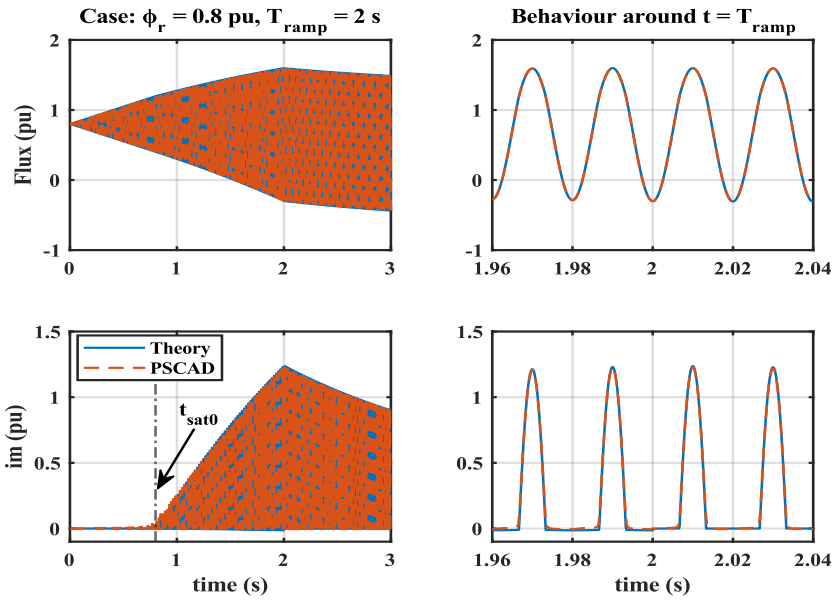

Figure 3.19: Theoretical soft energization transformer model performance against PSCAD for $\phi_r = 0.8$ pu and $T_{ramp} = 2$ s.

The ramping action causes the flux and current to peak at $t = 2$, before starting to decay to steady-state values. Figure 3.18 and Figure 3.19 clearly exhibit saturation behavior despite the applied soft voltage ramp, which mainly stems from the high residual flux. It is also observed that higher ϕ_r produces higher flux and inrush current peaks.

A. Saturation-Time Definition in Soft Energization

It is noted in Figure 3.18 and Figure 3.19 that the transformer core goes into the saturation region at different time instants. This is because initially, the transformer core is operating in its linear region since $\phi_r < \phi_{sat}$. The gradual flux build-up due to the voltage ramp also prevents first-period saturation, unlike the case in hard energization. In the linear region, effective magnetizing inductance is very large (L_{nom}) and thus the decay-rate time constant is similarly long, essentially validating the decay-rate approximation to zero for short durations. This means that until the first instant of core saturation in the switched RL model, the flux ramping rate is nearly constant with negligible decay and may thus be approximated as a linear increment from the flux starting point (ϕ_r). This is valid unless the equivalent resistance is large enough to cause noticeable decay before the first saturation instant (i.e., if PIR is used or long resistive lines exist between the source and

the transformer). With this approximation, the first saturation time instant can be derived as shown, solving for the time variable (t) when $\phi = \phi_{sat}$.

$$\phi \approx \phi_r + \frac{t}{T_{ramp}} \phi_n \tag{3.29}$$

$$t_{sat0} \approx \frac{|\phi_{sat} - \phi_r|}{\phi_n} T_{ramp} \tag{3.30}$$

Equation (3.30) shows the correlation between residual flux and core saturation in transformers soft energization when $X \gg R$. Some key aspects can be inferred from this equation. Namely, when (ϕ_r) is closer to (ϕ_{sat}), saturation is reached faster and (T_{ramp}) should thus be extended further to damp the transformer after it runs into saturation and reduce high inrush peaks. Also, it can be observed from this equation that when $|\phi_{sat} - \phi_r| > 1$, the simulated transformer does not go to saturation in first place, since the required time is higher than the ramping time. This is clearly the case in Figure 3.16, where $|\phi_{sat} - \phi_r| = 1.1$ pu, and thus the transformer did not go into saturation. Whereas when $\phi_r = 0.5$ pu, saturation took place around $t_{sat0} = (1.2 - 0.5)x2 = 1.4\,s$, as compared to $t_{sat0} = (1.2 - 0.8)x2 = 0.8\,s$ at $\phi_r = 0.8\,pu$ (see Figure 3.18 and Figure 3.19). After (t_{sat0}), the transformer goes deeper into the saturation region with each cycle before the flux reaches its peak value at T_{ramp}.

B. Soft Energization Extension to Three-phase Transformers

To show (T_{ramp}) impact on the flux and current peaks, a three-phase $Y_g - Y_g$ transformer is simulated in MATLAB/Simulink software and soft energized with the residual flux in the three phases set to $\phi_r = [0.8, 0, -0.8]$ pu. T_{ramp} is varied between 1 s and 10 s, and the impact on phase A flux and current envelopes is illustrated in Figure 3.20. Clearly, the flux and inrush current peaks are reduced because of the additional time given for the exponential decay in the saturation region before the voltage ramp is concluded. Equation (3.30) can similarly be applied here to accurately predict the first saturation instant for each applied voltage ramp-rate despite being derived for a single-phase transformer. This leads to $t_{sat0} = [0.4\,s, 0.8\,s, 2\,s, 4\,s]$ for $T_{ramp} = [1\,s, 2\,s, 5\,s, 10\,s]$.

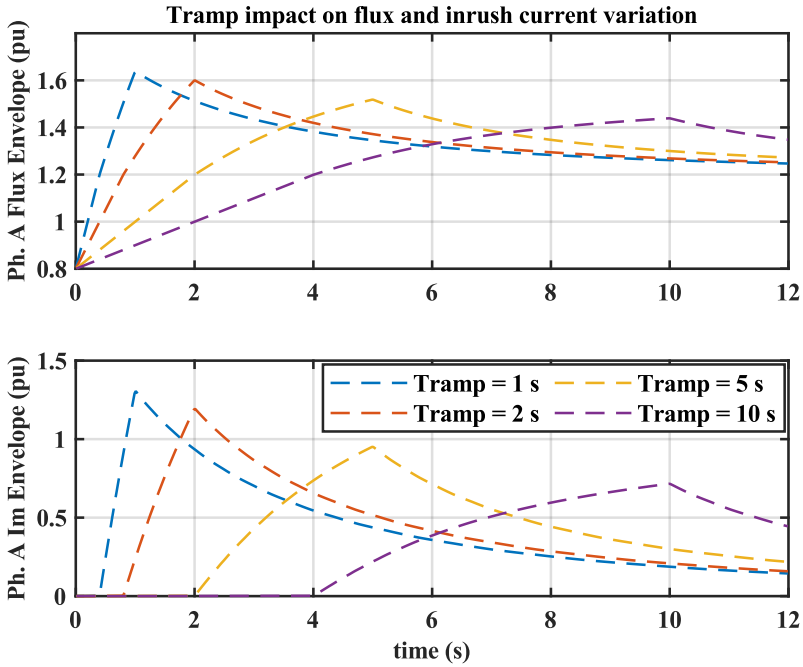

Figure 3.20: Impact of varying the voltage ramp time on peak flux and magnetizing current (Ph. A of a Y-Y transformer with $\phi_r = 0.8$ pu).

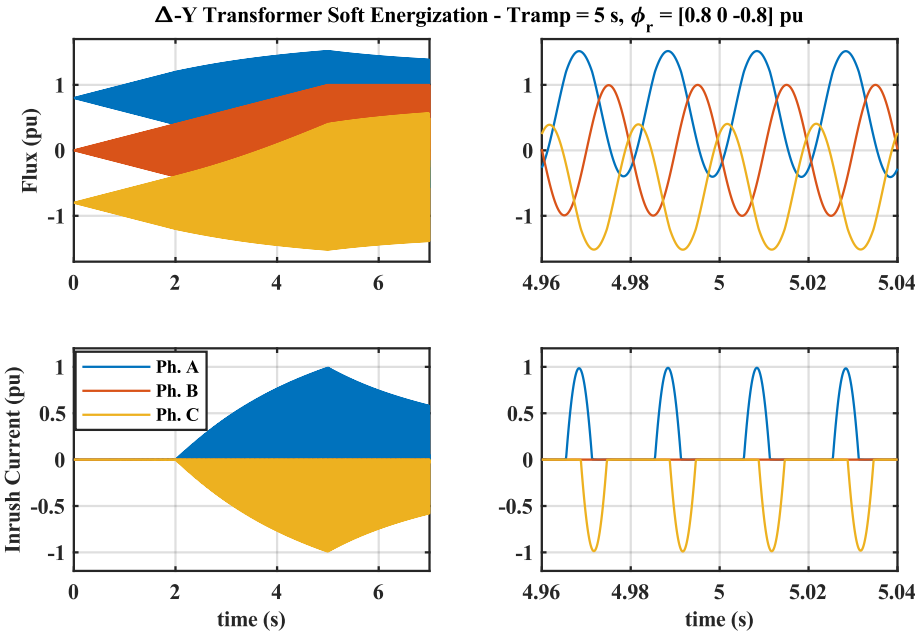

Figure 3.21: Soft energization for $\Delta - Y_g$ transformer with $\phi_r = [0.8, 0, -0.8]$ pu in MATLAB/Simulink.

Finally, another example of extending the results to three-phase transformers is presented for a $\Delta - Y_g$ transformer also with $\phi_r = [0.8, 0, -0.8]$ pu and $T_{ramp} = 5\ s$. Theoretically, it is expected for phase A to exhibit similar behavior to the that in Figure 3.20 (yellow curve), and for phase C to exhibit the same behavior with opposite signs as it has the opposite residual flux amplitude since the phase angle impact is effectively neutralized at $T_{ramp} = 5\ s$. Phase B of the transformer is expected to have near-zero inrush current as it does not go into saturation since $|\phi_{sat} - \phi_r| > 1$. The theoretical estimates are validated in the simulation results presented in Figure 3.21.

3.5. Theoretical Models: Advantages and Limitations

The derived theoretical models for constant-amplitude and ramping voltage sources can be used in time-domain simulations to illustrate the inrush amplitude, decay rate and the saturation behavior in correlation to relatable mathematical terms based on switched passive circuit components. The analysis and comparisons presented showcase the derived models effectiveness under a wide range of operating conditions. That said, the models approximate nature that is used to mimic a more complex behavior inevitably introduces some limitations that should be considered when the models are used:

- The constant-amplitude source model has higher accuracy when the transformer operates in the saturation region during the first few cycles. Flux deviations may start to appear when the transformer exits the saturation region and the flux decays back to $\pm$ 1 pu range. The derived model is observed to exhibit steady-state errors when run for long periods. A similar observation has been reported in [77].
- The soft energization model is also observed to produce more accurate results when $X \gg R$. If the resistive impedance is considerable, some per-unit deviation is observed during the ramp-up.
- Even in the special cases where the mentioned deviations exist, the model is still observed to produce relatable results that can be used to interpret transformer saturation trends.

In most cases, the derived models should be effective to produce estimates of inrush behavior through programming scripts. For three-phase transformers, the model can be used to simulate the worst-case phase or winding. For instance, the results in Figure 3.21 for phase A can be reproduced with high-level of accuracy using the derived theoretical single-phase model on per-unit basis. Mathematical extensions for simultaneous three-phase calculations using the derived models are, in principle, feasible and can use the models as the 'building blocks' for such extensions. Finally, the simulation step-size should be selected to a reasonably low value to minimize calculation errors.

3.6. Summary

Utilizing GFCs to energize AC networks can result in inrush currents exceeding the converter rating. Understanding the behavior and driving factors of transformers during the energization process has thus been determined to be an important factor to identify suitable inrush current suppression methods, with the aim of preventing possible damage to the energizing converter or network assets. This chapter has thus presented a comprehensive overview of key transformer energization techniques, based on derived models that are suitable for energization from a constant-amplitude source, a ramping source, or a combination of both. The derived models consider single-phase transformers and are then extended into three-phase applications due to the core similarities between both topological families. Constant-amplitude source energization model has been used for hard energization, PIR and classical controlled switching. Soft energization has been considered separately through a new model to accommodate the ramping time variable in the circuit differential equations. The impact of energization instant α is shown to be neutralized after the first few cycles, and ϕ_r is shown to be a key influencing parameter in soft energization. From the presented analysis, the following observations are deduced:

- Unless high impedance exists between the voltage source and the transformer, hard (uncontrolled) energization is not recommended due to the high dependency of the core flux and inrush current magnitudes on the energization angle (α).

- PIR largely limits the flux and inrush current amplitudes during saturation. Higher resistance values lead to lower inrush amplitude. This is also accompanied by higher losses. Dedicated breakers are also required, which adds to system cost and footprint.
- Classical controlled switching effectively eliminates inrush current and prevents core saturation. However, the technique is also prone to errors that are proportional to ϕ_r measurement accuracy, and the circuit breakers closing delays. This method also requires PoW relays and single-pole breakers for effective implementation.
- Soft energization requires the availability of a flexible voltage source capable of ramping up the terminal voltage at a user-defined duration. The power converters used for storage and renewables integration are, in principle, capable of achieving this task, thus making them compatible with applying this technique.

Considering the abovementioned points, two main aspects are identified for further investigation in the next chapter. These are:

- Given the lack of large-scale availability of single-pole circuit breakers in distribution networks, with larger presence of three-pole breakers [78], an investigation is deemed required to study the application extension of controlled switching to three-pole circuit breakers in the context of GFC-based energization.
- Identifying suitable procedure for setting up the soft energization voltage ramp-up rate in larger networks that require energizing multiple transformers from a centralized grid forming converter, under different operating conditions.

Chapter 4 Transformer Energization Techniques for GFCs Dominated Grids

Three key transformer energization techniques were presented and evaluated in the previous chapter, with detailed analysis covering modeling and simulation aspects to identify their advantages and limitations within the context of limiting the inrush current that could damage the energizing GFC. As highlighted in the chapter summary, the availability of single-pole circuit breakers is limited in many distribution networks. Single-pole breakers allow for controlling the closing instant of individual phases to meet PoW switching closing requirements. In contrast, this chapter investigates controlled switching from three-pole circuit breakers, being the more dominant breakers type in many distribution networks. Theoretical analysis is first presented to assess the technique merits and limitations, and to identify conditions where it could lead to acceptable transformer inrush current mitigation. Then, the question of soft energization ramp-rate definition is addressed through introducing a new framework for T_{ramp} estimation. Both controlled switching and soft energization are benchmarked through a comprehensive case study to energize a network consisting of multiple transformers from a GFC under different energization techniques combinations and assumptions.

4.1. Three-pole Breakers Controlled Switching

Many circuit breakers in distribution networks follow the three-pole circuit breaker configuration. In this case, all phases are controlled by the same signal and close simultaneously. Obviously, this leads to limited controlled switching applicability since less degrees of freedom are available to achieve optimal closing instants across all transformer phases. Controlled switching from three-pole breakers is a rarely analyzed technique in the literature and has been covered in a limited number of previous works. For instance, the authors of [79] presented analysis of this method for three-phase transformers and showed diminished inrush currents in all phases under different residual flux combinations in each phase. However, near-demagnetized core states are not considered, and the generalized impact of varying the transformer core characteristics has

not been investigated. On the other hand, the authors of [60] presented limited analysis on the technique application and highlighted that it is more suitable for residual flux combinations of the form $[-r, r, 0]$ with high r values. That is, when two phases have opposite residual flux, and the third phase has zero residual flux. On the other hand, the authors of [80] proposed a simultaneous-closing strategy that infers residual flux impact from the previous transformer disconnection time instant and showcase the technique performance based on this approximation in reducing the peak inrush to 2.5 pu for transformers in low voltage networks. Practical results were also presented in [81] based on a flux error function, with limited focus on ϕ_r variability.

Since an increasing proportion of generation assets is integrated in distribution networks and can participate in black-start, industrial efforts are aiming to develop and test solutions that integrate controlled switching to classical breakers that lack the required controllability. This can be done by using dedicated point-on-wave (PoW) relays to control the three-pole circuit breaker closing at instants that could generate simultaneous minimum inrush across all phases. An industrial example is presented in Distributed ReStart UK project where the use of a three-pole PoW relay is planned for a large transformer energization in a black-start scenario [65]. As a result, detailed analysis is presented in this chapter to shed light on this technique and its feasible application spectrum.

4.1.1. Theoretical Flux Error Impact

When the three transformer phases are energized simultaneously from controlled three-pole circuit breaker, the common PoW energization time should coincide with low prospective flux to residual flux error instants to achieve good results. In Chapter 3, controlled switching was presented with the assumption that the flux error is around zero, which is rarely the case for all phases in three-pole breakers closing. Instead, equation (4.1) defines this error ε_ϕ with respect to residual ϕ_r and prospective ϕ_{prosp} fluxes as follows.

$$\varepsilon_\phi = \phi_r - \phi_{prosp} \tag{4.1}$$

The highlighted 'good results' terminology here is relative and difficult to generalize. This is because different transformer cores have different characteristics such as saturation curve knee-point and air-core inductance in their saturation region. This variability is influenced, for instance, by the core material [82-84]. That is to say, the same error in (4.1) at the energization instant can result into two different per unit inrush current magnitudes for two different transformers. Mathematically, the flux error can be translated to obtain an analogous expression to the optimal switching angle equation (3.17) in Chapter 3, by equating the dc terms in (3.13) to ε_ϕ instead of zero and solving for α, obtaining the following expression.

$$\alpha_{cs(err)} = \sin^{-1}\left(\phi_{r(pu)} - \varepsilon_\phi\right) + \beta = \sin^{-1}\left(\phi_{prosp(pu)}\right) + \beta \tag{4.2}$$

The two forms of equation (4.2) demonstrate that the optimal closing instant deviation is proportional to the flux error, or the prospective flux at the closing point. This mathematical correlation is useful for testing the impact of choosing a closing instant with a particular flux error on the peak flux and inrush current. That is, controlled switching with zero error maintains the flux between -1 and 1 pu. The introduction of this error causes a peak flux that exceeds $|1|$ pu, which can lead to saturation and high inrush current. To quantify this behavior, equation (3.13) is re-written, substituting the terms $\phi_r - \phi_{pk} \sin(\alpha - \beta)$ with ε_ϕ as the flux error, and solving it at $t = t_{pk}$ to neutralize the sinusoid term, while also dividing both sides by ϕ_{pk} to obtain a pu expression.

$$\phi_{pu}(t_{pk}) \approx \phi_{pk(pu)} + \varepsilon_{\phi(pu)} \approx 1 + \left|\varepsilon_{\phi(pu)}\right| \tag{4.3}$$

This equation is simplified since it does not take the exponential decay after t_{sat0} into consideration (the period between entering saturation region and reaching peak flux). This simplification results into higher peak flux estimate, generating the worst-case scenario peak irrespective of the X/R ratio and impedance. That is, equation (4.3) can be used to predict the worst-case peak for $\phi_{pu}(t)$ at any switching flux error for single or three phase transformers. Two arbitrary examples are illustrated using the transformer model from Table 3.1 with $\phi_r = 0.6$ pu. The closing error for this transformer model should be less than $\varepsilon_{\phi(pu)} = 0.2$ pu to avoid the possibility of going into saturation (since

$\phi_{sat} = 1.2$ pu), and less than 0.52 pu to avoid the inrush current exceeding 1 pu (given that $i_m = 1$ pu @ $\phi(t) = 1.52$ pu). Practically, a 0.52 pu flux error will lead to less current than 1 pu due to the mentioned high circuit damping within the saturation region. Neglecting this damping in the derived equation adds a safety margin that prevents the current from exceeding the rating. The two cases $\varepsilon_{\phi(pu)} = 0.2$ pu and 0.52 pu are demonstrated in Figure 4.1 for a single-phase transformer using the derived constant-amplitude transformer model in Chapter 3, combined with equation (4.2) for $\alpha_{cs(err)}$ calculation. The expected behavior in equation (4.3) is validated, where the peak flux when $\varepsilon_{\phi(pu)} = 0.2$ pu is indeed 1.2. The damping effect does not appear here since $X_{nom} \gg R_1$ in the linear region. When $\varepsilon_{\phi(pu)} = 0.52$ pu, the peak flux falls short of 1.52 pu as expected due to the faster damping beyond $\phi = 1.2$ pu, leading to inrush current amplitude around 0.8 pu instead of 1 pu.

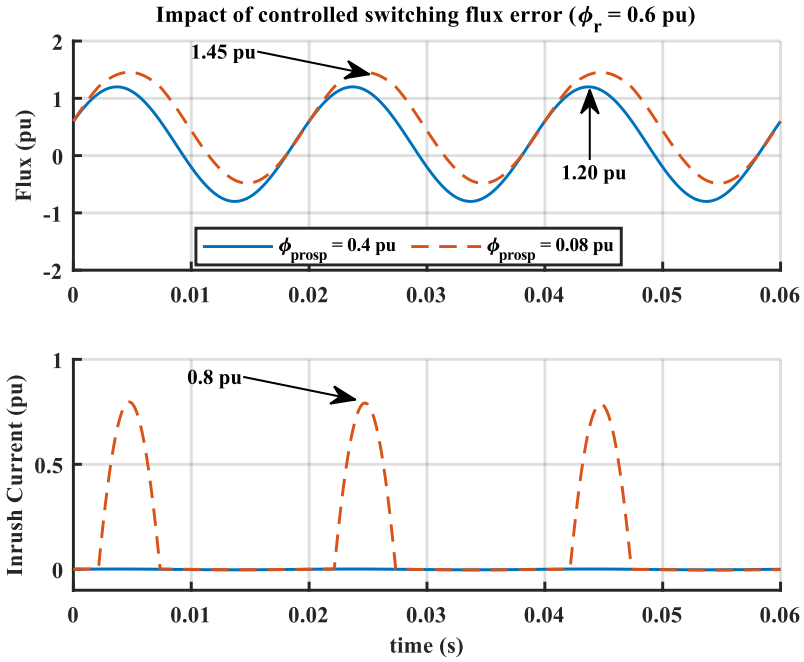

Figure 4.1: Impact of controlled switching error on: (a) flux peak, (b) resulting inrush current amplitude.

4.1.2. Extension to Three-Pole Breakers Transformer Energization

Going back to three-phase transformers, then the best breaker closing point should aim to minimize the error across all phases simultaneously. The requirement to select α_{CB} is

mathematically formulated in (4.4) to estimate the optimal CB closing instant (α_{CB} is defined with respect to phase A voltage waveform). An additional constraint can be considered to limit the application to instances where the maximum flux error is ceilinged to avoid excessive inrush. For a transformer with similar per unit parameters to those used for Figure 4.1 results, ε_{ceil} may be considered around 0.52 pu. However, the ceiling in equation (4.4) is left as a variable to reflect the highlighted variation in transformer core materials through properties such as losses, saturation flux, and air-core inductance.

$$\alpha_{CB} \approx \alpha\big(\min\big(|\varepsilon_{\phi a}| + |\varepsilon_{\phi b}| + |\varepsilon_{\phi c}|\big)\big) : \max(\varepsilon_{\phi} < \varepsilon_{ceil}) \tag{4.4}$$

If the CB is closed at α_{CB} when $\max(\varepsilon_{\phi} \geq \varepsilon_{ceil})$, then the inrush current can be of high magnitude that risks damaging the equipment. Having an optimal switching angle is not guaranteed and depends highly on the available residual flux combination in the different transformer phases. This is demonstrated through the following examples.

The first case is illustrated in Figure 4.2(a), where the residual flux combination $[0.8, 0, -0.8]$ pu is found to have a common minimum error point around $\alpha_{CB} = 210°$, with a maximum pu flux error in phase A and C that is equal to 0.065 pu, such that the flux remains below ϕ_{sat} from (4.3). That is, closing the three-pole breaker at this instant should generate negligible magnetizing current across all phases.

In contrast, a different residual flux combination (e.g., zeros in all phases - demagnetized core) does not have a similar global minimum error points when applying (4.4), and the minimum error value in this case is much higher since a single angle where the three phases have near zero values of ε_{ϕ} is missing as illustrated in Figure 4.2(b). The flux error behavior is oscillatory here in a similar fashion across all phases since the error is essentially equal to $\phi_{prosp(pu)}$. This means that no matter what angle is selected to energize the transformer under this combination, the pu inrush current is likely to be very significant in at least one phase. For instance, if the breaker is closed at 90°, then the flux error in phase A is zero, but is equal to ±0.866 pu in phases B and C. Substituting in equation (4.3) shows that deep saturation in these two phases is expected in this case.

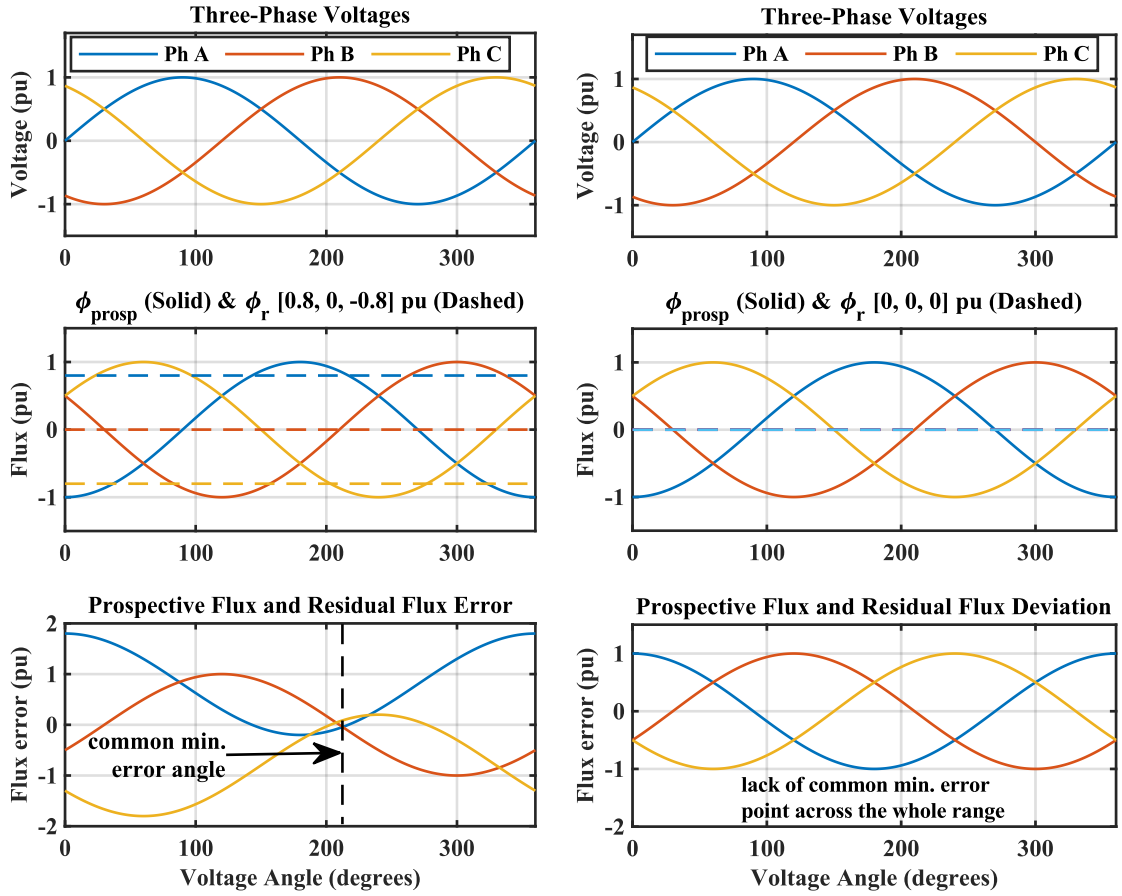

Figure 4.2: Three-pole closing flux errors comparison between (a): $\phi_r = [0.8, 0, -0.8]$ pu, b) $\phi_r = [0, 0, 0]$.

Simulations are performed to confirm these theoretical predictions using the standard MATLAB/Simulink transformer model with default core-saturation characteristics (see Table 3.1) from an ideal voltage source. The results of worst-case inrush current scenarios for $0 < \alpha_{CB} < 360°$ are presented in Figure 4.3 for both the residual flux combinations, where each dot represents a separate simulation. As expected, the first residual flux sequence $[0.8, 0, -0.8]$ pu results into a near-elimination of magnetizing inrush current around $\alpha_{CB} = 210°$. Whereas the second residual flux sequence $[0, 0, 0]$ pu results into a pattern of inrush currents that has a global minimum of 1.63 pu, signifying a violation of the transformer rating throughout the complete 360° range. The same test was performed on three-core and single core transformers in wye and delta configurations with similar results. This consistency is expected since all phases are energized simultaneously.

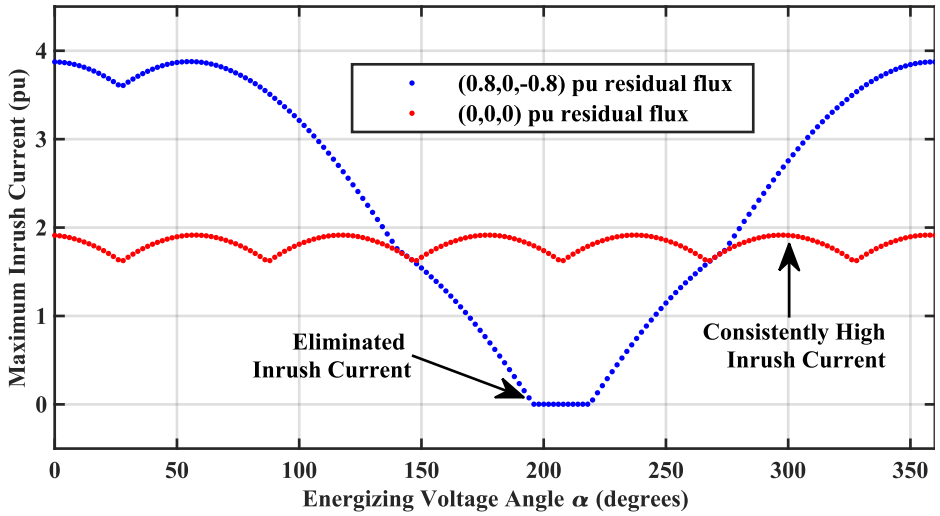

Figure 4.3: Three-pole closing peak inrush current at different voltage angles. Each dot on the graph is a distinct power simulation.

The demonstration presented here serves to illustrate that while three-pole controlled switching technique can be quite effective in many cases when access to independent phase CBs is not available, it can still lead to significant inrush currents under other residual flux combinations for the whole PoW angles range. This can cause more significant issues when combined with the inherent power converters limited overcurrent capabilities.

4.1.3. Generalization of Three-Pole CBs Controlled Switching

The presented examples only show two possible residual flux combinations. However, many other combinations can exist in power transformers. This subsection sheds light on these combinations and the maximum flux error that may result from applying three-pole controlled switching to transformers with arbitrary ϕ_r. Statistical analysis is thus carried out, covering a residual flux range for each phase between -0.8 and 0.8 pu. This range is selected considering the estimates reported in [85] that cites field measurements for various transformers with the residual flux ranging typically from 0.2 pu to 0.7 pu, and up to 0.85 pu in limited cases.

The selected step size for the statistical analysis is 0.02 pu. This translates into a total of $3^{81} = 534{,}441$ simulations to cover all the different possible ϕ_r combinations with high

resolution. The aggregated results for this unrestricted-flux scenario are presented in Figure 4.4(a), where x-axis shows absolute maximum residual flux across all phases. Negative ϕ_r values are mirrored into the positive side since they exhibit a similar behavior.

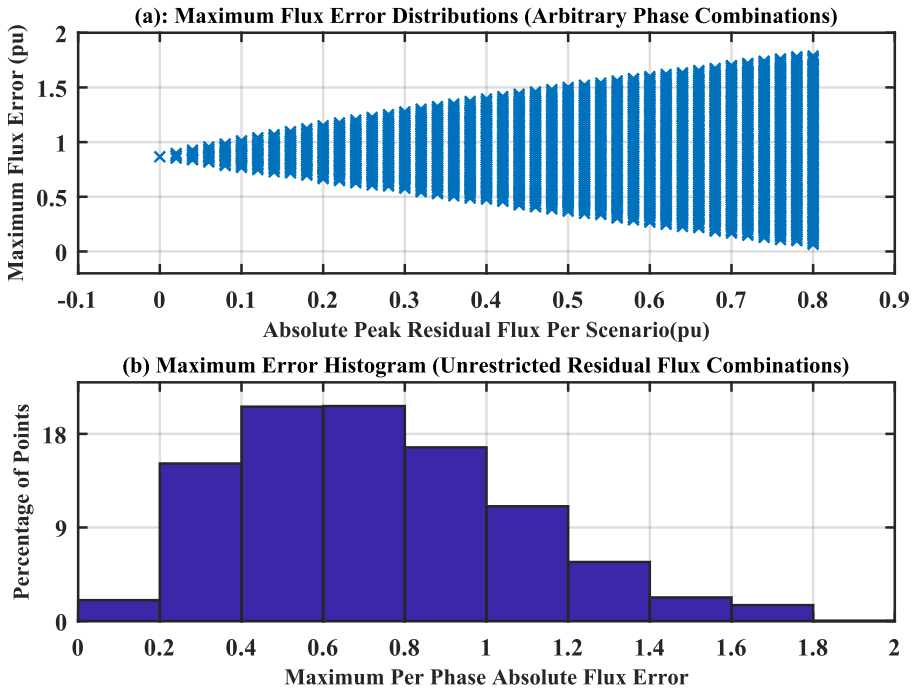

Figure 4.4: Peak flux error estimation for different ϕ_r combinations (unrestricted by topology): (a) peak flux error, (b) histogram of flux error distribution.

Some patterns can be deduced from Figure 4.4. For instance, having a phase with high residual flux increases the probability of getting a lower common flux error point. On the other hand, the demagnetized transformer case appears as the left-most point with a peak phase error equal to 0.866 pu as presented before. A histogram is used to statistically demonstrate the error distribution in Figure 4.4(b). The histogram illustrates that 18% of the covered scenarios have an absolute peak flux error across all phases of 0.4 pu or less, and that 60% of cases have an absolute peak error that is greater than 0.6 pu, which would lead to inrush current near or exceeding 1 pu if considering the transformer simulated earlier in Figure 4.3 with three-pole CB switching. That said, the covered residual flux combinations are not all equally likely in practice. Most combinations in Figure 4.4 require very extreme cases and imbalances preceding the transformer disconnection to be feasible

in practical transformers, such as cases where the residual flux in all phases does not add to zero (a special case that is compatible with some $Y - Y$ transformer topologies). Given that such transformers are not widely used in distribution networks and that extreme ϕ_r are less likely to be encountered in practice, it is reasonable to analyze three-pole CBs closing, with a limited number of residual flux combinations to mimic more realistic operating conditions. Namely, it is typical that when a Δ winding or a single-core configurations are used for the ϕ_r combination to add up to zero.

$$\phi_{ra} + \phi_{rb} + \phi_{rc} = 0 \tag{4.5}$$

The number of cases that satisfy this criteria is 3,013 (0.57%), clearly justifying dedicating a separate analysis to cover this subset. In this case, the absolute maximum flux error pattern is observed to peak at the demagnetized case, with a decreasing trend as the maximum residual flux increases. This is illustrated in Figure 4.5.

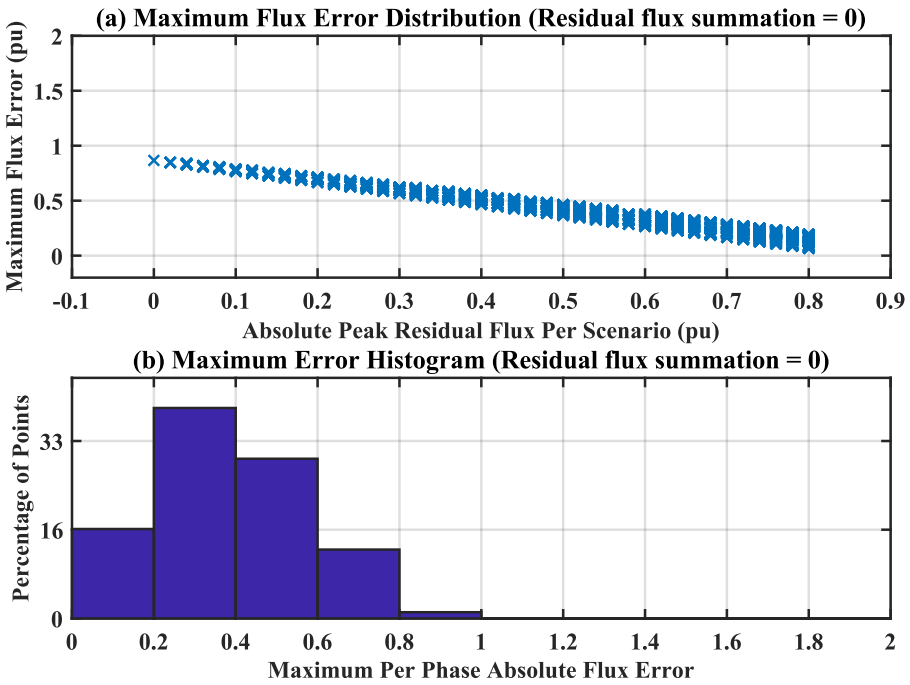

Figure 4.5: Peak flux error estimation for different ϕ_r combinations (restricted to $\sum \phi_r = 0$): (a) peak flux error, (b) histogram of flux error distribution.

Looking at the statistical histogram for this case, the number of cases with peak flux error below 0.4 pu increases to around 56%, clearly showing a higher success probability of

applying this technique to transformers where the residual flux summation follows the pattern in (4.5). A peak of 0.4 pu error translates into a worst-case peak flux at the corresponding phase, equal to 1.4 pu, which for many transformer designs falls into saturation region, but may produce current that is less than 1 pu (depending on the air-core inductance and damping losses).

Finally, another common pattern for residual flux in three-phase transformers is for a positive value to appear on one phase core, the opposite of this value to appear on another phase, and a zero residual flux to form on the last phase, following the $[-r, r, 0]$ pattern as reported in [60]. This ϕ_r combination is a subset that also satisfies equation (4.5). The number of investigated scenarios that achieve this pattern is only 81 out of the covered set. It is found that the results here form the lower envelope of the results presented earlier, as illustrated in Figure 4.6.

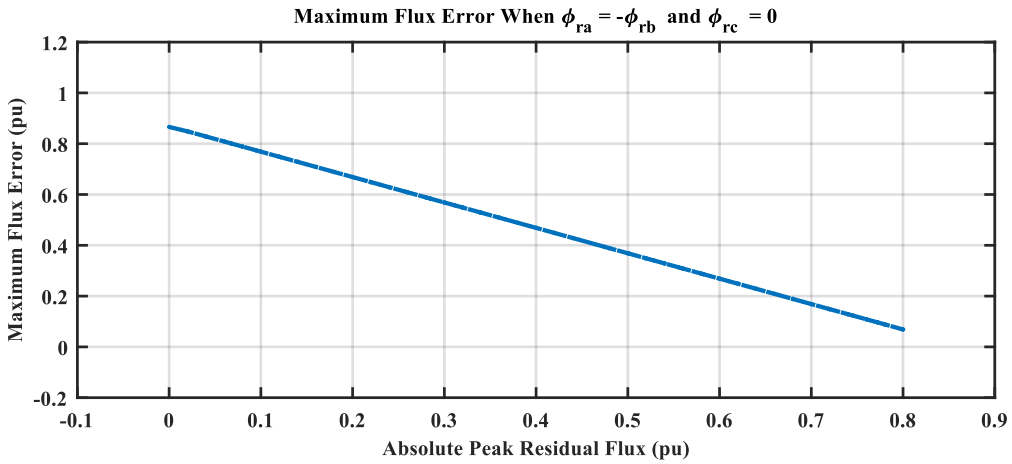

Figure 4.6: Peak flux error estimation for different ϕ_r combinations (restricted to [r,-r,0] combinations).

Transformers following this combinations with three-pole CB controlled switching are likely to avoid high inrush currents if ϕ_r is high. In fact, the first covered three-phase transformer scenario in this chapter with $\phi_r = [0.8, 0, -0.8]$ pu, produces the lowest possible inrush current from the 534,441 investigated combinations. Lower residual flux values following this pattern (down to $\phi_r = 0.35\ pu$) satisfy the requirement of having the peak resulting flux not exceeding 1.52 pu for the used transformer characteristics from Table 3.1. Although the results should not be generalized to all transformer core types, it

can be stated that transformers with similar saturation characteristics to the one studied, and a residual flux combination around this value (following the $[-r, r, 0]$ pattern) should not produce higher inrush currents than the transformer rating. In case the transformer has different saturation characteristics such as lower normalized ϕ_{sat} and air-core inductance, then it is advised to implement the analysis to the transformer using equation (4.4).

Overall, this section demonstrated the operating principle of three-pole controlled switching technique for transformer energization. It has been shown that this technique can be quite effective in inrush suppression under certain combinations of residual flux, while also acknowledging and identifying the regions where applying the technique is not advisable due to the lack of a global low flux error point across the full $360°$ range. Thus, theoretical evaluation using the presented equations is advised with knowledge of the field transformer residual flux and saturation characteristics before applying this technique, or the transformer disconnection time as proposed in [79].

4.2. New Soft Energization Ramp-Rate Estimation Framework

Soft transformer energization has been shown in Chapter 3 to be influenced by the ramp-rate selection. It has been demonstrated that shorter ramp durations lead to higher peak inrush current than higher ramp times. It has also been demonstrated that when energizing from a non-distorted voltage source, the peak flux and inrush current occur at $t = T_{ramp}$ followed by decay once the voltage settles at 1 pu. The inrush amplitude is also impacted by the studied network impedance between the source and the energized transformer. Taking these points into account, a new framework for estimating suitable ramp rates for various power networks is introduced in this thesis. The framework aims to answer the question of how fast a voltage ramp should be to limit the peak source current and power to the rated source values. Moreover, the framework aims to provide a flexible approach that can impact sizing the converter if it is yet to be installed mainly for the network energization purposes. The methodology is tailored and extended to grid-forming converter applications with larger networks consideration that may consist of a single or multiple transformers with various ratings.

4.2.1. Framework Data Requirements

The ramping time estimation approach presented here is iterative and model based in nature (i.e., it requires access to the energized transformer and parameters). Knowledge of the energizing network configuration and the energizing source control is recommended for improved estimation accuracy, such as the impedance between energizing source and transformer terminals (e.g., cables impedance), transformer saturation characteristics and residual flux, as well as the used source control. This is because the flux (being the voltage integral) is influenced by this control.

Such requirements, in principle, should not be a limiting factor in various networks since an emerging trend is for many distribution and transmission networks to have digital twins with estimates of the required parameters. That said, in cases where parameters are partially missing (e.g., residual flux readings), then worst-case assumptions can be used (i.e., to the higher $\phi_{r(pu)}$ end). The framework can be used with various power network simulation tools with automation such as MATLAB/Simulink or PSCAD/EMTDC in combination with Python. The idea is to iteratively run the simulation while varying T_{ramp} until stopping criteria is achieved.

The new framework flowchart is presented in Figure 4.7, and is configured to accommodate networks with q transformers, where q is an arbitrary number. To implement the proposed methodology, the network model is first initialized, with all the circuit breakers in the routes to be energized in their on-state. The worst-case assumptions for missing parameters, if any, are also made at this stage. The soft energization T_{ramp} is set to a minimal value close to zero (e.g., $0.2\ s$) to initialize the simulations. The peak MVA and source currents (in the three-phases) are recorded and compared to the defined stopping criteria. If this condition is not satisfied, then T_{ramp} is increased and the process is repeated. Typically, the next simulation should produce lower peak current and converter MVA due to the increased ramp-time. The iterations are repeated until the stopping criteria is met, and T_{ramp} is set to the value meeting the constraints defined within the framework.

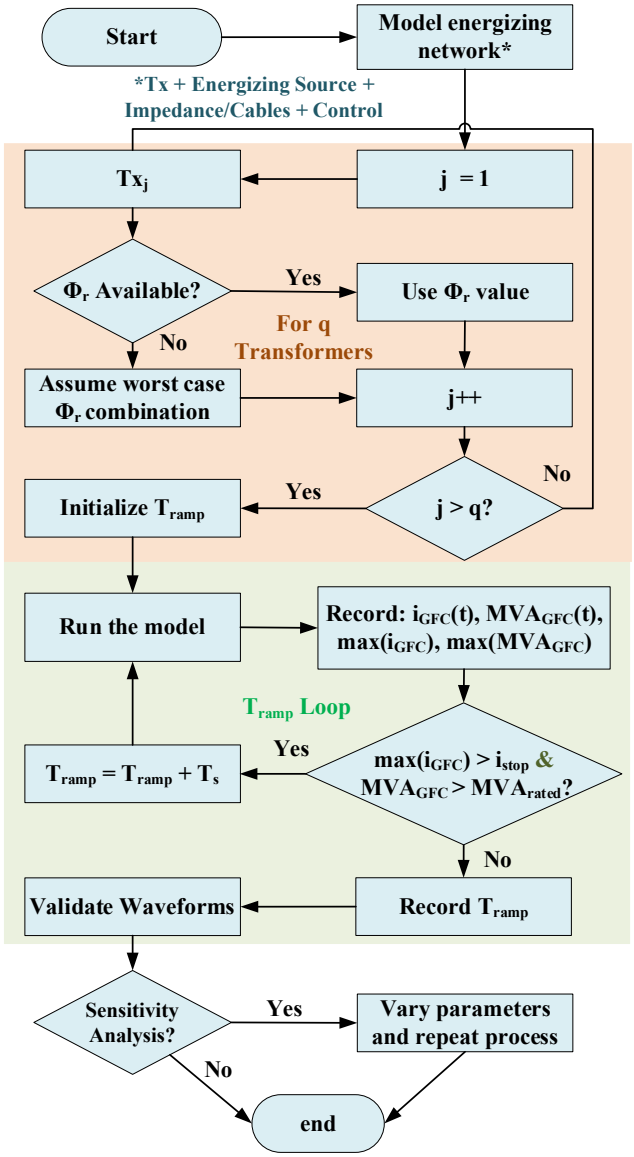

Figure 4.7: Flowchart of the proposed soft energization ramp time estimation framework.

4.2.2. Stopping Criteria Definition

The stopping criteria can be with respect to flux or transformer magnetizing current if only a single transformer is energized. To maintain generality, the stopping criteria are defined with respect to the grid-forming converter current and rated power due to:

- Limited power converters overcurrent capability.
- Accommodating the existence of multiple transformers in the energized network.

The peak stopping current i_{stop} is defined to balance between the source converter and the energized transformers requirements. Equation (4.6) mathematically defines i_{stop} based on both equipment limits: a) when the converter rating is the energizing network bottleneck (with smaller MVA than the smallest transformer), and b) when smaller MVA transformers than the converter rating exist in the network.

For instance, if a 10 MVA converter energizes a network of transformers including a 7.5 MVA unit, then a preferable current stopping criterion should consider the transformer rating as well as the converter to protect all the equipment since the small transformer is the energization bottleneck. This way, i_{stop} ensures that both the converter and transformer limits are respected. Figure 4.8 illustrates an example to further clarify this point, with the energization bottleneck highlighted in red for each case.

$$i_{stop} = \begin{cases} F_s i_{GFCmax} : MVA_{GFC} \leq \min(MVA_{Tx})_{j_j} \\ F_s i_{Tx_i} : MVA_{GFC} > \min(MVA_{T_x}) \end{cases} \quad (4.6)$$

where, MVA_{GFC} refers to the source converter rating, $\min(MVA_{Tx})$ refers to the lowest transformer MVA in the network, i_{GFCmax} is the maximum GFC rated current (peak value), i_{Tx_i} is the rated current of the smallest transformer and F_s is a user-defined factor between 0 and 1 that sets the desired current stopping criterion safety margin below the equipment rating.

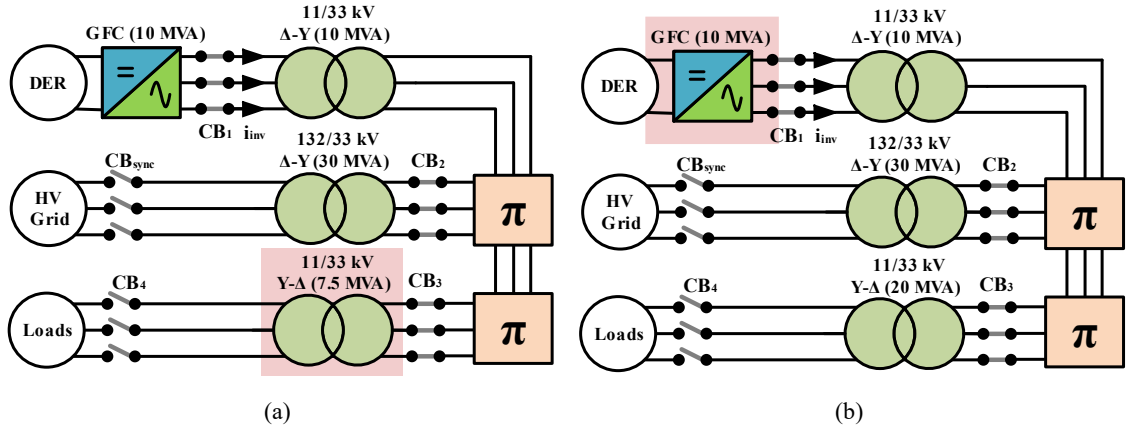

Figure 4.8: Impact of converter and transformer size on the framework stopping criteria defintion, with: (a) a transformer as the energizing bottleneck, (b) the GFC rating as the energization bottleneck.

On the other hand, it may be the case that one or some of the energized transformers are much smaller than the source converter rating (e.g., 10 MVA to 500 kW). Defining the stopping limit with respect to very small transformers is impractical and likely to result in excessively long ramp-times, which is not advisable to mitigate the possibility of undetected faults for long durations in the energized network. In this case, the small units may either be energized separately, or using a ramp-rate that ignores their rating since their normalized inrush current with respect to the converter rating is unlikely to cause a measurable impact (this option is feasible if the small transformers protection is deemed able withstand short-term inrush).

Another criterion is related to the converter MVA power rating that should also be satisfied. This is because in some cases, the current has been observed to be below its stopping threshold while the peak MVA is slightly higher than the rating due to the non-symmetrical nature of inrush current and voltage conditions. It is also recommended that the time-domain waveforms for key parameters are also inspected at the selected T_{ramp} to validate the compatibility of used equipment in withstanding any resulting imbalances during the energization process.

Sensitivity analysis is also incorporated into the framework and can be optionally coded to run automated testing for different combinations of uncertain parameters, such as different network impedances. This helps establishing ranges that can be correlated with field results. i_{stop} can also be varied to account for different converter ratings, considering the tradeoff of using small converters to energize large transformers, which may lead to higher T_{ramp} when compared to larger (but more costly) converters.

Finally, the chosen simulation time-step for the application can impact the results. Sufficiently low time-steps are advised within the order of magnitudes of microseconds to produce consistent results. To avoid excessively long algorithm execution times, some intermediate T_{ramp} values may be skipped. For instance, if $T_{ramp} = 1\ s$ does not meet the stopping criteria, and $T_{ramp} = 5\ s$ does not also meet it, then it is generally safe to assume that the target ramp-rate does not fall between these two values. Implementation can start with large intervals that are used to 'bracket' the target value, followed by finer adjustment

in T_{ramp}. This concept is not applied in the examples shown later in this chapter since it aims to showcase high-resolution trends of the framework implementation. Though, it is presented for the reader as an option to achieve faster calculations.

By following the proposed framework, adequate T_{ramp} definition can be achieved and tested under varying operating conditions to: a) provide a deeper technical understanding of the soft energization process, and b) provide a technical benchmark for the soft energization requirements in different transformer models under varying network conditions and c) avoid the practical need to apply arbitrary ramps that can still lead to damage or protection tripping if applied too fast.

4.3. Comprehensive Network Energization Case Study

The presented transformer energization techniques in this chapter, in addition to classical controlled switching, are benchmarked in a realistic case study in this section to identify their merits and practical limitations. The target network is inspired from a distributed network in Scotland, which is being investigated as part of the Distributed ReStart project. This project is a partnership between the UK National Grid, ScottishPower Energy Networks and TNEI, and it aims to assess the feasibility of black-start provision through DERs, including those connected through VSCs [65, 86]. In this case study, the network is composed of multiple transformers and cable sections that should be energized from a grid-forming converter. The methodology to test and benchmark the presented energization techniques is presented here. First, the network to be energized is illustrated in Figure 4.9. The network is composed of the energizing GFC, interfaced to a 50 MVA 11/33 kV transformer ($\Delta - Y_g$). Local loads on the GFC primary side are disconnected during the energization to minimize the converter loading. The 33 kV network is then divided into two parallel lines, the first extends for 30 km before the second MV/HV transformer from 33 kV to 132 kV is connected ($Y_g - \Delta$), with a 90 MVA rating. The second segment extends for 20 km to reach a distribution 11 kV grid through a step-down transformer ($\Delta - Y_g$). This combination of transformers is selected for the purpose showcasing the energization of multiple transformer topologies from Δ and Y windings. The lines are modeled as $\pi - \text{sections}$ with the default MATLAB/Simulink library

parameters. The base case network and transformers parameters are detailed in Table 4.1. The transformers saturation curve is unified in per-unit and is also based on the default MATLAB/Simulink per-unit parameters for consistency.

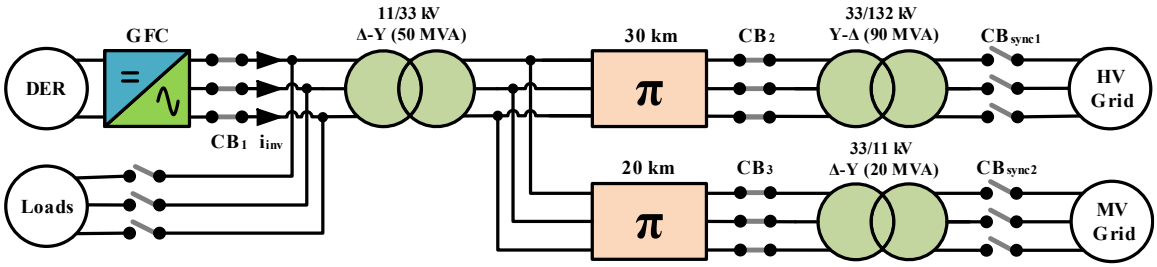

Figure 4.9: Block diagram of the network used for the energization case study.

The base converter rating is chosen to be 15 MVA (lower than transformer ratings) to investigate the energization techniques capability in inrush suppression. A successful inrush mitigation during the network energization implies that the resulting active and reactive power consumption is minimal, meaning that small power sources can achieve the task successfully. Given the rising penetration of DERs in power networks, assessing the feasibility of using small units in energizing large networks is particularly important for network operators looking for available units for black-start in contingencies cases.

Table 4.1: Case study test network parameters (for the base case).

GFC parameters			
Rating (MVA)	15	$f\ (Hz)$	50
$Z_{filter}\ (pu)$	0.075	$Z_{filter}\ X/R$ ratio	12.5
Transformer pu parameters			
$R_{p,s}\ (pu)$	0.002	$R_m\ (pu)$	500
$L_{p,s}\ (pu)$	0.08	$R_{CB}\ (pu)$	$1.46x10^{-5}$
$L_0\ (pu)$	0.5	$T_{x1}\ \phi_{r(a,b,c)}\ (pu)$	$0.8, 0, -0.8$
$T_{x2}\ \phi_{r(a,b,c)}\ (pu)$	$-0.4, 0.7, -0.3$	$T_{x3}\ \phi_{r(a,b,c)}\ (pu)$	$0, 0, 0$
Transformers saturation curve			
$i_m\ (pu)$		$[0, 0, 0.0024, 1]$	
$\phi\ (pu)$		$[0, 0.85, 1.2, 1.52]$	
Cable Parameters			
$R_{cable}\ (m\Omega/km)$		12.73	
$L_{cable}\ (\mathrm{mH}/km)$		0.9337	
$C_{cable}\ (\mathrm{nF}/km)$		12.74	

4.3.1. Controlled and Soft Energization: Grid Forming Control Benchmark

Since these two techniques are applied in this case study, a brief overview of their compatibility with grid-forming converter applications is first introduced. Controlled and soft energization vary significantly in their operation and requirements. Controlled switching (from both single-pole and three-pole circuit breakers) requires residual flux and prospective flux measurements for each energized transformer for reliable operation, as well as compatible controlling relays. Missing any of these inputs (or their indicators such as transformer disconnection/de-energization time) can jeopardize the technique applicability. From GFC perspective, the controlled switching techniques do not require modifications to the control, except that a 1 pu voltage should be applied at the energized breaker terminals by the converter control at the energization instant. If all required measurements are available with minimum or compensated delays, then the performance of single-pole CB controlled switching is globally superior to that of three-pole CB.

For soft energization, all breakers along the energization path are pre-closed to establish electrical connection, and then the voltage ramp is applied simultaneously to the energized assets. The voltage control loop of the GFC requires direct modification in this case to enable the ramping reference. Soft energization performance for appropriately timed ramps can result in a significant inrush current reduction. The availability of network measurements such as residual flux and network impedance are not pre-requisites in this case, although they help improving the technique effectiveness. Figure 4.10 summarizes the differences between the considered techniques in terms of breakers operation and GFC control. A simple GFC is used for illustration based on basic droop as in (4.7)-(4.9).

$$V_{GFC} = V \angle \delta_i \tag{4.7}$$

$$V = (V_{ref} - V_{meas})(K_p + \frac{K_i}{s}) \tag{4.8}$$

$$\delta_i = \frac{1}{s}\left(\omega_{ref} + m_p\left(P_{ref} - P_{meas}\right)\right) \tag{4.9}$$

where, V_{ref} is the main manipulated term between the different transformer energization techniques, K_p and K_i are the PI proportional and integral gains, $1/s$ is the integral, m_p is

the droop factor, ω_{ref} is the reference angular frequency of the grid-forming converter, and P is the converter power. During energization, P_{ref} can be set to low values since transformers and cables inrush power are mostly reactive. Inner voltage and current regulation loops can also be incorporated into the GFC but are not used in this chapter. This brief control requirements overview is later expanded into a detailed investigation in Chapter 5 to assess the feasibility of using different grid-forming control techniques for black-start, as well as the perceived impact of inner control loops incorporation.

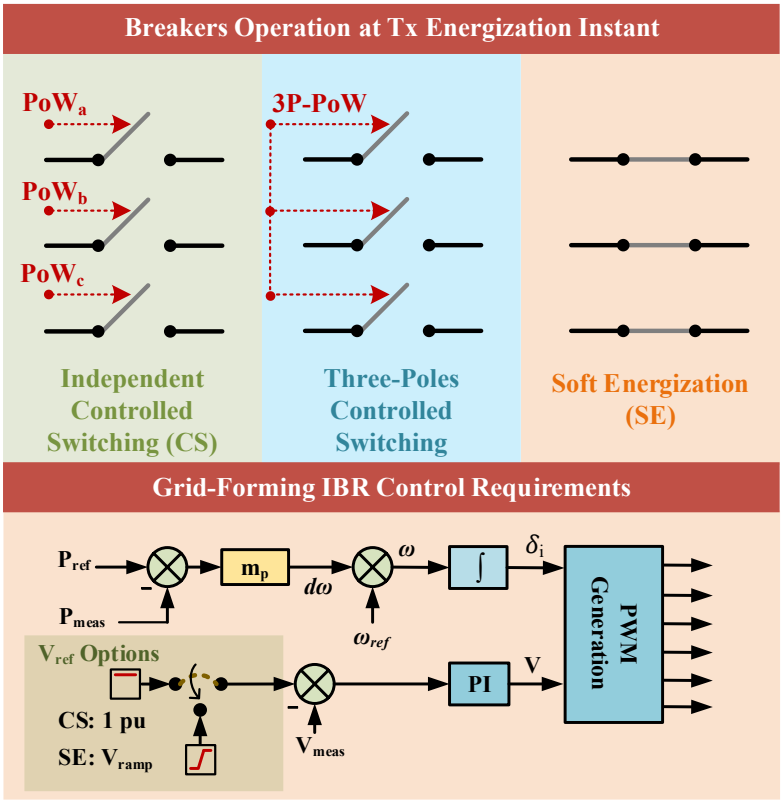

Figure 4.10: Breakers and GFC requirements for different transformer energization technique.

4.3.2. Case Study Testing Methodology

Controlled switching in its single and three-pole CB forms is tested with the assumption that residual flux and prospective flux measurements are available for all transformers. The delay effect between sending the CB closing command and the actual contact closing instant is ignored and assumed to be properly compensated by the algorithm, a

compensation technique example is presented in [87]. The case study assumes that CB_1 is three-pole breaker type, and that CB_2 & CB_3 are single-pole type breakers. This combination sheds light on practical cases when both circuit breaker types exist in the same network.

The selected three transformers also provide a topology combination that cover various types (i.e., energizing from Δ or Y side). The controlled switching sequence in this case study is such that the grid-forming converter control first provides 1 pu voltage at CB_1 input, then the breaker is closed at its combined least-error PoW point from equation (4.4). Following the first transformer energization, CB_2 & CB_3 are closed independently to draw least inrush current using separate single-pole closing algorithms that are adjusted to accommodate their individual configuration. The next black-start step is typically connecting load blocks and synchronizing to the HV and MV grids through CB_{sync1} and CB_{sync2}. This can be achieved separately depending on the energizing converter rating and load requirements. A detailed investigation and a proposal of compatible synchronization techniques is presented in Chapter 6.

Soft energization is tested under the new defined T_{ramp} framework. Residual flux measurements are also assumed to be accessible here to demonstrate their impact. CBs between the converter and the transformers are initially closed, followed by simulating the network at a minimum T_{ramp}. Based on the ramp-time estimation framework, the simulation is run with gradually increased T_{ramp}, and the process is repeated until satisfying the stopping criteria. The current threshold is based on the limit $F_s = 0.95$ from (4.6). This equates to $787\sqrt{2} \times 0.95 = 1.056$ kA for a 15 MVA @ 11 kV power converter. Since the converter is smaller than all energized transformers, the current stopping criterion is defined with respect to the converter rating.

4.3.3. Test Scenarios Definition

Base and sensitivity cases are defined through multiple scenarios covering controlled switching and soft energization. The scenarios (and their sensitivity variations) are summarized in Table 4.2. The controlled switching sensitivity case only considers varying

the residual flux of the first transformer ($T_{x\,1}$), since it is energized with a three-pole CB. Varying ϕ_r of the other transformers does not have a noticeable impact since their single-pole CBs are able to track and largely mitigate the inrush impact. Whereas two sensitivity cases are considered for soft energization: a) varying the core characteristics of all transformers, and b) demagnetizing all transformers by setting ϕ_r to zero across all phases. The considered transformers sensitivity saturation curve has a lower knee-point than the one used for the base case in Table 4.1 (1.1 pu vs. 1.2 pu). The sensitivity curve also has a steeper saturation characteristics through lower air-core inductance to emulate a case closer to worst-case scenario (3 pu inrush current at $\phi = 1.52\ pu$, compared to 1 pu inrush current against the same flux in the base case). Accordingly, the first sensitivity case aims to demonstrate the impact of multiple transformer core types with different saturation-curve knee-voltage and air-core inductance, whereas the second case is considered to demonstrate the paramount impact of residual flux on setting T_{ramp}.

Table 4.2: Network energization case study - scenarios definition

Technique	Case #	Parameters Variation from Base Case
Controlled Switching	Case 1	Base Case
	Case 2	$\phi_r(T_{x1}) = [0, 0, 0]$
Soft Energization	Case 1	Base Case
	Case 2	Saturation curve: $i_m = [0, 0, 0.0024, 3]$, $\phi = [0, 0.85, 1.1, 1.52]$
	Case 3	$\phi_r(T_{x1}, T_{x2}, T_{x3}) = [0, 0, 0]$ (Demagnetized cores)

4.3.4. Controlled Switching Results

The results for controlled switching are presented in this subsection starting with the base network case. T_{x1} is connected to a three-pole circuit breaker with $\phi_r = [0.8, 0, -0.8]$ pu, while T_{x2} and T_{x3} phases are energized independently. At $t = 0.2\ s$, T_{x1} energization is initiated, and the breaker is closed at $\theta_{CB} = 210°$ (voltage angle) as determined from equation (4.4). Given the ϕ_r combination, the inrush current is nearly zero and the energization occurs smoothly despite the simultaneous phases closing. The two cable segments (30 km and 20 km) are energized simultaneously with T_{x1}. A settling period of

10 cycles is introduced before energizing T_{x2} and T_{x3} to mitigate any transients' impact, which can be modified as needed. Then the two remaining transformers are energized. T_{x2} is switched from the Y side, and T_{x3} from the Δ side. The breakers are closed independently at instances when the error between residual and prospective flux is around zero, producing near-zero magnetizing currents. A 0.02 s delay is added between the single-pole breakers individual-phases activation for improved visualization. Transformers flux and magnetizing current results at the energization moments for all transformers are summarized in Figure 4.11, demonstrating negligible inrush current. The energizing GFC parameters are presented in Figure 4.12, showcasing its instantaneous output MVA and current throughout the energization process. The spikes at T_{x1} energization instant are due to the cables energization, since cables can develop their own transient inrush current [88]. The cables inrush is within the base converter rating (below 15 MVA) and peak per-phase current (1.11 kA). Longer cables are observed to generate higher inrush current. Without dedicated mitigation strategies (e.g., controlled switching through dedicated line/cable PoW breakers), the risk of having high inrush from long cables should be considered when using controlled switching under such configuration. If the resulting current exceeds converter rating, then soft energization with sufficient T_{ramp} can mitigate this issue.

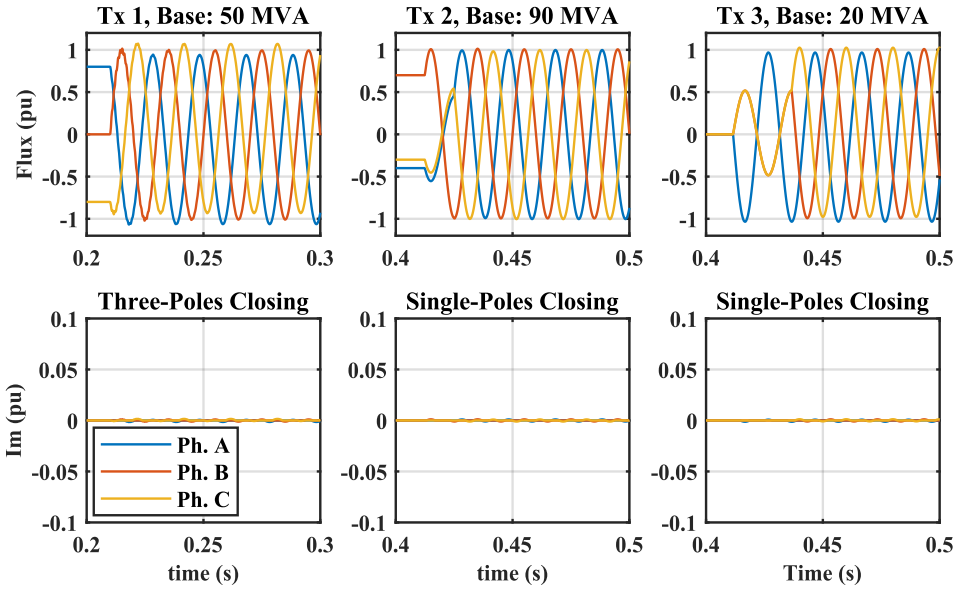

Figure 4.11: Controlled switching case 1 results - transformers flux & magnetizing currents at energization instants.

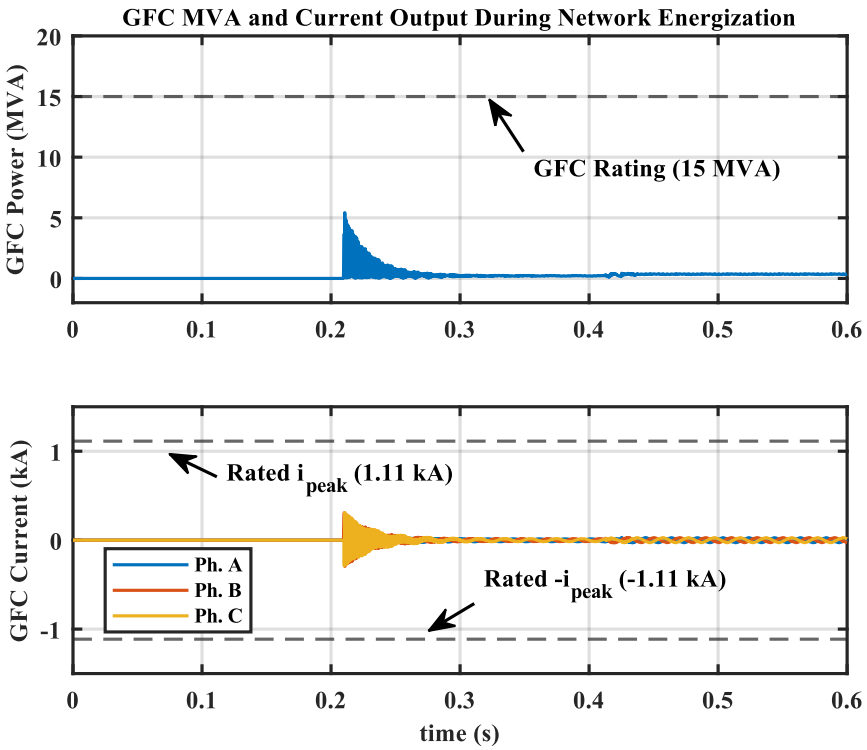

Figure 4.12: Controlled switching case 1 results - converter peak MVA and current outputs.

Controlled Switching case 2 tests the network energization performance under a different ϕ_r combination for T_{x1}. The chosen combination [0, 0, 0] generates high minimum common ε_ϕ across the full 360° as illustrated earlier in Figure 4.3. T_{x1} is observed to generate high inrush current (~ 1 pu) due to the simultaneous phases closing at a high error point for phase A and phase C, as summarized in Figure 4.13. The other two transformers exhibit similar behavior to that in Figure 4.11 from case 1. Overall, the required inrush current from the converter peaks at 56.8 MVA, severely exceeding the chosen base rating of 15 MVA. The converter MVA and current output for this scenario are illustrated in Figure 4.14. Between the two presented extremes in the base and sensitivity cases, three-pole breaker closing for T_{x1} at different ϕ_r combinations is shown to exhibit a behavior proportional to the minimum combined ε_ϕ point as in (4.4). This further validates the observation that using a three-pole breaker for energizing a network or part of a network (especially through a power converter) should be preceded by similar analysis to validate the ϕ_r combination suitability.

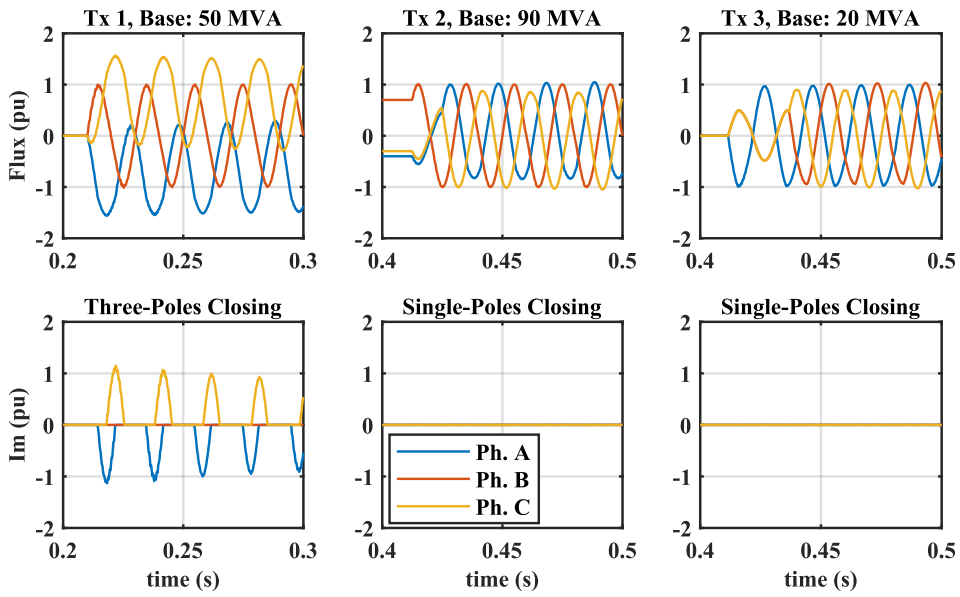

Figure 4.13: Controlled switching case 2 results - transformers flux & magnetizing currents at energization instants.

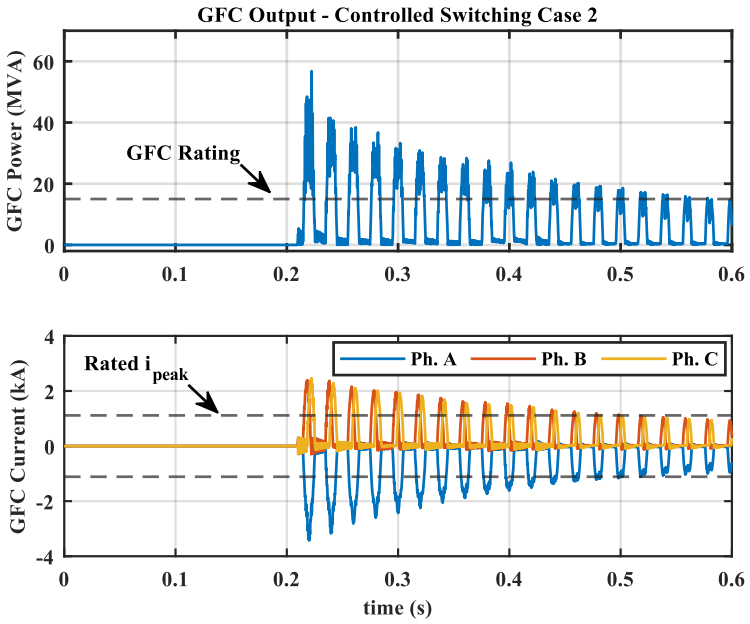

Figure 4.14: Controlled switching case 2 results - converter peak MVA and current outputs.

In this case, CB_1 was the network energization bottleneck. If this breaker was instead composed of three single-pole controlled units, then T_{x1} would have followed a similar behavior as the other two transformers with near-zero inrush current, independent of the

ϕ_r combination. It is also observed from Figure 4.13 that the peak inrush current in phase A and C is around 1.1 pu, as opposed to 1.67 in Figure 4.3, although the same residual flux combination (demagnetized core) is used in both tests. This is because in the generic test in Figure 4.3, the transformer was energized from an immediate voltage source that is connected directly to the transformer, whereas here, the transformer is connected behind an additional impedance that causes further damping to the flux peak, and consequently, inrush current.

4.3.5. Soft Energization Results

Soft energization has been shown to provide more flexibility in reducing the peak converter current demand during network energization by selecting an appropriate ramping time. The new T_{ramp} estimation methodology presented in Figure 4.7 is used in this subsection and applied to the test network. The initial T_{ramp} is set to 0.2 s and the network is energized, increasing T_{ramp} iteratively until satisfying the stopping criteria. The results are presented in Figure 4.15, where the total number of independent simulations carried in this experiment is 34, ranging from $T_{ramp} = 0.2 \text{ to } 30\ s$.

Initially, the converter output MVA and current are significantly high, as expected. The decreasing peaks trend is evident for consequent simulation points, and the current stopping criterion defined by $i_{stop} = 1.056\ kA$ from (4.6), combined with a peak converter MVA below the rated value is satisfied around $T_{ramp} = 8\ s$. Figure 4.15 also demonstrates the stopping T_{ramp} if 10 MVA or 20 MVA converters had been used instead of the adopted 15 MVA converter. Increasing the rating by 5 MVA can accelerate the ramp to 3 s without violating the converter rating, whereas decreasing the converter size to 10 MVA requires using a slower ramp of at least 15 s to avoid violating the unit rating. In these cases, the stopping criterion current is approached before the actual $T_{rampmin}$ highlighted in the results figure. This is because the measured MVA peak is still slightly above rating at these instants, due to the inrush current non-symmetry and the slight voltage distortions towards the end of the voltage ramp. This signifies the framework design preference of combining both current and power measurements within the stopping

criteria definition for improved reliability. Overall, the three presented GFC ratings illustrate soft energization flexibility in accommodating the limitations of existing equipment at different ratings, or to economically size new converters.

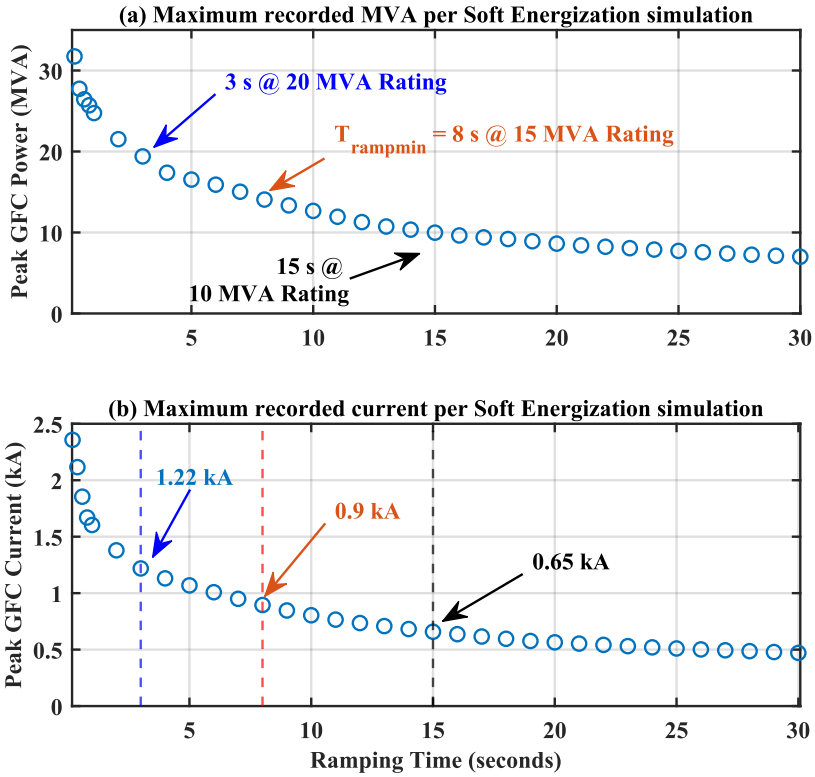

Figure 4.15: Soft energization base case: (a) peak inverter MVA; (b) peak inverter current. Different GFC sizes are also demonstrated for comparison.

Narrowing down to the considered 15 MVA converter rating, time-domain simulation results are presented with in-depth analysis for $T_{ramp} = 8\,s$. Around this time, the peak converter power is 14.5 MVA, just below the defined base converter rating. Simulation results for this scenario are first summarized in Figure 4.16, illustrating the ramping and decaying behavior for both apparent power and the GFC current. The figure also shows zoomed-in versions near $t = T_{ramp}$. Since multiple transformers with different ϕ_r are energized, their cores approach saturation region at different times per phase and per transformer. As expected, the measured GFC parameters reach their peak around T_{ramp}, and then continue decaying following the ramp since the flux transient from this point onwards is primarily influenced by the damping factor.

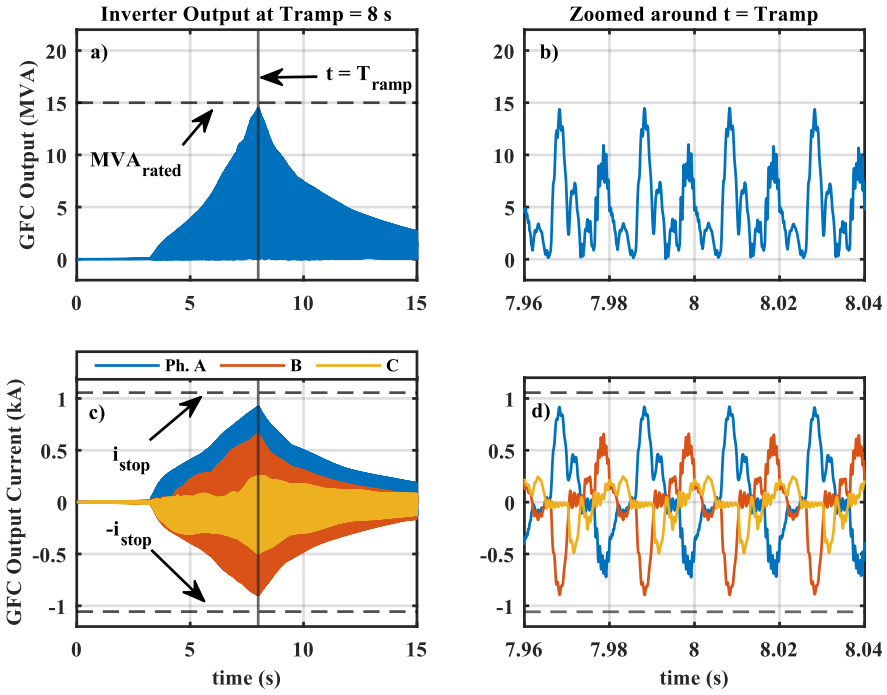

Figure 4.16: Soft energization base case with $T_{ramp} = 8$ s, showing instantaneous results for: converter power output: (a) full-range, (b) around T_{ramp}, and converter current: (c) full range, (d) around T_{ramp}.

Looking at the current around $t = 8\,s$ reveals opposing peaks for the different phases. This is due to energizing transformers with different configurations, including delta (Δ) windings. When delta windings are considered, then the core magnetizing current naturally differs from the source (line) current to create a complete current path. This is illustrated in Figure 4.17 for T_{x1} $(50\,MVA, \Delta - Y_g)$. Another observation is that the currents in Figure 4.16 are noisy. This is due to the energizing source large loading by the network during the process, as well as the cascaded transformers energization. The output voltage of the first transformer (which is already impacted and distorted by the inrush current) is the primary voltage of T_{x2} and T_{x3}, leading to higher voltage noise, which, when applied to transformer cores, lead to noisy flux and resulting inrush current signals. This behavior is observed to be temporary and fades out as the inrush current diminishes after the voltage ramp-up is concluded. Results are illustrated in Figure 4.18 at $t = 8\,s$ and $t = 14\,s$.

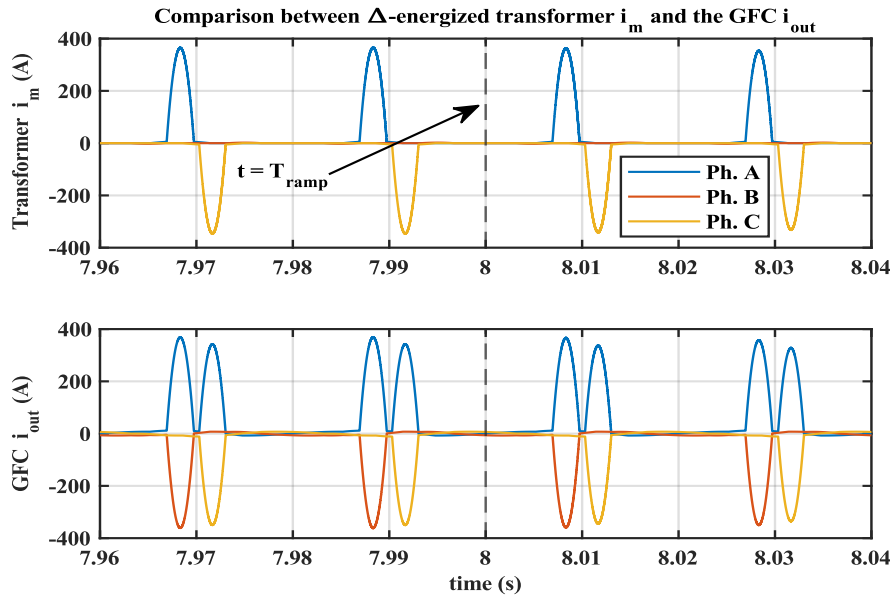

Figure 4.17: Demonstration of transformer and source currents when a $\Delta - Y_g$ transformer is energized.

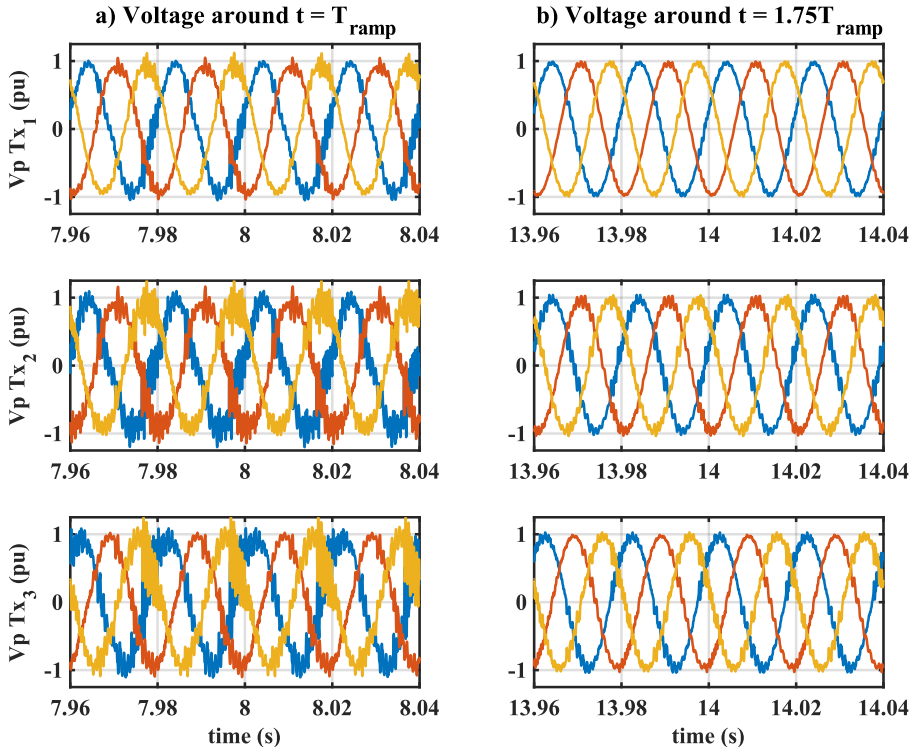

Figure 4.18: Voltage distortion during the test network soft energization: (a) at $t = 8$ s (highly distorted), (b) at $t = 14$ s (highly reduced distortions).

The first sensitity scenario for soft energization considers varying the core saturation curve of the network transformers as in Table 4.2. Reducing knee-voltage means that the

saturation region is reached faster, while decreasing the air-core inductance leads to higher inrush current per flux increment within the saturation region. The new voltage ramp-up time estimation algorithm is re-applied to the network model with the new transformers saturation curve, and the results are summarized in Figure 4.19. Longer ramps are required for 10, 15 and 20 MVA converters in the sensitivity case to avoid violating the GFC ratings. The minimum ramp-time for 20 MVA converter increased from 3 s in the base case to 8 s in this case, and from 8 s to 12 s for the 15 MVA converter. Lastly, the 10 MVA converter requires a 22 seconds ramp as opposed to the 15 seconds for the base case. This clearly illustrates that obtaining universally suitable ramp-rates may not be feasible due to the unique features for each network, transformers, converter control, residaul flux combinations … etc.

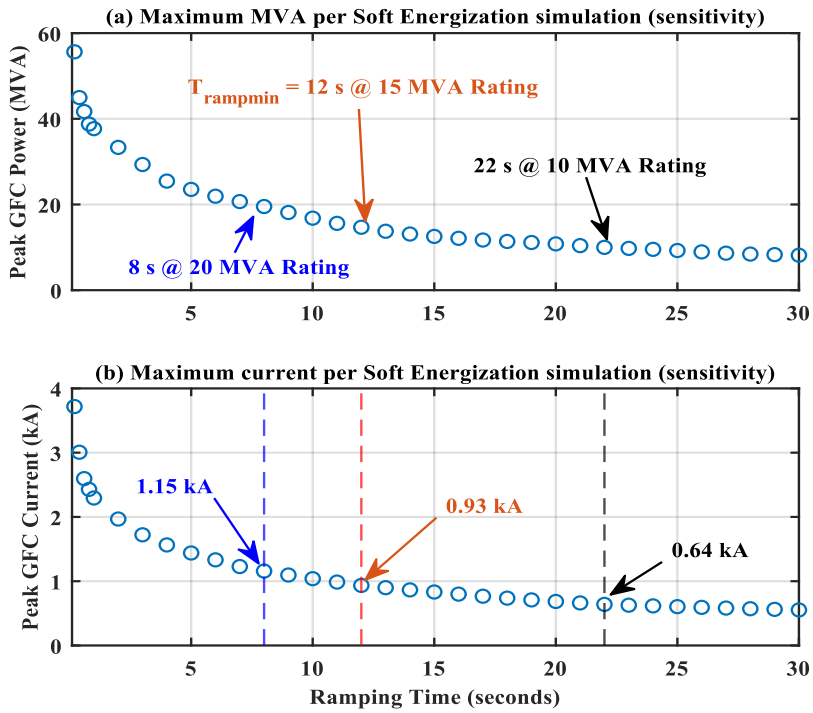

Figure 4.19: Soft energization sensitivity case results, showing peak inverter MVA and peak inverter current. Different GFC sizes are also demonstrated for comparison.

Another observation from varying the transformers core characteristics is that the steeper saturation curve impact is more evident at lower T_{ramp} values. Comparatively, the peak converter power at $T_{ramp} = 0.2\ s$ is 55.6 MVA compared to 31.7 MVA in the base case

(75% increment). At $T_{ramp} = 5\ s$, the peak power is 23.5 MVA compared to 16.5 in the base case (42% increment). At $T_{ramp} = 26\ s$, the difference in peak converter power diminishes to 18%, between 8.9 MVA for the sensitivity case, and 7.5 MVA for the base case. This is because increasing (T_{ramp}) eventually minimizes the imapct of going into the saturation region for both curves.

The final sensitivity case for soft transformer energization investigates the impact of energizing the studied network when all transformers are demagnetized (i.e., with zero residual flux). Figure 4.20 shows the result of this sensitivity scenario, showing successful energization of all transformers with $T_{ramp} = 0.2\ s$ only. This is because since transformer inrush current is a consequence of the flux reaching saturation region, having a demagnetized core means that the flux has to first ramp up from zero to the saturation curve knee-point before starting to cause a noticeable inrush current.

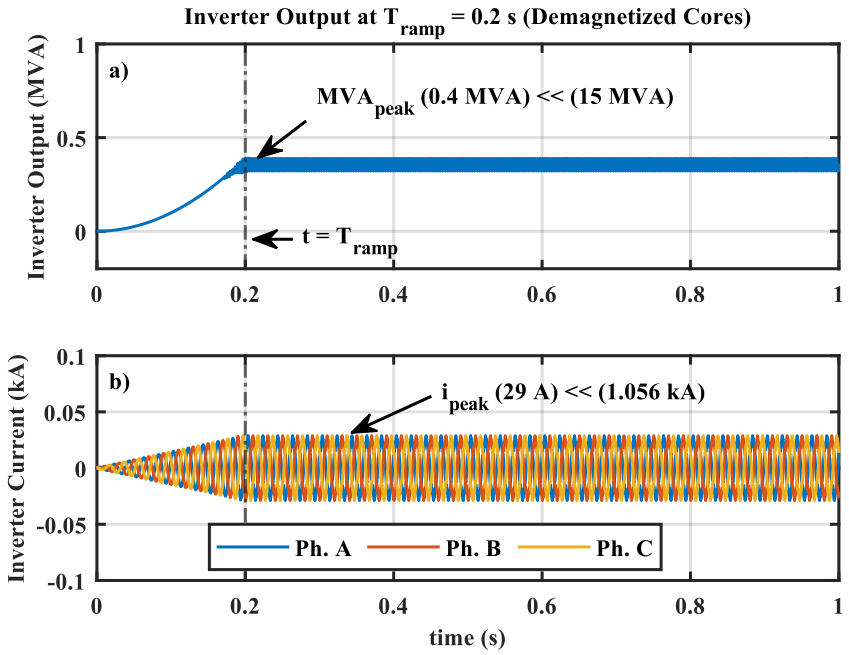

Figure 4.20: Soft energization second sensitivity case: instantaneous results for: a) GFC MVA, b) GFC current when the network transformers are demagnetized.

This provides a significant headroom that allows for faster ramps, as opposed to the base case where T_{x1} flux in phase A, for instance, is already at 0.8 pu. Meaning that the

headroom for the base case is more limited (between 0.8 pu and 1.2 pu, spanning 0.4 pu), compared to 1.2 pu span for the demagnetized core. Applying equation (3.30) indicates that the network transformers (with $\phi_{sat} = 1.2$ pu) do not go to saturation region in this case if T_{ramp} is selected large enough to bypass α energization impact. The applied 0.2 s voltage ramp is sufficient to neutralize α influence, thus avoiding saturation in all three transformers. The peak recorded converter power is limited only to 0.4 MVA, with a peak current of 29 A. The cables are also assumed to be initially discharged, leading to similar neutralization of their inrush impact. This sensitivity case clearly demonstrates the impact of residual flux on soft energization, and the edge of applying this technique on demagnetized, or nearly demagnetized, transformers.

Finally, the case study results consider a generic single-loop GFC implementation. Preliminary simulations were carried out in MATLAB/Simulink software and RSCAD/RTDS real-time simulator, incorporating inner voltage and current loops to the control. Results show that for soft energization, the stopping criteria with inner loops can be achieved with shorter ramp durations due to the imposed control dynamics. A brief discussion on this aspect is highlighted in Chapter 5.

4.4. Transformers Energization Techniques Assessment

In addition to the covered transformer energization techniques in this chapter, two other techniques have been presented earlier. The first is the 'do-nothing' technique, known as hard energization. This basically means that no measures are taken when energizing the transformer or series of transformers, and that they are energized at a random α from a 1 pu source. Hard energization can essentially work in very limited situations, such as having sufficiently large impedance existing between the source and the transformer, with non-extreme residual flux combinations. Adopting this technique is not recommended unless the network conditions are known, protection aspects are considered, and the energizing source is able to withstand any resulting inrush.

The improved version of hard energization relies on pre-insertion-resistors (PIR) brief connection between the source and the transformer only during energization to suppress inrush. The effectiveness of this technique is high if the resistors are sized appropriately

as demonstrated in Chapter 3, although the current is still influenced by α. Controlled switching from single-pole (1PL) and three-pole (3PL) circuit breakers has been covered thoroughly in this chapter, as well as soft energization in its improved form through the new proposed T_{ramp} estimation framework. Overall, all the discussed techniques are summarized in Table 4.3 to present an overview on their requirement measurements, breakers requirements and inrush suppression effectiveness.

Table 4.3: Performance summary of different transformer energization techniques.

	Principle of Operation	Required Measurements	Independent CB Control?	Inrush Mitigation Effectiveness
Hard Energization	Simultaneous energization for all phases at a random instant	None	No	Low
PIR	Same as previous but with series resistors to limit inrush current	None	No	Medium/High
Controlled Switching	**1PL-CB:** Eliminating the effect of flux transient through PoW switching	Flux and input voltage (including residual flux)	Yes	High
	3PL-CB: Finding the minimum flux error point across the three-phases		No	Medium/High (ϕ_r *dependent*)
Soft Energization	Ramping the source voltage to slow core saturation effect until reaching sufficient transient decay	**Basic:** None **Improved (*Optional*):** V, ϕ and Tx/network parameters	No	**Basic:** Medium **Improved:** High

4.5. Summary

The analysis presented in this chapter addressed the GFC-based network energization feasibility through controlled switching and soft energization techniques. The investigation covering controlled switching in its different forms aimed to answer the question of the three-pole controlled switching effectiveness against the classical energization through single-pole circuit breakers, given the high availability of three-pole CBs in distribution networks. In addition, the study has extended the analysis into soft energization as a feasible alternative due to the highlighted voltage control flexibility of power converters. A new framework has been developed to provide an answer to the industrial question of how fast the applied voltage ramp should be for effective inrush

elimination. The key findings and practical/industry implications based on the results reported in this case study are summarized as follows:

- Three-pole CBs can perform reasonably well under a range of ϕ_r combinations (especially at high ϕ_r of $[r, 0, -r]$ form such as [0.8, 0. -0.8] pu) but may still lead to high inrush under other ϕ_r (e.g., demagnetized transformers or with low ϕ_r).
- Controlled switching techniques require ϕ_r measurements, or indirect estimates through disconnection time. These requirements may not always be accurately available at the required energization points. Industrial relays, such as SynchroTeq [89] may be used in such cases (considering the added cost as a constraint).
- Soft energization can be used as an alternative technique that, in principle, does not require additional installations or measurements. This technique can also avoid inrush currents resulting from cables energization without requiring additional hardware.
- The new framework for T_{ramp} estimation showcases a model-based methodology that can be adopted using industrial software tools such as PSCAD/EMTDC.
- While ϕ_r availability helps achieving better T_{ramp} estimates, it is not a necessity for the new framework implementation since worst-case assumptions for ϕ_r can be made.
- An interesting contrast is that soft energization of demagnetized transformers can be achieved with very fast ramps, whereas high inrush current is obtained when applying the controlled switching technique from three-pole CBs with $\phi_r = [0,0,0]\ pu$.

The voltage control flexibility of power electronic converters, combined with the limited availability of PIR breakers, PoW relays and single-pole circuit breakers in distribution networks are considered as key factors to expand soft energization studies in this thesis. It has been established that this technique, in principle, does not require access or control of additional assets other than the GFC and its control, in addition to the inrush suppression effectiveness demonstrated for soft energization through the case study.

Chapter 5 Grid-Forming Converters Control

The analysis presented thus far on transformer energization has identified suitable techniques for black-start that take into account the GFCs limited overcurrent capabilities. A key identified technique is soft energization due to its flexibility and independence, in its basic from, from network measurements. The next step is to identify suitable GFC control techniques that are compatible with black-start requirements. To that end, this chapter investigates different grid-forming converter control techniques and benchmarks their performance and black-start readiness. Theoretical study of the different controllers is first presented, followed by a case study to assess their response against common disturbances and validate their soft energization compatibility. A suitable GFC controller is then selected for further investigations in the remaining chapters, and the influence of incorporating current control loops on inrush current is also introduced, with preliminary test results showing the potential positive inner loops impact on transformer energization.

5.1. Classification of grid-forming control techniques

GFCs are characterized by their ability to synthesize voltage output without relying on external source such as PLLs, thus enabling them to act as anchor sources in black-start network restoration events. In chapter 4, basic droop was briefly illustrated to benchmark the high-level control requirements between soft energization and controlled switching transformer energization techniques. However, different control methods are presented in literature that qualify as grid-forming controllers. The objective is thus to investigate common controllers, and their compatibility with the black-start application in terms of direct voltage control flexibility. In addition to their robustness against different types of disturbances. Ultimately, one of these controllers will be selected and used to expand the GFC-based black-start investigations in the remaining chapters.

The main control objective of a “grid-forming” control mode of a voltage source converter (VSC) is to operate as an independent voltage source that can create and maintain grid-compliant voltage and frequency at its terminals, in an analogous fashion to a synchronous generator. In terms of control structure, the required parameters for operating a converter

in grid-forming control mode can typically be a subset of, or all of the following: 1) active power; 2) reactive Power; 3) AC output voltage 4) DC link voltage and 5) frequency. The active power-frequency $(P-f)$ and reactive power-voltage $(Q-V)$ control loops for any GFC control technique provide a reference voltage and angle for the converter to track. In their basic form, the control design equations in these loops depend on active and reactive droop characteristics and may incorporate additional blocks for inertia emulation or to capture relevant (DC voltage – frequency) dynamics. These outputs can then be used to drive additional protective inner voltage/current control loops, where the control voltage angle in this case is generated internally by the main GFC power loop rather than the grid PLL as in grid-following control case.

Many works in literature have proposed and analyzed GFCs for different applications such as inertia support, grid-connected and islanded microgrids operation, ancillary services provision to the grid, and more [8, 9]. Though, the number of published studies investigating their use for black-start applications has been limited, with some reported industrial tests [90, 91]. Several classifications of GFCs exist in literature, such as classifying grid-forming techniques into inertial and non-inertial, or DC side vs. AC side reliant. For a black-start scenario, an important classification can also be based on the technique compatibility with a direct voltage reference control to be able to use a ramping reference as not all techniques inherently provide such flexibility. An example of such technique is the inducverter controller, first proposed in [92]. This technique aims to mimic the control behavior of induction machines, and in its basic form, the inducverter does not include a flexible reference voltage control. Reference [93] presents an interesting performance comparison of four grid-forming control techniques for transient stability assessment in grid-connected applications (Simple Droop, Power Synchronizing Control (PSC), Droop with Low-Pass-Filter and Virtual Synchronous Machine (VSM)). The paper classifies these four techniques into inertial and non-inertial, concluding that while inertial techniques provide faster frequency response, they can be more susceptible to transient instability. Though, a proper selection of power filters cutoff frequency can alleviate the impacts of this issue. The next level of control is the interactions between different co-existing converters within the grid along with the existing synchronous generators. The

interactions between grid-forming and grid-following converters in terms of their optimal placement within a network are studied in [94], while a dynamic study of the different converters control interactions is investigated in [95] following different system disturbances between an inertial synchronverter GFC and a PLL-based grid-following converter operating in close proximity. The authors of [96] have also thoroughly investigated and compared the interactions between four different grid forming techniques (droop, dispatchable virtual oscillator control (dVOC), matching and VSM) with and without the existence of synchronous generation using the IEEE 9-bus test system. The study highlighted that a controller selection for a satisfactory AC side (i.e., Rate-of-Change-of-Frequency (RoCoF) and frequency nadir reduction) may not necessarily yield similar results for operating the DC side source near its saturation limits. This shows the necessity of studying the often neglected coupled reaction between the DC and AC side dynamics to achieve a global control objective that maintains stability against disturbances in both sides of operation, especially when utilizing the analogous operation of the DC link capacitor voltage as a source of inertial frequency support as in [97].

5.2. Current Control in Grid-Forming Converters

Many VSC implementations require internal voltage and current protection loops to prevent overcurrent flowing through the converter switches and causing damage or equipment failure. In addition to their main protection features, some internal voltage and current control types are used to mitigate the output harmonics distortion and improve the system closed loop response [7, 98, 99]. The internal loops can be implemented using different control types, mainly:

- Standard three-phase (abc) control, which adds more control complexity.
- Stationary ($\alpha\beta 0$) reference control, which utilizes Proportional-Resonant (PR) controllers capable of eliminating individual harmonics [7].
- Synchronous (dq0) reference control, which converts AC voltages & currents to DC equivalent dynamic terms, making them easier to control through conventional Proportional-Integral (PI) controllers [99].

The voltage synchronization task in grid-following converters utilizes a PLL for external voltage tracking. On the other hand, an anchor GFC generates its own reference and only uses a PLL when grid-synchronization is required. The synchronous reference frame control is the most used configuration in literature and industry due to its effectiveness and simplicity and is thus adopted here. The current control concept using the synchronous dq0 frame for a GFC is illustrated in Figure 5.1. The GFC control reference angle is used to drive transformation blocks between abc and synchronous (direct-quadrature-zero, dq0) frames through Park transformation.

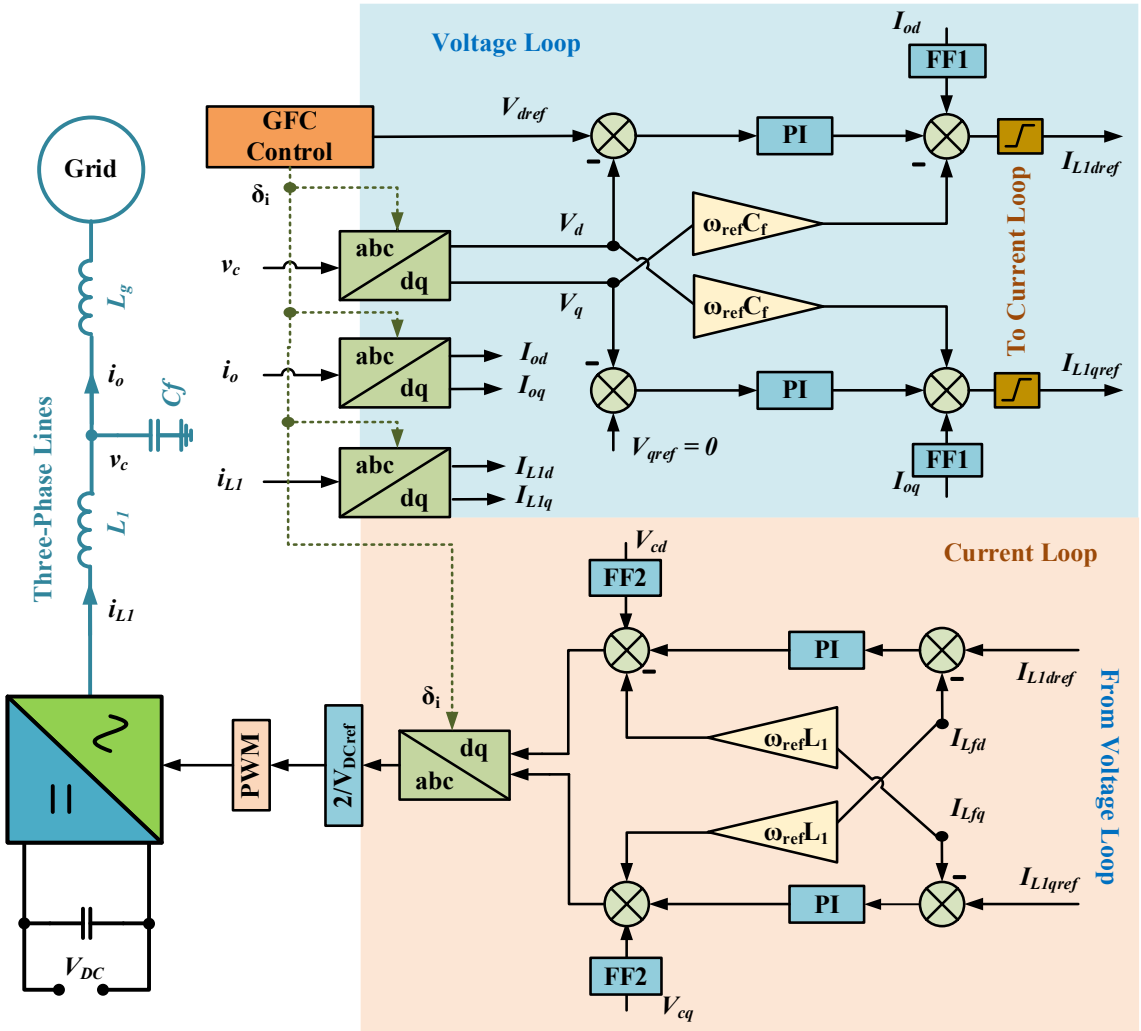

Figure 5.1: Dual-loop voltage and current control structure for a VSC with LC/LCL filters.

Voltages and currents in the synchronous frame rotate with the GFC frequency. This way, they appear as DC stationary values that can be controlled using classical techniques such as PI controllers. The transformation steps from abc-dq0 frames are derived in [100], and demonstrated in equations (5.1)-(5.2) in a 90° delay form, such that d-axis values are equal to the balanced three-phase sinusoid peak.

$$X_{dq0} = T_{\delta_i} X_{abc} \tag{5.1}$$

$$\begin{bmatrix} X_d \\ X_q \\ X_0 \end{bmatrix} = \frac{2}{3} \begin{bmatrix} \sin(\delta_i) & \sin\left(\delta_i - \frac{2\pi}{3}\right) & \sin\left(\delta_i + \frac{2\pi}{3}\right) \\ \cos(\delta_i) & \cos\left(\delta_i - \frac{2\pi}{3}\right) & \cos\left(\delta_i + \frac{2\pi}{3}\right) \\ \frac{1}{2} & \frac{1}{2} & \frac{1}{2} \end{bmatrix} \begin{bmatrix} X_a \\ X_b \\ X_c \end{bmatrix} \tag{5.2}$$

X here denotes the studied signal (i.e., voltage or current), and δ_i is the output GFC control phase angle (oscillating each cycle between 0 and 2π). Inverse transformation is obtained by inverting the T_{δ_i} matrix. If equation (5.1) is applied to a three-phase sinusoid signal with amplitude A and DC offset B, then the resulting dq0 components are $X_d = A, X_q = 0, X_0 = B$. Considering the LC filter circuit in Figure 5.1, it is known that capacitor current and inductor voltage are dependent on time-derivatives as in (5.3)-(5.4).

$$i_c = C\ dv/dt \tag{5.3}$$

$$v_L = L\ di/dt \tag{5.4}$$

Applying abc-dq0 transformation on a time-derivative results into cross coupling between d-axis and q-axis components for voltage and current. This appears in inductor current and capacitor voltage solutions of the differential equations in dq0 frame. Namely, the reference inductor current equations are calculated as in (5.5)-(5.6) [101].

$$I_{L1dref} = FF1\ I_{od} + \Delta V_d (k_{pv} + \tfrac{k_{iv}}{s}) - \omega_{ref} C_f\ V_q \tag{5.5}$$

$$I_{L1qref} = FF1\ I_{oq} + \Delta V_q \left(k_{pv} + \tfrac{k_{iv}}{s}\right) + \omega_{ref} C_f\ V_d \tag{5.6}$$

Where FF1 (and FF2) are optional feedforward term that can be enabled to improve the controller disturbance rejection, and k_{pv}, k_{iv} are the voltage loop PI control gains. Similarly, the internal GFC voltage equations include cross-coupling terms between d and q axes as in (5.7)-(5.8).

$$V_{id} = FF2\ V_{cd} + \Delta I_{L1d}(k_{pi} + \frac{k_{ii}}{s}) - \omega_{ref} L_1\ I_{L1q} \tag{5.7}$$

$$V_{iq} = FF2\ V_{cq} + \Delta I_{L1q}\left(k_{pi} + \frac{k_{ii}}{s}\right) + \omega_{ref} L_1\ I_{L1d} \tag{5.8}$$

The PI gains for current loop are k_{pi} and k_{ii}, respectively. Generally, when the abc-dq0 reference transformation is applied for converter control, then the direct axis (d) current is responsible for controlling the active power, whereas the quadrature axis (q) current controls the reactive power flow. The outer voltage loop sets the reference current values to the inner current loop and ensures that both dq reference currents are maintained within the converter operating limits. The cross-coupling terms $\omega_{ref} C_f$ & $\omega_{ref} L_f$ are imposed to decouple synchronous frame axes as seen in (5.5)-(5.8). The controlled current loop output is eventually reverted to the abc frame through inverse Park transformation to generate the Pulse-Width-Modulation (PWM) driving signals to the grid-forming converter switches. Inevitably, the inclusion of dual voltage and current loops affects the overall operation of the grid-forming converter control as it affects the converter dynamic performance. The analysis presented in this chapter tackle the main properties of each studied controller under the assumption of inner loops inclusion.

5.3. GFC Control Techniques Theoretical Comparison

This section investigates four different GFC control techniques to assess their capabilities. In particular, their suitability to black-start applications in terms of robustness and voltage control flexibility. The four compared GFC control techniques are: Droop, PSC, matching and VSM control. The selection of these four techniques is based on the following aspects:

- Droop and PSC are selected due to the wide use of the former, and the similarities between both techniques [93, 102]. Studying their performance simultaneously thus provides a valuable assessment and benchmarking tool.

- VSM control performed best in terms of AC side disturbances study, whereas matching control performs best against DC side source saturation in [96].
- dVOC is not considered due to its intermediate performance against both AC and DC disturbance types [96].
- Similarly, inducverter GFC is not considered based on its lack of flexible, controllable, AC voltage reference, which affects its suitability for black-start applications without modifying its basic form.

The principle of operation for each of these four techniques in addition to their market maturity are summarized in Table 5.1. Droop, VSM, dVOC and Matching control techniques are similarly evaluated in [103].

Table 5.1: Generic description of the four selected GFC control techniques.

GFC Technique	Principle of Operation	Flexible V_{ref}?	Market Maturity
Droop	Mimicking speed droop in SGs.	Yes	The basic shared structure of both techniques is widely implemented. Moderate research focus is still observed especially for Droop.
PSC	Mimicking power synchronizing behaviour between SGs.		
Matching	Exploiting the analogy between V_{DC} and SGs frequency variations.		Early Research Stage with different possible implementations.
VSM	Mimicking the speed droop and inertia of SGs swing equation.		Strong research focus, prototyping, pilot implementations and feasibility studies.

5.3.1. Droop Control

VSC droop control technique is inspired by the droop characteristic of synchronous generators, which aims to balance the power supply between different generators and to maintain their power sharing and stabilize the network frequency [104]. Droop is a common technique that is used for several converter control applications in literature papers and industry, especially when power sharing between various VSCs is required in a similar fashion to that of SGs. Though, droop is reported in the literature to result in power sharing mismatch under variable network conditions (e.g., the network X/R ratio and the impedance variation at the PCC of different grid converters) [105]. Virtual

impedance has been proposed as a remedy to this limitation by several researchers. A fully optimized droop implementation for VSC applications is still an active question that attracts research until today [106]. Conventional droop control under inductive network assumption includes a $P-f$ loop and a $Q-V$ loop, thus inherently achieving grid-forming operation compatibility. The former loop is responsible for frequency control and angle reference generation and is demonstrated in Figure 5.2, where 1/s denotes an integrator and LPF refers to the power measurement low pass filter. Equations (5.9)-(5.10) demonstrate the droop power loop equation and calculation of its droop coefficient m_P.

$$\omega_{ref} - \omega = m_p(P_{meas} - P_{ref}) \tag{5.9}$$

$$m_P = -\frac{\Delta\omega_{droop}}{\Delta P_{droop}} \tag{5.10}$$

where ω_{ref} and ω are the reference and measured angular frequency, respectively, with similar notions for P (active power). $\Delta\omega_{droop}$ is the frequency deviation resulting from a power reference mismatch ΔP_{droop}. Both parameters are used for droop factor m_p design.

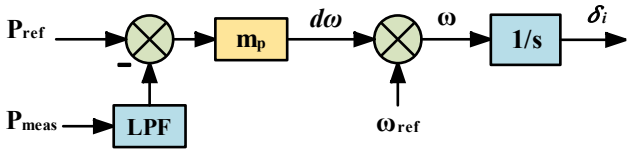

Figure 5.2: Basic grid-forming droop control power loop.

The $Q-V$ loop in droop control is responsible for voltage and reactive power regulation. Different implementations are found in the literature for this control loop. A common method considers both reactive power and voltage control, whereas other implementations consider voltage control. Given that the GFC control objective of interest is focused on voltage tracking, the simple voltage loop is considered as in Figure 5.3.

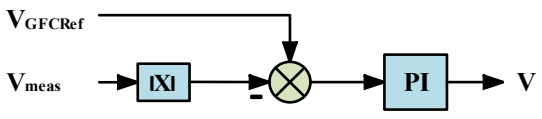

Figure 5.3: Basic grid-forming control voltage tracking loop.

The amplitude detection block utilizes a synchronous frame abc-dq0 transformation to calculate the voltage waveform peak using (5.11).

$$V_{GFC_{pk}} = \sqrt{V_d^2 + V_q^2 + V_0^2} \tag{5.11}$$

In this voltage loop implementation, the converter consumes/produces the necessary reactive power level to maintain the voltage reference. A protective feature can be added to the dual-loop control to limit quadrature current (I_q) within converter rating by simultaneously maintaining the overall apparent power $S = \sqrt{P^2 + Q^2}$ to rated value.

5.3.2. Power Synchronizing Control (PSC)

This VSC control technique was first introduced in [102], mainly for HVDC applications in order to mitigate the stability issues of PLLs when connected to weak grids. The proposed controller includes a Power Synchronizing Loop (PSL), in addition to voltage and reactive power control loops. These loops are connected or disconnected depending on the application needs (e.g., voltage support, reactive power support, grid synchronization … etc). For instance, a backup PLL is proposed in the original design to provide synchronization under fault conditions, where a modified current control structure alters the operating mode between PSL and PLL based on the measured current threshold to maintain grid synchronism. The basic PSL loop is illustrated in Figure 5.4.

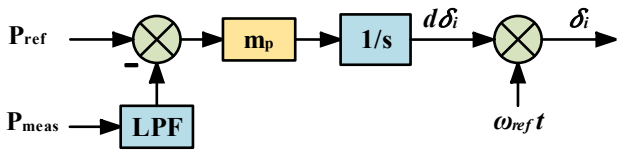

Figure 5.4: PSC Controller - Power Loop.

The grid-forming and synchronization capability of PSC is embedded into the PSL. Similarities between the PSL loop in PSC and the $P - f$ loop in droop control are easy to notice. The main observable variation is in the angle synthesis. In Figure 5.4, the power mismatch generates an error signal that is integrated to compose a deviation to the reference angle, whereas droop control integrates the summation of ω_{ref} and its deviation

to compose the angle based on $\omega = d\theta/dt$. The coefficient m_p can be set similarly to that in droop control. In such case, it is expected that the performance of both droop and PSC techniques to be similar under normal operating conditions, assuming the use of a unified voltage loop implementation. The PSC $Q - V$ loop in this comparison is maintained to an analogous structure to that adopted for droop control, as illustrated in Figure 5.3.

5.3.3. Matching Control

This grid-forming control technique has recently been introduced in [107], similarly aiming to exploit structural similarities between VSCs and SGs. The matching control principle is based on the observation that DC link voltage variations may indicate power imbalances in an analogy to SGs frequency, this analogy is discussed in more details in [97]. The power loop uses this analogy to drive the converter frequency from the dynamic DC link voltage as illustrated in Figure 5.5(a). The matching control power loop mainly transforms the DC link voltage to a converter frequency signal using the transformation factor K_m defined in (5.12), which is then integrated to generate the converter voltage angle.

$$K_m = \frac{\omega_{ref}}{V_{DC_{ref}}} \tag{5.12}$$

In matching control, the active power regulation is implicitly implemented through the DC link voltage control. That is, the converter tracks the power reference defined by V_{DC} controller. A possible DC voltage control implementation, presented in [96], is shown in (5.13), composed of proportional and feedforward control terms, in addition to power reference tracking (5.13).

$$I_s = k_{pdc}\Delta V_{DC} + \frac{P_{ref}}{V_{DC_{ref}}} + \frac{V_{DC}}{R_{dc}} + \frac{I_{DC}V_{DC} - P_{meas(ac)}}{V_{DC_{ref}}} \tag{5.13}$$

where I_s is the source DC current, k_{pdc} is the proportional controller gain and ΔV_{DC} is the DC voltage error. In this investigation, the DC source is implemented as a controlled current source feeding a DC link capacitor as illustrated in Figure 5.5(b). Any DC voltage

reference variation during converter operation should be reflected in real time on K_m to avoid controller setpoint mismatches.

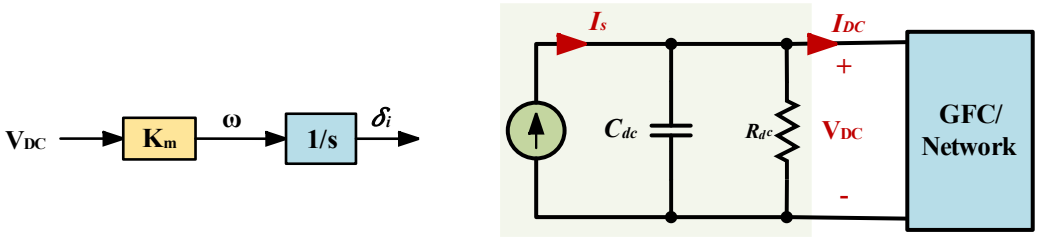

(a) (b)

Figure 5.5: Matching control: (a) DC voltage/Power loop on the AC side, (b): Dynamic DC voltage representation.

Based on matching control dynamic DC voltage nature, the use of a stiff, ideal, DC voltage source to simulate this technique behavior is not practical. The voltage loop in matching control also has various implementations in literature. The voltage control factor (μ) in matching control can be derived to meet various control objectives such as PCC voltage regulation as in [96] or reactive power tracking as in [108]. The matching control voltage loop theory proposes implementation in the stationary $\alpha\beta$ reference frame, though, a similar implementation to that of voltage tracking mode in Figure 5.3 has been tested to produce the voltage magnitude parameter (μ), and showed identical behavior. The same structure is thus maintained (i.e., a common grid-forming voltage loop is used for droop, PSC and matching controllers).

5.3.4. Virtual Synchronous Machine (VSM)

The concept of virtual inertia provision through VSC control has been receiving a significant traction in academia and industry. The used terminology differs between various papers such as synchronverter, Virtual Synchronous Generator (VSG) or Machine (VSM) based on the implementation. The term "VSM" is used in this thesis to refer to the technique introduced in [109]. As the name suggests, VSM grid-forming control concept also stems from SGs characteristics emulation. A VSM can be designed to emulate a

variable subset of SM capabilities based on the application requirements. Most existing implementations focus on emulating the SM inertial response to frequency events.

In contrast to the other techniques discussed in this chapter, VSM power control loops include additional term(s), which emulate frequency dynamics through adding the frequency derivative $d\omega/dt$ into the control design as in equation (5.14).

$$J\frac{d\omega}{dt} = \frac{1}{\omega_{ref}}(P_{ref} - P) + D_p(\omega_{ref} - \omega) \tag{5.14}$$

where J is the virtual moment of inertia, and D_p is the damping factor. The value of J influences the rate of change of frequency (RoCoF) and its minimum/maximum (nadir/zenith) value in case of a frequency event. J is related to D_p through a time constant τ_f such that $J = D_p\tau_f$. The VSM time constant can be made much smaller to that of physical SGs. As reported by previous works, τ_f value selection ranged between 0.002 s and 0.02 s [96, 109]. For the present GFC control techniques comparison, 0.02 s is selected to utilize a higher inertia constant.

The conventional voltage-reactive power control loop in VSM is also inspired by SM excitation and control theory. The authors of [109, 110] present detailed analysis and theoretical derivations for the VSM – SM control analogy, including torque, reactive power and voltage. Though, it is assumed for this study that active and reactive powers can be calculated through direct converter measurements, and thus the focus is on the VSM voltage amplitude formula, which is presented in (5.15).

$$|V| = \omega M_f i_f \tag{5.15}$$

Here, M_f analogy is inspired from the mutual inductance between a SM field and stator coils, and i_f is inspired from the rotor excitation current. The calculation of the $M_f i_f$ term in VSM control is mathematically presented as in equation (5.16).

$$M_f i_f = \int \frac{1}{K_v}(D_q\, \Delta|V| + \Delta Q)\, dt \tag{5.16}$$

where $1/K_v$ is the integrator gain scaling factor, D_q is the voltage damping factor, $\Delta|V|$ and ΔQ are the voltage and reactive power errors, respectively. On the other hand, the

angular frequency ω is obtained from $P-f$ loop. Collectively, Figure 5.6 shows the conventional implementation of the interconnected VSM control loops, this connection is established through ω.

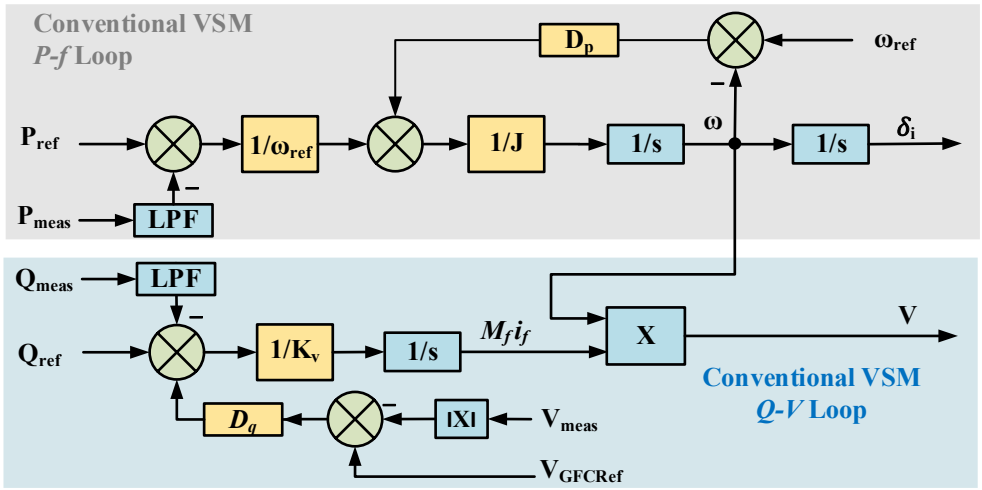

Figure 5.6: Classical VSM control block diagram.

The conventional VSM voltage loop illustrates combined voltage and reactive power tracking terms. If accurate voltage or reactive power tracking is required, then the voltage loop can be tuned to dampen D_q to the required extent. Another possibility is to separate the loop and maintain voltage tracking objective. A similar distinction is implemented in [96] using a PI voltage controller without reactive power tracking. Unlike PSC, the paper that introduced the VSM in 2011 did not include a current control in its implementation. Active on-going research efforts are investigating alternatives that maintain the VSM performance while switching to current limiting mode under fault conditions [111].

5.4. Performance Evaluation of GFC Controllers: Case Study

The performance of the four presented grid-forming converter control techniques is benchmarked and compared through a comprehensive case study. The assessment methodology aims at targeting each control technique individually to measure its response under various operating conditions in both grid-connected and islanded configurations. The network used for the simulated tests is presented in Figure 5.7, where the variable between the different simulation scenarios is the content of the 'GFC Control' box.

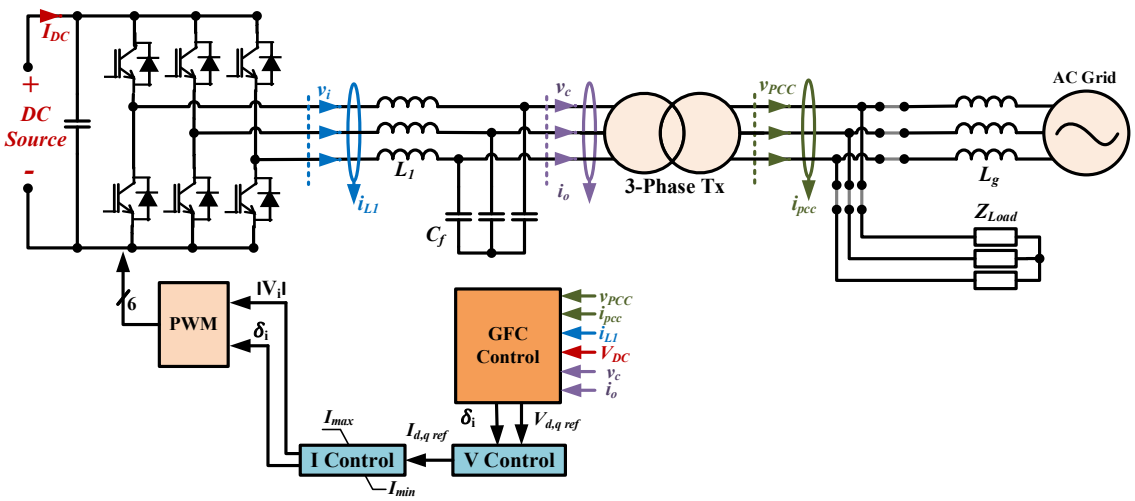

Figure 5.7: Test network for grid-forming control techniques comparison.

The four grid-forming controllers are tested under a unified steady state $P-f$ slope to mitigate the impact of control design variations between the different techniques. The same dynamic DC link voltage control is applied for all controllers for consistency. The test system is representative of a realistic power plant rating that is connected to 33 kV AC network through a $\Delta - Y_g$ (11/33 kV) transformer. The system parameters are summarized in Table 5.2.

Table 5.2: GFC Test system parameters

Parameter	Value	Parameter	Value
GFC Output Voltage (LL-kV)	11	Converter Rating (MVA)	40
DC Link Voltage (kV)	20	Transformer Rating (MVA)	53
$L_f\ (mH)$	0.48	Transformer Voltage Ratio	11/33
$C_f\ (\mu F)$	23	Network XR Ratio	10
Nominal Frequency (Hz)	50	Short-Circuit-Ratio (SCR)	5

Considering that a network is classified as weak if it has a Short-Circuit-Ratio (SCR) < 3 [112], an intermediate value of SCR = 5 is selected, whereas the network X/R ratio is selected as 10 to reflect the upper range from [113]. The transformer linear region impedances are equal to those used in Chapters 3 and 4, and the common steady state $P-f$ slope is estimated for all techniques as in (5.17).

$$\omega_{ref} - \omega = m_p(P_{meas} - P_{ref}) \tag{5.17}$$

The selected value of m_p is such that a 100% swing in rated power results in 1% swing in frequency (i.e., 49.5 Hz – 50.5 Hz). For all controllers in this case study, P_{ref} is set to 1 pu. ($m_p = 7.85x10^{-8}$). Equation (5.17) is common between droop and PSC controllers since they share a similar power loop. Equivalent steady-state equations for VSM and matching controls can be obtained as in (5.18)-(5.19), respectively, from [96].

$$\Delta\omega = -\frac{1}{D_p \omega_{ref}} \Delta P \tag{5.18}$$

$$\Delta\omega = -\frac{\omega_{ref}}{K_{pdc} V_{DC_{ref}}^2} \Delta P \tag{5.19}$$

where K_{pdc} is the proportional DC voltage control gain. The slopes in (5.18)-(5.19) are designed to match the common m_p. Inner PI control loops in the synchronous frame are incorporated with all controllers, with the parameters listed in Table 5.3.

Table 5.3: Proportional Integral Control Parameters for Inner GFC Control Loops

Voltage Loop		**Current Loop**	
$K_{pv} = 0.1$	$K_{iv} = 1$	$K_{pi} = 9.025$	$K_{ii} = 0.287$

In droop, PSC and matching controllers, voltage loop tracks the set reference through a PI control as illustrated in Figure 5.3. The controllers are tuned with $K_p = 0.35, K_i = 15$. The technique with different voltage loop is the VSM as illustrated in Figure 5.6. To maintain the comparison on common grounds, the reactive power tracking terms are disabled here, and the voltage tracking objective is prioritized. Simulations are performed using the VSC average model in Simulink with a sampling time of $T_s = 100\ \mu s$. The model is run by a separate MATLAB script to automate and accelerate the process.

5.4.1. Test Scenarios Definition

The robustness of the selected controllers to different disturbances, in addition to their ability to track a ramping voltage reference are tested to validate their performance and black-start readiness. The outcomes of this study will help to determine suitable controllers

for black-start from the four candidates and to identify performance advantages and shortcomings. First, three disturbance types are considered in grid-connected mode and applied to the network in Figure 5.7 for each of the four control techniques. The considered disturbances are listed here as:

- Load disturbance at the PCC rated at 0.5 pu power.
- DC link voltage reference step change (+0.2 pu).
- GFC active power reference step change (+0.5 pu).

For each disturbance, the effect on frequency, RoCoF, active power, PCC voltage and DC voltage is recorded. The monitored AC voltage is the instantaneous synchronous frame voltage calculated from equation (5.11) at the GFC output (after the LC filter). This voltage captures the fast transients in the voltage waveforms and is used here to identify any variations in the techniques voltage control response that may not be captured by Root-Mean-Squared (RMS) measurements. Then, the soft energization compatibility of each technique is tested where a ramping voltage reference with $T_{rmap} = 10\ s$ is applied.

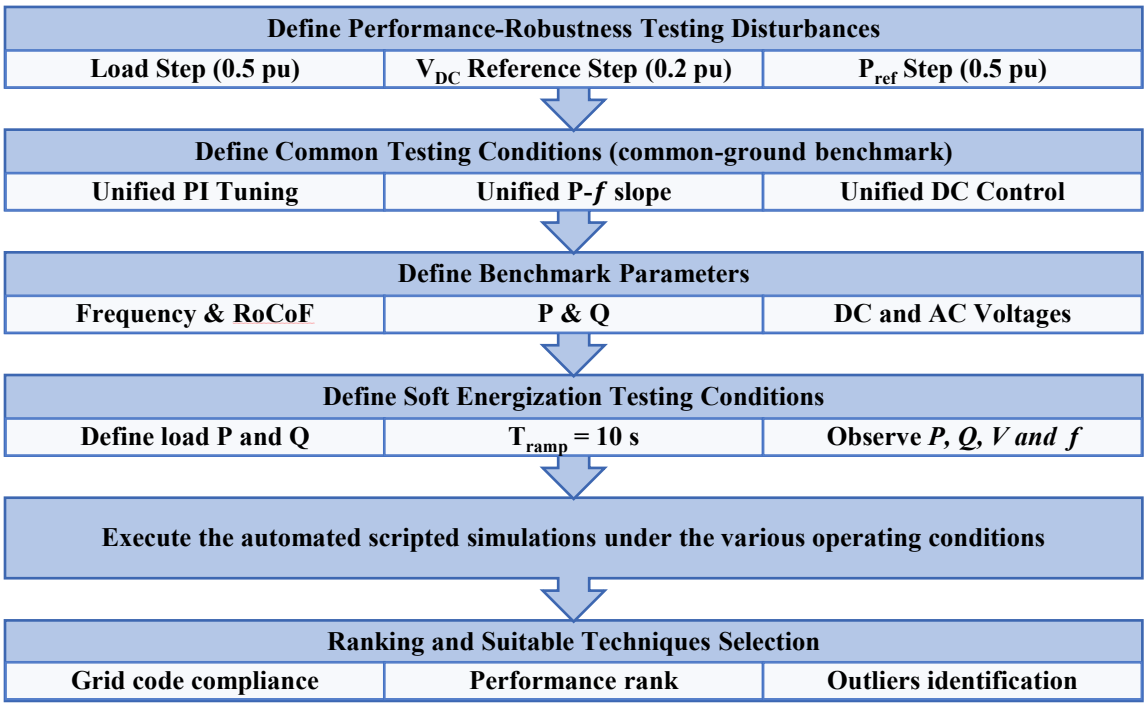

Figure 5.8: Grid-forming control techniques assessment methodology.

Soft energization is combined with load pickup with active power around 1 pu. Reactive power is also observed to ensure that $\sqrt{P^2 + Q^2}$ does not violate the GFC rating. Eventually, the control techniques performance is compared based on their measured responses, and one of them is adopted for the extended black-start testing in the following chapters. The described assessment methodology is summarized in Figure 5.8.

One of the used parameters for performance benchmark is the RoCoF, which is defined as the frequency variation rate (time derivative). Instantaneous measurement of RoCoF is more prone to measurement noise and may capture higher rates of change due to the initial transients. It is thus common to measure this parameter over a moving average time window. The maximum accepted RoCoF threshold in the UK according to [114] is set to 1 Hz/s, with a similar magnitude set by EirGrid in Ireland [115], for a rolling window of 500 ms. To demonstrate the impact of instantaneous versus moving average RoCoF measurement, a simulation case with load disturbance at $t = 3\ s$ is presented, where the RoCoF is measured according to equations (5.20)-(5.21).

$$f(t)_{ma} = \frac{1}{T_w}\int_{t_o}^{t_o+T_w} f(t)dt \tag{5.20}$$

$$RoCoF(t) = \frac{df(t)_{ma}}{dt} \tag{5.21}$$

where, $f(t)_{ma}$ is the moving average frequency and T_w is the moving average period. Four cases are tested, starting with the instantaneous measurement (i.e., $T_w \to 0$), in addition to $100\ ms, 300\ ms,$ and $500\ ms$ time-windows. The results are illustrated in Figure 5.9, showing the impact of moving average on the RoCoF estimate. Clearly, instantaneous measurements are not recommended as they produce RoCoF peaks that exceed the described maximum permissible limit (e.g., 1 Hz/s). Whereas the RoCoF for the same disturbance against a 500 ms measurement window complies to the highlighted standard. Thus, a 500 ms window is adopted in this case study for the grid-forming converters control assessment.

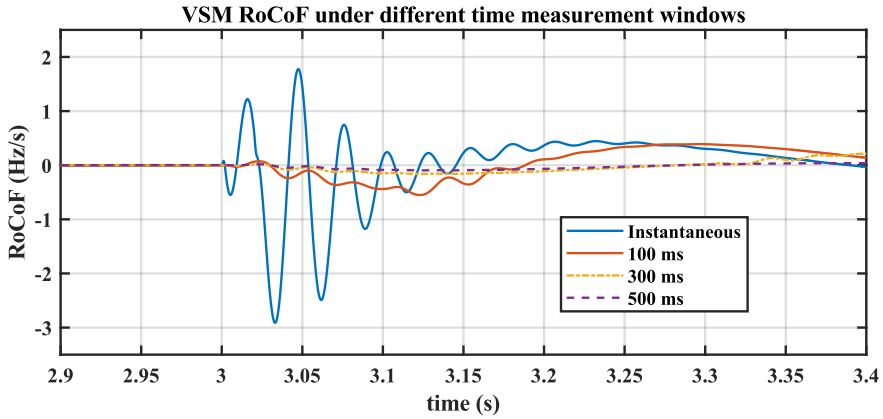

Figure 5.9: Impact of measurement time window on RoCoF estimate.

5.4.2. Case Study Results

A. Load Disturbance Response: 0.5 pu

Simulations are run for all techniques under this disturbance with the default parameters in Table 5.2 to Table 5.3 The GFC export power reference is initially set to 0.5 pu. Then at $t = 1.5\ s$, an active load with rated power 0.5 pu is connected at the PCC between the GFC and the grid. Since the GFC reference does not change, it is expected for a momentary power disturbance to be observed before the GFC power goes back to the control reference and the grid supplies the connected load. This disturbance is also expected to manifest itself into the frequency and RoCoF as minimal variations due to the used low frequency variation factor m_p for the four controllers. These predictions are verified in Figure 5.10, and are observed to be common across the different grid-forming techniques in terms of variation orders of magnitude. That is, while VSM has the lowest variation in frequency, the other controllers also exhibit similar behavior with frequency deviations that are also within acceptable limits. Droop and PSC controllers in particular exhibit nearly identical behavior due to the similarity in their $P - f$ loop structure. All controllers do not violate the peak RoCoF standard of 1 Hz/s, and the maximum GFC frequency variation is limited to around 0.2%. Reactive power supplied by the GFC is increased after the disturbance to maintain the controlled converter voltage to its setpoint, with similar behavior among the compared controllers.

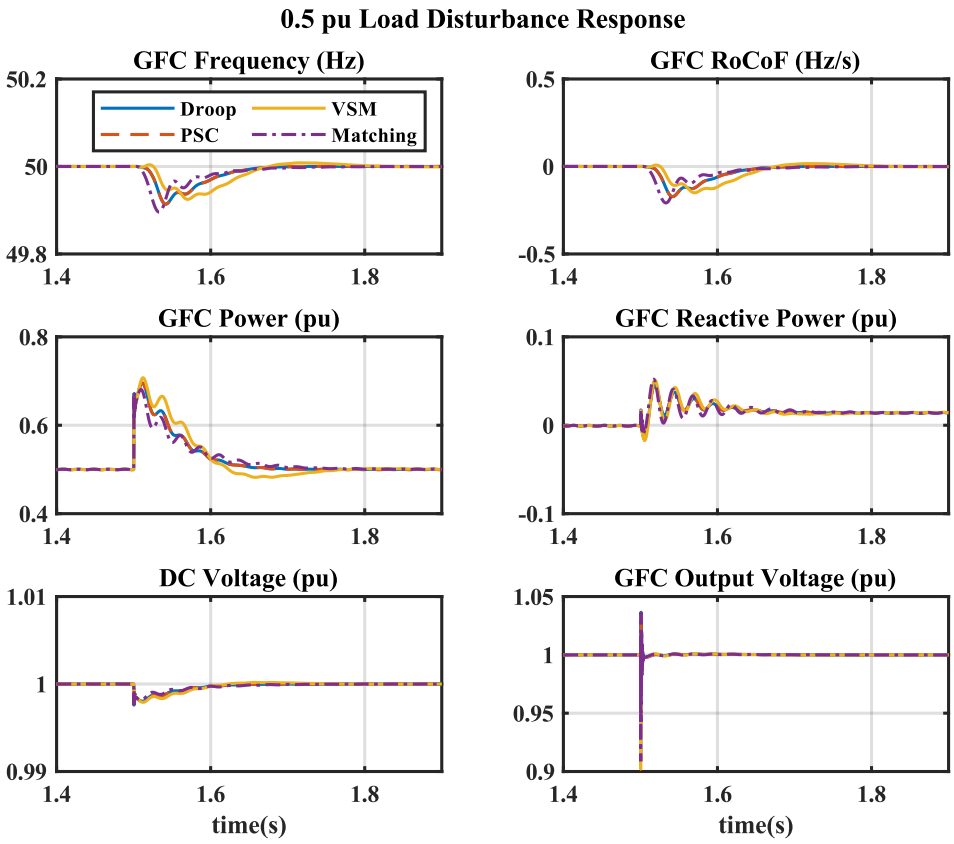

Figure 5.10: GFCs control response to the load disturbance scenario.

A small DC voltage disturbance is also observed but quickly overcome by the DC controller. The GFC output instantaneous AC voltage behavior is also very similar for the four techniques against this disturbance, dropping to nearly 0.9 pu before a quick recovery through the voltage loop. Overall, the presented results show very similar performance from the four GFC controllers against this disturbance with reasonable parameters variation margin that is aligned with grid requirements.

B. DC Voltage Disturbance Response: 0.2 pu

Three of the four techniques exhibit nearly neutral response to this type of disturbance as shown in Figure 5.11, except for matching control as it depends on DC voltage variations as an input to its $P - f$ control loop. Regardless, the four controllers demonstrate similar compliance with the grid code against the different applied disturbances, with minimal frequency and RoCoF variations. Since no AC side disturbance took place, the GFC reactive power export goes back to zero for all controllers after the disturbance.

The implemented current control in Figure 5.1 employs a division by DC reference voltage to normalize the output sinusoids that drive PWM signals. To improve matching control response against DC voltage variations, it is observed that this reference should be adjusted to be dynamically following the DC voltage measurements to improve the controller response speed in the presence of such large disturbance. If the 0.2 pu step DC reference change applied here is not reflected on the current control output, then the step effect on the modulation index variation will be compensated by the PI controllers, causing higher oscillations, and longer settling time. Whereas an immediate reflection on the DC reference division in the controllers output suppresses these oscillations significantly. Finally, the analysis presented in [96] demonstrated a favorable performance of matching control against DC current operating near its source saturation, whereas the scenario analyzed in this case measures the controller response against a disturbance in the DC link voltage under unsaturated conditions.

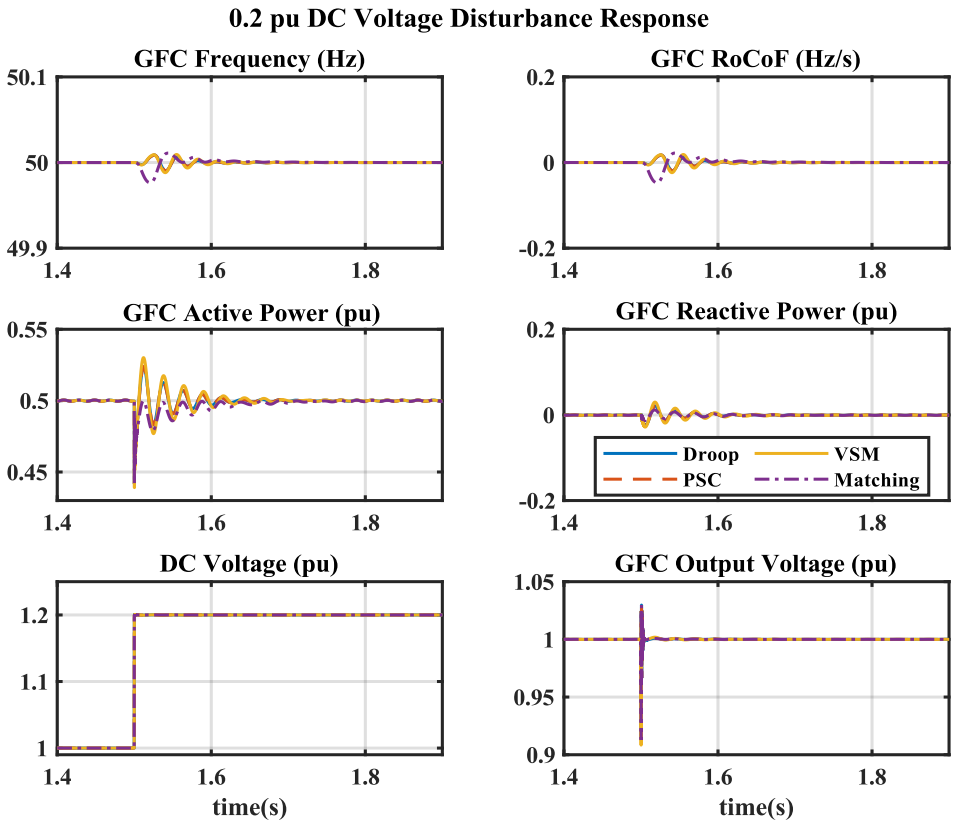

Figure 5.11: GFCs response to the DC voltage disturbance scenario.

C. Pref Disturbance Response: 0.5 pu

The last considered disturbance in the grid connected mode is a 0.5 pu active power reference step for the grid connected converter (from $P = 0.5\,pu$ to $P = 1\,pu$). The test response is presented in Figure 5.12. The main impact is on the frequency and RoCoF, while other parameters exhibit minimal variations following the disturbance. Unlike previous tests, the frequency and RoCoF responses in this case are in the positive direction since the converter has to increase its output power to a new steady state value, before the frequency is balanced again after the power error reduces to zero. The steady-state reactive power also increases to maintain the GFC output voltage level that is required to accommodate the increased power export. If this test had been conducted in islanded mode without grid-connection or a load increase matching the reference power increment, then the mismatch in power reference would have resulted into a steady-state frequency deviation. In a black-start scenario, active and reactive power consumptions are not always

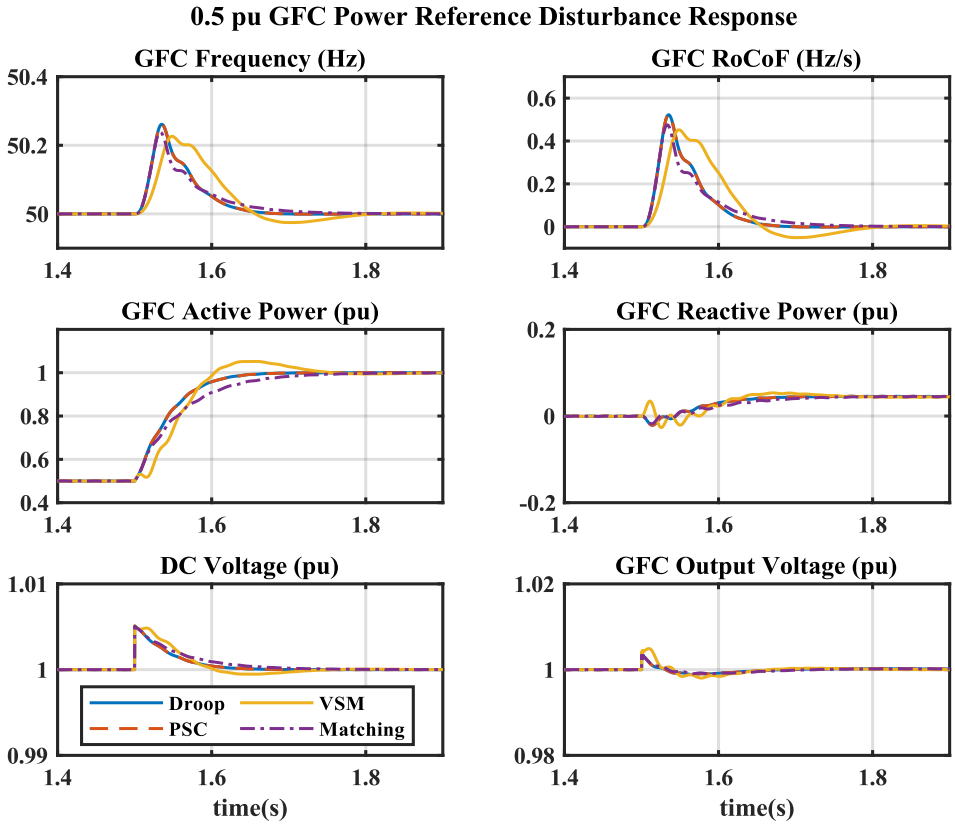

Figure 5.12: GFCs response to the active power reference 0.5 pu disturbance scenario.

known a priori, and thus a proposed grid code modification in a recent UK National Grid report is to relax the frequency regulations in this period of uncertainty until grid-connection is restored [10]. Similarly, this test has also demonstrated the comparable, and satisfactory, response of the tested controllers in following power reference variations without significant frequency or voltage changes.

D. Soft Black-Start Capability Validation

GFCs, in principle, should be compatible with the soft energization capability given that an adequate controller is implemented. As presented in Chapters 3 and 4, soft energization is an effective technique for transformers and cables energization for inrush current mitigation. It has also been established earlier in this chapter that a reason for selecting these four grid-forming controller for the comparison is their perceived compatibility with this requirement through direct voltage reference manipulation. The test scenario presented here aims to validate this feature, and to identify any tracking limitations for the investigated controllers. Since droop, PSC and matching controllers utilize a PI for voltage reference tracking, the control gains should be selected to enable effective ramping reference tracking without causing additional delays. The speed at which this voltage reference is synthesized is influenced by selected controller gains. Smaller gains can lead to slow convergence, whereas excessively higher gains can lead to instability. Soft-start ramps up the voltage to a reference at a specific slope (e.g., within 10 seconds in this test), and thus the P/PI control design should take into consideration having a minimal effect on slowing this rate. The tuning can be easily verified by testing the voltage ramp-up and confirming that 1 pu voltage is measured at $t = T_{ramp}$, and not after.

Figure 5.13 summarizes the test results for the selected $T_{ramp} = 10\ s$, and illustrates successful GFC output voltage tracking for all controllers. Since a load is simultaneously connected, the measured power ramps up in a quadratic fashion until reaching its steady state value at $t = 10\ s$. The reactive power, for all controllers, ramps up similarly until around 0.12 pu, mainly due to the transformer leakage inductance. All controllers are able to supply the required P, Q with nearly identical performance, demonstrating their ability to perform the voltage ramping assignment in a black-start scenario.

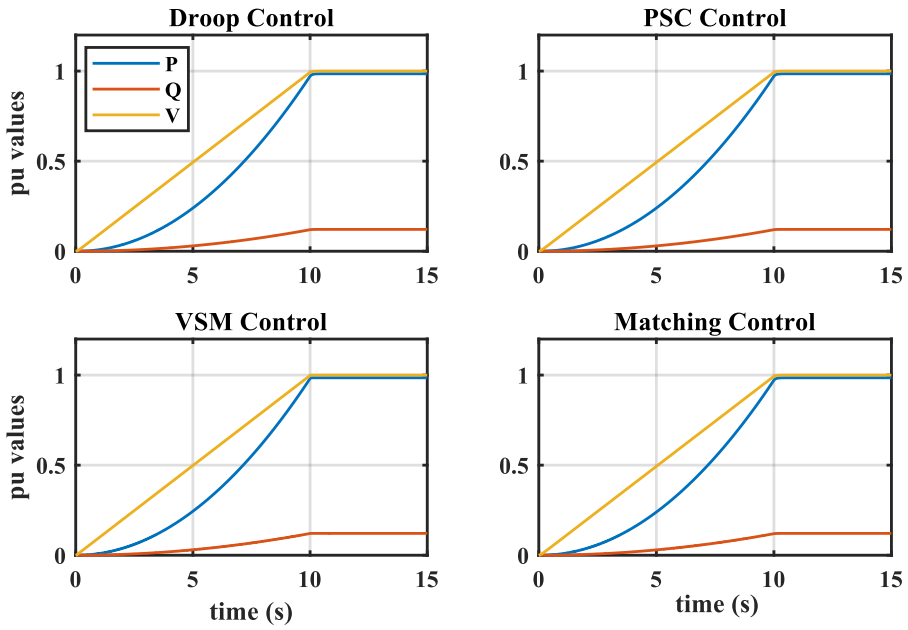

Figure 5.13: GFCs response to the islanded soft-start scenario.

Finally, the GFC frequency has also been recorded for all controllers during the voltage ramp-up. Since $P_{ref} \approx 1\,pu$, the frequency mismatch is initially 0.5 Hz due to the common used $\Delta\omega/\Delta P$ factor for the four controllers that results into 0.5 Hz against 1 pu reference power error. As both the voltage (and active power) ramp up, the power measurement increases gradually, leading to decreased ΔP that approach zero at $t = T_{ramp}$, thus leading to zero frequency error from this point onwards. This is illustrated in Figure 5.14, demonstrating the similar frequency response for the compared controllers. If load pickup is performed after the voltage ramp is concluded, then the frequency would have remained around $50.5\,Hz$ for the ramp duration since active power consumption is minimal, and then switched momentarily towards 50 Hz as block loads are connected. These two load connection models (simultaneous and separate load pickup) will be considered in the extended black-start scenarios in the coming chapters to present the different possibilities, while taking into account that utilities prefer that some load types are connected only after 1 pu voltage is established at the connection point [16].

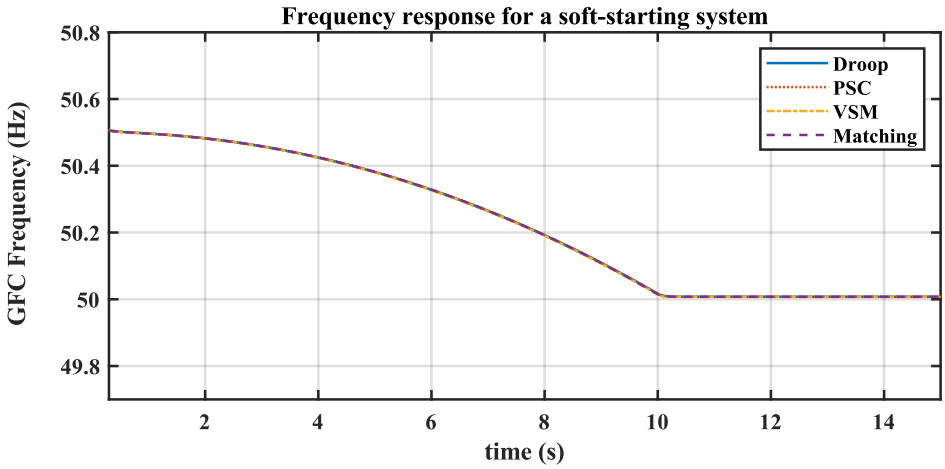

Figure 5.14: GFCs frequency response to soft-energization scenario with simultaneous load pickup.

5.4.3. GFC Controller Selection

The comparison between droop, PSC, matching and VSM grid-forming controllers demonstrated that the four techniques performed well against common disturbances in grid-connected mode, while complying to main grid-connection requirements related to voltage, RoCoF and the other measured parameters. The four controllers also performed in a nearly identical fashion when tested for islanded soft energization compatibility.

Given the performance similarity, the selection of any presented controller should in principle provide adequate performance for black-start. That said, it is decided to select VSM control for the extended tests reported in this thesis. This is because, in addition to its demonstrated capabilities, VSM possesses direct similarities to synchronous generators with relatable parameters to physical quantities that are familiar to many network operators, namely, the virtual inertia constant J, and virtual damping D_p that have direct analogy to conventional SGs. The steady-state slope tuning in equation (5.18) for VSM did not include the inertia constant J, which effectively adds a tuning degree of freedom to the control that impacts the inertial frequency response while maintaining the required power-frequency slope to its design value.

To demonstrate the impact of virtual inertia and damping factors on the control performance, an additional simulation is carried out for the same network used in this case study with a 0.5 pu load disturbance at the PCC in the grid-connected mode. A total of eight simulations are performed with VSM, maintaining all parameters to their base values

while only varying J in the first four simulations, and D_p in the remaining four, using the following per-unit values with respect to the main case: $[0.5, 1, 2, 5]$, where $J_{base} = 810.5$, and $D_{p_{base}} = 40{,}528$. The results are recorded for active power and frequency waveforms. Figure 5.15 shows the variation impact on f, whereas Figure 5.16 shows the variation impact on P.

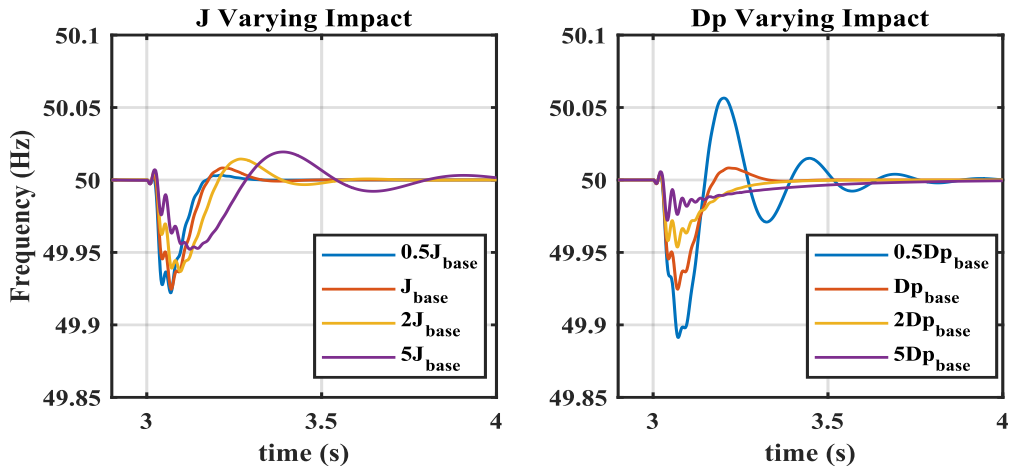

Figure 5.15: Impact of varying virtual inertia and damping constants on VSM frequency response against load disturbance.

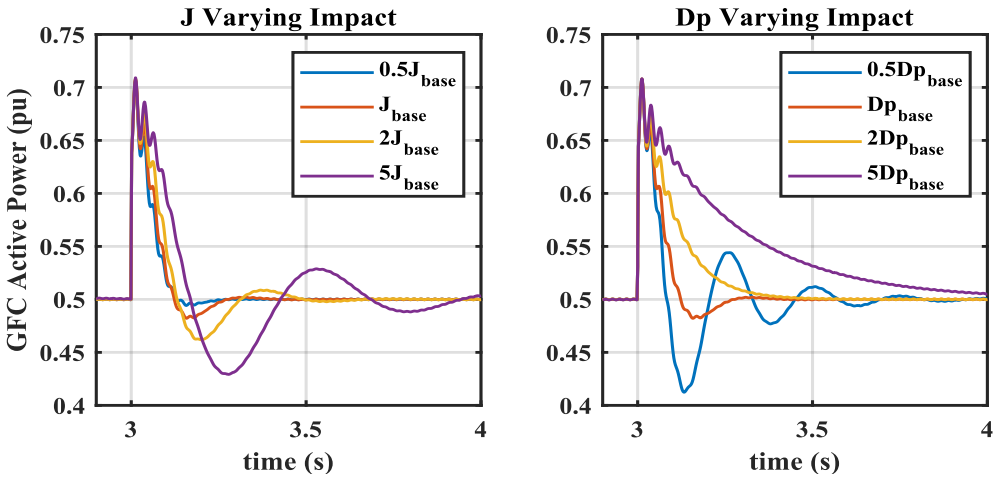

Figure 5.16: Impact of varying virtual inertia and damping constants on VSM active power response against load disturbance.

Increasing the inertia constant J is observed to improve the frequency nadir response (i.e., reducing the frequency disturbance magnitude), while increasing the settling time with higher magnitude oscillations. The oscillations are also reflected on the GFC output power

with similar oscillatory behavior. On the other hand, increasing the virtual damping is also observed to improve the frequency response nadir with less oscillations, however, with the tradeoff reflected on longer settling time than cases with lower D_p. Proper J tuning should be considered for optimized VSM frequency response. That is, synchronous generators have constant inertias that are related to their physical properties, whereas the virtual inertia tuning capability provides more operational flexibility for VSMs that can be utilized to improve the control performance.

5.5. Impact of GFC Inner Loops on Transformers Energization

The incorporation of inner voltage and current control loops in converters control is a common practice in industry for grid-following converters for protection considerations. This allows a limit to be imposed on current references in the synchronous frame (I_{dref} and I_{qref}), such that the output current is restricted to these values (see Figure 5.1). In grid-following converters, the voltage reference is obtained from a PLL, so limiting the current does not violate the voltage reference tracking as it is being 'followed' from an external source. However, if the current is limited in a grid-forming converter control in a similar fashion, and the current hits the set saturation limit, then the voltage source behavior of the converter is essentially violated during the current saturation period, resulting into irregular voltage waveform shape. Comprehensive analysis on this phenomenon is presented in [116], where the authors demonstrate the converter stability margin when current saturation takes place and propose variable voltage and current saturation limits as a remedy.

It has been established in Chapter 3 in the theoretical derived model that the transformer flux is dependent on the core voltage, where the voltage across the core is integrated to generate the flux. Thus, if current control is activated and the current is exceeding the set saturation limit, then the voltage as a result enters a temporary 'random-behavior' state that may generate irregular voltage values during this period. This, as a result, causes the flux behavior to change according to the voltage integral, and as a result, the transformer magnetizing current to change following the new dynamics.

This is illustrated through a series of simulations to compare hard energization of a transformer through a grid-forming converter with VSM control, first with disabled inner control loops, then with incorporated current control under different I_{dref} and I_{qref} saturation limits. The energized transformer is rated at 53 MVA $(\Delta - Y_g) - 11/33$ kV and energized from the Δ side, whereas the energizing GFC rating is 40 MVA. In all scenarios, the residual flux is set to $\phi_r = [0.8, 0, -0.8]$ pu, and the energization takes place at $\alpha = -30°$ with respect to the source voltage. This angle is selected to induce a high magnitude inrush currents. It should be noted that the average VSC model from MATLAB/Simulink library is used for these preliminary simulations (i.e., without considering modulation-index, input DC voltage … etc) to demonstrate generic trends.

In the first example, the inner loops are disabled. The circuit breaker connecting the GFC with VSM control to the transformer is closed at $t = 38.3\ ms$ to comply with the selected α. The peak recorded voltage does not significantly exceed 1 pu and is recorded at the transformer's phase A with an amplitude of 1.14 pu.

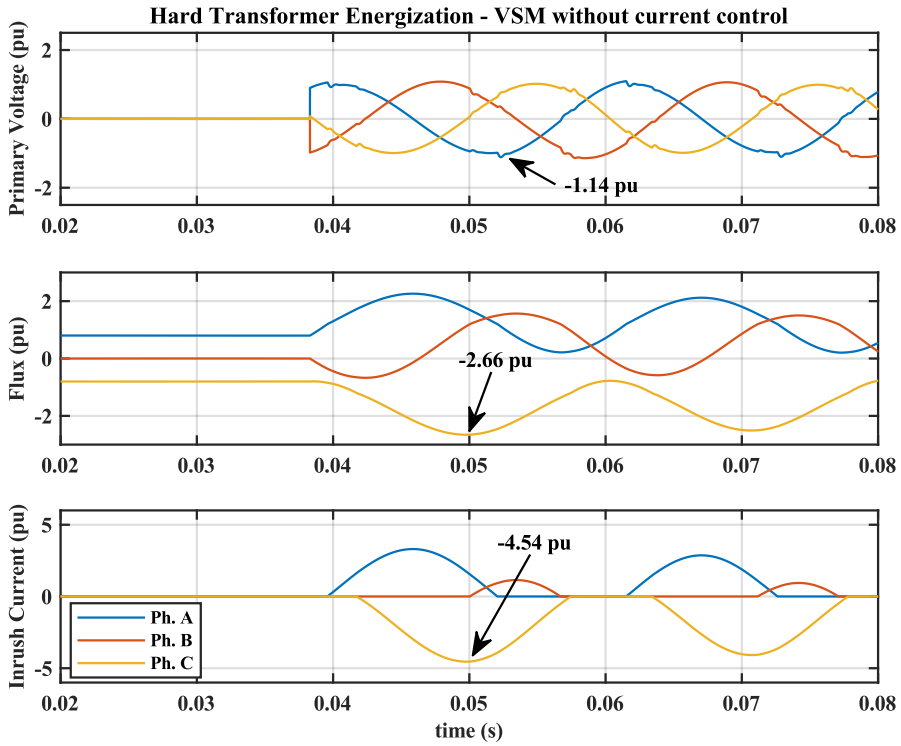

Figure 5.17: Transformer energization through VSM control, without inner current control.

As expected, the peak flux reaches high values that peak at an amplitude of 2.66 pu. This contributes to very high inrush current in the corresponding transformer phase, with a 4.54 pu amplitude. Figure 5.17 demonstrates the energization results for this scenario, with highlighted peaks for each waveform. The observations here follow the expected energization behavior reported in Chapter 3, since the source voltage mostly maintains its shape.

In the second scenario, current control is activated, and saturation limits are set such that $I_{drefsat} = 1\,pu$ and $I_{qrefsat} = 1\,pu$, with respect to the converter 40 MVA rating. The same procedure is repeated, and the results are presented in Figure 5.18. In this case, the voltage waveforms are highly distorted once the current limits are violated and the current hits its saturation limit. The voltage in phase A of the transformer exceeds 2 pu in amplitude, signifying a voltage limit violation. On the other hand, it is also observed that integrating these voltage waveforms results into reduced peak flux and consequently, reduced inrush current. Compared to the previous case, phase C flux peak reduces from

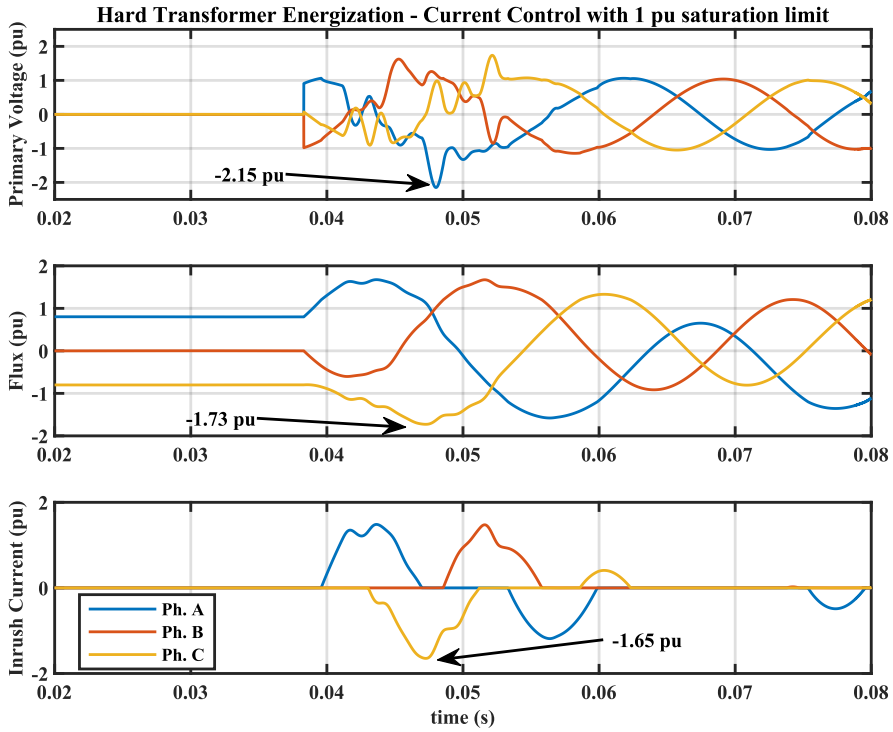

Figure 5.18: Transformer energization through VSM control, with activated current control set to 1 pu in both d and q axes.

2.66 pu to 1.73 pu, leading to significantly reduced inrush current peak. The irregularity in voltage waveform in this case is observed to last for nearly one cycle ($\approx 0.02\ s$).

Current control is similarly activated in the final scenario, but this time with reduced saturation limits to $I_{drefsat} = 0.5\ pu$ and $I_{qrefsat} = 0.5\ pu$. The results are summarized in Figure 5.19, where a similar distorted behavior is also observed. However, some differences can be noted here compared to Figure 5.18, namely, the distortion lasts for longer ($\approx 27\ ms$), with further reduced flux peak and inrush current. In this example, the peak inrush current is pushed back below 1 pu, at the expense of a temporary voltage violation that peaks around 2 pu. The observed trends indicate that reducing the inner loops reference current saturation limits may contribute to limiting the inrush current, and that the stricter the limit, the more is the perceived peak inrush current reduction. Results are presented based on MATLAB/Simulink simulations, and the same trends are also observed in RSCAD/RTDS real-time simulator.

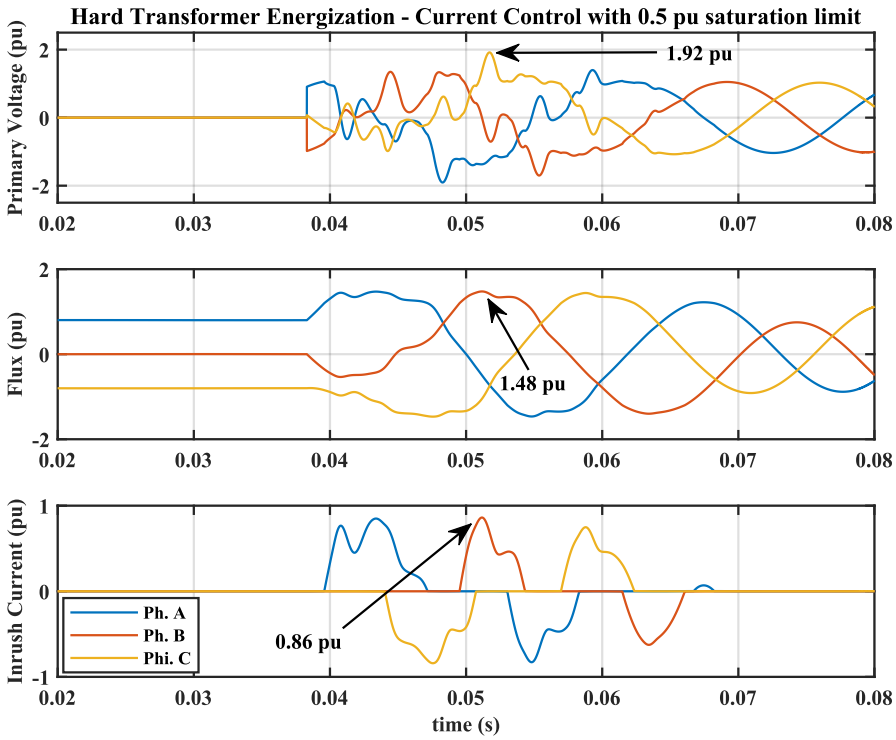

Figure 5.19: Transformer energization through VSM control, with activated current control set to 0.5 pu in both d and q axes.

This section has been incorporated into the thesis to present the current control reference limiting as a potential new technique for transformers inrush current mitigation through GFCs. For instance, a possible investigation route may consider a temporary reduction in the current reference saturation limit during the initial network energization phase, before reverting the limits back to their nominal values during normal operation. Though, further analysis is recommended to quantify the voltage distortions impact, consider detailed VSC models, confirm the observed trends consistency under different energization cases, and to identify possible mitigation strategies that could minimize the perceived voltage limit violations. Finally, another interesting observation in relation to current control incorporation in grid-forming control is that it could lead to accelerated T_{ramp} convergence to the desired limits when combined with the proposed SE ramp-rate estimation framework in Chapter 4.

5.6. Summary

This chapter presented a comprehensive overview of grid-forming converter control techniques, their principle of operation, and their key characteristics. Four common grid-forming controllers were analyzed, namely: droop, power synchronizing control (PSC), matching control, and virtual synchronous machine (VSM). The control techniques performance has been tested in both grid-connected and islanded modes of operation with the aim of identifying the most suitable techniques for black-start and relevant ancillary services provision.

- The controllers were configured similarly in terms of inner loops tuning, AC droop slope and DC voltage control.
- It has been observed that all the compared technique performed well against an array of applied disturbances in load, converter power and DC voltage references, with acceptable deviations in the observed parameters such as frequency, RoCoF and active/reactive power.
- The four controllers' ability to track a ramping voltage reference has also been validated to assess their soft energization compatibility, and all of them were able to smoothly follow the reference.

- VSM has been selected for the remaining analysis in this thesis due to its good performance, as well as the direct correlation between its parameters and conventional synchronous generators, in addition to the possibility to tune its inertia constant *J*.
- The impact of varying VSM's virtual damping and inertia constants (D_p and J) has also been investigated, showing lower frequency deviation at increased inertia constant values.

Then, the impact of the incorporated inner voltage and current control loops on VSM performance for transformer energization has been investigated. The preliminary tests reveal a perceived influence of the synchronous-frame current reference limits on the inrush current amplitude, and the converter voltage. This behavior is recommended for further investigation to identify the possibility of harnessing the current reduction advantage, with minimized voltage distortions. In addition to investigating the impact of distortions propagation when energizing multiple transformers.

In the next chapter, an investigation on VSM required modifications for a complete black-start scenario implementation is carried out. The black-start scenario is characterized here by the converter ability to perform the following tasks: Network energization, load pickup and grid synchronization.

Chapter 6 Modified VSM Control for Black-Start and Grid Synchronization Applications

This chapter investigates and proposes modifications to the classical VSM control to achieve the requirements of black-start and grid synchronization applications. The ramping voltage reference tracking capability has been validated for VSM in Chapter 5. Practically, once the voltage is established following a ramping or a steady voltage reference, additional load pickup is performed within the island (for loads that are not simultaneously energized through the voltage ramp). This load connection can be in a successive manner to mitigate voltage disturbances at the point-of-common-coupling (PCC). Though, connecting large loads behind an impedance may lead to measurable voltage drop at the PCC. A VSM voltage loop modification is thus proposed in this chapter to tackle this issue. On the other hand, synchronizing to neighboring AC islands or the main grid is an important step to consider in a black-start sequence. This aspect is also investigated by proposing a modified VSM power loop.

Two main modifications to the classical VSM presented in Chapter 5 are thus considered here, which are PCC voltage control capability in islanded mode, in addition to a control-based grid-synchronization technique. The next sections cover the following aspects:

- Proposing a modified VSM grid-forming control for black-start applications with soft black-start, voltage control and improved power synchronization capabilities.
- Presenting a complete black-start sequence based on the modified controller, starting from transformer energization, load pickup to grid synchronization to demonstrate and validate the control effectiveness.

6.1. Modified VSM Voltage Control Loop

The system configuration for a black-start a network relies on several factor such as the number of compatible present DERs and circuits routing. In this investigation, it is assumed that a single GFC is connected to an energizing DER, in a configuration similar to that used for grid-forming techniques evaluation in Chapter 5 (illustrated in Figure 5.7). The test converter 40 MVA rating is maintained for the tests carried out in this chapter.

The voltage between the GFC and grid-connection point (PCC) may experience a drop in island mode due to the impedance existing between both terminals. The extent of this drop is dependent on the electrical distance, as well as the normalized cable impedance, transformers, and the level of loading at the PCC. That is, under no-load or light-loading conditions, the voltage drop is commonly negligible. However, if load pickup takes place at the PCC, then more significant voltage drops and reactive power supply by the converter are expected.

If load supply is planned for prolonged period in island mode prior to grid synchronization with other network segments as part of the black-start procedure, then the objective should be for an adequate voltage levels at the connection point to be maintained. On-Load Tap Changer (OLTC), when present [117, 118] can mitigate this issue. Another option investigated here is to incorporate a PCC voltage correction loop within the VSM to ensure the voltage compliance with grid code. That is, VSM voltage loop can be modified to accommodate a correction factor for PCC voltage through integrating an additional control path with a PI compensator. This concept is presented in Figure 6.1, highlighting that the additional PI path can be activated only when required (e.g., if the steady-state voltage drop is significant, for instance, exceeding 5%), and mainly in island mode.

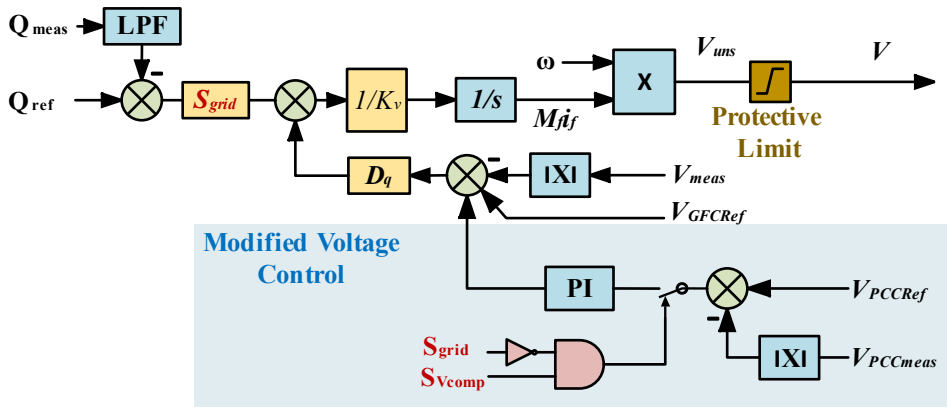

Figure 6.1: Modified VSM voltage loop for PCC voltage compensation in island mode.

This is achieved by $S_{V_{comp}}$ *and* S_{grid} switching logic and is combined with simultaneous PI control reset to avoid uncontrolled behavior after disconnection. Equation (6.1) illustrates the mathematical expression for the modified VSM voltage loop unsaturated

output. Saturation is added here to provide an upper limit on the GFC voltage compensation as illustrated in (6.2).

$$V_{uns} = \frac{\omega}{sK_v}\left(D_q\left(\Delta|V_{GFC}| + S_{V_{comp}}\Delta|V_{PCC}|\left(K_{p_{pcc}} + \frac{K_{i_{pcc}}}{s}\right)\right) + S_{grid}\Delta Q\right) \tag{6.1}$$

$$V = \begin{cases} V_{sat} & : \quad V_{uns} \geq V_{sat} \\ V_{uns} & : \quad V_{uns} < V_{sat} \end{cases} \tag{6.2}$$

The saturation is added for two purposes: First, to protect the converter from steady-state overvoltage that may violate its protection limits. Second, to avoid overvoltages that may exceed knee-point of connected transformers, leading to a high steady-state magnetizing current. If a significant voltage drop exists in the network due to excessive loading or long, lossy, cables, then VSM voltage compensation may still be provided, but up to a limit that does not violate these two constraints (converter and transformer limits). Assuming a voltage reference saturation limit of 1.1 pu, the impact of reference saturation on PCC voltage is demonstrated in the following example.

6.1.1. Voltage Reference Saturation Impact

In this scenario, a 30 km $\pi - section$ line is added between the transformer and PCC in Figure 5.7. The line in Table 4.1 is modified to represent a sensitivity case with degraded cable parameters. Namely, the resistive impedance is multiplied by 2.5 and the inductive impedance is tripled to simulate higher voltage drop at the PCC. An active load is connected at the PCC with 0.5 pu power. Figure 6.2 shows a comparison of GFC output reactive power and PCC voltage between two cases (i.e., with and without the 1.1 pu voltage reference limit). Compensation is activated at $t = 2.5\ s$. When the voltage limit is not applied, the voltage compensation control pushes the PCC voltage from 0.867 pu to 1 pu. This leads to a consequent increase in reactive power supply from 0.19 pu to 0.253 pu. On the other hand, activating the VSM reference voltage saturation, restricts the PCC voltage to around 0.95 pu as the GFC voltage peaks at 1.1 pu, leading to reduced reactive power supply of 0.23 pu. The VSM reference saturation can refer to the inner GFC terminal voltage (when no current control is activated), or to the converter low-pass filter

capacitor voltage when inner loops are activated. Inner control loops are also incorporated in the reported tests in this chapter.

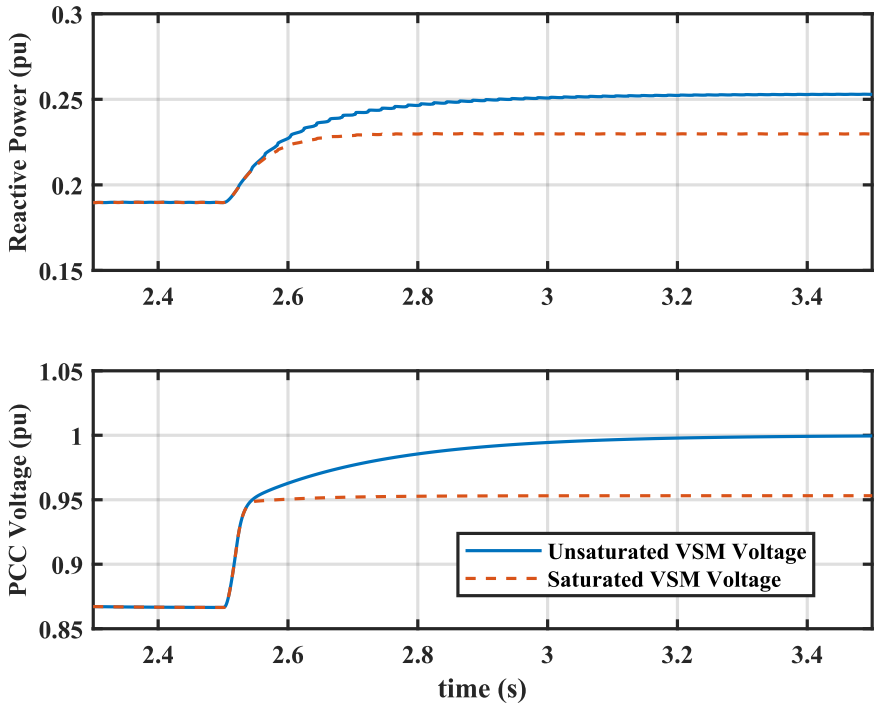

Figure 6.2: Impact of VSM voltage reference saturation on the converter reactive power supply and the PCC voltage compensation ($V_{sat} = 1.1$ pu). Compensation is activated at $t = 2.5$ s.

Finally, some severe voltage drop cases may result in voltage levels below those accepted by the adopted grid code even after compensation with saturated voltage reference. In such scenarios, additional equipment should be considered such as VAR compensators.

6.1.2. PCC Voltage Compensation Test

The test presented here also uses the same network in Figure 5.7 with 30 km $\pi - section$ line. The line parameters are modified here to reflect lower line voltage drops at the PCC in this case, such that the drop can be fully compensated to 1 pu using the PCC voltage controller (i.e., 2.5 the resistive impedance and 1.5 the inductive impedance reported in Table 4.1). The full scenario results are presented in Figure 6.3 for P, Q, S and the RMS voltages at the GFC output and PCC points. The active 0.5 pu load is connected at the PCC at $t = 2\ s$. This leads to an increase in GFC power output, that falls short of the rated

load power due to the reduced voltage at the PCC (0.94 pu). The GFC voltage is inherently controlled by the VSM voltage loop, and thus it is maintained close to 1 pu through injecting additional reactive power. Then, at $t = 2.5\ s$, the PCC voltage compensation path is activated in the VSM voltage loop, leading the PCC voltage to be driven to 1 pu, and the active power to be around the target $0.5\ pu$ (plus resistive line and transformer losses). The PCC voltage compensation drives the GFC voltage to a higher level, but below the 1.1 pu threshold. Since this threshold is not violated, the PCC voltage is able to be compensated to 1 pu, unlike the case in Figure 6.2.

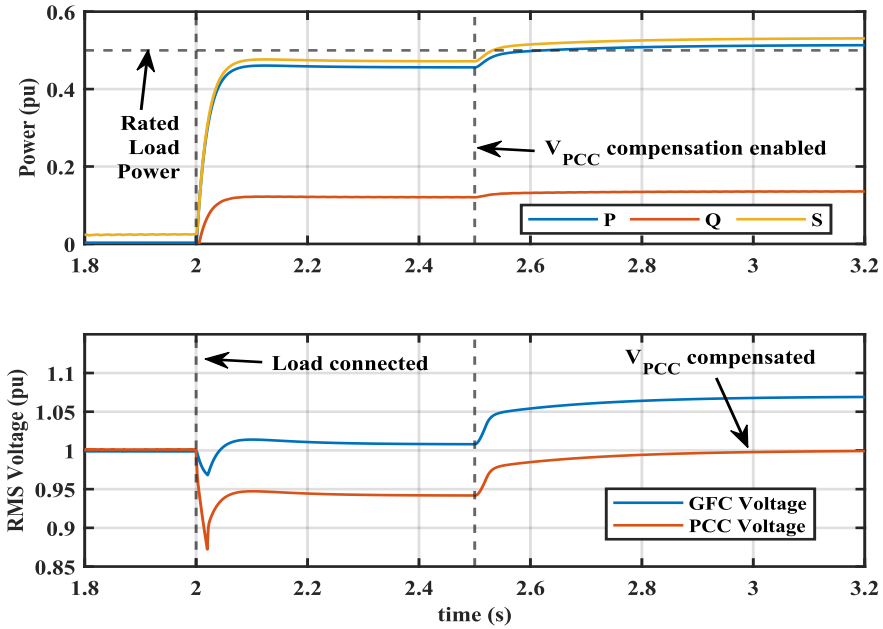

Figure 6.3: Modified VSM with PCC voltage compensation – test case results with impact on P,Q,S and voltage across the converter output and PCC.

The additional reactive power consumption noticed here is minimal. This consumption depends on the line reactive impedance and the compensation required to overcome its voltage drop impact and drive the PCC voltage to 1 pu. Overall, the presented case shows the effectiveness of this compensation techniques to partially or fully correct voltage deviations at the PCC, while maintaining transformer and converter limits.

6.1.3. Thevenin's based PCC Voltage Estimation Technique

The use of the proposed modified VSM voltage control loop with direct PCC voltage measurement is subject to the availability of such measurement, which may be limited in cases where the converter and PCC are distant (e.g., the presented example uses a 30 km line). High-speed fiber cables or communication systems with minimal latency may be utilized to provide such measurement but may not always be available. Alternatively, a method is proposed here for PCC voltage estimation in real-time based on local measurements at the converter terminal, in addition to knowledge of the distribution circuit topology between the GFC and the PCC (such as transformer and cable parameters … etc). Such information is assumed to be available for many Distribution System Operators (DSOs). The idea is to calculate the GFC network Thevenin's circuit as seen from the PCC when such calculation is feasible by the network topology, and to estimate the voltage from this equivalent circuit. Considering the test network in Figure 5.7 as an example, then the network circuit can be simplified on a per-phase basis as illustrated in Figure 6.4, consisting of the LC filter, transformer and $\pi-$ section. Theoretically, the PCC open circuit terminal is termed as the Thevenin's voltage v_{Th}, and is found as $19.28\ kV_{rms}$, considering the case with inner VSM control loops integration.

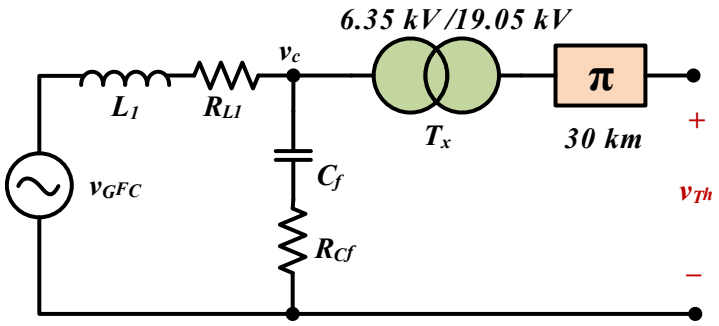

Figure 6.4: Per-phase simplified circuit of the test network.

The Thevenin impedance Z_{Th} is calculated from the PCC terminals after shorting the equivalent voltage source that represent the converter as shown in Figure 6.5. The nominal transformer magnetizing inductance should be used (linear region operation).

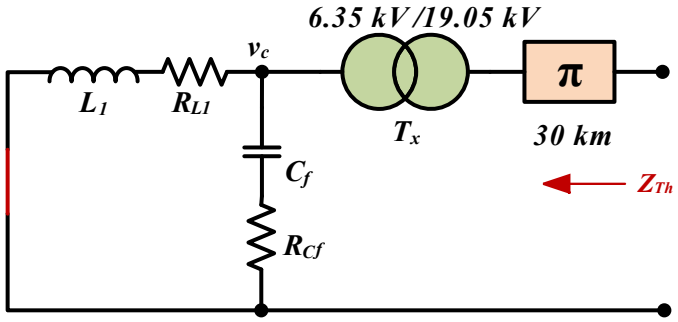

Figure 6.5: Per-Phase Thevenin impedance estimation circuit.

For the case presented in section 6.1.2. , the Thevenin impedance is calculated for the single-phase equivalent circuit using MATLAB/Simulink impedance measurement feature at 50 Hz, and found to be $Z_{Th} = 1.176 + j17.865$. The breakdown of this impedance is expressed in (6.3).

$$Z_{Th} = R_{Th} + jX_{Th} \tag{6.3}$$

The next step is to build the Thevenin's circuit using the obtained voltage and impedance.

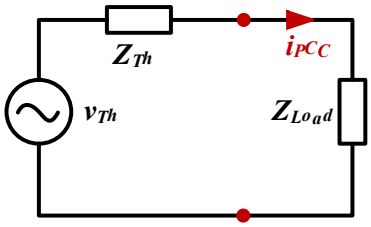

Figure 6.6: Thevenin's equivalent circuit of the test network (per-phase).

Here, i_{PCC} can be approximated through multiplying converter output current by inverse transformer turns ratio (Tx_{ratio}), with similar analogy to v_{Th} from v_{GFC} as below.

$$i_{PCC} \approx \frac{i_{L1}}{Tx_{ratio}} \tag{6.4}$$

$$v_{Th} \approx v_{GFC}\, Tx_{ratio} \tag{6.5}$$

Then, applying KVL to the circuit in Figure 6.6 yields the following for v_{PCC} estimation.

$$v_{PCC} = v_{Th} - i_{pcc}(R_{Th} + jX_{Th}) \tag{6.6}$$

In the modified VSM voltage loop, the PCC voltage compensation requires estimating the voltage amplitude, which can be extracted from (6.6).

Equations (6.4)-(6.5) are specific the test network in Figure 5.7, whereas equation (6.6) is generic and can be applied to different topologies as it is based on the Thevenin's equivalent voltage and impedance. Finally, the implemented PCC voltage estimation technique in the control loop for the present test network is illustrated in Figure 6.7.

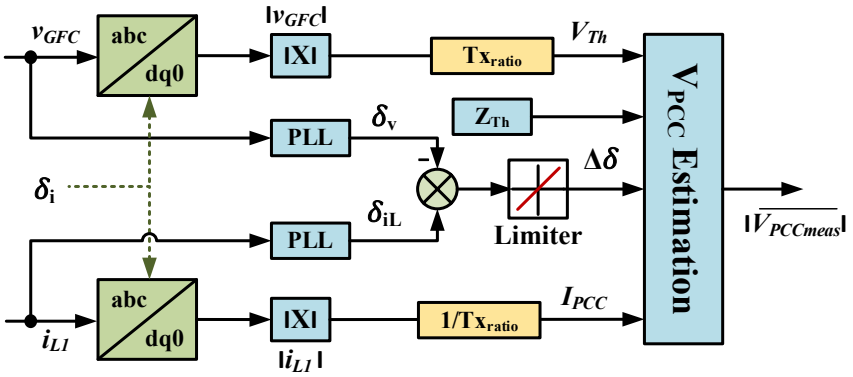

Figure 6.7: PCC voltage estimation algorithm based on Thevenin's circuit.

Synchronous reference frame transformations are used to extract the signals amplitude instead of RMS because of the averaged and delayed nature of the latter. PLLs are used to extract the phase angle of voltage and current, which are subtracted to obtain the impedance phase angle. The phase angle difference $\Delta\delta$ is passed through a rate-limiter to suppress the impact of PLL output fluctuating between 0 and 2π each period. The V_{PCC} estimation block calculates the voltage amplitude based on equation (6.6) from the provided inputs.

An important merit for the proposed technique is that it can be agnostic to the load impedance, which may be variable by nature following different consumption patterns. Instead, the estimation relies only on the fixed impedance between the source and the PCC. Finally, the mathematical impedance representation should be adjusted to accommodate variations in the network topology, such as the inclusion of multiple transformers.

The PCC voltage estimation technique for the islanded operation mode has been validated using the same test scenario presented in Figure 6.3. Similar to that case, the compensation

is enabled at $t = 2.5\,s$, this time using the Thevenin circuit-based technique. As demonstrated in Figure 6.8, the PCC voltage is compensated to 1 pu in a nearly identical fashion to that obtained through direct voltage measurement, showcasing the effectiveness of this estimation when accurate impedance data of the connected network between the energizing converter and the PCC is available.

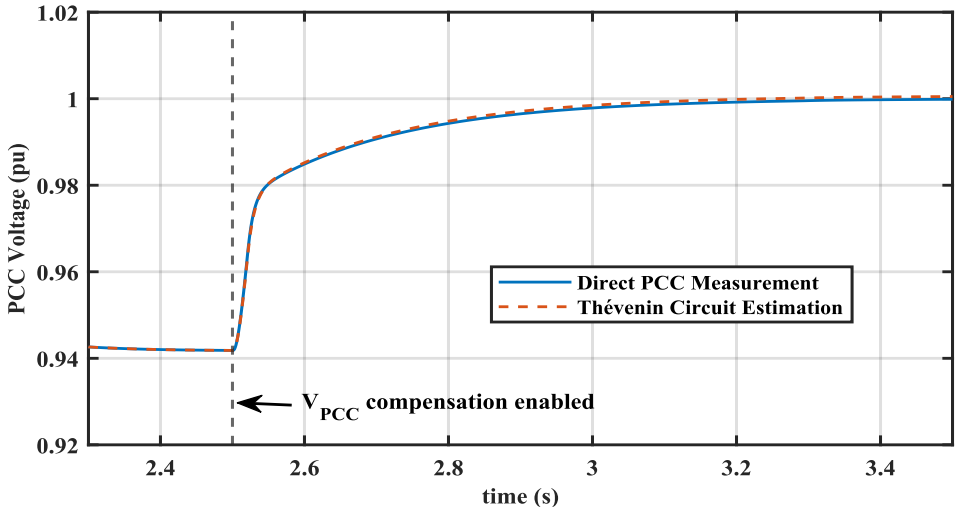

Figure 6.8: Validation of the Thevenin-based PCC voltage estimation technique.

6.2. Modified VSM Synchronization Control

Synchronizing the restored system island is also an important black-start step to group different neighboring electrical islands and/or to achieve synchronized operation with the main grid. This requires matching the phase sequence, amplitude $|V|$, frequency (f), and phase angle (δ) between the synchronized voltages prior to closing circuit breakers [119]. Phase-angle matching can be implemented through setting a reference frequency that is slightly above or below the grid frequency, which creates a phase drift between both voltage phases in a specific direction, leading to eventual crossing between the phases, at which point the sync relays close the circuit breakers. However, this technique is classically prone to delays and mismatches that may lead to measurable variations at the closing instant [120]. Instead, an additional modification is proposed in this chapter for VSM, whereby the outer power loop reference can be adjusted to sync with the grid voltage angle and maintain zero error, thus mitigating the potential mismatch impact. The

literature is constantly updated with new research articles to propose modified GFCs grid synchronization techniques, particularly for voltage angle and frequency, aiming to achieve improved performance [121, 122].

Practically, if synchronizing requirements in terms of voltage amplitude, frequency and phase are not satisfied and two voltage sources are connected at random points, then large spikes in voltage and current could occur. The worst possible scenario is to synchronize two sources that are 180 degrees out of sync. Equation (6.7) mathematically summarizes the synchronization requirements to close the synchronizing circuit breaker CB_{sync} for the three key parameters.

$$CB_{sync} = \begin{cases} 1 \Leftrightarrow & \begin{matrix} |V_{grid}| - \Delta|V| \leq |V_{PCC}| \leq |V_{grid}| + \Delta|V| \\ f_g - \Delta f \leq f_{PCC} \leq f_g + \Delta f \\ \delta_g - \Delta\delta \leq \delta_{pcc} \leq \delta_g + \Delta\delta \end{matrix} \end{cases} \tag{6.7}$$

where the subscript g is used to denote grid parameters. Synchronization tolerances vary by the adopted grid code and the rating of synchronized sources. For instance, the IEEE standard described in [92] requires that an islanded system is re-synchronized after achieving certain frequency, voltage and phase angle requirements. Table 6.1 summarizes these requirements for distribution networks up to 10 MVA. It is thus logical to assume that larger converters require tighter tolerances to achieve a smooth transition.

Table 6.1: IEEE Grid synchronization requirements in distribution systems.

DER Rating	**Δf (Hz)**	**$\Delta\|V\|$ (%)**	**$\Delta\delta°$**
0 – 500 kVA	0.3	10	20
>500 – 1500 kVA	0.2	5	15
>1500 – 10000 kVA	0.1	3	10

Synchronizing of power converters to the grid is classically achieved in the grid-following operating mode through tracking the grid PLL output. In grid-forming control (including VSM), voltage is established independently, and the phase angle is the output of power-frequency loop. It has been shown earlier that the power loop error influences the converter frequency, and consequently, its angle (see Figure 5.14). VSM power reference

manipulation may thus be used as a synchronization technique that controls the converter output phase. The proposed $P-f$ loop modification can either drive the power loop angle directly [122], or adjust the converter power reference [123]. The latter configuration is used here. This is because preliminary simulations have shown that the direct angle adjustment option may require a continuously changing PI controller output as the power reference error input is typically a non-zero value. A non-zero input to the angle integrator causes the voltage angle to be in consistent looping, which leads to a moving angle that needs to be countered continuously by the controller, potentially leading to controller overflow or sudden output jumps if not accounted for properly.

6.2.1. Mathematical formulation

In terms of the required inputs to the modified synchronization controller, then the grid and PCC voltage angles δ_g and δ_{PCC} can be extracted from voltage signals using PLLs as shown in Figure 6.7. Since synchronization takes place at the PCC, the grid and PCC voltage measurements are required to operate the modified controller, or at least, the error signal between the synchronizing voltage phase angles, which can be measured locally using a relay and transmitted to the converter control. Measurements from the closing relay side can be monitored by the operator to validate the phase error elimination before sending the synchronizing breaker closing command.

The aim is to drive the phase difference between both angles ($\Delta\delta_{g\_pcc}$) to zero through a controller that outputs a temporary VSM power reference adjustment in island mode. Mathematically, the VSM power loop equation is modified to include a temporary power term P_{sync} that is only activated when synchronization is required to influence δ_i and match it to the grid angle, resulting in (6.8).

$$J\frac{d\omega}{dt}=\frac{1}{\omega_{ref}}(P_{ref}-P+S_{sync}P_{sync})+D_p(\omega_{ref}-\omega) \tag{6.8}$$

The switching variable S_{sync} is set to 1 only when synchronizing sequence is initiated and remains as 0 otherwise. The synchronizing power P_{sync} is the output of synchronizing control between the restored island and the grid to drive voltage angle and frequency

difference to zero. Proportional-Integral (PI) control is used here to achieve this task as shown in equation (6.9).

$$P_{sync} = G_P \frac{\Delta\delta_{g\_pcc}}{2\pi}\left(k_{psync} + \frac{k_{isync}}{s}\right) \tag{6.9}$$

$\Delta\delta_{g\_pcc}$ is the angle difference between the grid voltage angle δ_g and the PCC voltage angle δ_{pcc}. Depending on the power control unit (e.g., in watts or mega-watts), the value of G_P can be set to 1 in the former case or 10^6 in the latter to limit the controller gains and facilitate the tuning task. Figure 6.9 illustrates the modified VSM power loop, showing P_{sync} estimation steps.

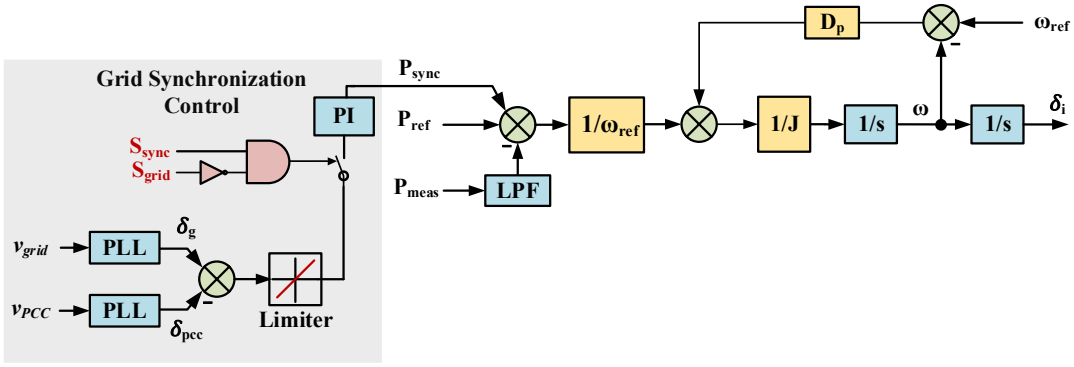

Figure 6.9: Modified VSM power loop for grid-synchronization.

Deploying a PI integrator reset when the synchronizing control is activated is recommended. K_{psync} may also be defined as a ramping value, starting from 0 at the activation time to a design specific steady-state value in a time period T_{sync}. This is to avoid sudden jumps in P_{sync} to excessive values. The PI output may also be limited to the rated converter power value, to avoid the impact of $P_{sync} + P_{ref}$ exceeding the converter rating and leading to higher frequency deviations than the design range.

When a PLL is used to extract phase angles, the output in many software tools (e.g., MATLAB/Simulink, PSCAD/EMTDC and RSCAD/RTDS) is typically wrapped between 0 and 2π, this means that the comparator between the grid and PCC voltage can have an output angle that varies between -2π and 2π, depending on which signal is leading. To avoid that, a rate limiter is added (as in the modified voltage loop before) to extract the

average angle difference value and avoid violent variations that may negatively impact the control performance. A rate limiter manipulates the input signal by restricting the output rate of change whenever the input exceeds a particular rising or falling slew rate *(du/dt).* This is mathematically expressed in equation (6.10), where y is the output, u is the input, and SR_r and SR_f represent the maximum rising and falling slew rates, respectively.

$$y(t) = \begin{cases} T_s\, SR_R + y(t - T_s) & : \frac{du}{dt} \geq SR_r \\ u(t) & : SR_f < \frac{du}{dt} < SR_r \\ T_s\, SR_f + y(t - T_s) & : \frac{du}{dt} \leq SR_f \end{cases} \tag{6.10}$$

where T_s refers to the model step-time. The rising slew rates are set for the angle comparator here as 10 and -10, respectively. The impact of implementing the rate limited is graphically expressed in Figure 6.10.

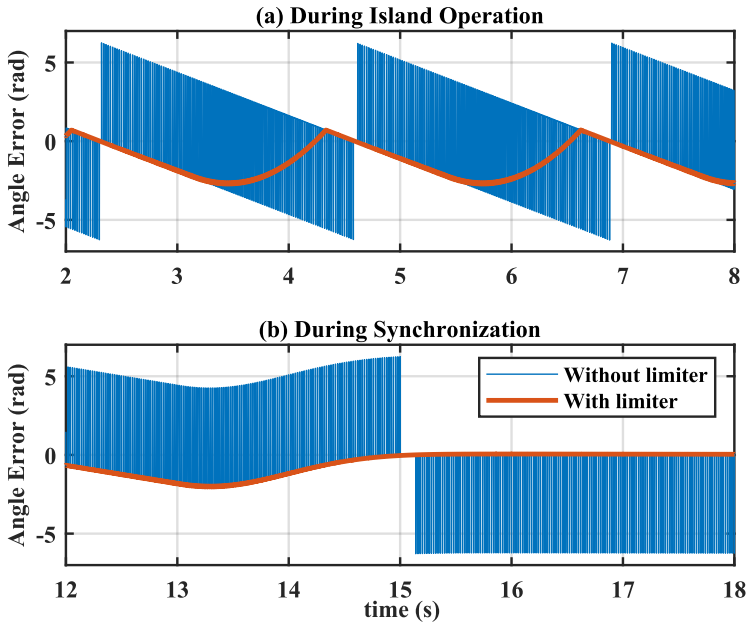

Figure 6.10: Rate limiter impact on angle error (synchronization control input).

It is observed from this figure that using the rate limiter produces smoother angle difference signal and captures the trends of the unfiltered angle error, without experiencing significant delays, whether in cases where the angle difference is fluctuating or when it is around zero

near the synchronization point. Though, it should be noted that using very small slew rates may lead to such delays, whereas using very large rates on the other hand leads to the output converging to the input. Thus, it is recommended to use an intermediate rate in a similar fashion to the one selected in this analysis.

6.2.2. Synchronizing Control Testing

The proposed synchronizing control is tested in this subsection to validate its operation. Given the higher power rating of the tested converter (40 MVA) compared to the ratings reported in Table 6.1, stricter voltage synchronization requirements are adopted. Namely: $\Delta f < 0.1\ Hz$, $\Delta|V|$ (%) < 1%, and $\Delta\delta < 5°$ at the PCC. The synchronizing PI control gains are set to $k_{psync} = 0 \rightarrow 1000\ in\ 2\ seconds$, $k_{isync} = 1000$, while $G_P = 1x10^6$. The proportional gain is set as a ramp to limit the first peak overshoot. The high PI gains are used to accelerate the synchronization for improved visualization of the different stages. In practice, relaxed synchronization gains can be used since the control settling time is not a priority. Figure 6.11 illustrates the synchronizing control simulation results. In this test, the synchronizing control activation signal is received at $t = 4\ s$, but the control is not activated until the next angle error zero crossing. Although this step is not mandatory, it helps minimizing the synchronizing power overshoot. The power reference is set to 20 MW (0.5 pu), and no load is connected in the island mode. Thus, the power loop initially has an error that manifests itself into a continuously changing angle deviation between the converter output voltage and the grid voltage until synchronizing control is activated, as in Figure 6.11(a). Then, P_{sync} starts acting in a direction to push $\sum P$ in the VSM power loop to zero such that the phase output is constant. This requires that P_{sync} settles at -20 MW (-0.5 pu) since the connected load is zero, the closed-loop controller ensures that the steady-state P_{sync} is combined with the instant where the phase error is zero, as observed in Figure 6.11(b). This figure also shows snapshots of phase A grid and PCC voltages when receiving the synchronizing command, and the moment of grid synchronization at $t = 8\ s$. Thus, clearly showing the matching phase angle at the synchronization instant. The control impact on power and frequency is also demonstrated in Figure 6.12.

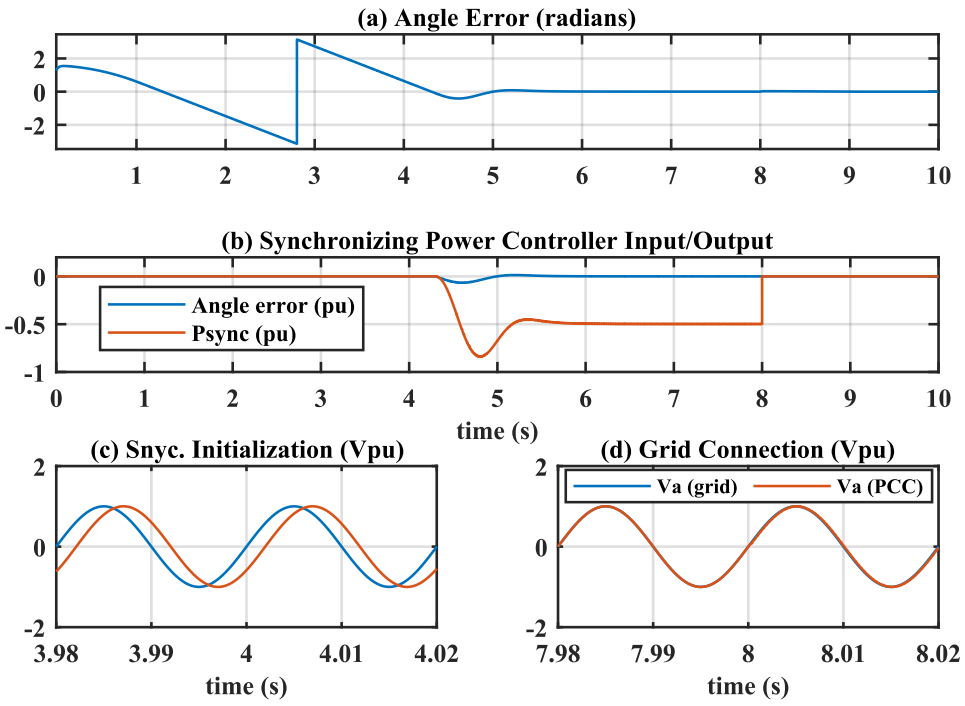

Figure 6.11: Synchronizing control testing: (a) angle error, (b) synchronizing PI control input/output, (c) phase difference at synchronization command point, (d) phase difference at synchronization.

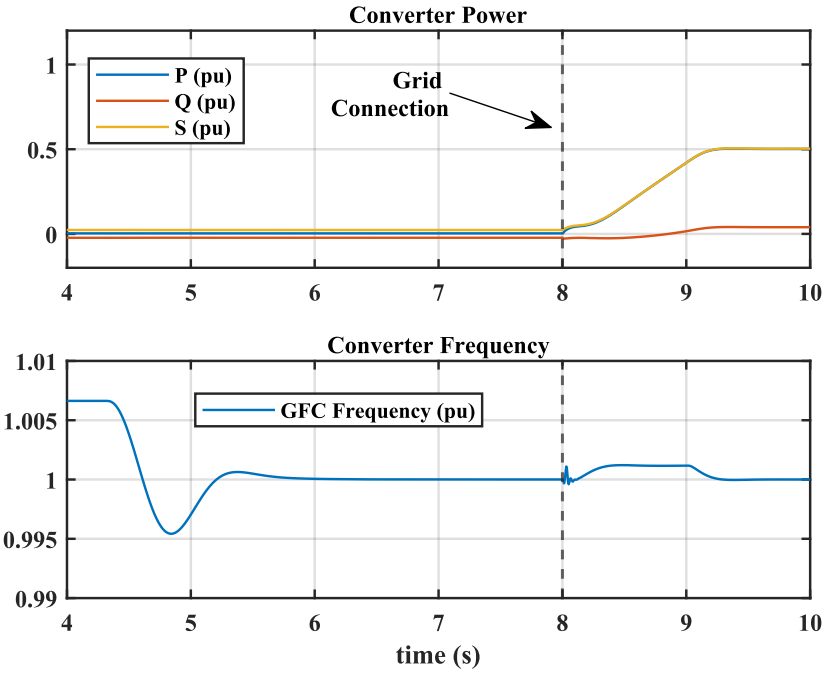

Figure 6.12: Synchronizing control testing: (a) smooth island-grid connected mode transition; (b) impact of synchronizing control on converter frequency).

P, Q and S remain mainly constant during the synchronization control action. On the other hand, the frequency is impacted by the power loop reference variation and follows a similar pattern to P_{sync} when the control is operational. The frequency goes back to 1 pu when P_{sync} settles at -0.5 pu, since no power deviation is feeding the frequency calculation in the VSM loop. Finally, when synchronization takes place at $t = 8\ s$, a smooth transition to grid-connected mode is observed with no observable power spikes. At $t = 8\ s$, the synchronizing control is disconnected, and the power reference is set to ramp up from zero to 20 MW (0.5 pu) over a period of one second. Thus, validating the modified power loop operation and showing a successful grid synchronization scenario while also maintaining grid-forming control operation.

6.3. Modified VSM: Combined Case Study

In this case study, a complete scenario is presented whereby the modified VSM control functionalities presented in this chapter are tested and validated. The combined modified VSM block diagram is illustrated in Figure 6.13, showcasing both $P - f$ and $Q - V$ control loops, and incorporating the soft energization through ramping voltage reference, PCC voltage support and grid-synchronization.

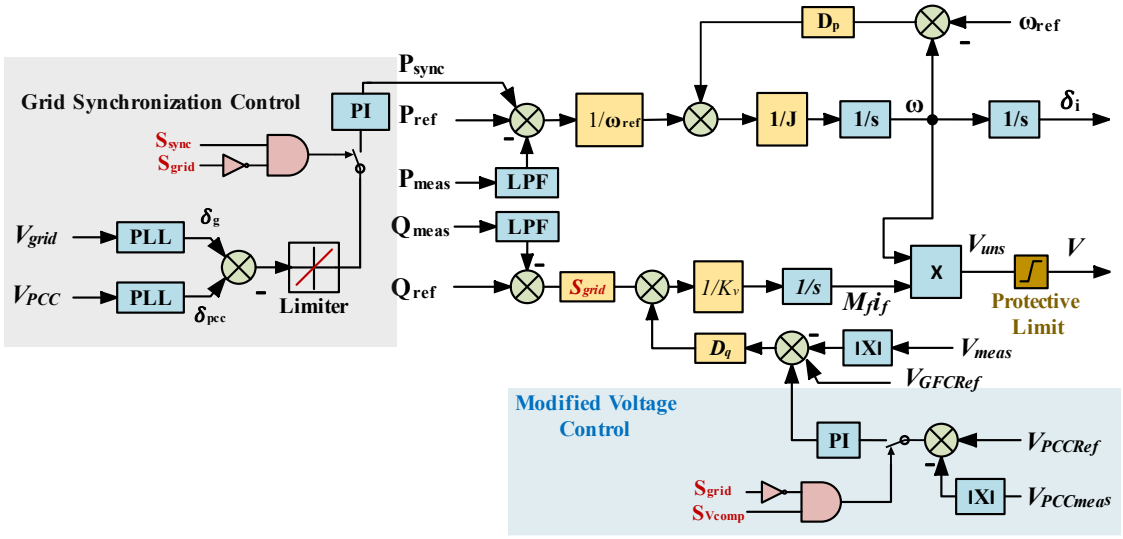

Figure 6.13: Modified grid-forming VSM control with PCC voltage support and grid synchronization.

6.3.1. Test Scenario Definition

The GFC rating is maintained in this test at 40 MVA, and the 53 MVA three-phase transformer residual fluxes are set to $\phi_r = [0.2, 0.65, -0.85]$ pu. The $\pi - section$ line RLC parameters are also set to 2.5 the resistive impedance, 1.5 the inductive impedance and the same capacitive impedance compared to the data in Table 4.1.

The VSM active power reference is set to 35 MW (0.875 pu). Soft energization is initiated at $t = 0$ with $T_{ramp} = 6\ s$. After the voltage ramp-up is complete, a 20 MW (0.5 pu) load is connected at the PCC. Then, the V_{PCC} compensation loop is connected to drive the voltage back to 1 pu, followed by synchronization sequence activation to drive the angle error to zero. Finally, the grid synchronization circuit breaker is closed, and the system operates smoothly in grid-connected mode. The test network and simulation steps are demonstrated in Figure 6.14.

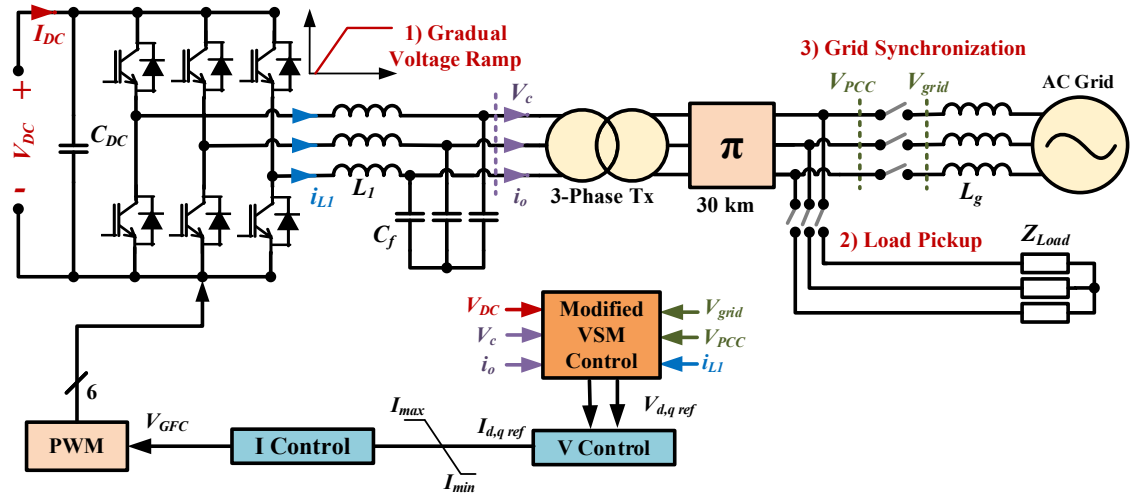

Figure 6.14: Modified VSM validation scenario steps.

6.3.2. Simulation Results

The defined test is implemented using MATLAB/Simulink, and the complete scenario results are presented in Figure 6.15. The GFC voltage ramp to 1 pu concludes at $t = 6\ s$, where the transformer inrush current is observed to be well within the converter rating limit (40 MVA), with a peak around 5% of the GFC rated current. The low peak energization inrush current is influenced by: a) the use of soft energization, b) the influence

of the higher used cables impedance compared to the case study in Chapter 4, and c) the activation of inner GFC control loops. The last point is observed to have a significant impact here. Namely, the inrush current is recorded at 0.2 pu if the inner loops are not activated. This supports the initial observations and simulations performed in Chapter 5 about the potential role of inner loops in inrush current suppression, and the acceleration of T_{ramp} convergence under the new ramp-rate estimation framework.

At $t = 8\,s$, the 0.5 pu load is connected at the PCC, causing a voltage drop that is compensated by the modified VSM through increasing the converter reference voltage. In this case, the GFC can fully compensate the voltage without violating the 1.1 pu set limit in the voltage loop. Inrush current and voltage waveforms are illustrated in Figure 6.15(a). The load connection naturally increases the GFC power supply, in addition to Q to supply the required transformer and $\pi - section$ reactive power, as illustrated in Figure 6.15(b). The synchronizing control activation signal is sent at $t = 10\,s$. However, the control is activated around the angle error zero-crossing point, which takes place around $t = 10.5\,s$. Then, the controller drives the synchronizing angle error to zero by adjusting P_{ref}. The controller operation is illustrated in Figure 6.15(c), where the angle error initially oscillates between $-\pi$ and π ($-180°$ and $180°$) because of the initial mismatch between the reference and actual power. After load connection, the angle error oscillation slope decreases because of the decreased power loop reference error ($35\ MW\ to\ 15\ MW$).

If the initial angle error variation slope is lower, the next zero-crossing point might be significantly delayed. This should be considered if the synchronizing control is programmed to activate at zero-crossing, possibly through: a) introducing an activation window around zero (e.g., between $-30°$ and $30°$), or b) using PI limits with anti-windup to minimize the impact of large overshoots on the converter frequency. As observed in Figure 6.15(c), the angle error settles at zero around $t = 12\,s$. Then, the synchronizing circuit breaker can be closed by the operator once the synchronization conditions are met. This takes place at $t = 15\,s$. The impact of the different steps on the converter frequency is illustrated in Figure 6.15(d), showing operation with a maximum deviation around 1% of the nominal frequency throughout the process.

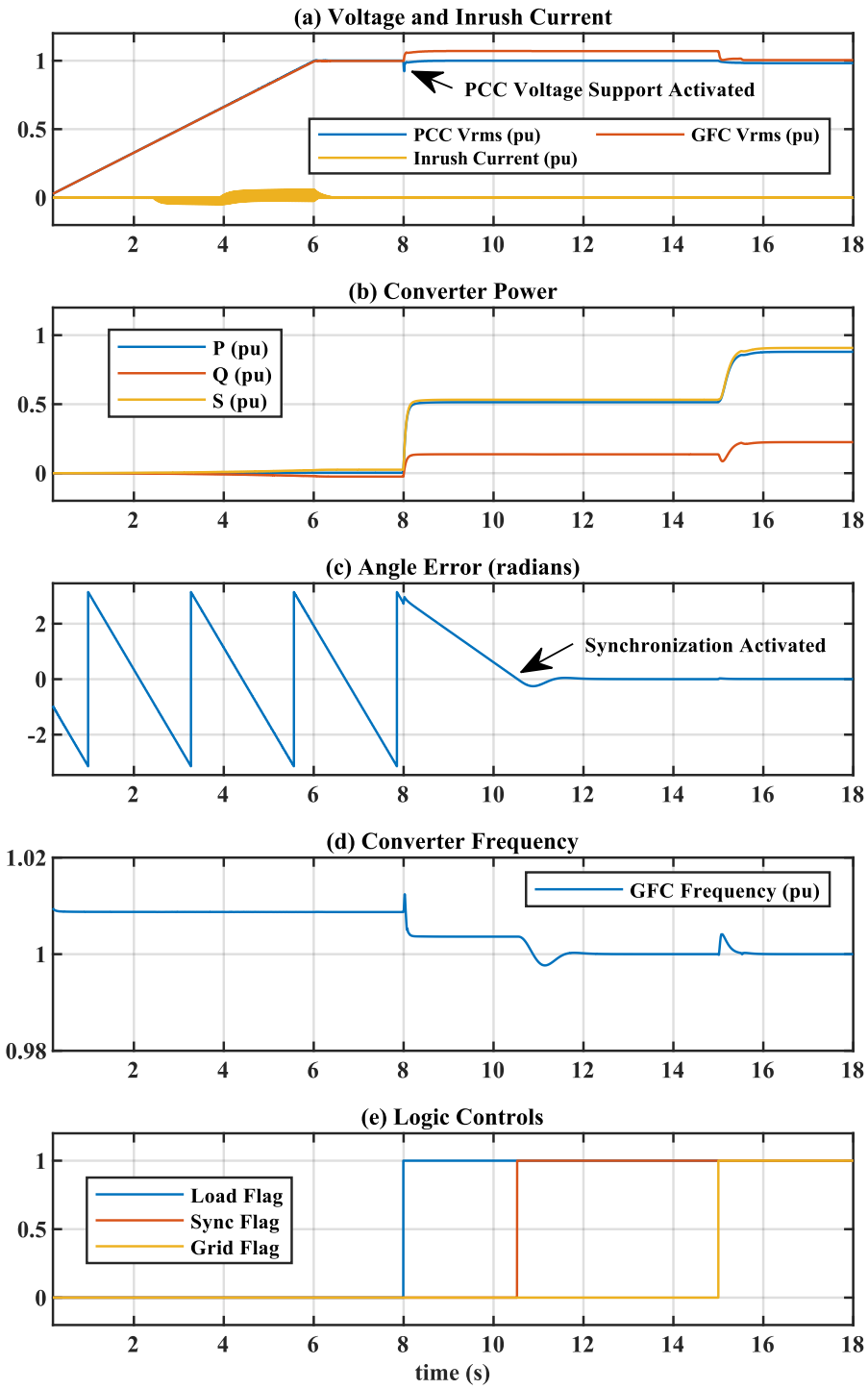

Figure 6.15: Modified VSM complete black-start test scenario: (a): GFC power, (b): time stamps, (c): angle error, (d) Voltages and inrush current, (e) GFC frequency.

After synchronization is achieved, the following behavior is observed:

- Active power smoothly tracks its reference set by the VSM power loop $0.875\ pu$. The load supply is maintained by the grid-forming converter, and the excess power is exported to the grid.
- PCC voltage compensation is disabled, but the voltage is maintained through the power exchange between the GFC and the grid.
- Reactive power supply is adjusted, as required, to maintain the converter voltage at 1 pu. This can be changed by enabling the reactive power path in Figure 6.13 and adjusting the gain ratios between voltage and reactive power control based on the control objective (voltage control vs. reactive power reference tracking).

The conducted test showcases and validates the modified VSM capabilities to participate in a complete black-start scenario with successful soft energization, load pickup and smooth synchronization with grid-connected operation.

6.4. Summary

This chapter presented a modified grid-forming VSM control suitable for black-start and grid-synchronization applications. The modified VSM is capable of soft energization, voltage support at the PCC after establishing the black-start power island, as well as synchronizing to a neighboring island or grid-connection point. The following aspects summarize the key findings in this chapter.

- PCC voltage compensation is influenced by the level of voltage drop due to loading or lines impedance. Protective limits should be imposed on the converter voltage compensation to avoid steady over-voltages exceeding the GFC limits.
- The PCC voltage compensation is a feature that may be activated when needed. For instance, if a grid-code violation is detected and can be rectified by the VSM.
- Grid synchronization can be achieved by adjusting the VSM power loop reference to drive the angle error between the PCC and grid voltage to zero. This requires the angle error as an input, which may be obtained through dedicated relays and communicated to the converter controller.

- Implementing the modified control should lead to steady-state zero angle error before synchronization, which provides room for the operators to visually validate the error elimination and voltage waveforms matching before closing the synchronization circuit breaker.
- Direct PCC voltage measurement may not always be accessible, a method for its estimation using a Thevenin equivalent circuit is thus proposed and tested on a simplified network.
- A combined case study to validate the modified VSM control is presented in this chapter with successful soft energization, PCC voltage compensation and grid-synchronization.
- In principle, the modified voltage and power loops may be applied to different grid-forming controllers such as droop by similarly adjusting the power and voltage loops.

Next, an experimental expansion of this investigation is presented to assess the feasibility of using a GFC as the hardware-under-test (HuT) in a real-time power hardware in the loop (PHiL) environment, with the aim of using the hardware converter equipped with the modified VSM controller to energize (black-start) a scaled network that is simulated into a real-time digital simulator, and to validate the hardware GFC capabilities.

Chapter 7 PHiL Testing of Grid-Forming Converters

The presented grid-forming converters control and transformer energization analysis have thus far been based on MATLAB/Simulink and PSCAD/EMTDC simulations. An expansion of these investigations into a hybrid hardware-software domain is presented in this chapter for further validation under more realistic operating conditions. This extension is carried under power hardware in the loop (PHiL) configuration, where an external hardware GFC can be used to energize a simulated network in a digital real-time simulation (DRTS) platform, and synchronize to the simulated grid. This allows for flexible grid-forming control testing in a controlled environment, under different network configurations and dynamic scenarios. The perceived benefits of such configuration are thus based on the large and flexible number of scenarios that a converter can be subjected to during its development stage. First, an overview is presented on different real-time hardware in the loop configurations. Interface techniques suitable for PHiL grid-forming converters hardware-software integration are also presented, followed by the adopted PHiL configuration for the modified VSM experimental validation, while considering key points such as scaling ratios and time-delay compensations. A complete PHiL case study is then presented, which is believed to be one of the first tests carried out in this domain within the literature for PHiL black-start and synchronization. Key challenges, limitations and lessons learned from this investigation are also identified.

7.1. Hardware in the Loop Overview: CHiL vs. PHiL

Real-time Hardware in the Loop (HiL) techniques can be employed to test the external hardware impact on a real-time simulated network using platforms such as RTDS and Opal-RT. Two key HiL variations are summarized below.

7.1.1. Control Hardware in the Loop (CHiL)

The test network in CHiL is entirely simulated in the DRTS, including the grid-forming converter. However, the converter control board is external, and receives current and

voltage measurements from within the DRTS platform. Measurements processing and converter control decisions are performed on the external board (e.g., microcontroller). Control signals are then fed-back into the DRTS network through dedicated ADC channels to drive the simulated converter in real-time. This technique is effective in an array of applications such as validating industrial control boards or different control techniques [124]. However, it falls short of testing the converter hardware, and relies instead on the DRTS numerical models. Figure 7.1 shows a generic block-diagram for closed-loop CHiL testing of a GFC.

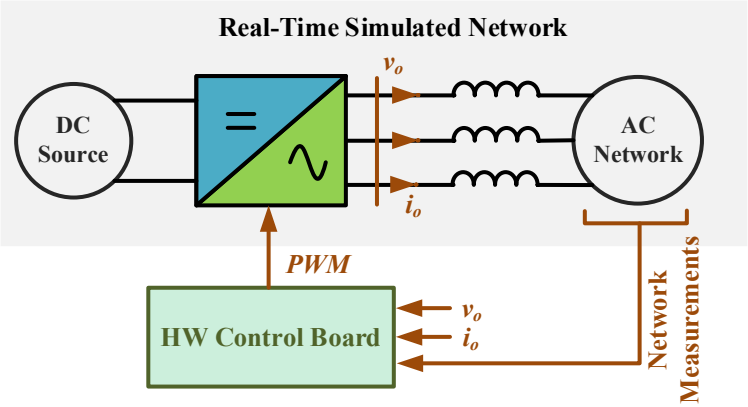

Figure 7.1: Generic CHiL Block Diagram for GFC Testing.

7.1.2. Power Hardware in the Loop (PHiL)

In PHiL, the test network is similarly simulated in a DRTS platform. However, the hardware under test (HuT), which in this case is the grid-forming converter, is represented by a physical external converter that can have its separate control. PHiL allows to test actual devices in conditions where they exchange real power with the simulated network under controlled conditions, adding an extra degree of validation. This also allows to perform repeated and non-destructive experimental assessment of emerging power apparatus in a de-risked environment. The testing can be performed on networks with flexible configurations and ratings, that are scaled up or down at the interface points to match between the simulated network and the external hardware. A generic PHiL diagram is shown in Figure 7.2. PHiL has been a commonly used technique for testing relays, protection equipment, flywheels, inverters, and many other applications [125-128].

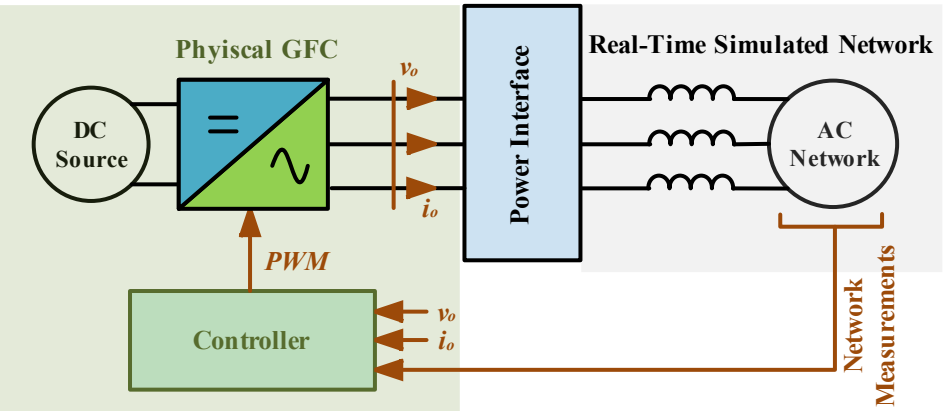

Figure 7.2: Generic PHiL Block Diagram for GFC Testing.

That said, applications where the external hardware is used to energize the network simulated in the DRTS platform have been quite limited, and preliminary work has been shown for PHiL with grid-forming converters in [129]. Thus, the work presented in this chapter aims to investigate the feasibility of applying PHiL for black-start testing of grid-forming converters with grid-synchronization.

7.2. PHiL Interfacing Techniques Classification

Applying PHiL requires establishing a power interface between the external hardware and the simulated network. The power interface plays the 'bridging' role between both sides. Various interface techniques are presented in the literature for PHiL, with the ideal transformer method (ITM) technique being used widely for different applications [130]. Partial-Circuit Duplication (PCD) has also been presented recently for grid-forming converters PHiL applications in [129]. However, this technique requires installing a physical impedance between the converter and the power interface that should be replicated inside the DRTS platform. Mismatches in impedance measurement can lead to deviations in PHiL accuracy [131]. The investigation thus focuses on ITM methods for power converters testing. ITM can mainly be classified into voltage and current type interfaces, which are discussed in the following subsections.

7.2.1. Voltage-type ITM (V-ITM)

This technique has been typically used for grid-following converters testing and HuT devices that are energized externally. In grid-following power converters testing, the HuT normally acts as a current source, which synchronizes to the voltage received from DRTS (grid). However, applying this method in grid-forming converter operating mode implies connecting two devices operating in voltage source mode with potentially unsynchronized voltages. This is more likely to lead to unstable operation as reported in [132]. The topology difference for V-ITM between grid-forming and grid-following implementations is demonstrated in Figure 7.3, showing that direct application of this technique is more suitable for grid-following applications. In V-ITM, the power amplifier (PA) at the hardware side receives its voltage reference from the simulated network, and sends back current reference to drive the current source at the DRTS side, thus closing the PHiL loop. This reference exchange is subject to appropriate voltage and current scaling factors to match the hardware and software-simulated network ratings.

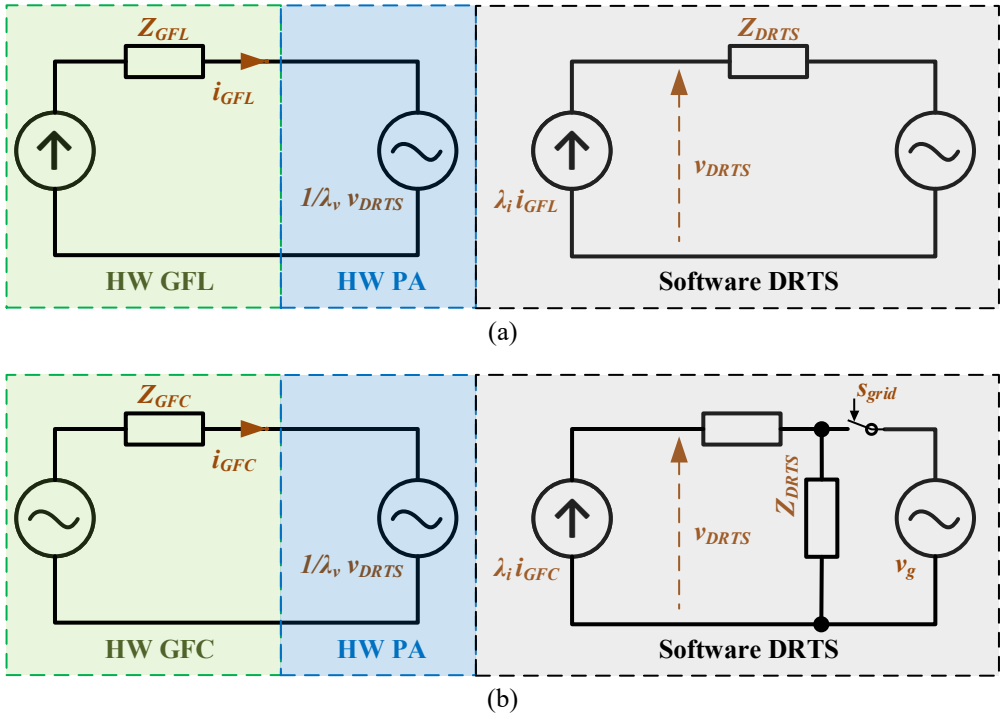

Figure 7.3: V-ITM generic implementation for: (a) grid-following converter testing, (b) grid-forming converter testing.

7.2.2. Current-type ITM (I-ITM)

In this configuration, the power interface on the software and hardware sides is exchanged. That is, the hardware side power amplifier acts as a controlled current source receiving its reference from the simulated network, whereas the DRTS voltage reference is supplied from the hardware side. The I-ITM diagram for a grid-forming converter energized network is presented in Figure 7.4. The initial angle synchronization at the hardware side between HuT and PA is not required, and thus stable operation can be achieved since the interface power amplifier uses the measured angle from the GFC output terminals to drive its PLL. In other words, the GFC acts as the hardware voltage source, whereas the power amplifier acts as a 'grid-following' converter that tracks power or current references supplied from the simulated network. Given this interface technique advantages for grid-forming PHiL testing, I-ITM it is adopted for the remaining experiments in this chapter.

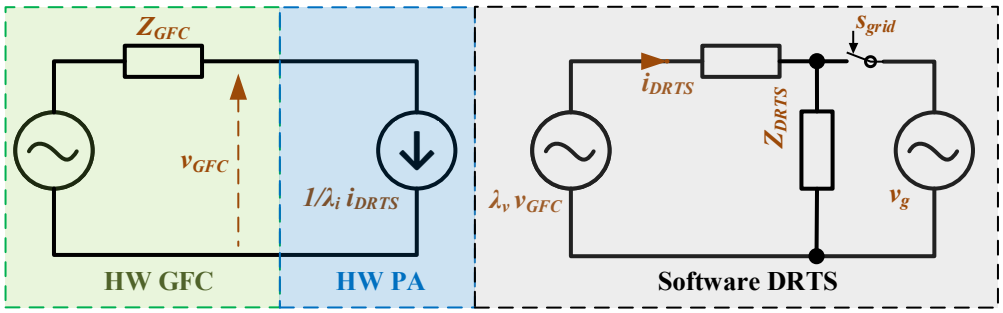

Figure 7.4: I-ITM generic implementation for grid-forming converters testing.

7.3. PHiL as a Validation Tool for GFCs Black-Start Testing

Stability and accuracy are key aspects and performance evaluation metrics in PHiL implementations. Stable closed loop experiments are impacted by the impedance ratios of the simulated real-time network as reported in [133]. On the other hand, PHiL power interface is typically deployed using hardware linear or a switched-mode amplifiers. Linear amplifiers are more accurate and present lower time delays than switched-mode amplifiers. However, they suffer high power losses, are larger in size and more expensive than switching amplifiers for the same power level [128, 134]. Thus, a switched-mode power amplifiers is used for the presented tests.

As established, PHiL allows for evaluating the dynamic performance of hardware converters under realistic conditions and in a scaled environment. The physical rating of PHiL experiments is limited by the rating of the HuT (the grid forming converter in this case), in addition to the power amplifier used to interface the HuT to the simulated network. In the experiments presented here, the GFC control is implemented into a Triphase 90 kVA converter (TP90kVA). Though, the experiments are restricted to 15 kVA since the used switched-mode power amplifier is rated at this limit (TP15kVA). In principle, hardware converters rating is not a restrictive factor to PHiL testing involving MVA-scale simulated networks, and the HuT-PA pair are used to build a proof-of-concept experiment and investigate the feasibility of using hardware GFCs to demonstrate black-start provision through PHiL. To achieve high accuracy, appropriate scaling factors λ should be used for voltage, current and power between the hardware and real-time software domains as shown in (7.1)-(7.3).

$$\lambda_v = \frac{V_{DRTS}}{V_{GFC}} \tag{7.1}$$

$$\lambda_i = \frac{I_{DRTS}}{I_{GFC}} \tag{7.2}$$

$$\lambda_{pq} = \lambda_v \lambda_i \tag{7.3}$$

The recommended steady-state phase voltage in Triphase converters in the conducted experiments is $230\ V_{rms}(325\ V_{peak})$. The analysis conducted in this thesis have thus far concentrated on connecting the GFC output to 11 kV line voltage level ($8981\ V_{peak}$). The ratio thus translates to $\lambda_v \approx 27.5$. As a result, the GFC output voltage (v_o) sent to the DRTS side is multiplied by λ_v before being fed to the simulated network in real-time. On the other hand, the peak TP15kVA current is recommended to be less than 20 A to comply with protection requirements. The peak simulated network power has been set to 35 MW, and thus the DRTS current is scaled down by a factor $\lambda_i = 150$ to comply with the physical equipment limit. Consequently, the power scaling ratio is calculated as 4125 between the hardware HuT-PA pair, and the DRTS simulated network. Figure 7.5 demonstrates the experimental setup for the conducted PHiL tests. In addition to the main

exchanged parameters (voltage and current/power references), additional signals can be exchanged between hardware and software domains as required by the control. For instance, the synchronizing voltages phase error is transmitted from the DRTS platform to the HuT for the modified VSM control operation.

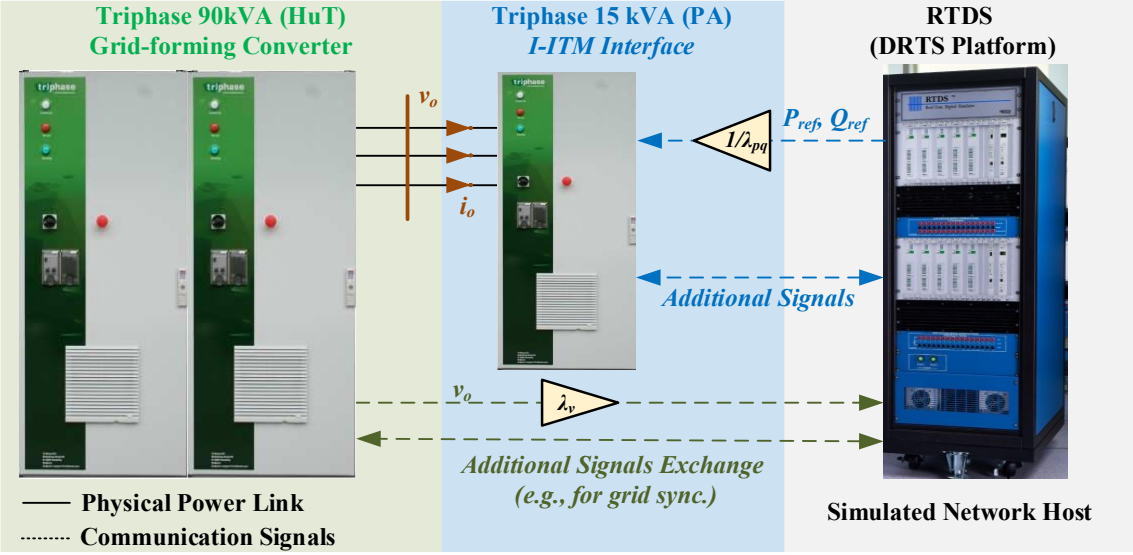

Figure 7.5: Experimental layout used for PHiL validation of GFCs black-start testing.

7.4. PHiL Time-delay Compensation

In PHiL, time delays can arise from A/D conversion, power amplifier, and the used communication links [135]. Time delay is a critical determinant of the stability and accuracy of any PHiL experiment. Large uncompensated time delays may lead to undesirable hardware measurement mismatch, which impacts the experiment accuracy. For instance, the scaled reference might be 20 MW, but the actual tracked power may deviate above or below this value, depending on the compensation mismatch. Large delays may also influence the PHiL stability as analyzed in [133]. This reference also notes the impact of network impedance ratios on PHiL stability. Special techniques are typically deployed to compensate for average delay values.

Time delay exists in the HuT-DRTS path when sending the voltage reference from the hardware grid-forming converter side to the DRTS platform. Delays also occur in the DRTS-PA path through the exchange of power or current reference from the DRTS to the

hardware power amplifier. This also applies to any additional signals required for the control operation (e.g., the synchronization angles error being fed back from the DRTS to the hardware grid-forming converter VSM control). In this investigation, the HuT-DRTS path communications are carried out using the high-speed advanced Aurora Protocol in RSCAD/RTDS. On the other hand, the DRTS-PA path is connected through a Giga-transceiver analog output card (GTAO) in RSCAD/RTDS to minimize delay impact.

7.4.1. Time-delay compensation technique

The i_{DRTS} feedback signal from DRTS to PA in I-ITM can be sent as a three-phase sinusoid, which is more sensitive to time-delays. Alternatively, power references can be shared as scaled P_{ref} and Q_{ref} to the power amplifier, which can then be converted to currents within the PA with minimized delay impact. Additional sources of delay and mismatches may still exist in the system such as the ones arising from the HuT-DRTS path. Thus, an aggregate compensation framework is proposed and applied to the DRTS-PA path, with the objective that the scaled active and reactive power measurements in hardware closely match those measured within the DRTS in real-time. The time delay compensation adopted is based on compensating the synchronous dq0 frame angle for the measured output voltage as illustrated in Figure 7.6. The physical GFC output voltage is measured by the power amplifier, operating in grid-following mode, as the voltage to be followed. This voltage (v_o) is passed through a PLL to extract its phase angle δ_v, which is used to drive the synchronous frame controller. Simultaneously, the active and reactive power references P_{ref} and Q_{ref} are received through the DRTS platform. The GFC output voltage and power references are used to calculate the synchronous frame currents for the PA grid-following control as in (5.4)-(5.5).

$$I_{odref} = \frac{2}{3}\frac{(V_{od}P_{ref}+V_{oq}Q_{ref})}{V_{od}^2+V_{oq}^2} \tag{7.4}$$

$$I_{oqref} = \frac{2}{3}\frac{(V_{oq}P_{ref}-V_{od}Q_{ref})}{V_{od}^2+V_{oq}^2} \tag{7.5}$$

These reference currents are then compared to the measured input currents at the PA terminal (GFC output current).

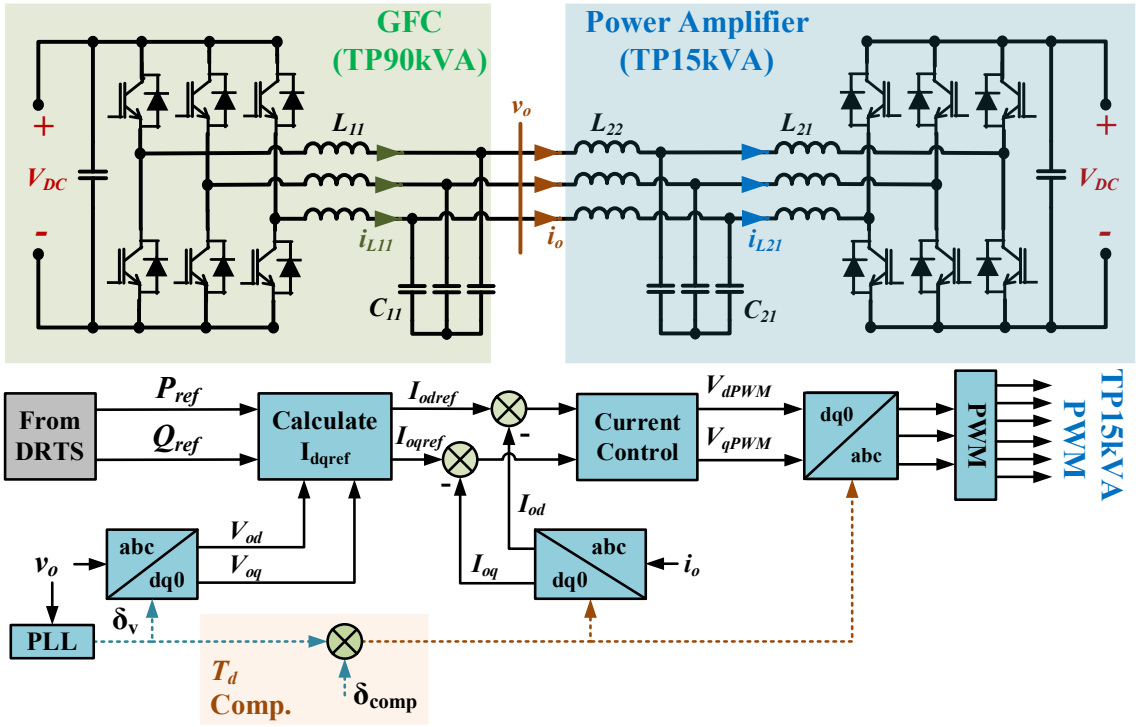

Figure 7.6: Implemented PHiL time delay compensation for the power amplifier (TP15kVA).

The synchronous frame conversion for i_o is driven here by the compensated angle δ_v', which is calculated as in (7.6).

$$\delta_v' = \delta_v + \delta_{comp} \tag{7.6}$$

where, δ_{comp} is a compensating value between 0 and 2π, which is used to adjust the accuracy of the scaled PHiL hardware measured power and to maintain it within acceptable limits against the DRTS power measurements. The current control block includes a PI control, and the control outputs V_{dPWM} and V_{qPWM} are already normalized with respect to the DC voltage. Simplified mathematical representation for the current control is summarized in equations (7.7)-(7.8) based on available current measurements.

$$V_{dPWM} = \frac{2}{V_{DC}}\left(\Delta I_{od}\left(k_{p(PA)} + \frac{k_{i(PA)}}{s}\right)\right) \tag{7.7}$$

$$V_{qPWM} = \frac{2}{V_{DC}}\left(\Delta I_{oq}\left(k_{p(PA)} + \frac{k_{i(PA)}}{s}\right)\right) \tag{7.8}$$

where, the PI gains are termed as $k_{p(PA)}$ and $k_{i(PA)}$, respectively. Finally, the $dq - abc$ conversion of the PA PWM voltage is similarly driven by the compensated angle δ_v', and the PWM signals are generated from the PWM voltage through a triangular wave comparator. The PA current direction is recommended to follow the convention illustrated in Figure 7.6, such that the current entering PA results into positive power (consumed), since the reference P and Q received from the DRTS side follow similar convention. This way, the scaled physical power is injected from the GFC to the PA when P_{ref} is positive.

7.4.2. Testing of time delay compensation

To demonstrate the impact of the remaining time delay and its average compensation, an experiment is carried out where δ_{comp} is varied between 0 and 180°. The angle is changed gradually over a period of 360 seconds (i.e., with a slope of $0.5\ °/s$). The power references sent from the DRTS side are fixed at $P_{ref} = 10.05\ MW$ and $Q_{ref} = 4.22\ MVAR$. The hardware power (P and Q) are measured from the PA side (multiplied by $\lambda_P = 4125$), and recorded over the full testing range. Experimental results for this test are summarized in Figure 7.7. The high measurement sensitivity to the delay and the compensation angle variation is evident for both P and Q in this figure. For instance, the maximum recorded deviation for P is around 3 pu near $\delta_{comp} = 180°$. Although such extreme delays are unlikely to exist unless the delay sources are significant such as large electrical distance or filters, the presented experiment illustrates how uncompensated, or poorly compensated, time delays can contribute to accuracy deviations. For the presented power references, a common compensation point that is in the vicinity of these references is found at $\delta_{comp} = 1.688°$ $(0.0295\ rad)$ as illustrated in Figure 7.7(b), which amounts to $94\ \mu s$ compensation according to (7.9).

$$T_{d(PA)} = \frac{\delta_{comp(rad)}}{2\pi f} \tag{7.9}$$

This value is thus used for the remaining of the experiments conducted in this chapter, which as will be shown in the case study, resulted in accurate tracking of both P and Q

references. Running a similar experiment for PHiL setups is recommended to characterize the average time delay and compensate it accordingly.

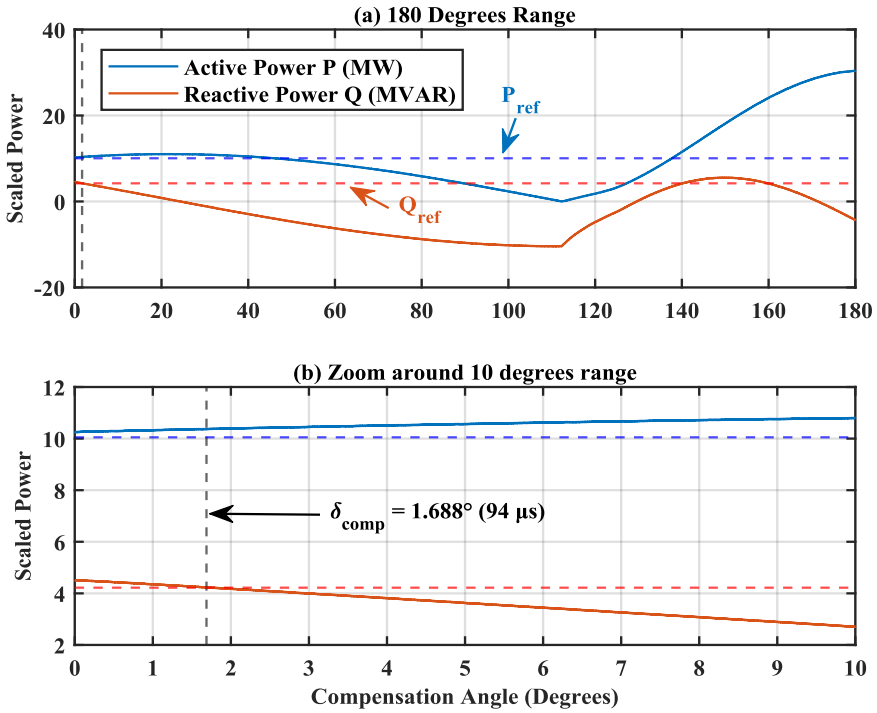

Figure 7.7: Time delay compensation impact showing: (a) 180-degree compensation range, (b) reduced scale to illustrate the chosen compensating angle.

7.5. GFC Black-Start Testing Case Study

This case study and the presented test scenarios aim to validate the use of grid-forming converters for black-start testing under PHiL configuration. The test is conducted for a particular network topology. Though, testing Extension to different network configurations is feasible through the flexibility provided by the simulated nature of the test network implemented into the DRTS platform.

7.5.1. Test Network Definition

Black-start service provision through grid-forming converters in PHiL is validated through a similar test network to that used in Chapter 6 for the modified VSM, with the main differences being: a) load pickup is performed simultaneously to the soft energization at the secondary transformer terminals to expand the testing scenarios spectrum, b) test

transformer parameters are modified to be closely correlated to reported data in a Chapelcross network model in Scotland. The transformer rating is maintained at 53 MVA, and the saturation curve knee-point is set to 1.25 pu, with saturation inductance value of $L_{sat} = 0.265\ pu$ and a leakage inductance equal to 0.1 pu. Similarly, the π-section line is used with slight variations to those reported in Table 4.1. Overall, the test network maintains similar structure for consistency. The network loads are divided into a main (initially closed) 20 MW load, and a 10 MW disturbance load that is connected post-synchronization to test the control robustness. The test network is illustrated in Figure 7.8.

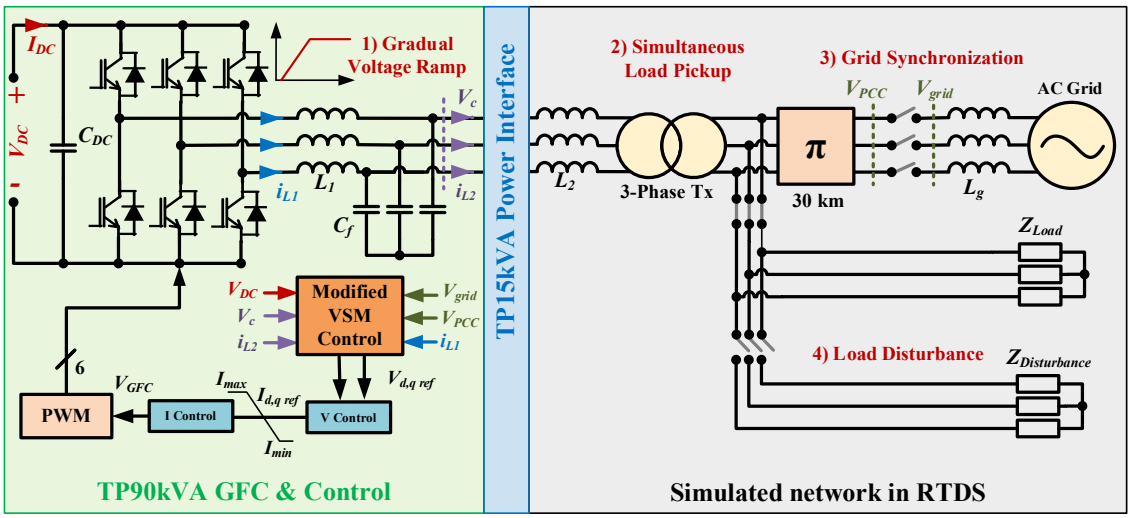

Figure 7.8: Test network block-diagram used for PHiL black-start experiments.

The hardware part of the network (converter & LC filter) are interfaced to the simulated network in RSCAD/RTDS. The modified VSM control utilizes inertia and damping factors that maintain minimum frequency variations at rated power disturbances. In the previous chapters, the VSM was designed for a 40 MW GFC rating in the pure-simulation tests, whereas the controlled converter rating in PHiL is in the kW range. The virtual inertia and damping constants for voltage and power loops are thus re-tuned.

The voltage scale $\lambda_v = 27.5$ is applied for the network simulated in RSCAD. The simulation real-time input voltage is scaled to a base value of 11 kV_{LL} from 400 V_{LL}. An extra inductance is added after the emulated voltage source in the RSCAD model to

represent L_2 of an LCL filter, which is added to improve the PHiL system stability. This value is calculated at 0.1 pu as shown in (7.10).

$$L_2 = 0.1\frac{V_{i\_DRTS_{LL}}^2}{\omega S_{DRTS}} \tag{7.10}$$

where, $V_{i\_DRTS_{LL}} = 11\ kV$, $S_{DRTS} = 40\ MVA$, and $\omega = 2\pi 50\ rad/s$. Leading to $L_2 \approx 1\ mH$. Collectively, key network test parameters are summarized in Table 7.1.

Table 7.1: Key test network parameters for PHiL Black-start experiments.

PHiL Interface Parameters			
λ_v	27.5	λ_i	150
Hardware GFC Parameters (TP90kVA)			
DC Voltage	700 V	Switching Frequency	16 kHz
LCL Filter L_1	0.5 mH @ 400 V	LCL Filter C_f	47 µF @ 400 V
AC Voltage	230 V_{rms}	Sampling Time	62.5 µs
GFC Control Parameters			
VSM Loop			
Power Loop D_p	14.28	Virtual Inertia J	0.028
Voltage Loop D_q	306	k_v	5771
Inner Loops PI gains			
k_{pv}	0.2	k_{iv}	1
k_{pi}	0.2	k_{ii}	10
DRTS Simulated Network Parameters			
LCL Filter L_2	1 mH @ 11 kV	Power Base	40 MVA
Transformer Parameters ($\Delta - Y$)			
Power Rating	53 MVA	Voltage Ratio V_o/V_i	33/11 kV
Knee-Voltage	1.25 pu	L_{sat}	0.265 pu
Leakage Inductance	0.1 pu	ϕ_r	[0.25, -0.1, -0.15] pu
Transmission Line Parameters ($\pi - model$)			
(R, L, C) per km	12.73 $m\Omega$, 1.07 mH, 9.95 nF	Length	30 km
Network Loads			
Main Load	20 MW	Disturbance Load	10 MW
Grid Parameters (33 kV_{LL})			
Short-Circuit Power	500 MVA	X/R Ratio	14.5

Soft energization technique is used with a ramp duration of 10 seconds. The peak absolute ϕ_r for the energized transformer is 0.25 pu, and thus negligible inrush current is expected according to equation (3.30). The soft network energization is simultaneous to the main 20 MW load pickup. Grid synchronization is then performed using the modified VSM controller in Figure 6.13. In this experiment, the PCC voltage phase error is sent from RSCAD/RTDS to TP90kVA in real time to drive P_{sync} to the value resulting in zero phase error. Beyond synchronization, the grid-forming VSM continues to operate in voltage-control mode and is capable of reactive power injection/absorption as potential ancillary services. A load disturbance is presented in grid-connected mode to validate the hardware converter response, with the aim that the VSM maintains the voltage required to exchange power with the grid after synchronization.

7.5.2. Experimental Test Results

The results presented in this section show a combination of hardware and software results obtained from the black-start experiment. Initially, the grid-forming VSM implemented in TP90kVA unit is activated with a 10 seconds voltage ramp between 0 and 325 V_{peak}. This voltage is sensed and sent to RTDS and scaled up by 27.5 to represent 8981 V_{peak} (11 kV V_{LL} equivalent) in real-time. The scaled-up voltage is fed into the simulation network to energize the 53 MVA transformer, line and 20 MW load. Then the restored island is synchronized to the grid after the angle error is driven to zero, followed by power reference variation and a load disturbance. The synergy in trends between hardware and software sides is illustrated, starting by GFC output voltage waveforms as illustrated in Figure 7.9. The similar behavior for both voltages throughout the experimental scenario is evident.

As expected from the ϕ_r combination reported in Table 7.1, the transformer barely approaches the saturation region due to the 1 pu difference between the peak residual flux and the saturation curve knee point. Thus, the energization is carried without noticeable inrush current. Certainly, higher residual flux combination would have generated a higher peak inrush. The flux and inrush currents for the studied scenario from RSCAD/RTDS are demonstrated in Figure 7.10.

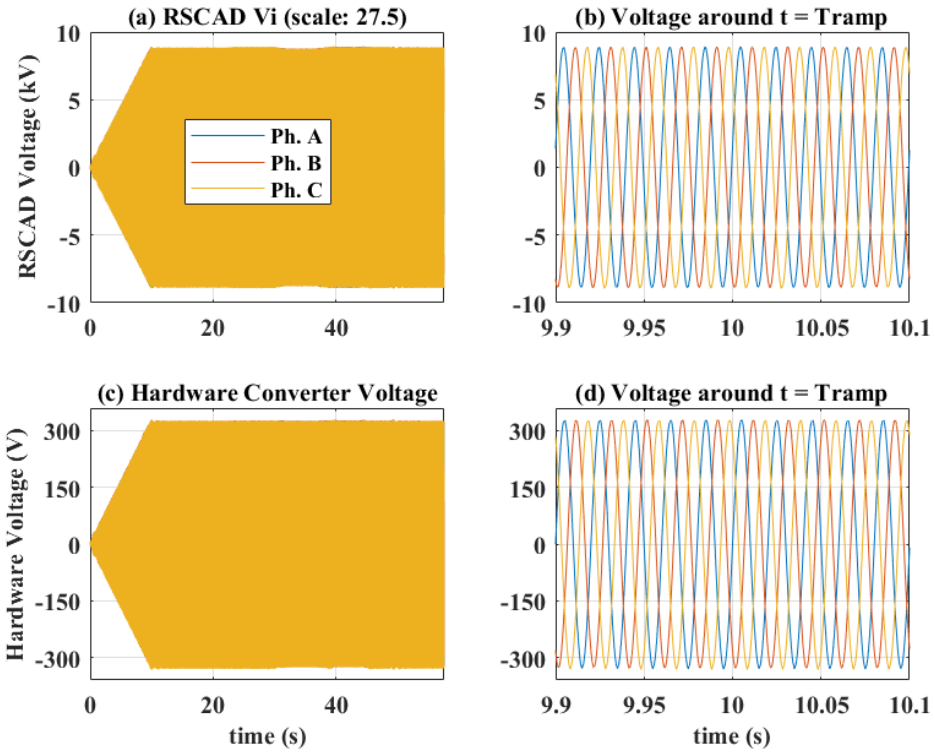

Figure 7.9: RSCAD vs. Hardware Input Voltage Measurements.

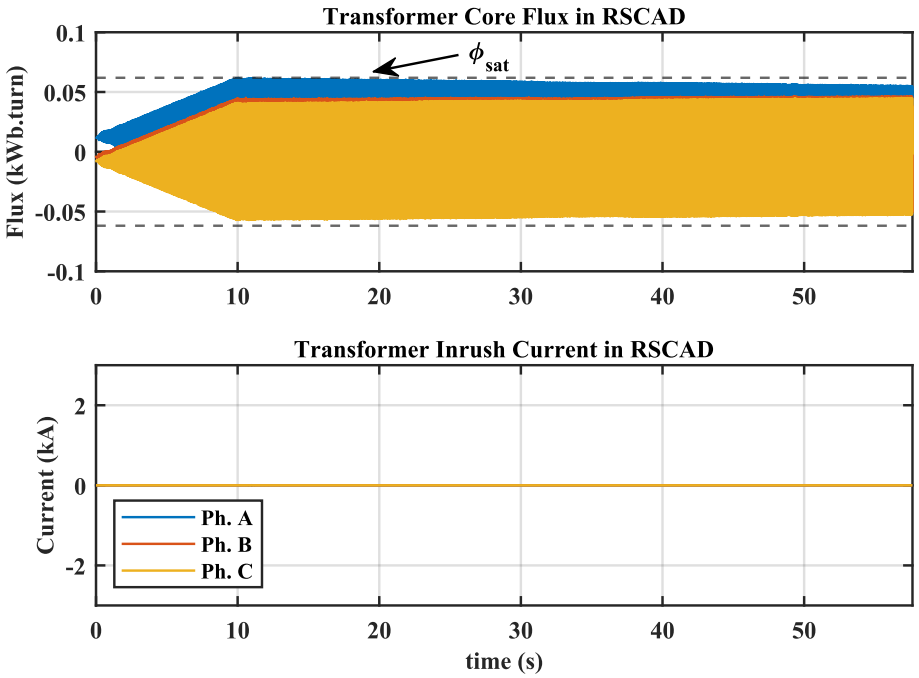

Figure 7.10: Transformer flux and magnetizing current during PHiL simulated network energization.

On the other hand, the synchronizing control is activated during the ramp to accelerate the phase-matching. Initially, a variable phase-shift is observed, and as the synchronizing PI control tracks the zero-angle point error, the phase-angle between PCC and grid voltages in the simulated DRTS network approaches zero. This is demonstrated in Figure 7.11. Both PCC and grid voltages around the moment of controlled synchronization are illustrated in Figure 7.11(b), where the process is done smoothly. The synchronization switch is closed around $t = 22.75\ s$. The power exchange between the VSM and the grid is initiated following the VSM power reference. The converter tracks the power reference which is initially set to 20 MW. The phase angle error throughout the process is monitored and presented in Figure 7.11(c), showcasing steady-state error around zero before closing the synchronizing switch, thus validating the synchronizing control operation in PHiL.

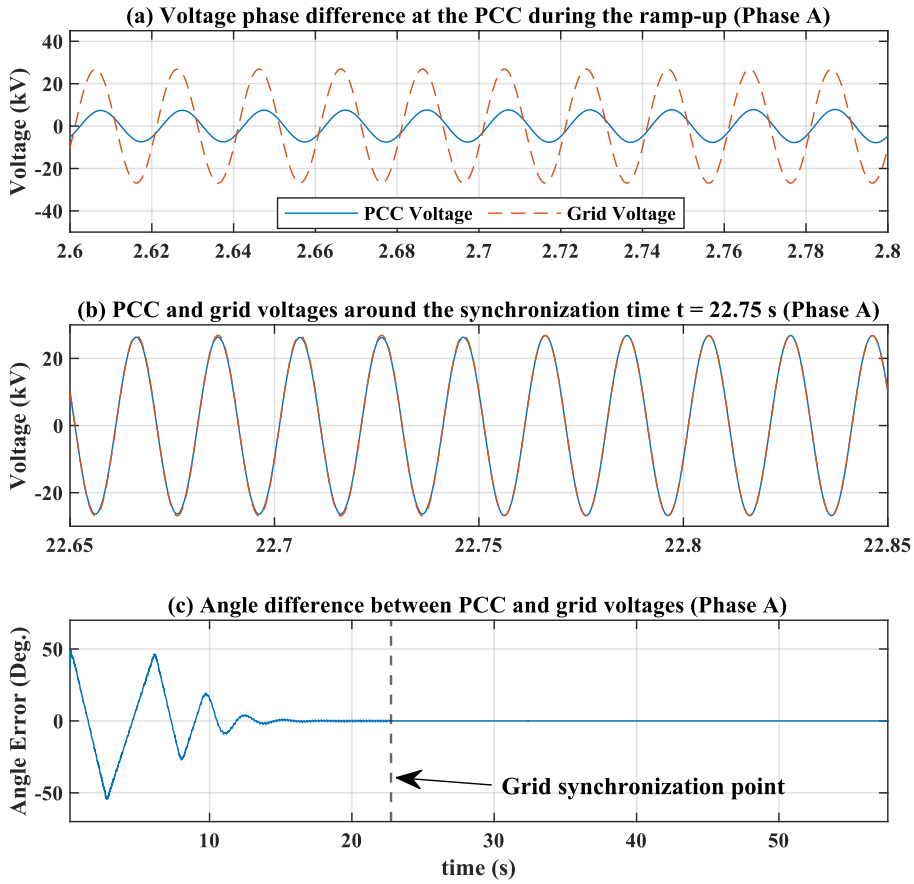

Figure 7.11: Synchronizing control impact in reducing the phase shift between PCC voltage and grid before synchronization.

Then, at $t = 29.75\ s$ (seven seconds after synchronization), the power reference is ramped to 35 MW using a 7.5 MW/s slope. After 7 additional seconds, the reference is ramped down with a similar slope to 10 MW, before ramping up again to the initial 20 MW point around $t = 43.75\ s$. Finally, a load disturbance is applied at $t = 48.75\ s$ where an additional 10 MW load is connected ($Z_{disturbance}$ in Figure 7.8). The impact of these events on both hardware and RTDS VSM currents is illustrated in Figure 7.12, where similar trends can be observed between the RTDS input current and the measured hardware converter current with a factor around 150, similar to the chosen scaling ratio. Notably, slight drifts are observed over time in the phase angle, which is overcome by sending P_{ref} and Q_{ref} to the power interface, rather than the sinusoid current references. Thus, maintaining a precise trends duality with correct scaling, combined with the applied compensation technique to maintain power, and consequently current, tracking accuracy.

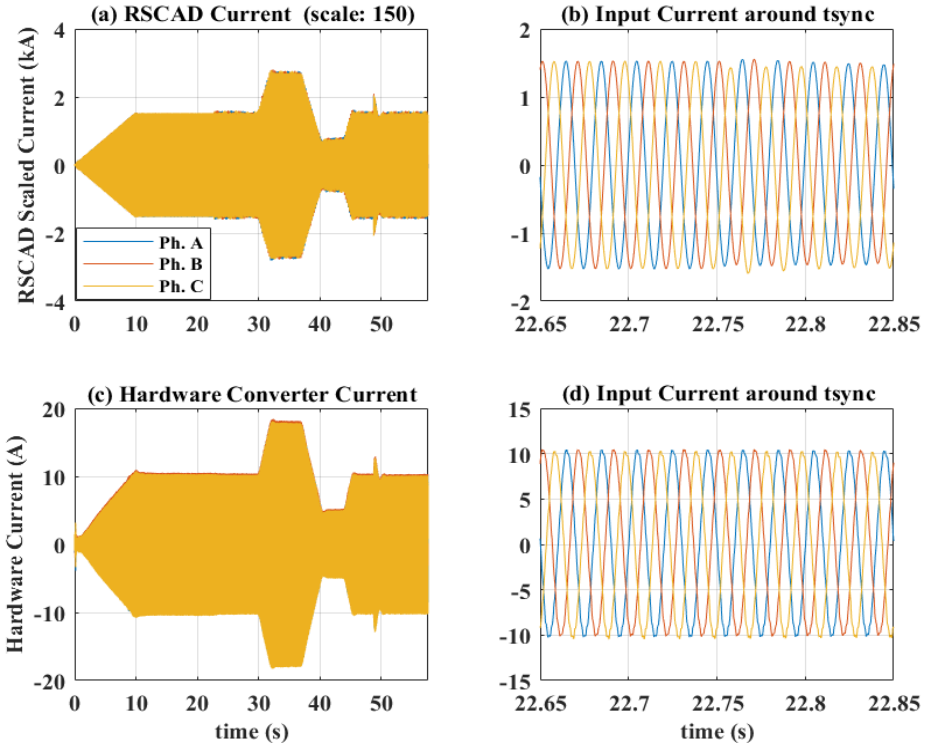

Figure 7.12: RTDS vs. Hardware Input Current Measurements.

The software vs. hardware active and reactive power tracking performance is also benchmarked for the PHiL application as illustrated in Figure 7.13. For this comparison,

the hardware power, measured from TP90kVA side, is scaled up by $\lambda_{pq} = 4125$ to match the network power scale simulated in RSCAD. Filtered power measurements are used in both hardware and software sides for noise reduction using low-pass filters. As observed in Figure 7.13, the active and reactive power reference tracking performance is satisfactory between hardware and software, with the applied additional time-delay compensation of around $94\ \mu s$. The hardware converter reacts successfully in real-time to the local reference adjustments. For instance, adjusting the reference from 20 MW to 35 MW at $t = 29.75\ s$, which corresponds to a hardware power ramp from 4.85 kW to 8.48 kW that is fed to the power interface amplifier. The reactive power tracking path is not prioritized throughout the experiment compared to GFC voltage control. Q consumption or injection between TP90kVA and TP15kVA follow the requirement to maintain the voltage signal to its control setpoint, with a peak, filtered, value that does not exceed 1 MVAR (in its scaled-up form) as shown in Figure 7.13(b).

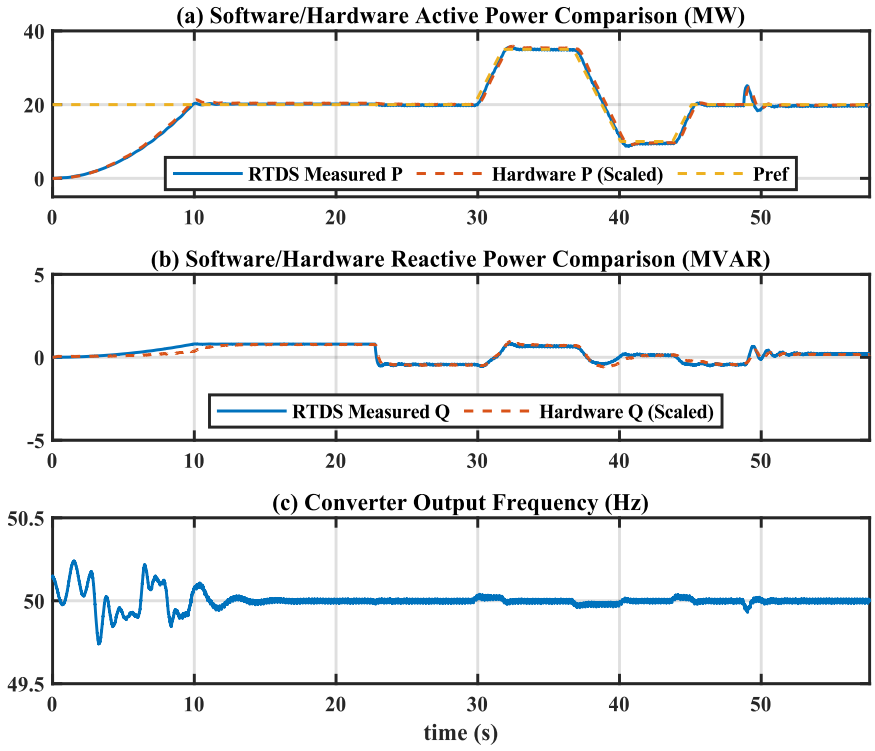

Figure 7.13: PHiL Active and Reactive Power Tracking Performance (Software vs. Hardware) throughout the experiment, in addition to the GFC output voltage frequency.

Figure 7.13(c) also illustrates the VSM voltage frequency trace throughout the experiment, showing slight variations around the steady 50 Hz points during the ramp and synchronizing control action, and small changes as a result of the power reference adjustments.

Finally, the current exported to the grid in RSCAD, and the grid active power and reactive power measurements during the PHiL experiment are presented in Figure 7.14. Between $t = 22.75\ s$ and $t = 29.75\ s$, the grid current and power are close to zero. This is because the GFC power reference is set to 4.85 kW (which is scaled to 20 MW in RSCAD). This power is equal to the load demand prior to grid-synchronization, and thus the grid connection initially does not involve significant power exchange. In the next stage, the grid imports 15 MW as illustrated in Figure 7.14(c) after the GFC export in RSCAD is increased to 35 MW. Then, the grid exports 10 MW of power when the GFC setpoint is changed to 10 MW, before temporarily going back to around zero at t = 43.75 s when GFC P_{ref} is back to 20 MW. When the 10 MW load disturbance is applied at $t = 48.75\ s$, the

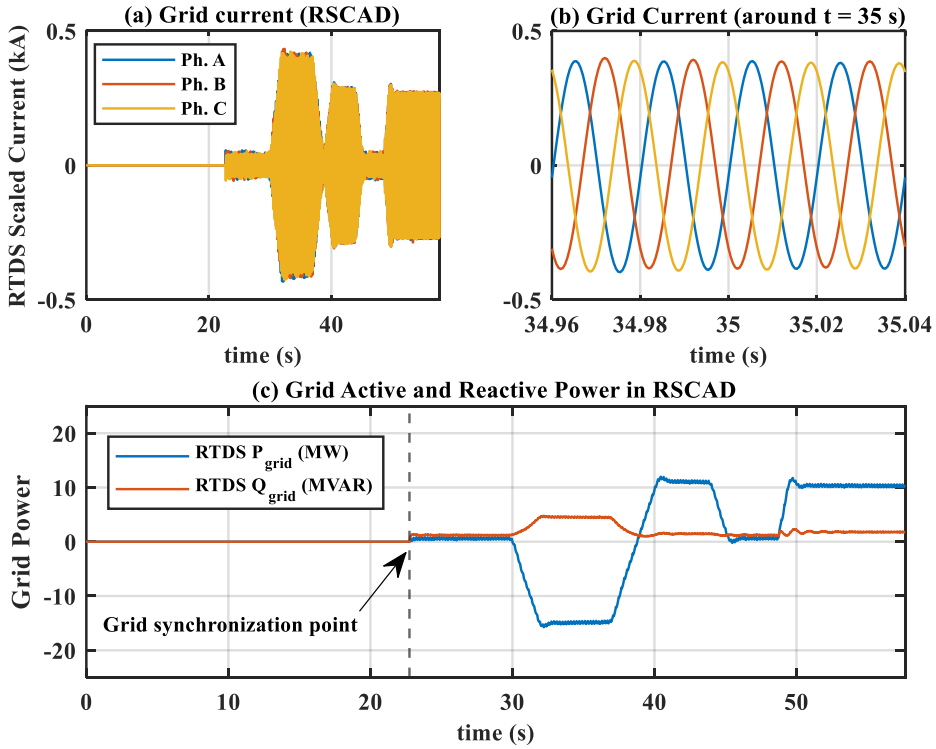

Figure 7.14: Grid current and power monitoring throughout the experimental PHiL scenario.

grid exports this power to supply the load since the GFC power reference remains constant. Meanwhile, the reactive power exchange with the grid is adjusted as required to maintain the system MVAR demand and voltage.

Overall, the presented analysis in this section successfully demonstrates the application of PHiL technique (with I-ITM interface) to test black-start provision for a network simulated in a DRTS platform, from an external GFC acting as the anchor energizing source. Successful tracking of voltage and current references has been achieved in real-time between the hardware and the scaled-up simulated network. In addition, synchronizing between the hardware GFC and an internal grid simulated in RSCAD/RTDS has been achieved by relaying the required measurements from within the simulated network to the external hardware GFC control, closing the control and synchronization loop.

7.6. Lessons Learned from PHiL Testing

Based on the successful PHiL test demonstration, different network topologies can be similarly tested, in principle, with industrial converter models and compatible power interfaces in a non-destructive and controlled environment to assess and validate their control capabilities for black-start and network support applications, where the dynamic network behavior is reflected in real-time on the power interface amplifier. That said, PHiL application is also prone to certain challenges, many of which were experienced during the reported experiments. The main challenges and lessons learned from this investigation are reported in the following subsections.

7.6.1. PHiL GFC Control Implementation

Two main options have been investigated to implement GFC control for PHiL. a) in the DRTS platform itself, where all the control functions are performed there, and the output reference is then sent for the hardware converter to replicate and share back with the RTDS software to drive its scaled voltage source. b) directly in the external hardware converter (HuT) through its dedicated software interface (e.g., MATLAB/Simulink, dSPACE or a vendor specific software). After testing both options, it is found that direct control implementation in the external hardware provides an improved performance, easier to

troubleshoot, and directly utilizes hardware measurements which is more representative of realistic operating conditions, since vendors typically implement the control software in the converter board. Table 7.2 summarizes high-level pros and cons of each control implementation type.

Table 7.2: High-level PHiL Control Implementation Approaches Benchmark.

	Advantages	Limitations
HuT Control	Direct control consideration of hardware filter dynamics with internal measurements.	Requires access to RT-DRTS readings for some functions (e.g., synchronization).
	Direct control implementation on the actual target hardware board.	More prone to variable delays.
DRTS Control	Direct access to all control measurements in the simulated network.	Indirect consideration for hardware GFC filter measurements.
	Direct time delay compensation for the control voltage input/output.	Control is not implemented on real control board to mimic real conditions.

7.6.2. Digital Interface and Numerical Models Nature Impact

The PHiL setup interfaces physical power measurements with a simulated network in real time through analog and digital communication links. Signals exchange between these two domains is subject to analog to digital (ADC), and digital to analog (DAC) conversions, which may result into some deviations and quantization errors, that can be amplified by the numerical nature of the modeled network. Such issues are not observed to appear when the same network is tested using a simulated power source. An example is presented to explain this phenomenon, with the adopted remedy.

A. Impact of Non-Zero/Non-Symmetric Average Voltage on Simulated Transformers

Initial PHiL experiments were observed to generate high steady-state magnetizing current for the 53 MVA simulated transformer in RSCAD. In one test, the transformer model is parameterized to operate with 1% magnetizing current in steady-state. However, consistent deviation has been observed in the magnetizing current when the simulated transformer is connected, leading to upward of 20x the designed steady-state i_m. Further investigation revealed that the input RSCAD measurement, which is received from the

GFC and scaled up in software had non-zero and non-symmetric average values in RSCAD, as illustrated in Figure 7.15.

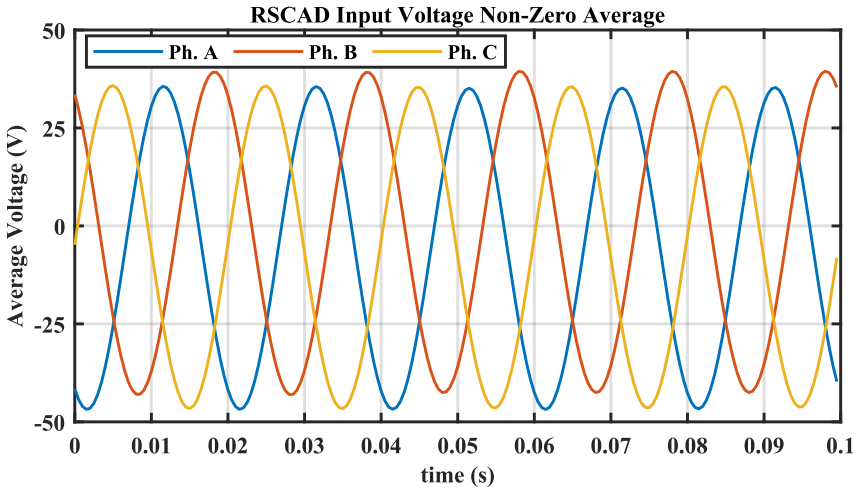

Figure 7.15: Non-Zero RSCAD input voltage (scaled up from TP90kVA).

The software transformer model estimates its flux as the input voltage integral. The non-zero average voltage is observed to cause a noticeable deviation in the transformer flux over time as a result of applying this integral. Thus, driving the transformer windings partially into the saturation region. It has been established in Chapter 3 that the magnetizing current variability is a consequence to the flux operating point (i.e., between linear and saturation regions). Flux within saturation region leads to high magnetizing current, which is not caused by actual network operating condition in this case and is reflected on the physical power amplifier by adjusting its reference to an incorrect value. If a physical transformer is connected to the GFC, then the power exchange is through real voltage and current and such issue would not exist. In fact, the Triphase hardware units used in this PHiL experiment are equipped with isolation transformers, which did not exhibit similar behavior. On the other hand, the reported issue was detected in the RSCAD simulation since the GFC output is sensed and used to drive the transformer in digital domain, making it more sensitive to the highlighted conversion errors.

B. Proposed Solution

The amplified transformer magnetizing current due to the observed non-symmetric voltage average issue was observed to follow an oscillatory pattern with a low-frequency envelope forming at the peaks. Thus, the proposed solution is to pass the RSCAD input voltage (V_{i_DRTS}) of each phase through low-pass filters to extract the low-frequency oscillatory component. Then, to subtract this component from the actual voltage. This way, the observed envelope can be eliminated, while still allowing for the unfiltered voltage to pass without restricting its dynamics or fast variations that could exceed the low-pass filter cutoff frequency. The selected cutoff frequency for the used Butterworth filters is set to 15 Hz, and the block diagram of the proposed signal-processing solution is demonstrated in Figure 7.16.

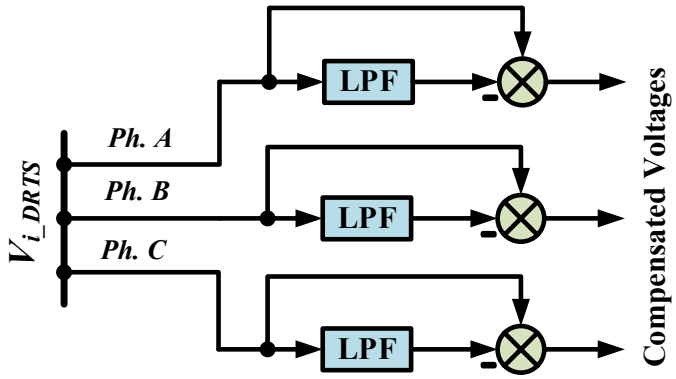

Figure 7.16: Adopted non-zero average voltage compensation approach.

The results of applying this technique are shown in Figure 7.17, demonstrating the correction impact on the GFC output current (RSCAD input). Between $t = 0$ and $t = 5\ s$, the compensation loop is not active, resulting into the high steady-state magnetizing current in transformer. The highlighted low-frequency envelope is also visible. At $t = 5\ s$, the compensation is activated, resulting into a current adjustment once the source of error is eliminated in the input voltage. This voltage compensation has been activated throughout the PHiL experiments. For instance, the core flux results in Figure 7.10 are collected with activated compensation. Finally, it has also been observed that applying a moving average instead of low-pass filter produce a similar compensatory effect.

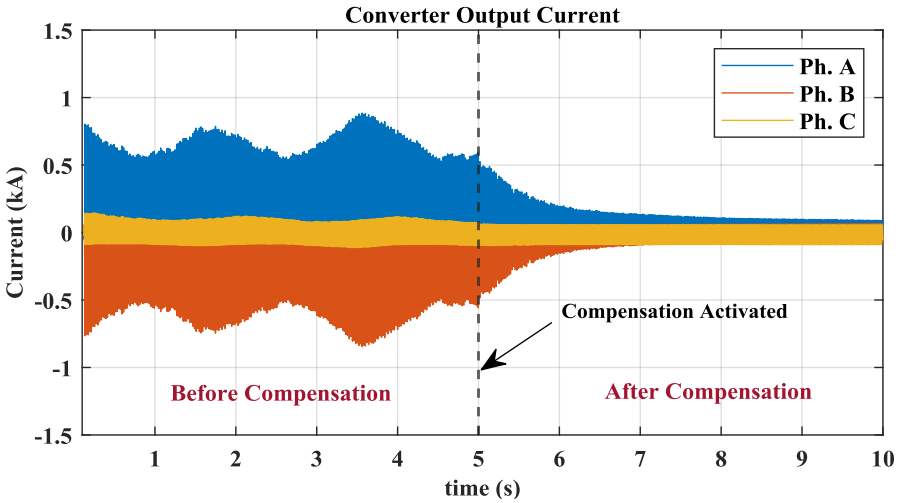

Figure 7.17: Average PHiL voltage compensation impact on steady-state transformer current.

7.6.3. DRTS Platform Simulation Capabilities

The presented case study covered a simplified power network that consists of a small number of components as a proof of concept to PHiL testing compatibility with GFCs black-start. That said, larger networks may be of interest for extended scenarios, such as those covering real networks. In order to maintain the real-time requirement of PHiL testing, the simulated network electromagnetic transient (EMT) model and differential equations are solved at each time-step (µs order of magnitude). This requires the use of advanced real-time simulators with sufficiently powerful processing cores to accommodate the high computational demand. That is, if the test network presented is extended to include a large number of transformers and EMT cable segments, then the used DRTS platform (RTDS with PB5 processors) would have not been sufficient, and the use of higher number of RTDS racks, or the newer generation NovaCor would be required instead. For instance, RTDS Technologies provide a guide on the number of load units required to simulate major network components such as transformers and EMT cables [136], which can be taken as a guide to estimate the number of required hardware processing cores for a given PHiL testing scenario.

7.6.4. PHiL Impedance Ratios

It has been observed that the nature of network impedance impacts the I-ITM PHiL performance under certain conditions (e.g., grid-synchronization). Selecting an inductive impedance for appropriate power transfer between the GFC and the grid in the simulated network within the conducted PHiL experiment has been noted to increase the system power tracking accuracy, especially after grid-synchronization.

7.6.5. Unbalanced Reference Replication in the Power Interface

In I-ITM interface technique, the power amplifier receives its current (or power) reference from the DRTS platform. In black-start and network energization studies, inrush currents are likely to be involved, which means the current reference can be highly unbalanced and rich in harmonics due to the non-symmetric inrush current nature. If the physical power amplifier is unable to replicate this reference due to its implemented control, then the hardware will not be able to track currents that correspond in shape to the irregularities generated in the DRTS. While this is not part of the VSM control implemented in the HuT, it still impacts the hardware performance since the GFC will not see similar conditions to these existing in the DRTS during inrush for its power exchange. An example is presented for illustration in Figure 7.18, where the reference current from the simulated network follows the asymmetrical inrush current form in Figure 7.18(a). However, the standard control implemented in the power amplifier converter (TP15kVA) is based on the synchronous frame PI tracking, which does not take harmonic components tracking into account in its basic form, resulting into the observed discrepancy in Figure 7.18(c). The power interface current control attempts to track the reference waveform with similar spiking trends but falls short of that due to its standard implemented control.

On the other hand, the control implemented in the power interface is able to track sinusoidal references appropriately as illustrated in Figure 7.18(b) and Figure 7.18(d). Understanding the control type implemented in the power amplifier interface thus becomes important if accurately studying such phenomenon is of an experimental interest, and the used power amplifier control on such occasions should be flexible and accessible to the user with the required measurements to implement different control structures.

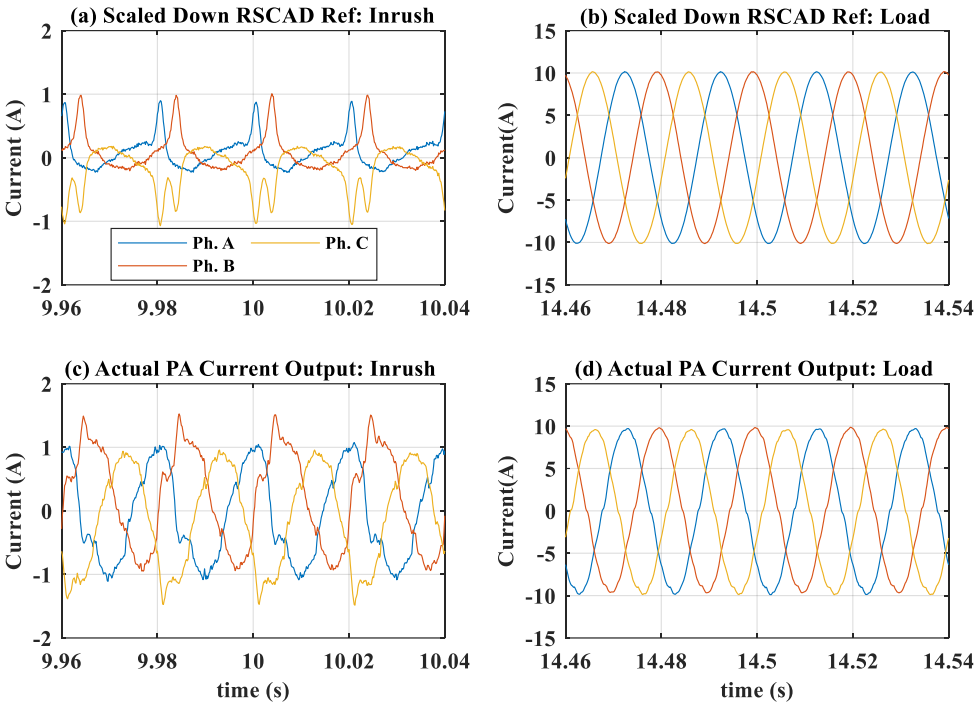

Figure 7.18: Impact of the current control implementation in the power interface amplifier on the current tracking performance under asymmetric and balanced reference conditions.

7.7. Summary

This chapter presented an investigation for the use of PHiL experimental testing of grid-forming converters for black-start and grid synchronization. This is believed to be one of the first reported tests for GFCs used in black-start with PHiL, and serves as a validation to the modified VSM control capabilities presented in the previous chapter. The successful demonstration of PHiL compatibility to black-start testing paves the way for more comprehensive experiments that can utilize industrial-scale converters in a controlled (non-destructive) environment, allowing for validating black-start scenarios in different simulated network configurations and connections. The key findings in this chapter are summarized in the following bullet points.

- I-ITM interfacing technique is used successfully for this PHiL experiment as it fits the application requirements and does not require the initial synchronization step between two voltage sources as is the case of V-ITM.

- In the conducted experiment, scaling ratio of 27.5 for voltage and 150 for current are applied, to utilize kW range hardware converter in energizing a simulated network rated in the MW range in real-time.
- A time-delay effect compensation method is proposed for I-ITM whereby the power references are sent from DRTS to PA instead of sinusoid currents, while implementing a synchronous frame compensation to neutralize the impact of any additional delays.
- A complete black-start scenario has been successfully carried out in PHiL, starting with soft energization and load pickup, followed by grid-synchronization and load disturbance. All while maintaining accurate reference tracking and stable operation.

On the other hand, the PHiL application is also prone to some challenges and limitations. Many of which were experienced during the reported experiment. The key lessons learned from the PHiL investigation were also reported in this chapter for the reader benefit.

Chapter 8 Conclusions and Future Work

8.1. Conclusions

This thesis presented extensive analysis for the use of grid-forming converters in black-start applications and the key factors impacting the technology utilization. The analysis considered the different stages of a black-start sequence from GFCs, starting from maintaining a reliable DC side supply through an innovative EMS design. The AC network energization requirements to comply with the limited VSCs overcurrent capabilities were addressed by looking into various inrush current mitigation techniques and identifying the ones suitable to converter-based black-start requirements. Suitable GFC controllers to achieve these requirements were also investigated and VSM control has been selected for the thesis investigations. Finally, PHiL has been proposed to facilitate flexible restoration experiments through hardware GFC under varying network conditions. The following subsections highlight key findings from the DC and AC networks, GFC control and PHiL testing standpoints.

8.1.1. DC Network Energy Management

GFCs can be supplied by a single or multiple sources through a common DC link. Given the emerging trend of DC networks for RES collection and distribution, a new energy management system has been proposed to maintain the DC side supply reliability and readiness to participate in AC network restoration following blackouts. The DC network EMS in this thesis maintains constant DC link voltage through shifting the RES operation between MPPT and VR modes based on the environmental, system loading, battery SoC and charge limits. A power sharing method between multiple RES that is activated in VR mode has been proposed for curtailment management. Black-start and grid-synchronization through GFC have been integrated within the EMS to achieve a smooth network restoration. The EMS has been validated through an array of case studies in MATLAB/Simulink (using two PV sources with power sharing functionality) and a centralized battery, in addition to successful laboratory validation of the MPPT-VR control mode switching of solar PV through a scaled-down experimental microgrid setup.

8.1.2. Transformers Inrush Current Mitigation

From the AC network side, the limited overcurrent capabilities of VSCs and the high transformer energization inrush currents were the basis to conduct a comprehensive investigation to identify and propose suitable transformer switching techniques for inrush current mitigation. Mathematical models were derived for constant-amplitude and ramping voltage sources to study their impact on inrush current mitigation. The derived models have been successfully benchmarked against industrial tools such as PSCAD/EMTDC with nearly identical behavior during the inrush transients. Hard transformer energization, PIR, controlled switching, and soft energization were tested and linked to the derived models to understand their operating patterns in inrush suppression.

A. Classical Techniques

PIR technique has been shown to be effective in inrush suppression but requires installing dedicated breakers, increasing the system cost and footprint. The impact of controlling the energizing angle α on inrush suppression through controlled switching has been presented, leading to inrush elimination when ϕ_r and ϕ_{prosp} are matching and access to single-pole circuit breakers is available. However, the availability of this breaker type with control relays is limited in distribution networks, and thus investigation of controlled switching through three-pole breakers has also been carried out in this thesis, where the three transformer phases are energized simultaneously. This technique has been shown to be quite effective in inrush suppression when the residual flux in the transformer core follows the pattern $[r, -r, 0]$ with a relatively high per-unit value for r (i.e., greater than 0.35-0.4 pu for the tested generic transformer in Chapter 4). Whereas applying the same technique with other ϕ_r combinations has been demonstrated to result into high inrush current due to the lack of simultaneous minimum flux error point across all phases. For instance, the demagnetized core case ($\phi_r = [0, 0, 0]$ pu) has been shown to have a minimum absolute global flux error of 0.866 pu throughout the $360°$ energization range, which would drive the transformer to deep saturation and draw high inrush currents that could exceed the unit rating in many cases.

B. Soft Energization

Given the arbitrary nature of the used soft transformer energization ramp-rate (T_{ramp}) in the literature, the question of soft energization ramp-rate appropriate setting has been addressed through a new proposed soft energization framework. The methodology considers the energizing GFC and transformer protection limits in its stopping criteria definition and is based on network model simulations. The framework can use supporting measurements such as ϕ_r for improved estimations. Though, the ramp-rate may also be estimated with limited access to such measurements through worst-case assumptions (e.g., high ϕ_r values). Both soft energization and controlled switching were benchmarked in a comprehensive case study in Chapter 4 with sensitivity analysis to quantify their merits and limitations. Soft energization has been shown to be effective in simultaneously energizing 50 MVA, 90 MVA and 20 MVA transformers with cable segments under various residual flux combinations without violating the GFC current or power ratings (15 MVA). The transformers residual fluxes were ranged between demagnetized cores (zero ϕ_r) and up to $\phi_r = [0.8, 0, -0.8]\, pu$. The stopping-criteria T_{ramp} has been estimated at 8 s for the base case. Sensitivity analysis demonstrated how this duration increased to 12 s when transformers core characteristic was varied to lower knee-point and steeper $\phi - i_m$ saturation slope. It has also been shown that applying a ramp-rate of 0.2 s was sufficient to energize the network with effectively eliminated inrush current in the case where all transformers were demagnetized. This shows the key impact of residual flux combinations on soft energization as a key influencing factor for T_{ramp} setting. Overall, soft energization has been identified as a suitable candidate for generic network energizations as it does not require additional control over circuit breakers.

8.1.3. GFC Control Techniques Investigation

Detailed assessment of four GFC control techniques (droop, PSC, matching and VSM) followed to identify suitable techniques that are compatible with soft energization and black-start requirements. The four controllers were tested against load disturbance, and step-changes in active power and DC voltage references, in addition to their capability to effectively track a ramping voltage reference. The analysis indicated that the four

techniques were essentially compatible with the requirements. VSM has been selected based on its resemblance of common SGs parameters such as virtual damping (D_p) and inertia (J) factors. The impact of inner-control loops incorporation into the VSM has then been shown through preliminary tests. Results revealed a perceived influence of current control on inrush characteristics in both MATLAB/Simulink and RSCAD/RTDS simulations. Dynamic adjustment of current control reference limit has been shown to influence the voltage once the current hits its saturation value, while simultaneously limiting peak inrush current from 4.54 pu without current control, to 0.86 pu when a current reference limit of 0.5 pu is applied to I_{dref} and I_{qref}. The preliminary observations are recommended for further theoretical analysis, and could potentially form a basis to a new inrush current suppression technique from GFCs that utilizes dynamic I_{dq} reference limits definition.

A modified VSM control structure has then been proposed with additional voltage support and grid-synchronization capabilities for black-start. The voltage support at the PCC utilizes the voltage measurement to compensate load-induced voltage drops through a PI control. A saturation limit on the VSM voltage reference is incorporated to avoid over-compensation to the steady-state voltage and to maintain it within the converter limits. The possible lack of direct access to real-time voltage measurement at the PCC has also been addressed by introducing a voltage estimation scheme based on Thevenin's circuit analysis. The grid-synchronization capability incorporation has been achieved and demonstrated based on the phase-error signal between the synchronizing voltages.

8.1.4. PHiL for Black-Start Testing of GFCs

The modified VSM capabilities were first demonstrated through a simulated case study for a complete black-start scenario including soft energization, load pickup and grid synchronization. Then, PHiL utilization for black-start testing of hardware GFCs has been validated through a current-type ITM interface that avoids the initial synchronization requirement at the hardware-side between the GFC and the power amplifier, as the latter operates here as a follower to the GFC voltage reference. Time-delay compensation in the synchronous frame has also been proposed. The experimental results showed a nearly

matching (scaled) behavior in real-time between the simulated network in the DRTS platform and the external GFC-PA hardware pair. The conducted experiments also demonstrated successful synchronization to a simulated grid in the DRTS platform. This reported success enables further comprehensive testing under flexible network configuration, while considering the reported PHiL limitations.

8.2. Research Contributions

Overall, the three elements of black-start from VSCs identified in the thesis introduction have been successfully addressed (DC side energy management, GFC control and AC network energization), through analysis and case studies that present key insights for readers from research and industrial backgrounds. The scientific contributions presented in this thesis are summarized as follows:

- Innovative energy management system proposal for maintaining DC networks supply reliability, considering different operating modes of RES assets to participate in DC voltage regulation. The EMS is also black-start compatible to allow for AC network restoration following blackout contingencies.
- Comprehensive analysis of transformer energization techniques, and derivation of a new theoretical transient model for soft-energization inrush current mitigation studies.
- Proposing and testing a new framework for soft energization voltage ramp-rate estimation, coupled with a detailed investigation of controlled transformer switching from three-pole circuit breakers in distribution networks.
- Proposing a modified VSM control, equipped with an altered $P - f$ loop (for grid synchronization) and $Q - V$ loop (for SE and PCC voltage support). In addition to a PCC voltage estimator based on Thevenin's equivalent circuit.
- Proposing PHiL experiments for black-start testing of GFCs, including the synchronization to the simulated grid in the DRTS platform. The utilized power interface technique (I-ITM) overcomes the initial synchronization requirement of V- ITM, which is typically used for grid-following converters testing.

8.3. Future Work

Based on the presented analysis, demonstrations and experiments in this thesis, future research routes are identified for the different themes covered by the thesis chapters. The recommended paths are listed below for each covered pillar.

8.3.1. DC Network Energy Management

Further work on the presented energy management system for the DC side of a GFC converter interfaced to a DC network may consider incorporating weather forecasts to dynamically adjust the storage SoC thresholds based on weather conditions and the expected RES output (e.g., day ahead prediction). Dynamic load demand forecasts may be similarly integrated to the EMS to support the load shedding and restoration planning through minimizing the shedding events, in addition to accelerating load restorations during network contingency events where the DC system is expected to operate in isolation for prolonged periods. The black-start objective can also be incorporated into a multi-objective EMS design that supports different operating conditions. For instance, shifting from preserving the system reliability in island mode to prioritizing the energy trading and economic aspects in grid-connected mode. Parallel operation of converters in grid-connected mode could also be considered to achieve optimized power sharing in a similar energy and ancillary services trading context.

8.3.2. Inrush Current Mitigation and GFC Control

Inner voltage and current loops that are cascaded to the outer GFC control output have been observed to positively influence the inrush current suppression in Chapter 5, at the perceived expense of highly volatile voltage. Further investigation to this technique feasibility as an inrush current mitigation technique is thus recommended to identify its limits and quantify the short-term voltage volatility behavior and impact. For instance, applying dynamic saturation limits to the current reference can be investigated. The reported behavior has been observed in both preliminary MATLAB/Simulink and RSCAD/RTDS tests using average VSC models to observe the generic trends. Detailed investigations using theoretical modeling and experimental tests are recommended as

future research routes to further validate the observations and link them to parameters such as the converter control modulation index and current control limits.

Another interesting investigation route is to identify inrush current mitigation techniques that are based on further exploitation of VSCs voltage control flexibility, such as using a dynamic ramp-rate based on transformer feedback measurements, or to investigate the possible role of interrogation signals applied to the interface transformer to extract its parameters and residual flux.

The modified VSM control proposed in this thesis for black-start applications may also be approached to address scenarios where the GFC is to be used as part of a converters cluster or for combined applications (e.g., to optimize power sharing and maintain adequate levels of inertia support at the different interconnection points).

8.3.3. PHiL Black-Start Testing

The reported PHiL tests in this thesis are based on a simplified simulated network in RSCAD/RTDS. Experimental validation using large-scale networks is thus suggested for future research using advanced DRTS platforms. This may also include utilizing multiple PHiL interface points, such as using two physical GFCs and power interfaces to establish two separate islands and synchronize their operation in a combined closed-loop PHiL configuration for black-start and ancillary services provision testing. Comparative analysis for different DRTS and PA platforms performance in the context of PHiL black-start testing with stability limits identification based on metrics such as time-delay is another suggested research path.

Identifying and proposing suitable current controllers that are able to produce accurate replicas of the reference power/current signals received from the used DRTS platform into the power amplifier interface is another possible route for PHiL black-start testing research. This is because classical synchronous dq0 frame control has been observed to fall short of replicating highly irregular and harmonics-rich current references such as those generated during transformer saturation.

References

[1] U. Tamrakar, D. Shrestha, M. Maharjan, P. B. Bhattarai, M. T. Hansen, and R. Tonkoski, "Virtual Inertia: Current Trends and Future Directions," *Applied Sciences,* vol. 7, no. 7, 2017.

[2] "New Energy Outlook 2019: Global Overivew," BNEF, 2019.

[3] J. Li, H. You, J. Qi, M. Kong, S. Zhang, and H. Zhang, "Stratified Optimization Strategy Used for Restoration With Photovoltaic-Battery Energy Storage Systems as Black-Start Resources," *IEEE Access,* vol. 7, pp. 127339-127352, 2019.

[4] F. F. Marie Petitet, Khalid Alhadhrami, "One Year After the Texas Blackout: Lessons for Reliable and Resilient Power Systems," KAPRSARC, Saudi Arabia, 2022.

[5] A. Ketabi, A. Karimizadeh, and M. Shahidehpour, "Optimal generation units start-up sequence during restoration of power system considering network reliability using bi-level optimization," *International Journal of Electrical Power & Energy Systems,* vol. 104, pp. 772-783, 2019.

[6] G. Patsakis, D. Rajan, I. Aravena, J. Rios, and S. Oren, "Optimal Black Start Allocation for Power System Restoration," *IEEE Transactions on Power Systems,* vol. PP, pp. 1-1, 05/22 2018.

[7] F. Blaabjerg, R. Teodorescu, M. Liserre, and A. V. Timbus, "Overview of Control and Grid Synchronization for Distributed Power Generation Systems," *IEEE Transactions on Industrial Electronics,* vol. 53, no. 5, pp. 1398-1409, 2006.

[8] R. H. Lasseter, Z. Chen, and D. Pattabiraman, "Grid-Forming Inverters: A Critical Asset for the Power Grid," *IEEE Journal of Emerging and Selected Topics in Power Electronics,* vol. 8, no. 2, pp. 925-935, 2020.

[9] J. Matevosyan *et al.*, "Grid-Forming Inverters: Are They the Key for High Renewable Penetration?," *IEEE Power and Energy Magazine,* vol. 17, no. 6, pp. 89-98, 2019.

[10] "Black Start from Non-Traditional Generation Technologies," National Grid, 2019.

[11] J. Wetzer. (2017) Transformer energisation after network blackout: Impact on network restoration and improvement of its process. *Transformers Magazine*.

[12] Z. S. Joukhah, "Operation of HVDC converters for transformer inrush current reduction," PhD Thesis, Electrical Engineering, Polytechnic University of Catalonia, 2017.

[13] Z. Chen, R. H. Lasseter, and T. M. Jahns, "Active Power Reserve Control for Grid-Forming PV Sources in Microgrids using Model-based Maximum Power Point Estimation," in *2019 IEEE ECCE Conference*, 2019, pp. 41-48.

[14] B. Pawar, E. I. Batzelis, S. Chakrabarti, and B. C. Pal, "Grid-Forming Control for Solar PV Systems With Power Reserves," *IEEE Transactions on Sustainable Energy,* vol. 12, no. 4, pp. 1947-1959, 2021.

[15] P. Hu *et al.*, "A Novel Grid-Forming Strategy for Voltage-Source Controlled PV Under Nearly 100% Renewable Electricity," *Frontiers in Energy Research,* Original Research vol. 10, 2022.

[16] M. Shahparasti, H. Laaksonen, K. Kauhaniemi, P. Lauttamus, S. Strandberg, and J. Strandberg, "Inrush Current Management During Medium Voltage Microgrid Black Start with Battery Energy Storage System," *IEEE Access,* pp. 1-1, 2022.

[17] A. Roscoe *et al.*, "Practical Experience of Providing Enhanced Grid Forming Services from an Onshore Wind Park," 2019.

[18] R. Ierna *et al.*, "Dispatching parameters, strategies and associated algorithm for VSM (virtual synchronous machines) and HGFC (hybrid grid forming convertors)," 2019.

[19] "MVDC Plus: Medium Voltage Direct Current Managing the Future Grid " Siemens, 2017.

[20] J. K. Steinke, P. Maibach, G. Ortiz, F. Canales, and P. Steimer, "MVDC Applications and Technology," in *PCIM Europe 2019.* 2019, pp. 1-8.

[21] S. Coffey, V. Timmers, R. Li, G. Wu, and A. Egea-Àlvarez, "Review of MVDC Applications, Technologies, and Future Prospects," *Energies*, vol. 14, no. 24.

[22] H. Aki, "Demand-Side Resiliency and Electricity Continuity: Experiences and Lessons Learned in Japan," *Proceedings of the IEEE,* vol. 105, no. 7, pp. 1443-1455, 2017.

[23] C. Marnay, H. Aki, K. Hirose, A. Kwasinski, S. Ogura, and T. Shinji, "Japan's Pivot to Resilience: How Two Microgrids Fared After the 2011 Earthquake," *IEEE Power and Energy Magazine,* vol. 13, no. 3, pp. 44-57, 2015.

[24] J. Kumar, A. Agarwal, and N. Singh, "Design, operation and control of a vast DC microgrid for integration of renewable energy sources," *Renewable Energy Focus,* vol. 34, pp. 17-36, 2020.

[25] S. Augustine, M. K. Mishra, and N. Lakshminarasamma, "A Unified Control Scheme for a Standalone Solar-PV Low Voltage DC Microgrid System With HESS," *IEEE Journal of Emerging and Selected Topics in Power Electronics,* vol. 8, no. 2, pp. 1351-1360, 2020.

[26] S. Sahoo, S. Mishra, S. Jha, and B. Singh, "A Cooperative Adaptive Droop Based Energy Management and Optimal Voltage Regulation Scheme for DC Microgrids," *IEEE Transactions on Industrial Electronics,* vol. 67, no. 4, pp. 2894-2904, 2020.

[27] A. Alassi and O. Ellabban, "Design of an Intelligent Energy Management System for Standalone PV/Battery DC Microgrids," in *2019 2nd IEEE SGRE Conference*, 19-21 Nov. 2019 2019, pp. 1-7.

[28] P. J. d. S. Neto, T. A. d. S. Barros, J. P. C. Silveira, E. R. Filho, J. C. Vasquez, and J. M. Guerrero, "Power Management Strategy Based on Virtual Inertia for DC Microgrids," *IEEE Transactions on Power Electronics,* vol. 35, no. 11, pp. 12472-12485, 2020.

[29] L. G. Marín *et al.*, "Hierarchical Energy Management System for Microgrid Operation Based on Robust Model Predictive Control," *Energies,* vol. 12, no. 23, 2019.

[30] L. O. P. Vásquez, V. M. Ramírez, and K. Thanapalan, "A Comparison of Energy Management System for a DC Microgrid," *Applied Sciences,* vol. 10, no. 3, 2020.

[31] B. Benlahbib *et al.*, "Experimental investigation of power management and control of a PV/wind/fuel cell/battery hybrid energy system microgrid," *International Journal of Hydrogen Energy,* vol. 45, no. 53, pp. 29110-29122, 2020.

[32] P. J. dos Santos Neto, T. A. S. Barros, J. P. C. Silveira, E. Ruppert Filho, J. C. Vasquez, and J. M. Guerrero, "Power management techniques for grid-connected DC microgrids: A comparative evaluation," *Applied Energy,* vol. 269, p. 115057, 2020.

[33] H. Matayoshi, M. Kinjo, S. S. Rangarajan, G. G. Ramanathan, A. M. Hemeida, and T. Senjyu, "Islanding operation scheme for DC microgrid utilizing pseudo Droop control of photovoltaic system," *Energy for Sustainable Development,* vol. 55, pp. 95-104, 2020.

[34] S. Batiyah, R. Sharma, S. Abdelwahed, and N. Zohrabi, "An MPC-based power management of standalone DC microgrid with energy storage," *International Journal of Electrical Power & Energy Systems,* vol. 120, p. 105949, 2020.

[35] B. Liu, F. Zhuo, Y. Zhu, and H. Yi, "System Operation and Energy Management of a Renewable Energy-Based DC Micro-Grid for High Penetration Depth Application," *IEEE Transactions on Smart Grid,* vol. 6, no. 3, pp. 1147-1155, 2015.

[36] A. Mirzaei, M. Forooghi, A. A. Ghadimi, A. H. Abolmasoumi, and M. R. Riahi, "Design and construction of a charge controller for stand-alone PV/battery hybrid system by using a new control strategy and power management," *Solar Energy,* vol. 149, pp. 132-144, 2017.

[37] H. Cai, J. Xiang, and W. Wei, "Decentralized Coordination Control of Multiple Photovoltaic Sources for DC Bus Voltage Regulating and Power Sharing," *IEEE Transactions on Industrial Electronics,* vol. 65, no. 7, pp. 5601-5610, 2018.

[38] N. Chowdhury, F. Pilo, and G. Pisano, "Optimal Energy Storage System Positioning and Sizing with Robust Optimization," *Energies,* vol. 13, no. 3, 2020.

[39] O. Ellabban and A. Alassi, "Optimal hybrid microgrid sizing framework for the mining industry with three case studies from Australia," *IET Renewable Power Generation,* vol. 15, no. 2, pp. 409-423, 2021.

[40] J. Wei, Y. Zhang, J. Wang, X. Cao, and M. A. Khan, "Multi-period planning of multi-energy microgrid with multi-type uncertainties using chance constrained information gap decision method," *Applied Energy,* vol. 260, p. 114188, 2020.

[41] H. Cui, F. Li, X. Fang, H. Chen, and H. Wang, "Bilevel Arbitrage Potential Evaluation for Grid-Scale Energy Storage Considering Wind Power and LMP Smoothing Effect," *IEEE Transactions on Sustainable Energy,* vol. 9, no. 2, pp. 707-718, 2018.

[42] J. W. Shim, G. Verbič, N. Zhang, and K. Hur, "Harmonious Integration of Faster-Acting Energy Storage Systems Into Frequency Control Reserves in Power Grid With High Renewable Generation," *IEEE Transactions on Power Systems,* vol. 33, no. 6, pp. 6193-6205, 2018.

[43] W.-Y. Chang, "The State of Charge Estimating Methods for Battery: A Review," *ISRN Applied Mathematics,* vol. 2013, p. 953792, 2013.

[44] D. Pagnani, F. Blaabjerg, C. L. Bak, F. M. Faria da Silva, Ł. H. Kocewiak, and J. Hjerrild, "Offshore Wind Farm Black Start Service Integration: Review and Outlook of Ongoing Research," *Energies,* vol. 13, no. 23, 2020.

[45] A. Alassi and A. Massoud, "High-gain DC-DC converters for high-power PV applications: Performance assessment," in *IEEE 12th International Conference on Compatibility, Power Electronics and Power Engineering (CPE-POWERENG)*, 2018, pp. 1-6.

[46] A. Alassi, A. Al-Aswad, A. Gastli, L. B. Brahim, and A. Massoud, "Assessment of Isolated and Non-Isolated DC-DC Converters for Medium-Voltage PV Applications," in *2017 9th IEEE GCCCE Conference*, 2017, pp. 1-6.

[47] N. Denniston, A. M. Massoud, S. Ahmed, and P. N. Enjeti, "Multiple-Module High-Gain High-Voltage DC–DC Transformers for Offshore Wind Energy Systems," *IEEE Transactions on Industrial Electronics,* vol. 58, no. 5, pp. 1877-1886, 2011.

[48] "Instrument Transformers: Application Guide," ABB Ludvika, Sweden, 2015.

[49] U. Parikh and B. R. Bhalja, "Mitigation of magnetic inrush current during controlled energization of coupled un-loaded power transformers in presence of residual flux without load side voltage measurements," *International Journal of Electrical Power & Energy Systems,* vol. 76, pp. 156-164, 2016.

[50] *Network Standard Standard for Plant Energisation*, C. Green, 2022.

[51] W. Ge, Y. Wang, Z. Zhao, X. Yang, and Y. Li, "Residual Flux in the Closed Magnetic Core of a Power Transformer," *IEEE Transactions on Applied Superconductivity,* vol. 24, no. 3, pp. 1-4, 2014.

[52] Y. Pan, X. Yin, Z. Zhang, B. Liu, M. Wang, and X. Yin, "Three-Phase Transformer Inrush Current Reduction Strategy Based on Prefluxing and Controlled Switching," *IEEE Access,* vol. 9, pp. 38961-38978, 2021.

[53] W. Neves, "Transformer Modeling for Transient Studies," PhD Thesis, Department of Electrical Engineering, The University of British Columbia, 1994.

[54] J. Faiz and S. Saffari, "Inrush Current Modeling in a Single-Phase Transformer," *IEEE Transactions on Magnetics,* vol. 46, no. 2, pp. 578-581, 2010.

[55] A. V. Radun, "Development of Dynamic Magnetic Circuit Models Including Iron Saturation and Losses," *IEEE Transactions on Magnetics,* vol. 50, no. 5, pp. 1-10, 2014.

[56] K. Deželak, M. Petrun, M. Rošer, D. Dolinar, and G. Štumberger, "The Impact of Iron Core Model on Dynamic Behavior of Three-Phase Power Transformer Dynamic Model," *IEEE Transactions on Magnetics,* vol. 51, no. 1, pp. 1-4, 2015.

[57] J. E. Holcomb, "Distribution Transformer Magnetizing Inrush Current," *Transactions of the American Institute of Electrical Engineers. Part III: Power Apparatus and Systems,* vol. 80, no. 3, pp. 697-702, 1961.

[58] Y. Wang, S. G. Abdulsalam, and W. Xu, "Analytical Formula to Estimate the Maximum Inrush Current," *IEEE Transactions on Power Delivery,* vol. 23, no. 2, pp. 1266-1268, 2008.

[59] S. Jazebi, F. d. León, and N. Wu, "Enhanced Analytical Method for the Calculation of the Maximum Inrush Currents of Single-Phase Power Transformers," *IEEE Transactions on Power Delivery,* vol. 30, no. 6, pp. 2590-2599, 2015.

[60] J. H. Brunke and K. J. Frohlich, "Elimination of transformer inrush currents by controlled switching. II. Application and performance considerations," *IEEE Transactions on Power Delivery,* vol. 16, no. 2, pp. 281-285, 2001.

[61] D. Bejmert, M. Kereit, and K. Boehme, "Controlled energization procedures of power transformers," *International Journal of Electrical Power & Energy Systems,* vol. 135, p. 107555, 2022.

[62] "PSCAD/EMTDC User Manual - Power Transformers: The Classical Approach," MHI.

[63] "MATLAB/Simulink User Manual: Saturable Transformer."

[64] J. Mitra, X. Xu, and M. Benidris, "Reduction of Three-Phase Transformer Inrush Currents Using Controlled Switching," *IEEE Transactions on Industry Applications,* vol. 56, no. 1, pp. 890-897, 2020.

[65] "Distributed ReStart: Power Engineering and Trials - Demonstration of Black Start from DERs Part 1," National Grid ESO, UK, 2021.

[66] F. Peng, H. Gao, and Y. Liu, "Transformer Sympathetic Inrush Characteristics and Identification Based on Substation-Area Information," *IEEE Transactions on Power Delivery,* vol. 33, no. 1, pp. 218-228, 2018.

[67] A. Jain, O. Saborio-Romano, J. N. Sakamuri, and N. A. Cutululis, "Virtual Resistance Control for Sequential Green-start of Offshore Wind Power Plants," *IEEE Transactions on Sustainable Energy,* pp. 1-1, 2022.

[68] Y. Guo, Z. Zheng, Q. Xie, and J. Zhao, "Study of Resistive Type SFCL for Limiting Inrush Current of LCC-HVDC Converter Transformer," *IEEE Transactions on Applied Superconductivity,* vol. 31, no. 8, pp. 1-4, 2021.

[69] A. Jain, O. Saborío-Romano, J. N. Sakamuri, and N. A. Cutululis, "Blackstart from HVDC-connected offshore wind: Hard versus soft energization," *IET Renewable Power Generation,* vol. 15, no. 1, pp. 127-138, 2021.

[70] C. Yu, S. G. Abdulsalam, C. Shiuming, and X. Wilsun, "A sequential phase energization technique for transformer inrush current reduction - Part I: Simulation and experimental results," *IEEE Transactions on Power Delivery,* vol. 20, no. 2, pp. 943-949, 2005.

[71] X. Wilsun, S. Abdulsalam, C. Yu, and L. Xian, "A sequential phase energization technique for transformer inrush current reduction part II: theoretical analysis and design guide," in *IEEE Power Engineering Society General Meeting, 2004.*, 6-10 June 2004 2004, p. 534 Vol.1.

[72] K. A. Bhatt, B. R. Bhalja, and U. B. Parikh, "Evaluation of controlled energisation of an unloaded power transformer for minimising the level of inrush current and transient voltage distortion using PIR-CBs," *IET Generation, Transmission & Distribution,* vol. 12, no. 11, pp. 2788-2798, 2018.

[73] C. P. J. Jansen, J. G. Slootweg, and R. A. C. T. d. Groot, "Calculation of Transformer Inrush Currents occurring during the Energizing of the Public Grid after a major Black Out," in *2005 IEEE Russia Power Tech*, 27-30 June 2005 2005, pp. 1-7.

[74] S. McGuinness *et al.*, "Coordination of AC protection settings during energisation of AC grid from a VSC HVDC interconnector," *15th DPSP Conference*, Liverpool, UK, 2020, pp. 1-6.

[75] J. Glassmire, S. Cherevatskiy, G. Antonova, and A. Fretwell, "Using Virtual Synchronous Generators to Resolve Microgrid Protection Challenges," in *2021 74th Conference for Protective Relay Engineers (CPRE)*, 2021, pp. 1-7.

[76] J. L. Rodríguez-Amenedo, S. A. Gómez, J. C. Martínez, and J. Alonso-Martinez, "Black-Start Capability of DFIG Wind Turbines Through a Grid-Forming Control Based on the Rotor Flux Orientation," *IEEE Access,* vol. 9, pp. 142910-142924, 2021.

[77] R. Oyanagi, T. Noda, and M. Ichikawa, "A Method for Estimating the Current–Flux Curve of a Single-Phase Transformer for Electromagnetic Transient Simulations of Inrush Currents," *Electrical Engineering in Japan,* vol. 204, no. 2, pp. 13-24, 2018.

[78] R. Cano-González, A. Bachiller-Soler, J. A. Rosendo-Macías, and G. Álvarez-Cordero, "Controlled switching strategies for transformer inrush current reduction: A comparative study," *Electric Power Systems Research,* vol. 145, pp. 12-18, 2017.

[79] R. Cano-González, A. Bachiller-Soler, J. A. Rosendo-Macías, and G. Álvarez-Cordero, "Optimal gang-operated switching for transformer inrush current reduction," *Electric Power Systems Research,* vol. 131, pp. 80-86, 2016.

[80] N. Chiesa and H. K. Høidalen, "Novel Approach for Reducing Transformer Inrush Currents: Laboratory Measurements, Analytical Interpretation and Simulation Studies," *IEEE Transactions on Power Delivery,* vol. 25, no. 4, pp. 2609-2616, 2010.

[81] P. Pachore, Y. Gupta, S. Anand, S. Sarkar, P. Mathur, and P. K. Singh, "Flux Error Function Based Controlled Switching Method for Minimizing Inrush Current in 3-Phase Transformer," *IEEE Transactions on Power Delivery,* vol. 36, no. 2, pp. 870-879, 2021.

[82] T. Canal, F.-X. Zgainski, and V.-L. Renouard, "Determination of the saturation curve of power transformers by processing transient measurements," *Electric Power Systems Research,* vol. 195, p. 107153, 2021.

[83] Z. M. Khurshid, N. F. A. Aziz, Z. A. Rhazali, and M. Z. A. A. Kadir, "Impact of Geomagnetically Induced Currents on High Voltage Transformers in Malaysian Power Network and Its Mitigation," *IEEE Access,* vol. 9, pp. 167204-167217, 2021.

[84] S. E. Zirka, D. Albert, Y. I. Moroz, and H. Renner, "Further Improvements in Topological Transformer Model Covering Core Saturation," *IEEE Access,* vol. 10, pp. 64018-64027, 2022.

[85] J. H. Brunke and K. J. Frohlich, "Elimination of transformer inrush currents by controlled switching. I. Theoretical considerations," *IEEE Transactions on Power Delivery,* vol. 16, no. 2, pp. 276-280, 2001.

[86] "Distributed ReStart: Power Engineering and Trials - Power Systems Studies Part 1," National Grid ESO, UK, 2020.

[87] G. Benmouyal, N. Fischer, D. Taylor, M. Talbott-Williams, and R. Chowdhury, "A Unified Approach to Controlled Switching of Power Equipment," in *72nd Annual Georgia Tech Protective Relaying Conference*, USA, 2018.

[88] I. Lafaia, M. T. C. de Barros, J. Mahseredjian, A. Ametani, I. Kocar, and Y. Fillion, "Surge and energization tests and modeling on a 225kV HVAC cable," *Electric Power Systems Research,* vol. 160, pp. 273-281, 2018.

[89] T. Rastall, "SynchroTeq - 3-Pole Transformer Switching," Enspec, United Kingdom, 2020.

[90] M. Aten, R. Shanahan, F. Mosallat, and S. Wijesinghe, "Dynamic Simulations of a Black Starting Offshore Wind Farm Using Grid Forming Converters," presented at the 18th Wind Integration Workshop, Dublin, 2019.

[91] O. Schomann, "Experiences With Large Grid-Forming Inverters on Various Island and Microgrid Projects," in *Hybrid Power Systems Workshop*, Crete, 2019.

[92] M. Ashabani, F. D. Freijedo, S. Golestan, and J. M. Guerrero, "Inducverters: PLL-Less Converters With Auto-Synchronization and Emulated Inertia Capability," *IEEE Transactions on Smart Grid,* vol. 7, no. 3, pp. 1660-1674, 2016.

[93] D. Pan, X. Wang, F. Liu, and R. Shi, "Transient Stability of Voltage-Source Converters With Grid-Forming Control: A Design-Oriented Study," *IEEE Journal of Emerging and Selected Topics in Power Electronics,* vol. 8, no. 2, pp. 1019-1033, 2020.

[94] B. K. Poolla, D. Groß, and F. Dörfler, "Placement and Implementation of Grid-Forming and Grid-Following Virtual Inertia and Fast Frequency Response," *IEEE Transactions on Power Systems,* vol. 34, no. 4, pp. 3035-3046, 2019.

[95] R. Rosso, S. Engelken, and M. Liserre, "Robust Stability Investigation of the Interactions Among Grid-Forming and Grid-Following Converters," *IEEE Journal of Emerging and Selected Topics in Power Electronics,* vol. 8, no. 2, pp. 991-1003, 2020.

[96] A. Tayyebi, D. Groß, A. Anta, F. Kupzog, and F. Dörfler, "Frequency Stability of Synchronous Machines and Grid-Forming Power Converters," *IEEE Journal of Emerging and Selected Topics in Power Electronics,* vol. 8, no. 2, pp. 1004-1018, 2020.

[97] J. Fang, H. Li, Y. Tang, and F. Blaabjerg, "Distributed Power System Virtual Inertia Implemented by Grid-Connected Power Converters," *IEEE Transactions on Power Electronics,* vol. 33, no. 10, pp. 8488-8499, 2018.

[98] J. Rocabert, A. Luna, F. Blaabjerg, and P. Rodríguez, "Control of Power Converters in AC Microgrids," *IEEE Transactions on Power Electronics,* vol. 27, no. 11, pp. 4734-4749, 2012.

[99] A. Timbus, M. Liserre, R. Teodorescu, P. Rodriguez, and F. Blaabjerg, "Evaluation of Current Controllers for Distributed Power Generation Systems," *IEEE Transactions on Power Electronics,* vol. 24, no. 3, pp. 654-664, 2009.

[100] C. J. O'Rourke, M. M. Qasim, M. R. Overlin, and J. L. Kirtley, "A Geometric Interpretation of Reference Frames and Transformations: dq0, Clarke, and Park," *IEEE Transactions on Energy Conversion,* vol. 34, no. 4, pp. 2070-2083, 2019.

[101] N. Pogaku, M. Prodanovic, and T. C. Green, "Modeling, Analysis and Testing of Autonomous Operation of an Inverter-Based Microgrid," *IEEE Transactions on Power Electronics,* vol. 22, no. 2, pp. 613-625, 2007.

[102] L. Zhang, L. Harnefors, and H. Nee, "Power-Synchronization Control of Grid-Connected Voltage-Source Converters," *IEEE Transactions on Power Systems,* vol. 25, no. 2, pp. 809-820, 2010.

[103] A. Khan, M. hosseinzadehtaher, M. B. Shadmand, S. Bayhan, and H. Abu-Rub, "On Stability of Power Electronics Dominated Grid," *IEEE Industrial Electronics Magazine,* vol. 14, no. 2, 2020.

[104] Y. Li and Y. W. Li, "Power Management of Inverter Interfaced Autonomous Microgrid Based on Virtual Frequency-Voltage Frame," *IEEE Transactions on Smart Grid,* vol. 2, no. 1, pp. 30-40, 2011.

[105] Q. Zhong, W. Ming, and Y. Zeng, "Self-Synchronized Universal Droop Controller," *IEEE Access,* vol. 4, pp. 7145-7153, 2016.

[106] W. Du *et al.*, "A Comparative Study of Two Widely Used Grid-Forming Droop Controls on Microgrid Small-Signal Stability," *IEEE Journal of Emerging and Selected Topics in Power Electronics,* vol. 8, no. 2, pp. 963-975, 2020.

[107] C. Arghir, T. Jouini, and F. Dörfler, "Grid-forming control for power converters based on matching of synchronous machines," *Automatica,* vol. 95, pp. 273-282, 2018.

[108] C. Arghir and F. Dörfler, "The Electronic Realization of Synchronous Machines: Model Matching, Angle Tracking, and Energy Shaping Techniques," *IEEE Transactions on Power Electronics,* vol. 35, no. 4, pp. 4398-4410, 2020.

[109] Q. Zhong and G. Weiss, "Synchronverters: Inverters That Mimic Synchronous Generators," *IEEE Transactions on Industrial Electronics,* vol. 58, no. 4, pp. 1259-1267, 2011.

[110] W. Wu *et al.*, "A Virtual Inertia Control Strategy for DC Microgrids Analogized With Virtual Synchronous Machines," *IEEE Transactions on Industrial Electronics,* vol. 64, no. 7, pp. 6005-6016, 2017.

[111] A. Abdelrahim, M. Smailes, K. H. Ahmed, P. Mckeever, and A. Egea-Àlvarez, "New Fault Detection Algorithm for an Improved Dual VSM Control Structure With FRT Capability," *IEEE Access,* vol. 9, pp. 125134-125150, 2021.

[112] A. Alassi, S. Bañales, O. Ellabban, G. Adam, and C. MacIver, "HVDC Transmission: Technology Review, Market Trends and Future Outlook," *Renewable and Sustainable Energy Reviews,* vol. 112, pp. 530-554, 2019.

[113] M. Ahmed, L. Meegahapola, A. Vahidnia, and M. Datta, "Analyzing the Effect of X/R ratio on Dynamic Performance of Microgrids," in *2019 IEEE PES Innovative Smart Grid Technologies Europe (ISGT-Europe)*, 2019, pp. 1-5.

[114] P. S. Wright, P. N. Davis, K. Johnstone, G. Rietveld, and A. J. Roscoe, "Field Measurement of Frequency and ROCOF in the Presence of Phase Steps," *IEEE Transactions on Instrumentation and Measurement,* vol. 68, no. 6, pp. 1688-1695, 2019.

[115] Guglielmo Frigo, "Rate of Change of Frequency: Measurement Challenges and Potential Applications," *Swiss Federal Institute of Metrology (METAS)*, 2020.

[116] J. Chen, F. Prystupczuk, and T. O. Donnell, "Use of voltage limits for current limitations in grid-forming converters," *CSEE Journal of Power and Energy Systems,* vol. 6, no. 2, pp. 259-269, 2020.

[117] J. Liu *et al.*, "An OLTC-inverter coordinated voltage regulation method for distribution network with high penetration of PV generations," *International Journal of Electrical Power & Energy Systems,* vol. 113, pp. 991-1001, 2019.

[118] H. A. Khan, M. Zuhaib, and M. Rihan, "Voltage fluctuation mitigation with coordinated OLTC and energy storage control in high PV penetrating distribution network," *Electric Power Systems Research,* vol. 208, p. 107924, 2022.

[119] D. L. Ransom, "Get in Step With Synchronization," *IEEE Transactions on Industry Applications,* vol. 50, no. 6, pp. 4210-4215, 2014.

[120] A. Vukojevic and S. Lukic, "Microgrid Protection and Control Schemes for Seamless Transition to Island and Grid Synchronization," *IEEE Transactions on Smart Grid,* vol. 11, no. 4, pp. 2845-2855, 2020.

[121] J. Wang, B. Lundstrom, and A. Bernstein, "Design of a Non-PLL Grid-forming Inverter for Smooth Microgrid Transition Operation," in *2020 IEEE PESGM Conference*, 2020.

[122] J. Wang, A. Pratt, and M. Baggu, "Integrated Synchronization Control of Grid-Forming Inverters for Smooth Microgrid Transition," in *2019 IEEE PESGM Conference*, 2019.

[123] C. Lee, R. Jiang, and P. Cheng, "A Grid Synchronization Method for Droop-Controlled Distributed Energy Resource Converters," *IEEE Transactions on Industry Applications,* vol. 49, no. 2, pp. 954-962, 2013.

[124] J. F. Morris, K. H. Ahmed, and A. Egea-Àlvarez, "Power-Synchronization Control for Ultra-Weak AC Networks: Comprehensive Stability and Dynamic Performance Assessment," *IEEE Open Journal of the Industrial Electronics Society,* vol. 2, pp. 441-450, 2021.

[125] G. Li *et al.*, "An improved DIM interface algorithm for the MMC-HVDC power hardware-in-the-loop simulation system," *International Journal of Electrical Power & Energy Systems,* vol. 99, pp. 69-78, 2018.

[126] S. Karrari, G. De Carne, and M. Noe, "Adaptive droop control strategy for Flywheel Energy Storage Systems: A Power Hardware-in-the-Loop validation," *Electric Power Systems Research,* vol. 212, p. 108300, 2022.

[127] E. García-Martínez, J. F. Sanz, J. Muñoz-Cruzado, and J. M. Perié, "Online database of Power Hardware In-the-Loop tests," *Data in Brief,* vol. 29, p. 105128, 2020.

[128] E. García-Martínez, J. F. Sanz, J. Muñoz-Cruzado, and J. M. Perié, "A Review of PHIL Testing for Smart Grids—Selection Guide, Classification and Online Database Analysis," *Electronics,* vol. 9, no. 3, p. 382, 2020.

[129] J. Hernandez-Alvidrez, N. S. Gurule, M. J. Reno, J. D. Flicker, A. Summers, and A. Ellis, "Method to Interface Grid-Forming Inverters into Power Hardware in the Loop Setups," in *47th IEEE PVSC Conference*, 2020, pp. 1804-1810.

[130] M. Bokal, I. Papič, and B. Blažič, "Stabilization of Hardware-in-the-Loop Ideal Transformer Model Interfacing Algorithm by Using Spectrum Assignment," *IEEE Transactions on Power Delivery,* vol. 34, no. 5, pp. 1865-1873, 2019.

[131] S. Resch, J. Friedrich, T. Wagner, G. Mehlmann, and M. Luther, "Stability Analysis of Power Hardware-in-the-Loop Simulations for Grid Applications," *Electronics,* vol. 11, no. 1, p. 7, 2022.

[132] Z. Feng, A. Alassi, M. Syed, R. Peña-Alzola, K. Ahmed, and G. Burt, "Current-Type Power Hardware-in-the-Loop Interface for Black-Start Testing of Grid-Forming Converter," in *IECON 2022*, Brussels, 17-20 2022.

[133] E. G. Sansano, "Novel methods for enhancing accuracy and stability of power hardware-in-the-loop simulations," PhD Thesis, Electronic and Electrical Engineering, University of Strathclyde, 2018.

[134] R. Brandl, "Operational Range of Several Interface Algorithms for Different Power Hardware-In-The-Loop Setups," *Energies,* vol. 10, no. 12, p. 1946, 2017.

[135] J. Ihrens, S. Möws, L. Wilkening, T. A. Kern, and C. Becker, "The Impact of Time Delays for Power Hardware-in-the-Loop Investigations," *Energies,* vol. 14, no. 11, p. 3154, 2021.

[136] "*Real Time Digital Simulator: Power System User's Manual"*, RTDS Technologies, 2012.